UNIVERSITÀ
DEGLI STUDI DI BARI
ALDO MORO

UNIVERSITA' DEGLI STUDI DI BARI ALDO MORO

Dipartimento di Chimica

DOTTORATO DI RICERCA IN SCIENZE CHIMICHE E MOLECOLARI

CICLO XXXVIII

Settore Scientifico Disciplinare CHEM-01/B

TITOLO TESI (approvato dal Collegio dei Docenti)

Approcci integrativi alla laser ablation ICP-MS: miglioramento della fedeltà del segnale e dell'accuratezza dell'imaging su materiali eterogenei

---

Dottoranda: Dott.ssa Cinzia Chiurlia

Firmato da:
CINZIA CHIURLIA
Data e ora: 11/01/2026 18:45:53
Indirizzo IP: 94.166.140.36

Supervisori : Prof.ssa Annarosa Mangone &

Prof.ssa Lorena Carla Giannossa

Annarosa Mangone
12.01.2026
08:00:22
UTC

PIETRO
FAVIA
19.01.2026
08:55:11
GMT+00:00

Coordinatore: Prof. Pietro Favia

LORENA
CARLA
GIANNOSSA
12.01.2026
09:58:54
GMT+01:00

ESAME FINALE 2026

UNIVERSITÀ DEGLI STUDI DI BARI ALDO MORO
DIPARTIMENTO DI CHIMICA

UNIVERSITY OF BARI "ALDO MORO"

DEPARTMENT OF CHEMISTRY

PhD in CHEMICAL AND MOLECULAR SCIENCES

XXXVIII cycle

Integrative Approaches to Laser Ablation ICP-MS: Enhancing Signal Fidelity and Imaging Accuracy Across Diverse Materials

Thesis Supervisor:

Prof. Annarosa Mangone

Prof. Lorena Carla Giannossa

Ph. D. Student:

Cinzia Chiurlia

Coordinator:

Prof. Pietro Favia

Part of the research for this PhD thesis was conducted at "National Institute of Chemistry" of Ljubljana, under the supervision of Dr. Martin Šala



TABLE OF CONTENTS

Abstract 1

CHAPTER 1 2

1.1 LA-ICP-MS 2

1.1.1 Laser sources 3

1.1.2 Ablation cell and transport system 3

1.1.3 ICP-MS system 5

1.2 State of the art: LA process and related disadvantages 6

1.2.1 LA process 6

1.2.2 Optimizing parameters to mitigate Elemental Fractionation and enhance analytical accuracy 7

1.2.3 Matrix effect, calibration and Internal Standard 12

CHAPTER 2 19

2.1 Imaging: state of the art 19

2.2 Fine-tuning of parameters 20

CHAPTER 3 26

3.1 Nanoparticle-Assisted Signal Enhancement 26

3.2 Application of Nanoparticles in laser-based spectroscopies 27

CHAPTER 4 33

4.1 Case study: glass artifacts founded at “Masseria Caione” 33

4.1.1 Glass: state of the art 33

4.1.2 Archaeological framework 34

4.1.3 Materials and methods 36

4.1.4 Results and discussion 38

4.1.5 Conclusions 47
4.2 Case study: certified human serum 47
4.2.1 Why LA-ICP-MS Matters 47
4.2.2 Evaluation of Gelatine as a Matrix-Matched Standard for Human Serum 49
4.2.2.1 Reagents and calibration standards 49
4.2.2.2 Dried serum and gelatines spot sample preparation 50
4.2.2.3 LA-ICP-MS Methodology 51
4.2.2.4 Results and discussion 55
4.2.3 PtNPs as signal enhancers for Serum Trace Elements 60
4.2.3.1 Materials and methods 61
4.2.3.2 Results and discussion 63
4.2.4 Conclusions 74

APPENDIX 79

ABSTRACT

Laser Ablation Inductively Coupled Plasma Mass Spectrometry (LA-ICP-MS) has emerged as a powerful tool for multi-elemental analysis across diverse sample matrices, from inorganic archaeological specimens to complex biological fluids. This study presents two representative case studies illustrating the technique's adaptability and analytical power. In the archaeological glass analysis, high-resolution LA-ICP-MS enabled the reconstruction of raw material provenance, technological practices, and post-depositional alteration processes, revealing compositional heterogeneity, recycling practices, and insights into Mediterranean and Middle Eastern trade networks. Depth-resolved mapping allowed the distinction between surface corrosion layers and bulk glass chemistry, providing unprecedented detail on elemental mobility and protective mechanisms within altered glass. For biological matrices, specifically human serum, we evaluated the challenges posed by matrix effects and trace-level analytes. Standardization strategies included non–matrix-matched calibration with droplet volume correction, while signal enhancement was achieved through platinum nanoparticles (Pt NPs) produced by pulsed laser ablation in liquid. Pt NPs improved analyte ionization and signal-to-noise ratios, allowing the reliable detection of essential and toxic elements at low-ppb concentrations. Comparative studies with LIBS highlighted the advantages of nanoparticle-assisted LA-ICP-MS in sensitivity, precision, and spatial resolution. Collectively, these investigations demonstrate that LA-ICP-MS, particularly when coupled with integrative workflows and nanoparticle-based signal enhancement, provides a versatile, high-sensitivity platform for both archaeological and bioanalytical applications, offering critical insights into material provenance, technological choices, and trace metal exposure.

CHAPTER 1

1.1. LA-ICP-MS

Since the introduction of laser ablation inductively coupled plasma mass spectrometry (LA-ICP-MS) for the analysis of solid samples by A. Gray in 1985[1], it has become an established elemental and mapping technique that is characterized by low limits of detection, high spatial resolution, a wide linear dynamic range and limited sample preparation. Initially the technique met with great success in the geological field. Over the decades then, with the notable advances in hardware and software, the technique has found notable applicability in various fields, such as geochemical, archaeological, biochemical, forensic, etc. thanks to his capability to allow the characterization of solid materials both in bulk and in spatially resolved analysis (with lateral and/or in-depth resolution), avoiding dissolution/digestion as one of the most time-consuming sample preparation procedures prior to analysis, which is associated with the risk of sample contamination, analyte loss, and the loss of spatial information. Moreover, by analysing the sample in its native solid state, LA-ICP-MS helps to address the problem of representativeness that can arise when dealing with heterogeneous materials, where traditional preparation methods may fail to preserve the true compositional distribution. Nevertheless, care must be taken to avoid errors arising from the ablation of inclusions or localized features that are not representative of the overall composition of the sample. The fundamental principle of the LA-ICP-MS technique as the instrument set-up (figure 1.1) has basically remained the same over the years. A short-pulsed, high power laser beam is focused onto the sample surface in an inert gas atmosphere under normal pressure, within an airtight ablation cell. The interaction between the laser beam and the sample leads to an aerosol formation and a carrier gas, generally helium or argon, flushes through the ablation cell and transports the particle-containing aerosol into the ICPMS, where it is vaporized, atomized, and ionized[2].

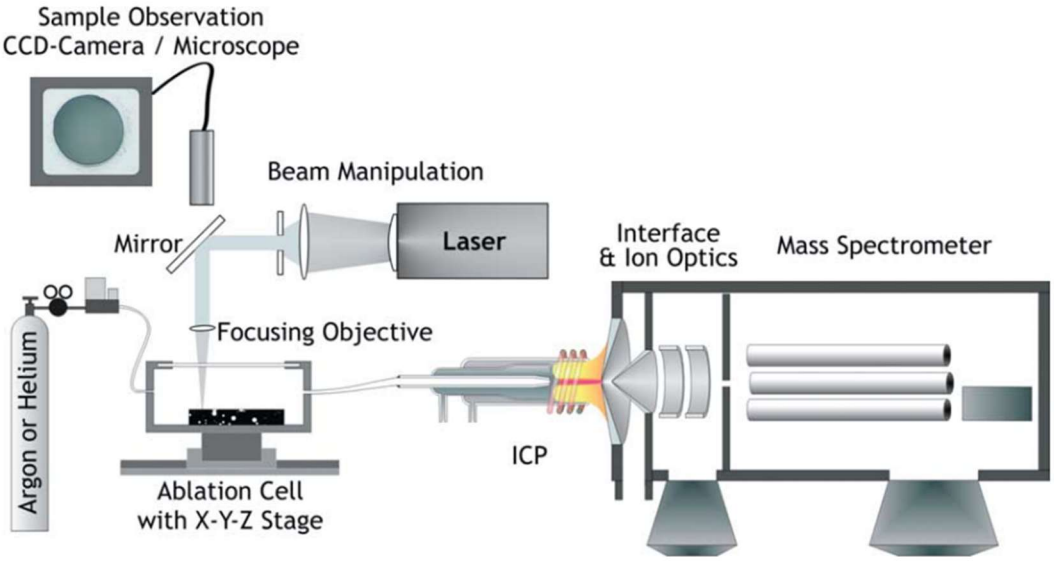


Fig 1.1. Schematic set-up of LA-ICPMS instrument[2].

1.1.1. Laser sources

The development in laser technology made possible a significant improvement in LA-ICP-MS. The lasers commonly used, mainly differ in wavelength (from IR to UV range) and pulse duration (ns, fs). The ruby laser, which showed the disadvantage of overheating at higher pulse rate, had been firstly substituted from Nd:YAG (neodymium-doped yttrium aluminium garnet; Nd:$Y_3Al_5O_{12}$) lasers, operating at the fundamental wavelength of 1064 nm[3]. Subsequently, with the introduction of optical components, it was possible to operate at the fourth[4] and fifth harmonics[5] (266 and 213 nm) of Nd:YAG lasers. While excellent results had been achieved by making shorter the wavelength, improving the characteristics of the ablation, further progress was achieved with the introduction of excimer lasers[6]. Most attention has been focused on the ArF once that has its fundamental wavelength at 193 nm and turns out to be more energetic. Further shortening the wavelength improves the energy transmission properties: this is concentrated more on the surface, without being absorbed, therefore generating a less catastrophic ablation and leading to a better reproducibility between multiple analyses[7]. Lastly, reducing the laser pulse at the range of femtosecond has been suggested to realize the ideal concept of representative sampling[8] thanks to the reduction of thermal effects, which means that the affected material is completely removed without or with minimal damage to the area surrounding[9]. Generally, these "ultrafast" lasers are produced by titanium doped sapphire (Ti:sapphire), whose fundamental wavelength is around 800 nm, but the 3rd and 4th harmonics (~265 and ~200 nm, respectively) are used[10].

1.1.2. Ablation cell and transport system

In the last decades, various cells different in volume, geometry and flow dynamics were built with the aim to speed up and improve the efficiency of aerosol capture, transport and detection[11]. Mainly the cells, usually mounted on a xyz - motorized stage controlled by software to arrange the sample under the laser beam, must be suitable for collecting smaller or bigger samples, for this reason the dimensions can vary from below 1 cm^2 to 10 cm^2. However, it supposed to be considered that the volume of the ablation cell and the flexible polymer transportation tube is influencing the dispersion and the sample density in the ICP. Smaller cell volumes reduce "sample-washout" time of the cell. A high carrier gas speed through the cell and transfer tubes reduces material deposition in the system, reducing memory effects and increasing transport efficiency[6]. However, it has been demonstrated that the dispersion increases with longer and larger internal diameter tubes and with the presence of junctions (figure 1.2) valves and/or bends. Much research has been done with a view to decreasing. The presence of Y- or T-junctions (fig. 1.2a) induces turbulence and eddy formation. Sharp bends cause unequal velocities between the outer and inner tubing walls, leading to swirling due to shear stress. To address these issues, co-axial mixing bulbs were introduced (fig. 1.2b), allowing make-up gas to be added on-axis, reducing turbulence and promoting laminar flow. Alternative designs, such as using an unbroken fused silica conduit, aim to improve performance by minimizing bends, reducing tubing lengths, and eliminating disruptions in the flow (fig. 1.2c). The ideal setup involves a short, straight, and narrow tubing with constant diameter, integrated with the ablation cell and ICP torch. However, practical lab constraints may prevent fully implementing this setup. Lastly, the Cobalt cell supposed to be mentioned regarding a huge improvement especially in mapping application[12]. The Cobalt ablation cell is useful because it provides a highly stable and reproducible environment for sampling and aerosol transfer. Its design ensures a consistent sampling distance and minimizes variations in aerosol particle trajectories, which enhances reproducibility across different sample positions. The cell's low dispersion, optimized internal layout, and high helium flow reduce particle settling and deposition on tubing walls, improving the efficiency of particle transport. Additionally, its compact design accommodates high-precision objectives and avoids collisions with uneven sample surfaces, allowing for precise laser ablation in diverse sampling conditions. Regarding the choice of the gas carrier, originally argon was used, then replaced by helium that allows higher analyte sensitivity reducing elemental fractionation[13,14]. The presence of helium in carrier gas could increase the plasma temperature due to its higher thermal conductivity[15]. Argon is mixed to the He aerosol before entering in ICP torch to ensure plasma stability. Carrier gas flow is variable -typically flow 0.3 – 1.1 L/min- and regulated by a mass flow controller.

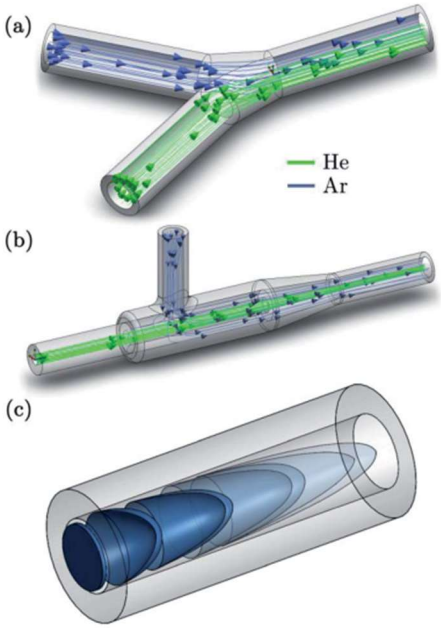


Fig 1.2. Junction models: a) Y-connector, b) coaxial mixing bulb and c) unbroken fused silica conduit[11].

1.1.3. ICP-MS system

In 1961 Reed introduced the plasma as source of atomization and ionization[16]. As mass spectrometry source, the Inductive Coupled Plasma (ICP) torch was presented few years later from Wendt and Fassel[17]. From then on, its configuration remained mostly the same: it consists of three concentric quartz tubes of different diameter in which the Ar gas flows, the outer tube of 18 mm id, the inner tube of 14 mm id and the injector of ~2 mm id. A coil surrounds the torch and generates a RF field that induced the ionization of Ar atoms that ignite and sustain the plasma which reaches temperatures of 10000 K. Here, all the particles (atoms and small agglomerates) transported from the LA by the gas carrier are first atomized, ionized and then sent to the mass analyzer where they are separated by their mass-to-charge (m/z) ratio. The optimization of the plasma power must balance carrier gas, auxiliary and sample gas based on Hattendorf et al. [18], to obtain maximum intensity for $^{238}U^{+}$ sensitivity while maintaining high sensitivity for a broad mass range, a low oxide ratio ($^{232}Th^{16}O^{+}$ / $^{232}Th^{+}$ < 0.3%) and similar $^{238}U^{+}$ and $^{232}Th^{+}$ sensitivities. As for mass analyzers, the commercially ICPMS are three types (figure 1.3), quadrupole, magnetic sector field and TOF. The quadrupole is the most widely used and it works by applying a complex electrical field of alternating and direct current potentials to an array of four (quad) rods (poles). Based on its operation, a single m/z at a time can pass and this makes the quadrupole working as a mass filter[19]. The mass analyzer system switches between different *m/z* channels rapidly and continuously, and it usually provides mass resolution of ~300 and the full mass range can be scanned within 100 ms[20]. However, further improvements in sensitivity and mass resolution are difficult to achieve, therefore most quadrupole instruments offer optional collision/reaction cell capability for interference and background reduction. The necessity to achieve higher mass resolution led to the introduction of sector field systems. This analyzer works by using an inductor and magnetic field to separate ions based on their m/z. The main disadvantage is that the process has a low scan speed because it requires several magnetic field changes to cover the full mass range, from light ions like ^{7}Li to heavy ions like $^{238}U^{16}O$. However, simultaneous measurement of different m/z became possible by introduction of multiple detectors into sector field instruments[21,22,23]. Employing Faraday cups as well as ion counters, this technique provides precise isotope ratios, founding its major application in geochemical and archaeological analysis[24,25]. With the increased interest in high speed and simultaneous detection of entire m/z range, the combination of the ICP ion source to time-of-flight mass spectrometry (TOFMS) aroused considerable

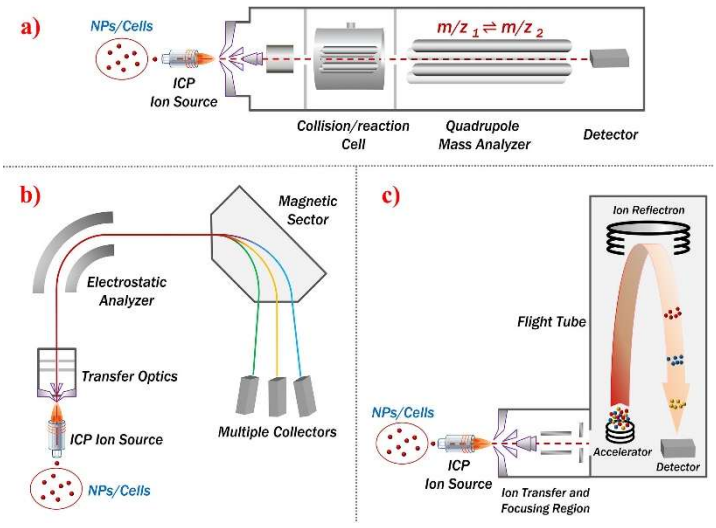


Fig 1.3. Schematics of a) ICP-Q-MS, b) MC-ICP-MS, and c) ICP-TOF-MS[19].

interest[26]. In a TOF, the continuous ion beam generated by the ion source is segmented into discrete packets. These ion packets are then accelerated in the instrument's extraction zone, where all ions ideally acquire the same momentum. As a result, their travel time through the field-free drift zone becomes mass-dependent. The time-resolved signal produced corresponds to the different masses reaching the detector at varying times. Fast scanning allows the detection of extremely fast transient signals while simultaneous sampling removes flicker noise, and these features increased the interest especially for imaging and isotope ratioing techniques, even if it appears to be limited in sensitivity and linear dynamic range[20].

1.2. State of the art: LA process and related disadvantages

With the increasing adoption of the LA-ICPMS technique in various fields of research, it has become crucial to thoroughly examine the entire workflow, particularly the sampling process and the subsequent transport of ablated material to the mass analyzer. This careful evaluation is essential for identifying potential challenges or inefficiencies that could compromise the accuracy and reliability of the results. Factors such as sample homogeneity, ablation efficiency, aerosol transport dynamics, and interactions within the plasma can introduce variability or systematic errors, which must be addressed to ensure robust data quality and reproducibility across different applications.

1.2.1. LA process

The name Laser Ablation itself refers to an explosive laser-material interaction[27]. Generically, it involves coupling of optical energy into a solid, resulting in vaporization; ejection of atoms, ions, molecular species, and fragments; shock waves; plasma initiation and expansion (figure 1.4). The initial stage of laser ablation is dominated by non-thermal interactions[28]. Here, the target

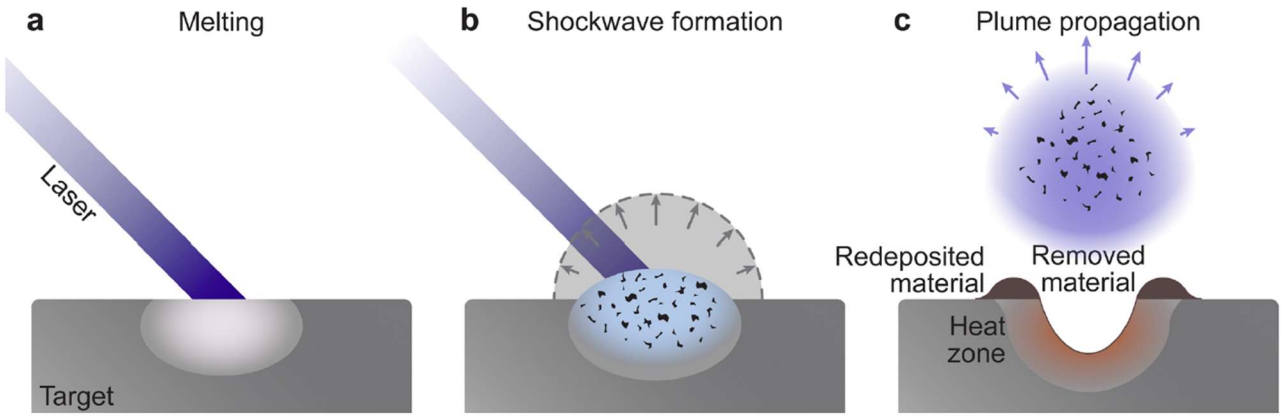


Fig 1.4. Schematic demonstrating the processes occurring during laser ablation[28].

material absorbs incident photons, which transfer enough energy to excite electrons and induce band transitions. These excited electrons subsequently relax back to their ground state

through vibrational relaxation. This process triggers the second type of interaction, known as thermal excitation. In this stage, rapid localized heating occurs, reaching temperatures that can exceed several thousand Kelvin. As a result, the material is expelled from the target through a combination of electronic and thermal ejection mechanisms. The vaporized material can also absorb laser light, leading to photoionization, where photons eject electrons from atoms. These free electrons gain additional energy through collisions with other particles in a process known as inverse Bremsstrahlung. Together, these processes create a cascade of free electrons, significantly increasing the plasma's ionization level. As vapor density rises, the collision frequency intensifies, and at atmospheric pressure, a shockwave forms between the expanding material and the surrounding chamber gas[29]. At this point, a strong explosion occurs, releasing an intense burst of energy that ignites a plasma above the crater. As the plume reaches its maximum size, the temperature and pressure begin to fall[30]. In this cooling phase, energy dissipates, allowing for the first formation of condensed particles. Condensational growth is the dominant mechanism, primarily forming particles smaller than 100 nm. Meanwhile, concurrent processes like coalescence and aggregation of smaller solidified particles lead to the formation of larger agglomerates. This variation in particle size contributes to inefficient transport and becomes apparent at the detector.

1.2.2. Optimizing parameters to mitigate Elemental Fractionation and enhance analytical accuracy

Given the heterogeneous nature and varied size distribution of aerosols generated by the laser ablation process, precise analysis necessitates meeting several critical conditions: (1) achieving a representative aerosol composition that accurately reflects the target sample, (2) ensuring efficient and stable transport of aerosols to the analytical interface, and (3) achieving complete decomposition of particles upon entry into the ICP. These steps are crucial for accurate quantification, as each one plays a distinct role in overcoming challenges posed by elemental fractionation, a process where non-stoichiometric ablation can lead to analytical signals that deviate from the true sample composition[31]. This phenomenon can take place both during the interaction between laser beam and sample, which in the phase immediately next[32]. In the first case, fractionation originates from the fusion of material due to thermal energy transfer from the laser to the sample, resulting in the formation of a crater. This process causes some particles to evaporate, forming clusters that tend to disperse and settle on the camera walls, which prevents their detection. In the second case, however, the fractionation is thought to be driven by Coulomb interactions. When the laser irradiates the material, it excites electrons and heats the sample to conditions resembling a dense plasma. As a result, ions separate based on their ionization energies, influenced by Coulomb forces -either attractive or repulsive- between ions and surrounding electrons. This interaction is believed to cause element separation and selective ablation. Discriminating between these mechanisms is challenging, and investigating the effects is essential, as laser dynamics, transport phenomena, and ICP vaporization efficiency interact in complex and interdependent ways.

Indeed, the laser ablation process inherently produces aerosols with a broad particle size range and compositional variability, which can lead to fractionation effects if the aerosols are not uniformly transported or fully decomposed. Additionally, the transport process is influenced by the aerodynamic and electrostatic properties of particles, as well as the environmental conditions along the transfer pathway. Variations in any of these factors can alter particle size distribution and, ultimately, affect the elemental makeup that reaches the ICP. Upon entering the ICP, the efficient decomposition and vaporization of particles are essential for reliable mass spectrometry detection. However, incomplete decomposition can introduce further bias, leading to signal discrepancies that do not accurately reflect the original sample. Thus, achieving consistent and accurate results requires a comprehensive understanding of each stage in the process and a careful optimization of parameters to minimize fractionation effects and align the analytical signal as closely as possible with the true sample composition. While studies on parameter optimization in laser ablation often yield controversial results due to a strong mutual dependence between parameters, gaining a deeper understanding of their influence on the ablation process remains essential[33]. The role of the laser wavelength and pulse duration has been previously discussed. The first one directly impacts how efficiently the target material absorbs energy from the laser beam. Shorter wavelengths, like those in the UV range specifically at 266 nm, 213 nm and 193 nm, generally interact more effectively with a wide range of materials[34]. The shorter is selected, the smaller (<150 nm) and more uniform aerosol particles are produced, which are more likely to fully decompose when they reach the plasma in the ICP and results in more stable transient signals and smaller variations of intensity ratios (figure 1.5). In contrast, longer wavelengths may result in larger or more varied particle sizes, which can lead to incomplete decomposition in the plasma and, consequently, to fractionation effects. Pulse duration - whether the laser emits nanosecond or femtosecond pulses- also makes a difference in how the aerosol is formed. Nanosecond lasers tend to generate larger particles and induce greater thermal effects[35]. This is particularly significant for metals and semiconductors, where the resulting heat-affected zone causes material redistribution, enrichment of certain constituent and raises the local temperature. Consequently, these conditions lead to preferential evaporation or condensation occurring at varying rates. Femtosecond lasers, on the other hand, generate smaller, more uniform particles with minimal thermal effects, leading to a more stoichiometric aerosol[36]. A further advantage of femtosecond lasers is their effect on crater

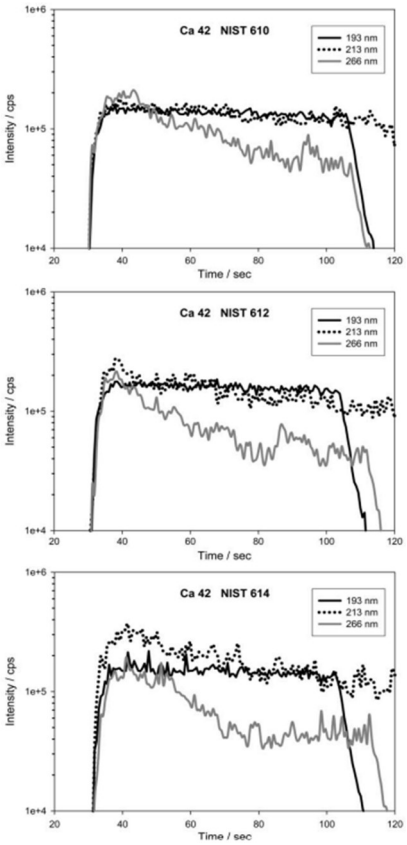


Fig 1.5. Comparison of the transient signals from NIST 610 (a), NIST 612 (b) and NIST 614 (c) ablation for Ca 42 for the three wavelengths[34].

morphology (figure 1.6)[37]. ns-LA tends to leave behind craters characterized by re-solidified melt zones, accompanied by scattered droplets of redeposited material around the crater edges (fig. 1.6b). This melting and redeposition compromise the resolution and accuracy of subsequent analyses. In contrast, femtosecond laser ablation creates craters with sharply defined edges and a lack of melted or redeposited material (fig. 1.6a). This precise crater formation is due to the extremely short pulse duration, which avoids phase changes in the material. These characteristics -the formation of stoichiometric aerosols and the clean, sharply defined craters- make femtosecond lasers the preferred choice. However, their diffusion remains limited due to the high cost and complexity of femtosecond laser systems, the need for specialized maintenance, and the relatively low availability of such equipment in routine analytical laboratories compared to more established nanosecond laser sources. Repetition rate, or the frequency of laser pulses, is another factor that supposed to be accurately balanced[38]. Higher laser frequencies improve sensitivity by increasing the quantity of material delivered to the plasma torch (figure 1.7). However, increased frequency also impacts elemental fractionation by affecting the heat that builds up at the ablation site. Higher repetition rates may create cumulative heating on the sample surface, which can change the ablation dynamics. This can alter the aerosol composition, as some elements may evaporate more than others, increasing fractionation risks (figure 1.8). Therefore, for balancing is essential to achieve both optimal sensitivity and stable, accurate measurements. Pulse energy and fluence -the amount of energy per unit area- play a big role in

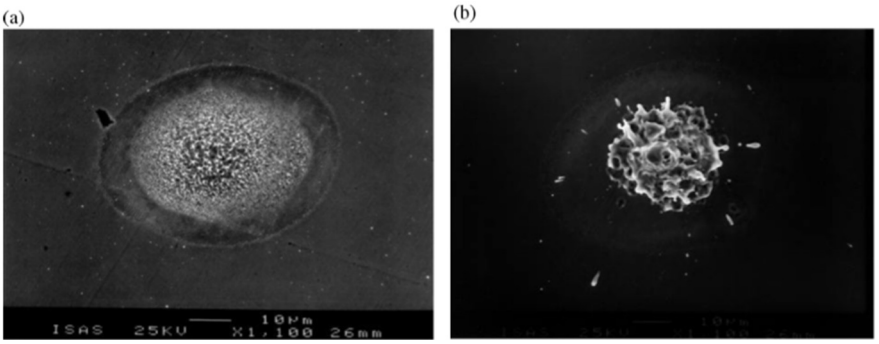


Fig 1.6. Laser craters on a brass sample: a) after 45 pulses with the fs-laser; b) after 45 pulses with the ns-laser[37].

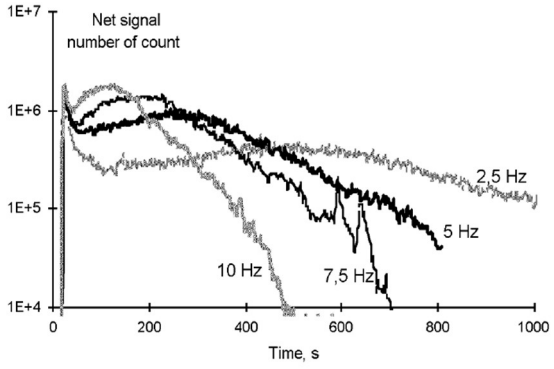


Fig 1.7. Evolution of the intensity of Co 59 signal in Nist 610 glass as a function of frequency[38].

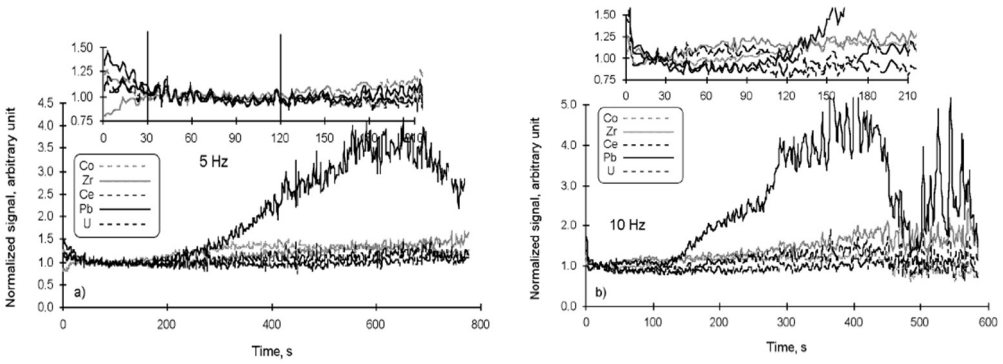


Fig 1.8. Element fractionation as a function of frequency: a) 5 Hz and b) 10 Hz[38].

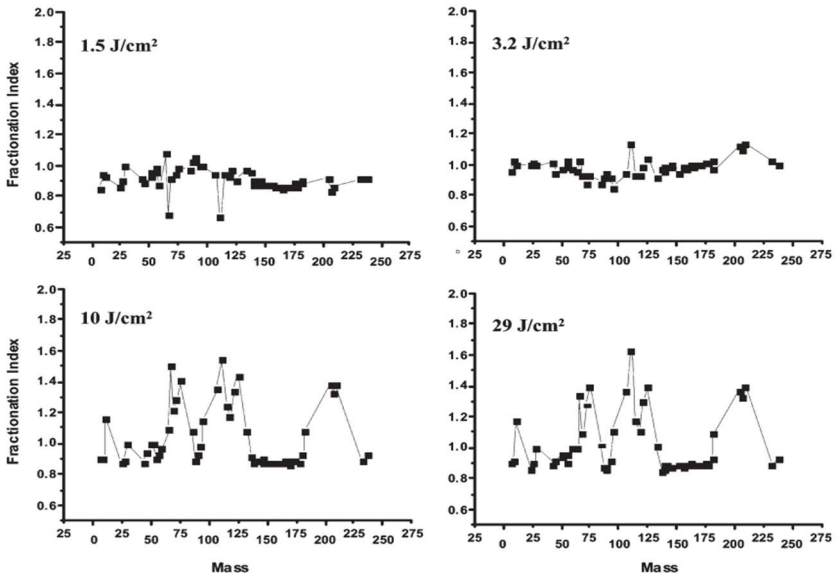


Fig 1.9. Fractionation indices at four laser fluences for fs-LA of NIST 610 glass[40].

determining how much material is ablated and the energy transferred to it[39]. Higher fluences usually result in a greater volume of material being ablated, but this can also mean that the aerosol particles vary more in size and composition. Too high a fluence can even cause "over-ablation," where the removal of material isn't stoichiometric, increasing the fractionation indices (figure 1.9)[40]. It is therefore necessary adjusting the fluence to an optimal level. Finally, spot size[41] and scan speed[42] determine the area and distribution of energy on the sample surface. Larger spot sizes can ablate more material but may produce aerosols with a wider size distribution, which makes transport and decomposition less predictable as well as decreasing spatial resolution. Faster scan speeds reduce local heating effects and generally yield a more representative aerosol, while slower scan speeds can concentrate energy in a smaller area, potentially enhancing selective ablation and fractionation effects. Another factor that influences the size of ablated particles is the choice of LA carrier gas. Studies have shown that when laser ablation occurs in an argon atmosphere, especially if energy densities are above the range of 5-10 J/cm^2, the particles produced are typically larger than 100 nm[43]. The introduction of pure helium as in-cell gas carrier results in enhanced signal intensities and reduced background noise as consequence of smaller particles, beyond a visibly reduced amount of material deposited around the ablation spot[44]. Numerous further studies explored the addition of other polyatomic gases as LA and/or ICP carrier gas to achieve an enhancement of the signal intensity. Oxygen (O_2) has been studied as a potential contaminant in helium within the ablation cell. Results are controversial: they indicate that even low concentrations of O_2 - on the order of a few hundred ppm- can significantly impact aerosol properties and cause elemental fractionation, evident in an increased presence of oxide ions in the ICP[45]. At the same time, intensity enhancement was observed for many elements in the order of 3 times for light elements and ca. 1.5 times for heavy elements, which was not directly associated with the formation of M^+ and MO^+ species. This enhancement may instead be attributed to improved atomization and ionization because of a better heat transfer between the gas and sample aerosol. For applications involving organic material analysis, the deliberate introduction of O_2 directly into the ICP has shown to enhance signal, primarily by oxidizing carbon and reducing the buildup of organic material on the sampling cone[46]. A higher electron temperature in the plasma is going to explain also the increased sensitivity from a factor of 2-4 up to 5-7 after the

addition of 4-9 ml/min of hydrogen (H_2) to the in-cell carrier gas (figure 1.10)[47]. Additionally, the limit of detection (LOD) improves by a factor of up to 4.5. An increased detection limit in hydrogen mode occurs only for elements that experience higher gas blanks due to hydrogen-based interferences, such as silicon, potassium, calcium, selenium, and antimony. The experiment has been repeated also for a fs-LA-ICP-MS, where both hydrogen and nitrogen were tested[48]. Enhanced sensitivity of most elements was observed as a result. The nitrogen as additional gas to the ICP is the most used due to its low cost and ease of handling and it had been found it generates a better thermal conductivity compared to Ar that may increase the ionization[49]. Adding N_2 also reduces molecular interference from MO^+[50]. This occurs because the formation of strong bonds in NO molecules effectively scavenges O^+ ions present in the ICP. That is proficient in reducing matrix interferences, increasing analyte signal responses, and improve the signal-to-noise beyond increasing plasma stability[51]. Recently, Neff *et al*.[52] presented the first study where N_2 replaces totally the Ar. This involved the introduction of a new system of plasma ignition, the microwave sustained, inductively coupled, atmospheric-pressure plasma (MICAP). This new system allowed to reach lower LODs for many elements, because of significantly less interferences originating from plasma species in the gas blank of the N_2-ICP-MS. This, in addition to the lower operating cost of the MICAP plasma source, has a high potential to compete with or even replace LA-(Ar)-ICP-MS in the future. Lastly, the effect of C-based molecule addition was investigated. The main difficulty was the severe clogging of the sampler and skimmer cone generated by the organic material that limited the determination of the maximum signal enhancement factors. Adding methane to the mixture[53], The maximum sensitivity of the signal occurs with a flow between 1.2 and 1.4 mL/min. Potential mechanisms for the intensity enhancement include 1) a charge transfer reaction as following:

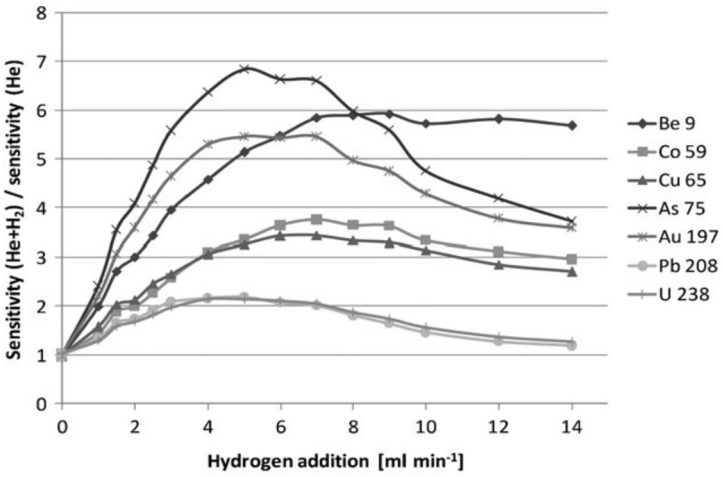


Fig 1.10. The sensitivities of selected elements as a function of H2[47].

$$C^+ + M \rightarrow M^{+*} + C$$

where M represents a target atom in the ground state, C a carbon atom in the ground state, C^+ the carbon cation and M^{+*} a cation in a potentially excited state above the first ionization potential; 2) a change in the ICP geometry and 3) an increase in plasma temperature. However, the use of methane also presents notable disadvantages: frequent cone cleaning or replacement due to carbon deposition; possible spectral interferences from polyatomic species such as C_2^+, CN^+, and CO^+; potential plasma instability; and an increased complexity of gas handling owing to methane's flammability and associated safety requirements. These

factors, combined with matrix-dependent enhancement effects, can limit the practical implementation of this approach in routine analyses despite its potential for sensitivity improvement. The second option was the aspiration of a methanol–water mixture into a cooled spray chamber. This type of mixing leads to a sensitivity enhancement up to a factor of 20. A custom-designed introduction system was developed to investigate the effects of adding water and/or ethanol vapor on system sensitivity[54]. Sensitivity was evaluated by measuring the intensity of ^{115}In as a function of both vapor composition and flow velocity. Results showed that maximum sensitivity decreases as ethanol concentration increases, having a better result when both water and ethanol vapours are present compared to a dry plasma environment. However, the addition of water introduces high oxide levels, likely due to the oxygen content, which may complicate the sensitivity measurements.

1.2.3. Matrix effect, calibration and Internal Standard

The optimization of the aforementioned parameters is intrinsically linked to the matrix of the analysed sample. Laser-sample interactions are profoundly influenced by the matrix's chemical and physical properties, including absorption, reflectivity, and thermal conductivity[55]. These properties directly impact the ablation volume, as well as the size, shape, and uniformity of the particles generated during laser ablation. Consequently, samples with identical analyte concentrations in different matrices can display significant variations in absolute signal intensity due to the matrix effect. This phenomenon underscores the critical importance of matrix-matched materials for accurate quantification and validation of analytical results[56]. Certified reference materials (CRMs) are critical tools for one-point external calibration in LA-ICP-MS, offering high traceability and designed to closely replicate the sample's analyte concentrations, chemical composition, and physical properties. However, their limited availability and high costs have spurred efforts to develop alternative calibration strategies. These approaches aim to reduce dependence on matrix-matched reference materials, making LA-ICP-MS analyses more versatile and accessible. In practice, matrix-matched standards are frequently produced in-house, following internal characterization and validation protocols. Several sample preparation techniques have been reported for creating such standards prior to LA-ICP-MS analysis, including fusion with borates, embedding in polymer resins, and pressing powdered samples into disks with binders[57,58,59,60]. These methods allow the incorporation of internal standards, spiked analytes for standard addition, or isotopically enriched tracers for isotope dilution, and analyte concentrations can be adjusted by controlled dilution. Elemental concentrations in these in-house calibration standards are typically determined by solution-based ICP-MS following acid-assisted digestion, and key performance metrics -such as calibration curve linearity, detection and quantification limits, precision, and long-term stability- are rigorously evaluated and reported[61]. In the specific case of biological samples, the complexity and heterogeneity of tissues present additional challenges in developing matrix-matched standards that ensure the desired accuracy, precision, and robustness. One successful approach is the use of gelatine,

primarily made of porcine skin, as a calibration matrix for elements in soft biological tissue and cells. Gelatine offers tuneable physical and chemical properties, enabling its preparation in various formats, including sections, micro-arrays[62], moulded forms[63], and (micro-)droplets produced via manual pipetting[64] or robotic micro-dispensing[65]. Highly homogeneous multi-element gelatine calibration standards have been fabricated for quantitative LA-ICP-MS bioimaging. While heterogeneity issues -such as those arising from the "coffee-stain" and "Marangoni" effects- were found to be element-dependent, they could be mitigated through careful control of drying and setting conditions[66]. Isotope dilution analysis (IDA) in LA-ICP-MS offers traceable, matrix-independent quantification with high accuracy and precision, making it attractive for bioimaging and protein quantification[67]. The method involves adding an isotopically enriched spike to alter the analyte's isotopic composition, followed by measurement of isotope ratios[68]. While powerful, IDA is limited by the need for costly enriched spikes, inapplicability to monoisotopic elements, labour-intensive preparation, strict spike/sample ratio control, and the requirement for complete isotope equilibration -a challenge in biological tissues[69]. Various spike addition strategies have been proposed (e.g., solid spiking, post-ablation aerosol mixing), though some compromise full traceability. Nevertheless, IDA remains valuable for validating higher-throughput calibration strategies and for specialized quantitative bioimaging applications. A widely adopted technique to complement external calibration with CRMs or in-house standards is signal normalization using an internal reference or internal standard[70]. This method enhances quantification accuracy by mitigating the effects of residual discrepancies between samples and standards. Internal standards correct for variations in sample ablation, aerosol transport, and fluctuations in ICP signal intensity due to changing plasma conditions. Despite its benefits, the successful application of internal standardization is not without challenges. Identifying internal standard elements that share similar ablation, transport, and ionization behaviour with the analytes can be complex, particularly when dealing with heterogeneous samples. Ensuring a homogeneous distribution of the internal standard across the sample matrix is equally critical; otherwise, inconsistencies in ablation dynamics or transport efficiency could compromise the accuracy of corrections. Addressing these challenges requires careful selection and validation of internal standards, as well as rigorous sample preparation protocols to ensure uniformity. These criteria ensure that internal standardization effectively compensates for matrix effects and instrumental variability, thereby improving the reliability of LA-ICP-MS results. Sum normalization offers an alternative to single-element internal standardization for the quantitative determination of major, minor, and trace elements - particularly in homogeneous materials such as glass[71]. The method normalizes the total elemental concentrations, expressed as their corresponding oxides, to 100% [w/w], thereby eliminating the need for complementary analysis of a dedicated internal standard. In practice, an assumed concentration of a major oxide (e.g., SiO_2) is used as a provisional internal standard. The normalization algorithm iteratively adjusts this assumed value until the cumulative concentrations of all measured elemental oxides sum to exactly 100% [w/w]. Because the procedure relies on the simultaneous measurement of a large suite of elements (e.g., 54 elemental oxides), laser ablation is typically performed in raster mode to obtain representative sampling across the material. Calibration is carried out using external

glass standards -such as those replicating historic compositions -with the calibration graphs forced through the origin. When using SiO_2 as the internal standard, the relative standard deviation of the calibration slopes typically ranges between 0.1% and 6.6%, indicating good linearity and quantitative reliability. This approach provides a straightforward and robust strategy for semiquantitative to fully quantitative analysis, particularly in cases where internal standard homogeneity is difficult to guarantee or where independent internal standard data are unavailable. An emerging alternative to matrix-matched calibration is ablation volume normalization, in which LA-ICP-MS signals are normalized to the actual ablated volume measured post-ablation -typically via optical profilometry- rather than relying on an internal or external matrix-matched standard[72]. By employing a matrix-adapted fluence set just above the ablation threshold, this approach minimizes differences in ablation efficiency between matrices. In practice, replicate line scans are performed on both sample and standard, gas blanks are subtracted, and element signals are corrected for the measured ablation volume. While this method does not address variations in particle size distribution, aerosol transport, or plasma ionization efficiency, it significantly improves multi-element quantification when matrix-matched standards are unavailable. As such, ablation volume normalization complements other strategies -such as in-house matrix-matched standards, gelatine-based biological calibrants, isotope dilution analysis, and sum normalization- by providing a viable pathway to accurate results in cases where conventional calibration materials cannot be employed[73].

References

[1] Gray, A. L. Solid Sample Introduction by Laser Ablation for Inductively Coupled Plasma Source Mass Spectrometry. The Analyst, 1985, 110, 551. https://doi.org/10.1039/an9851000551.

[2] Günther, D.; Hattendorf, B. Solid Sample Analysis Using Laser Ablation Inductively Coupled Plasma Mass Spectrometry. TrAC Trends in Analytical Chemistry, 2005, 24, 255–265. https://doi.org/10.1016/j.trac.2004.11.017.

[3] Walder, A. J.; Abell, I. D.; Platzner, I.; Freedman, P. A. Lead Isotope Ratio Measurement of NIST 610 Glass by Laser Ablation Inductively Coupled Plasma Mass Spectrometry. Spectrochimica Acta Part B: Atomic Spectroscopy, 1993, 48, 397–402. https://doi.org/10.1016/0584-8547(93)80044-u.

[4] Jeffries, T. E.; Perkins, W. T.; Pearce, N. J. G. Comparisons of Infrared and Ultraviolet Laser Probe Microanalysis Inductively Coupled Plasma Mass Spectrometry in Mineral Analysis. The Analyst, 1995, 120, 1365. https://doi.org/10.1039/an9952001365.

[5] E. Jeffries, T.; E. Jackson, S.; P. Longerich, H. Application of a Frequency Quintupled Nd:YAG Source (Λ=213 Nm) for Laser Ablation Inductively Coupled Plasma Mass Spectrometric Analysis of Minerals. J. Anal. At. Spectrom., 1998, 13, 935–940. https://doi.org/10.1039/a801328d.

[6] Günther, D.; Horn, I.; Hattendorf, B. Recent Trends and Developments in Laser Ablation-ICP-Mass Spectrometry. Fresenius' Journal of Analytical Chemistry, 2000, 368, 4–14. https://doi.org/10.1007/s002160000495.

[7] Günther, D.; A. Heinrich, C. Comparison of the Ablation Behaviour of 266 Nm Nd:YAG and 193 Nm ArF Excimer Lasers for LA-ICP-MS Analysis. J. Anal. At. Spectrom., 1999, 14, 1369–1374. https://doi.org/10.1039/a901649j.

[8] Margetic, V.; Pakulev, A.; Stockhaus, A.; Bolshov, M.; Niemax, K.; Hergenröder, R. A Comparison of Nanosecond and Femtosecond Laser-Induced Plasma Spectroscopy of Brass Samples. Spectrochimica Acta Part B: Atomic Spectroscopy, 2000, 55, 1771–1785. https://doi.org/10.1016/s0584-8547(00)00275-5.

[9] Pisonero, J.; Fernández, B.; Günther, D. Critical Revision of GD-MS, LA-ICP-MS and SIMS as Inorganic Mass Spectrometric Techniques for Direct Solid Analysis. Journal of Analytical Atomic Spectrometry, 2009, 24, 1145. https://doi.org/10.1039/b904698d.

[10] Koch, J.; Wälle, M.; Pisonero, J.; Günther, D. Performance Characteristics of Ultra-Violet Femtosecond Laser Ablation Inductively Coupled Plasma Mass Spectrometry at ∼265 and ∼200 Nm. J. Anal. At. Spectrom., 2006, 21, 932–940. https://doi.org/10.1039/b603929d.

[11] Van Malderen, S. J. M.; Managh, A. J.; Sharp, B. L.; Vanhaecke, F. Recent Developments in the Design of Rapid Response Cells for Laser Ablation-Inductively Coupled Plasma-Mass Spectrometry and Their Impact on Bioimaging Applications. Journal of Analytical Atomic Spectrometry, 2016, 31, 423–439. https://doi.org/10.1039/c5ja00430f.

[12] Van Malderen, S. J. M.; Van Acker, T.; Vanhaecke, F. Sub-Micrometer Nanosecond LA-ICP-MS Imaging at Pixel Acquisition Rates above 250 Hz via a Low-Dispersion Setup. Analytical Chemistry, 2020, 92, 5756–5764. https://doi.org/10.1021/acs.analchem.9b05056.

[13] Eggins, S. M.; Kinsley, L. P. J.; Shelley, J. M. G. Deposition and Element Fractionation Processes during Atmospheric Pressure Laser Sampling for Analysis by ICP-MS. Applied Surface Science, 1998, 127–129, 278–286. https://doi.org/10.1016/s0169-4332(97)00643-0.

[14] Günther, D.; A. Heinrich, C. Enhanced Sensitivity in Laser Ablation-ICP Mass Spectrometry Using Helium-Argon Mixtures as Aerosol Carrier. J. Anal. At. Spectrom., 1999, 14, 1363–1368. https://doi.org/10.1039/a901648a.

[15] Sesi, N. N.; Mackenzie, A.; Shanks, K. E.; Yang, P.; Hieftje, G. M. Fundamental Studies of Mixed-Gas Inductively Coupled Plasmas. Spectrochimica Acta Part B: Atomic Spectroscopy, 1994, 49, 1259–1282. https://doi.org/10.1016/0584-8547(94)80108-8.

[16] Reed, T. B. Induction-Coupled Plasma Torch. Journal of Applied Physics, 1961, 32, 821–824. https://doi.org/10.1063/1.1736112.

[17] Wendt, R. H.; Fassel, V. A. Induction-Coupled Plasma Spectrometric Excitation Source. Analytical Chemistry, 1965, 37, 920–922. https://doi.org/10.1021/ac60226a003.

[18] Hattendorf, B.; Latkoczy, C.; Günther, D. Peer Reviewed: Laser Ablation-ICPMS. Analytical Chemistry, 2003, 75, 341 A-347 A. https://doi.org/10.1021/ac031283r.

[19] Tian, X.; Jiang, H.; Hu, L.; Wang, M.; Cui, W.; Shi, J.; Liu, G.; Yin, Y.; Cai, Y.; Jiang, G. Simultaneous Multi-Element and Multi-Isotope Detection in Single-Particle ICP-MS Analysis: Principles and Applications. TrAC Trends in Analytical Chemistry, 2022, 157, 116746. https://doi.org/10.1016/j.trac.2022.116746.

[20] Thomas, R. Practical Guide to ICP-MS. Marcel Dekker, Inc., New York, 2004, pp. ISBN: 49-59. 0-8247-5319-4.

[21] Walder, A. J.; Freedman, P. A. Communication. Isotopic Ratio Measurement Using a Double Focusing Magnetic Sector Mass Analyser with an Inductively Coupled Plasma as an Ion Source. Journal of Analytical Atomic Spectrometry, 1992, 7, 571. https://doi.org/10.1039/ja9920700571.

[22] Sylvester, P. J. LA-(MC)-ICP-MS Trends in 2006 and 2007 with Particular Emphasis on Measurement Uncertainties. Geostandards and Geoanalytical Research, 2008, 32, 469–488. https://doi.org/10.1111/j.1751-908x.2008.00924.x.

[23] Pramann, A.; Noordmann, J.; Rienitz, O. Investigation of Mass-scale Drift Effects in the Milli-mass Range: Influence on High Mass Resolution Mode Multicollector-inductively Coupled Plasma Mass Spectrometer Isotope Ratio Measurements. Journal of Mass Spectrometry, 2021, 56. https://doi.org/10.1002/jms.4732.

[24] Zhian, B.; Honglin, Y.; Chunlei, Z.; Ye, L.; Kaiyun, C.; Yulin, Z. Simultaneous Determination of Trace Elements and Lead Isotopes in Fused Silicate Rock Powders Using a Boron Nitride Vessel and fsLA-(MC)-ICP-MS. Journal of Analytical Atomic Spectrometry, 2016, 31, 1012–1022. https://doi.org/10.1039/c5ja00410a.

[25] Martin, L.; Galy, A.; Barbotin, G.; Claverie, F.; Pons-Branchu, E.; Tribolo, C.; Mercier, N.; Pécheyran, C. Isotopic Imaging Using fsLA Single-Collector ICP-SFMS for Direct U/Th Dating of Small Archaeological Carbonates. Analytical Chemistry, 2022, 94, 3046–3055. https://doi.org/10.1021/acs.analchem.1c02241.

[26] Guilhaus, M. Essential Elements of Time-of-Flight Mass Spectrometry in Combination with the Inductively Coupled Plasma Ion Source. Spectrochimica Acta Part B: Atomic Spectroscopy, 2000, 55, 1511–1525. https://doi.org/10.1016/s0584-8547(00)00261-5.

[27] Russo, R. E. Laser Ablation. Applied Spectroscopy, 1995, 49, 14A-28A. https://doi.org/10.1366/0003702953965399.

[28] Shepelin, N. A.; Tehrani, Z. P.; Ohannessian, N.; Schneider, C. W.; Pergolesi, D.; Lippert, T. A Practical Guide to Pulsed Laser Deposition. Chemical Society Reviews, 2023, 52, 2294–2321. https://doi.org/10.1039/d2cs00938b.

[29] Russo, R. E.; Mao, X. L.; Liu, H. C.; Yoo, J. H.; Mao, S. S. Time-Resolved Plasma Diagnostics and Mass Removal during Single-Pulse Laser Ablation. Applied Physics A: Materials Science & Processing, 1999, 69, S887–S894. https://doi.org/10.1007/s003390051553.

[30] Hergenröder, R. A Model for the Generation of Small Particles in Laser Ablation ICP-MS. J. Anal. At. Spectrom., 2006, 21, 1016–1026. https://doi.org/10.1039/b604453k.

[31] Bogaerts, A.; Chen, Z.; Gijbels, R.; Vertes, A. Laser Ablation for Analytical Sampling: What Can We Learn from Modeling? Spectrochimica Acta Part B: Atomic Spectroscopy, 2003, 58, 1867–1893. https://doi.org/10.1016/j.sab.2003.08.004.

[32] Garcia, C. C.; Lindner, H.; Niemax, K. Laser Ablation Inductively Coupled Plasma Mass Spectrometry—Current Shortcomings, Practical Suggestions for Improving Performance, and Experiments to Guide Future Development. J. Anal. At. Spectrom., 2009, 24, 14–26. https://doi.org/10.1039/b813124b.

[33] Hergenröder, R. A Model of Non-Congruent Laser Ablation as a Source of Fractionation Effects in LA-ICP-MS. J. Anal. At. Spectrom., 2006, 21, 505–516. https://doi.org/10.1039/b600698a.

[34] Guillong, M.; Horn, I.; Günther, D. A Comparison of 266 Nm, 213 Nm and 193 Nm Produced from a Single Solid State Nd:YAG Laser for Laser Ablation ICP-MS. J. Anal. At. Spectrom., 2003, 18, 1224–1230. https://doi.org/10.1039/b305434a

[35] Niemax, K. Laser Ablation - Reflections on a Very Complex Technique for Solid Sampling. Fresenius' Journal of Analytical Chemistry, 2001, 370, 332–340. https://doi.org/10.1007/s002160100796.

[36] Koch, J.; Lindner, H.; von Bohlen, A.; Hergenröder, R.; Niemax, K. Elemental Fractionation of Dielectric Aerosols Produced by Near-Infrared Femtosecond Laser Ablation of Silicate Glasses. Journal of Analytical Atomic Spectrometry, 2005, 20, 901. https://doi.org/10.1039/b503137k.

[37] Margetic, V.; Pakulev, A.; Stockhaus, A.; Bolshov, M.; Niemax, K.; Hergenröder, R. A Comparison of Nanosecond and Femtosecond Laser-Induced Plasma Spectroscopy of Brass Samples. Spectrochimica Acta Part B: Atomic Spectroscopy, 2000, 55, 1771–1785. https://doi.org/10.1016/s0584-8547(00)00275-5.

[38] Gratuze, B.; Blet-Lemarquand, M.; Barrandon, J.-N. Journal of Radioanalytical and Nuclear Chemistry, 2001, 247, 645–656. https://doi.org/10.1023/a:1010623703423.

[39] Shannon, M. A.; Mao, X. L.; Fernandez, Alberto.; Chan, W.-Tat.; Russo, R. E. Laser Ablation Mass Removal versus Incident Power Density during Solid Sampling for Inductively Coupled Plasma Atomic Emission Spectroscopy. Analytical Chemistry, 1995, 67, 4522–4529. https://doi.org/10.1021/ac00120a015.

[40] Russo, R. E.; Mao, X.; Gonzalez, J. J.; Mao, S. S. Femtosecond Laser Ablation ICP-MS. J. Anal. At. Spectrom., 2002, 17, 1072–1075. https://doi.org/10.1039/b202044k.

[41] Wegner, A. C.; Leitzke, F. P.; Porcher, C. C.; Conceição, R. V.; Gomes, M. E. B.; Cedeño, D. G.; Souza, M. R. W. de. High-Precision Laser Ablation Inductively Coupled Plasma Mass Spectrometry Determination of Trace Elements in Geological Glasses by Internal Standardization. Brazilian Journal of Geology, 2021, 51. https://doi.org/10.1590/2317-4889202120210018.

[42] Holá, M.; Salajková, Z.; Gregar, F.; Ondráček, J.; Pavliňák, D.; Šperka, P.; Hrdlička, A.; Kaiser, J.; Kanický, V. Laser Spot Overlap in Scanning Laser Ablation ICP-MS Analysis: Impact on Analytical Signal and Properties of the Generated Aerosol. Spectrochimica Acta Part B: Atomic Spectroscopy, 2024, 219, 106999. https://doi.org/10.1016/j.sab.2024.106999.

[43] Koch, J.; Günther, D. Laser Ablation Inductively Coupled Plasma Mass Spectrometry. Encyclopedia of Spectroscopy and Spectrometry, 2017, 526–532. https://doi.org/10.1016/b978-0-12-803224-4.00024-8.

[44] Günther, D.; A. Heinrich, C. Enhanced Sensitivity in Laser Ablation-ICP Mass Spectrometry Using Helium-Argon Mixtures as Aerosol Carrier. J. Anal. At. Spectrom., 1999, 14, 1363–1368. https://doi.org/10.1039/a901648a.

[45] Košler, J.; Jackson, S. E.; Yang, Z.; Wirth, R. Effect of Oxygen in Sample Carrier Gas on Laser-Induced Elemental Fractionation in U–Th–Pb Zircon Dating by Laser Ablation ICP-MS. J. Anal. At. Spectrom., 2014, 29, 832–840. https://doi.org/10.1039/c3ja50386k.

[46] Hutton, R. C. Application of Inductively Coupled Plasma Source Mass Spectrometry (ICP-MS) to the Determination of Trace Metals in Organics. Journal of Analytical Atomic Spectrometry, 1986, 1, 259. https://doi.org/10.1039/ja9860100259.

[47] Guillong, M.; Heinrich, C. A. Sensitivity Enhancement in Laser Ablation ICP-MS Using Small Amounts of Hydrogen in the Carrier Gas. Journal of Analytical Atomic Spectrometry, 2007, 22, 1488. https://doi.org/10.1039/b709489b.

[48] Shaheen, M.; Fryer, B. J. Improving the Analytical Capabilities of Femtosecond Laser Ablation Multicollector ICP-MS for High Precision Pb Isotopic Analysis: The Role of Hydrogen and Nitrogen. Journal of Analytical Atomic Spectrometry, 2010, 25, 1006. https://doi.org/10.1039/c003879b.

[49] Durrant, S.F. Feasibility of improvement in analytical performance in laser ablation inductively coupled plasma-mass spectrometry (LA-ICP-MS) by addition of nitrogen to the argon plasma. Fresenius J. Anal. Chem., 1994, 349, 768-771.

[50] Hu, Z.; Gao, S.; Liu, Y.; Hu, S.; Chen, H.; Yuan, H. Signal Enhancement in Laser Ablation ICP-MS by Addition of Nitrogen in the Central Channel Gas. Journal of Analytical Atomic Spectrometry, 2008, 23, 1093. https://doi.org/10.1039/b804760j.

[51] Beauchemin, D.; Craig, J. M. Investigations on Mixed-Gas Plasmas Produced by Adding Nitrogen to the Plasma Gas in ICP-MS. Spectrochimica Acta Part B: Atomic Spectroscopy, 1991, 46, 603–614. https://doi.org/10.1016/0584-8547(91)80064-a.

[52] Neff, C.; Becker, P.; Hattendorf, B.; Günther, D. LA-ICP-MS Using a Nitrogen Plasma Source. Journal of Analytical Atomic Spectrometry, 2021, 36, 1750–1757. https://doi.org/10.1039/d1ja00205h.

[53] Fliegel, D.; Frei, C.; Fontaine, G.; Hu, Z.; Gao, S.; Günther, D. Sensitivity Improvement in Laser Ablation Inductively Coupled Plasma Mass Spectrometry Achieved Using a Methane/Argon and Methanol/Water/Argon Mixed Gas Plasma. The Analyst, 2011, 136, 4925. https://doi.org/10.1039/c0an00953a.

[54] Liu, S.; Hu, Z.; Günther, D.; Ye, Y.; Liu, Y.; Gao, S.; Hu, S. Signal Enhancement in Laser Ablation Inductively Coupled Plasma-Mass Spectrometry Using Water and/or Ethanol Vapor in Combination with a Shielded Torch. Journal of Analytical Atomic Spectrometry, 2014, 29, 536. https://doi.org/10.1039/c3ja50329a.

[55] Zhang, S.; He, M.; Yin, Z.; Zhu, E.; Hang, W.; Huang, B. Elemental Fractionation and Matrix Effects in Laser Sampling Based Spectrometry. J. Anal. At. Spectrom. 2016, 31 (2), 358–382. https://doi.org/10.1039/c5ja00273g.

[56] Westheide, J. Th.; Becker, J. S.; Jäger, R.; Dietze, H.-J.; Broekaert, J. A. C. Analysis of Ceramic Layers for Solid Oxide Fuel Cells by Laser Ablation Inductively Coupled Plasma Mass Spectroscopy. J. Anal. At. Spectrom. 1996, 11 (9), 661–666. https://doi.org/10.1039/ja9961100661.

[57] Sinclair, D. J.; Kinsley, L. P. J.; McCulloch, M. T. High Resolution Analysis of Trace Elements in Corals by Laser Ablation ICP-MS. Geochimica et Cosmochimica Acta 1998, 62 (11), 1889–1901. https://doi.org/10.1016/s0016-7037(98)00112-4.

[58] Perkins, W. T.; Fuge, R.; Pearce, N. J. G. Quantitative Analysis of Trace Elements in Carbonates Using Laser Ablation Inductively Coupled Plasma Mass Spectrometry. J. Anal. At. Spectrom. 1991, 6 (6), 445. https://doi.org/10.1039/ja9910600445.

[59] Fitzpatrick, A. J.; Kurtis Kyser, T.; Chipley, D.; Beauchemin, D. Fabrication of Solid Calibration Standards by a Sol–Gel Process and Use in Laser Ablation ICPMS. J. Anal. At. Spectrom. 2008, 23 (2), 244–248. https://doi.org/10.1039/b712366c.

[60] Vassilev, S. V.; Vassileva, C. G.; Baxter, D. Trace Element Concentrations and Associations in Some Biomass Ashes. Fuel 2014, 129, 292–313. https://doi.org/10.1016/j.fuel.2014.04.001.

[61] Limbeck, A.; Galler, P.; Bonta, M.; Bauer, G.; Nischkauer, W.; Vanhaecke, F. Recent Advances in Quantitative LA-ICP-MS Analysis: Challenges and Solutions in the Life Sciences and Environmental Chemistry. Anal Bioanal Chem 2015, 407 (22), 6593–6617. https://doi.org/10.1007/s00216-015-8858-0.

[62] Van Malderen, S. J. M.; Vergucht, E.; De Rijcke, M.; Janssen, C.; Vincze, L.; Vanhaecke, F. Quantitative Determination and Subcellular Imaging of Cu in Single Cells via Laser Ablation-ICP-Mass Spectrometry Using

High-Density Microarray Gelatin Standards. Anal. Chem. 2016, 88 (11), 5783–5789. https://doi.org/10.1021/acs.analchem.6b00334.

[63] Westerhausen, M. T.; Lockwood, T. E.; Gonzalez de Vega, R.; Röhnelt, A.; Bishop, D. P.; Cole, N.; Doble, P. A.; Clases, D. Low Background Mould-Prepared Gelatine Standards for Reproducible Quantification in Elemental Bio-Imaging. Analyst 2019, 144 (23), 6881–6888. https://doi.org/10.1039/c9an01580a.

[64] Van Acker, T.; Buckle, T.; Van Malderen, S. J. M.; van Willigen, D. M.; van Unen, V.; van Leeuwen, F. W. B.; Vanhaecke, F. High-Resolution Imaging and Single-Cell Analysis via Laser Ablation-Inductively Coupled Plasma-Mass Spectrometry for the Determination of Membranous Receptor Expression Levels in Breast Cancer Cell Lines Using Receptor-Specific Hybrid Tracers. Analytica Chimica Acta 2019, 1074, 43–53. https://doi.org/10.1016/j.aca.2019.04.064.

[65] Schweikert, A.; Theiner, S.; Wernitznig, D.; Schoeberl, A.; Schaier, M.; Neumayer, S.; Keppler, B. K.; Koellensperger, G. Micro-Droplet-Based Calibration for Quantitative Elemental Bioimaging by LA-ICPMS. Anal Bioanal Chem 2021, 414 (1), 485–495. https://doi.org/10.1007/s00216-021-03357-w.

[66] Šala, M.; Šelih, V. S.; van Elteren, J. T. Gelatin Gels as Multi-Element Calibration Standards in LA-ICP-MS Bioimaging: Fabrication of Homogeneous Standards and Microhomogeneity Testing. Analyst 2017, 142 (18), 3356–3359. https://doi.org/10.1039/c7an01361b.

[67] Rodríguez-González, P.; Marchante-Gayón, J. M.; García Alonso, J. I.; Sanz-Medel, A. Isotope Dilution Analysis for Elemental Speciation: A Tutorial Review. Spectrochimica Acta Part B: Atomic Spectroscopy 2005, 60 (2), 151–207. https://doi.org/10.1016/j.sab.2005.01.005.

[68] Schweikert, A.; Theiner, S.; Šala, M.; Vician, P.; Berger, W.; Keppler, B. K.; Koellensperger, G. Quantification in Bioimaging by LA-ICPMS - Evaluation of Isotope Dilution and Standard Addition Enabled by Micro-Droplets. Analytica Chimica Acta 2022, 1223, 340200. https://doi.org/10.1016/j.aca.2022.340200.

[69] Heumann, K. G. Isotope-Dilution ICP-MS for Trace Element Determination and Speciation: From a Reference Method to a Routine Method? Analytical and Bioanalytical Chemistry 2004, 378 (2), 318–329. https://doi.org/10.1007/s00216-003-2325-z.

[70] Longerich, H. P.; Jackson, S. E.; Günther, D. Inter-Laboratory Note. Laser Ablation Inductively Coupled Plasma Mass Spectrometric Transient Signal Data Acquisition and Analyte Concentration Calculation. J. Anal. At. Spectrom. 1996, 11 (9), 899–904. https://doi.org/10.1039/ja9961100899.

[71] Jackson, S. E. CHAPTER 11: CALIBRATION STRATEGIES FOR ELEMENTAL ANALYSIS BY LA–ICP–MS. Laser Ablation ICP-MS in the Earth Sciences: Current Practices and Outstanding Issues, 2008, 169–188. https://doi.org/10.3749/9780921294801.ch11.

[72] Mervič, K.; Šelih, V. S.; Šala, M.; van Elteren, J. T. Non-Matrix-Matched Calibration in Bulk Multi-Element Laser Ablation – Inductively Coupled Plasma – Mass Spectrometry Analysis of Diverse Materials. Talanta 2024, 271, 125712. https://doi.org/10.1016/j.talanta.2024.125712.

[73] Mervič, K.; van Elteren, J. T.; Bele, M.; Šala, M. Utilizing Ablation Volume for Calibration in LA-ICP-MS Mapping to Address Variations in Ablation Rates within and between Matrices. Talanta 2024, 269, 125379. https://doi.org/10.1016/j.talanta.2023.125379.

CHAPTER 2

2.1. Imaging: state of the art

LA-ICP-MS is a transformative tool in elemental and isotopic imaging, offering unparalleled versatility and precision. This innovative technique enables the acquisition of detailed, quantitative images of elemental distributions across a wide variety of materials[1]. Compared to existing imaging methods, LA-ICP-MS boasts rapid throughput, a remarkably wide dynamic range, relatively clean mass spectra, and the ability to perform analyses at scales ranging from micrometres to centimetres. These attributes make it a powerful method for both broad and fine-scale investigations, as highlighted by researchers such as Woodhead[2]. The core strength of LA-ICP-MS lies in its capacity to provide high-resolution, multi-elemental, and isotopic imaging. Its ability to deliver quantitative data from major to trace elements with exceptional lateral resolution is particularly valuable for distinguishing intricate features within samples. The technique's high sensitivity, coupled with low limits of detection, ensures precise characterization of even the most subtle elemental variations, offering critical insights into sample composition and structure. Applications in biological sciences have underscored the immense potential of LA-ICP-MS. Research by Becker et al. (2005)[3], Jackson et al. (2006)[4], and Zoriy et al. (2006)[5] has demonstrated its utility in mapping trace elements such as copper and zinc within tissue sections. These studies have illuminated complex biological processes and offered insights into disease mechanisms, metabolic pathways, and nutrient distribution, highlighting the technique’s profound impact on understanding biological systems. Despite its advantages, LA-ICP-MS is not without limitations. The relatively large laser beam size can restrict spatial resolution compared to methods like electron microscopy or Secondary Ion Mass Spectrometry (SIMS). Its micro-destructive nature also precludes its use with irreplaceable specimens, and poorly optimized experiments can introduce artefacts that compromise data quality. However, these drawbacks are outweighed by the method’s unique capabilities. LA-ICP-MS stands out for its ability to analyse elemental concentrations across an extensive range, from sub-picograms per gram to percentages, and to perform multielement and isotopic analyses simultaneously, surpassing many traditional techniques that are limited to single-element imaging. Beyond biology, LA-ICP-MS has found applications in diverse fields. In geosciences, it is employed to study mineral compositions and trace element zoning, offering insights into geological processes and the evolution of Earth's crust[6]. In materials science, the technique aids in failure analysis, quality control, and the development of advanced materials by mapping element distributions in metals and ceramics. LA-ICP-MS also plays a pivotal role in cultural heritage studies, where it reveals the composition and origins of artifacts, contributing to both conservation and historical understanding. The future of LA-ICP-MS imaging is bright, driven by continual advancements in laser technology, resolution enhancement, and data processing capabilities. Recent advancements in ICP-TOFMS and low-dispersion laser ablation cells have significantly enhanced LA-ICP-MS, particularly for high-

speed, multielement, and high-resolution imaging[7]. ICP-TOFMS enables the simultaneous acquisition of complete mass spectra at extremely high frequencies, allowing all isotopes to be recorded in real time with improved quantification and reproducibility. At the same time, low-dispersion ablation cells with sub-millisecond washout times ensure efficient aerosol transport and sharp signal definition, which is crucial for fast scanning and minimizing spatial blurring. When combined with modern lasers capable of producing micrometre-scale spot sizes, the technique achieves sub-cellular spatial resolution, revealing fine structural and elemental details within biological tissues, minerals, and advanced materials. Together, these innovations provide unprecedented capabilities for comprehensive, high-throughput elemental imaging across diverse scientific fields.[8,9]. Innovations like overlapping scans and signal deconvolution improve spatial resolution, while low-dispersion cells ensure precise aerosol transport and short signal durations, boosting signal quality[10,11]. Despite these advancements, software development remains a bottleneck. Current tools emphasize data analysis over acquisition efficiency, but integrating software to control sample stages, lasers, and ICP-TOFMS could streamline processes[12]. This would enable advanced data analysis, such as phase-specific clustering and improved quantification of small features. ICP-TOFMS uniquely captures full isotopic data for each pulse, minimizing cumbersome processing and unlocking sophisticated imaging applications. Further innovations in timing synchronization and ablation techniques are essential to overcome challenges like spatial distortion in line scans. These developments position LA-ICP-MS as a powerful tool for geological, biological, and materials science imaging.

2.2. Fine-tuning of parameters

Performing mapping in the context of LA-ICP-MS involves analysing one pixel at a time and subsequently reconstructing the acquired image. This method allows for highly detailed spatial analysis of the elemental and isotopic composition of a sample. A critical factor governing imaging techniques is the balance between analysis time and the desired resolution, as achieving finer resolution often requires longer acquisition times. Historically, a major limitation in the widespread application of mapping techniques in LA-ICP-MS has been the long data acquisition times. These durations are primarily dictated by the washout time, which is the interval required for the ablation cell to clear the material from a single shot before the next pixel can be analysed. This parameter is influenced by instrumental factors, including the design of the ablation cell and the flow rates of carrier gases. The washout time determines how long each pixel, or shot, is detected and processed, impacting the overall speed and resolution of the imaging process. Recent advancements in instrumentation have dramatically reduced these washout times. While early systems required 5 to 10 seconds per pixel, modern innovations have decreased this to approximately 0.5 seconds. Cutting-edge technologies with low dispersion LA cells now allow acquisition times in the sub-millisecond range[13,14], opening up new possibilities for rapid, high-resolution mapping across diverse

applications[15,16]. These improvements have significantly enhanced the feasibility of rapid, high-resolution 2D and 3D mapping, making LA-ICP-MS more practical for high-throughput and large-area applications. However, achieving optimal image quality at these high speeds requires careful optimization of instrumental and acquisition parameters. Image fidelity can be compromised by distortions such as aliasing[17], smearing, and blur[18,19], and minimizing these artifacts while maximizing the signal-to-noise ratio is essential for accurate data interpretation. Blurring, for example, often result from the physical size of the laser beam interacting with sample features, compounded by inefficient aerosol washout and transport within the ablation cell and interface. These limitations can lead to visual defects like halo effects and smearing[20], which reduce spatial resolution and compromise the reliability of the data. To mitigate these issues, one approach involves firing the laser in a spot-by-spot ablation across the entire region of interest, which allows precise control over laser positioning and inter-shot timing (ranging from microseconds to seconds). While this method enhances data quality, it significantly increases total acquisition time, making it less practical for large-scale analyses. As a result, a more commonly used strategy involves continuous line scanning across the sample surface[21]. In this approach, the laser scans line after line using a fixed beam diameter, and the key parameters governing image quality become the laser repetition rate and scan speed, which must be carefully adjusted to prevent signal overlap and distortion. Advancements in fast-response ablation cells - initially developed for single-pulse LA-ICP-MS - have also improved performance in continuous scanning mode by reducing smearing caused by delayed aerosol transfer. Nevertheless, halo effects can still persist due to the interplay between beam size and surface topography and cannot be fully eliminated by hardware improvements alone. To further enhance image clarity, oversampling strategies can be applied. These involve reducing the pixel spacing relative to the laser spot size and/or increasing the laser dosage D (i.e., using more shots per pixel) as shown in figure 2.1 to boost signal intensity without overwhelming the system[22]. Such approaches improve data density and enable more accurate post-processing corrections. Advanced image reconstruction techniques—such as signal deconvolution and spatial correction algorithms—can then be applied to mitigate residual blurring and restore true spatial resolution. In addition to spatial accuracy, analytical precision in LA-ICP-MS is critically dependent on noise reduction and signal optimization[23]. Signal variability can be quantified by the total standard deviation, which includes two main components: Poisson noise and Flicker noise. Poisson noise, inherent to the counting nature of ion detection, is proportional to the square root of the signal intensity and becomes particularly relevant at low count rates, where statistical fluctuations are more pronounced. In contrast, Flicker noise increases linearly with signal intensity and is largely dictated by instrumental and operational parameters, including laser fluence, beam size, and aerosol transport dynamics. Experimental

data clearly demonstrate that both laser fluence, just above the ablation threshold, and beam size play a crucial role in determining the quality of the signal in single-pulse mode[24]. While increasing laser fluence or beam diameter generally boosts signal intensity—thus improving precision by generating more counts—these adjustments can have unintended consequences. Higher fluences tend to produce larger particles and more dense aerosol plumes, which may exceed the transport capacity of the system. This can result in incomplete transfer of material to the plasma, inefficient atomization and ionization, and ultimately, signal loss. Similarly, using excessively large beam sizes may generate surplus aerosol, which disrupts aerosol transport dynamics and can cause phenomena such as peak splitting and increased relative standard deviations (RSDs). These issues collectively impair the accuracy and precision of elemental imaging. To address these challenges, a modelling-based approach offers valuable insight into the optimization of key parameters for rapid, high-resolution mapping. This method focuses on minimizing imaging artifacts while maintaining efficient signal generation and transport. Crucial parameters - such as washout time (FW0.01M), beam size (BS), repetition rate (RR), scanning speed (SS), acquisition time (AT), and dwell time (DT) - can be systematically tuned to ensure stable and precise operation[25]. Maintaining square pixel geometry in the image requires adherence to the condition BS = SS × AT, while ensuring the delivery of *n* laser pulses within the acquisition window demands RR = n / AT[26]. Notably, excessively high scanning speeds compromise image quality, leading to signal instability and resolution loss. This is supported by image quality assessments using the Structural Similarity Index (SSIM), which indicate that optimal imaging conditions are achieved when SS ≤ 50 µm s^{-1} and AT ≥ 0.1 s. Importantly, AT is directly linked to the FW0.01M. This correlation is intuitive for non-oversampled pixels, where full integration of the ablation signal is required, but simulations show that the same applies even in oversampling regimes. Thus, for the fastest imaging without compromising quality, AT = FW0.01M should be used. Under this condition, the only difference between non-oversampled (n=1) and oversampled (n>1) modes is a higher repetition rate in the latter; all other parameters remain consistent. Accordingly, the general expression for areal mapping speed (AMS), as a function of beam size and washout time, is:

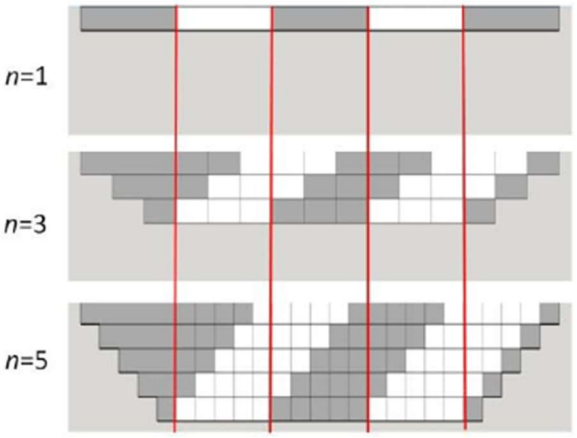


Fig 2.1. Visual representation of dosage using one (n=1), three (n=3), or five (n=5) shots per square pixel [25]

$$AMS(BS, FW0.01M) = BS \times SS = SS^2 \times AT = BS^2 \times \frac{RR}{n} = \frac{BS^2}{FW\ .01}$$

This equation highlights that for a given LA-ICP-MS configuration, the key parameters - SS, RR, and AT - are fully determined once BS, FW0.01M, and n are set. Therefore, reducing total mapping time requires increasing the areal mapping speed, which can only be achieved

(without loss in image quality) by using a system with a lower FW0.01M. This allows for faster scanning and higher repetition rates while preserving pixel resolution and minimizing image blur.

References

[1] Neff, C.; Keresztes Schmidt, P.; Garofalo, P. S.; Schwarz, G.; Günther, D. Capabilities of Automated LA-ICP-TOFMS Imaging of Geological Samples. J. Anal. At. Spectrom. 2020, 35 (10), 2255–2266. https://doi.org/10.1039/d0ja00238k.

[2] Woodhead, J. D.; Hellstrom, J.; Hergt, J. M.; Greig, A.; Maas, R. Isotopic and Elemental Imaging of Geological Materials by Laser Ablation Inductively Coupled Plasma-Mass Spectrometry. Geostandard Geoanalytic Res 2007, 31 (4), 331–343. https://doi.org/10.1111/j.1751-908x.2007.00104.x.

[3] Becker, J. S.; Zoriy, M. V.; Pickhardt, C.; Palomero-Gallagher, N.; Zilles, K. Imaging of Copper, Zinc, and Other Elements in Thin Section of Human Brain Samples (Hippocampus) by Laser Ablation Inductively Coupled Plasma Mass Spectrometry. Anal. Chem. 2005, 77 (10), 3208–3216. https://doi.org/10.1021/ac040184q.

[4] Jackson, B.; Harper, S.; Smith, L.; Flinn, J. Elemental Mapping and Quantitative Analysis of Cu, Zn, and Fe in Rat Brain Sections by Laser Ablation ICP-MS. Anal Bioanal Chem 2006, 384 (4), 951–957. https://doi.org/10.1007/s00216-005-0264-6.

[5] Zoriy, M. V.; Dehnhardt, M.; Reifenberger, G.; Zilles, K.; Becker, J. S. Imaging of Cu, Zn, Pb and U in Human Brain Tumor Resections by Laser Ablation Inductively Coupled Plasma Mass Spectrometry. International Journal of Mass Spectrometry 2006, 257 (1–3), 27–33. https://doi.org/10.1016/j.ijms.2006.06.005.

[6] Gundlach-Graham, A.; Burger, M.; Allner, S.; Schwarz, G.; Wang, H. A. O.; Gyr, L.; Grolimund, D.; Hattendorf, B.; Günther, D. High-Speed, High-Resolution, Multielemental Laser Ablation-Inductively Coupled Plasma-Time-of-Flight Mass Spectrometry Imaging: Part I. Instrumentation and Two-Dimensional Imaging of Geological Samples. Anal. Chem. 2015, 87 (16), 8250–8258. https://doi.org/10.1021/acs.analchem.5b01196.

[7] Borovinskaya, O.; Hattendorf, B.; Tanner, M.; Gschwind, S.; Günther, D. A Prototype of a New Inductively Coupled Plasma Time-of-Flight Mass Spectrometer Providing Temporally Resolved, Multi-Element Detection of Short Signals Generated by Single Particles and Droplets. J. Anal. At. Spectrom. 2013, 28 (2), 226–233. https://doi.org/10.1039/c2ja30227f.

[8] Wang, H. A. O.; Grolimund, D.; Giesen, C.; Borca, C. N.; Shaw-Stewart, J. R. H.; Bodenmiller, B.; Günther, D. Fast Chemical Imaging at High Spatial Resolution by Laser Ablation Inductively Coupled Plasma Mass Spectrometry. Anal. Chem. 2013, 85 (21), 10107–10116. https://doi.org/10.1021/ac400996x.

[9] Van Malderen, S. J. M.; Van Acker, T.; Vanhaecke, F. Sub-Micrometer Nanosecond LA-ICP-MS Imaging at Pixel Acquisition Rates above 250 Hz via a Low-Dispersion Setup. Anal. Chem. 2020, 92 (8), 5756–5764. https://doi.org/10.1021/acs.analchem.9b05056.

[10] Van Malderen, S. J. M.; van Elteren, J. T.; Vanhaecke, F. Submicrometer Imaging by Laser Ablation-Inductively Coupled Plasma Mass Spectrometry via Signal and Image Deconvolution Approaches. Anal. Chem. 2015, 87 (12), 6125–6132. https://doi.org/10.1021/acs.analchem.5b00700.

[11] Pisonero, J.; Bouzas-Ramos, D.; Traub, H.; Cappella, B.; Álvarez-Llamas, C.; Richter, S.; Mayo, J. C.; Costa-Fernandez, J. M.; Bordel, N.; Jakubowski, N. Critical Evaluation of Fast and Highly Resolved Elemental Distribution in Single Cells Using LA-ICP-SFMS. J. Anal. At. Spectrom. 2019, 34 (4), 655–663. https://doi.org/10.1039/c8ja00096d.

[12] Paul, B.; Woodhead, J. D.; Paton, C.; Hergt, J. M.; Hellstrom, J.; Norris, C. A. Towards a Method for Quantitative-LA-ICP-MS Imaging of Multi-Phase Assemblages: Mineral Identification and Analysis Correction Procedures. Geostandard Geoanalytic Res 2014, 38 (3), 253–263. https://doi.org/10.1111/j.1751-908x.2014.00270.x.

[13] Gundlach-Graham, A.; Burger, M.; Allner, S.; Schwarz, G.; Wang, H. A. O.; Gyr, L.; Grolimund, D.; Hattendorf, B.; Günther, D. High-Speed, High-Resolution, Multielemental Laser Ablation-Inductively Coupled Plasma-Time-of-Flight Mass Spectrometry Imaging: Part I. Instrumentation and Two-Dimensional Imaging of Geological Samples. Anal. Chem. 2015, 87 (16), 8250–8258. https://doi.org/10.1021/acs.analchem.5b01196.

[14] Burger, M.; Gundlach-Graham, A.; Allner, S.; Schwarz, G.; Wang, H. A. O.; Gyr, L.; Burgener, S.; Hattendorf, B.; Grolimund, D.; Günther, D. High-Speed, High-Resolution, Multielemental LA-ICP-TOFMS Imaging: Part II. Critical Evaluation of Quantitative Three-Dimensional Imaging of Major, Minor, and Trace Elements in Geological Samples. Anal. Chem. 2015, 87 (16), 8259–8267. https://doi.org/10.1021/acs.analchem.5b01977.

[15] Van Malderen, S. J. M.; Managh, A. J.; Sharp, B. L.; Vanhaecke, F. Recent Developments in the Design of Rapid Response Cells for Laser Ablation-Inductively Coupled Plasma-Mass Spectrometry and Their Impact on Bioimaging Applications. J. Anal. At. Spectrom. 2016, 31 (2), 423–439. https://doi.org/10.1039/c5ja00430f.

[16] Neff, C.; Becker, P.; Günther, D. Parallel Flow Ablation Cell for Short Signal Duration in LA-ICP-TOFMS Element Imaging. J. Anal. At. Spectrom. 2022, 37 (3), 677–683. https://doi.org/10.1039/d1ja00421b.

[17] van Elteren, J. T.; Šelih, V. S.; Šala, M.; Van Malderen, S. J. M.; Vanhaecke, F. Imaging Artifacts in Continuous Scanning 2D LA-ICPMS Imaging Due to Nonsynchronization Issues. Anal. Chem. 2018, 90 (4), 2896–2901. https://doi.org/10.1021/acs.analchem.7b05134.

[18] Bonta, M.; Limbeck, A.; Quarles Jr, C. D.; Oropeza, D.; Russo, R. E.; Gonzalez, J. J. A Metric for Evaluation of the Image Quality of Chemical Maps Derived from LA-ICP-MS Experiments. J. Anal. At. Spectrom. 2015, 30 (8), 1809–1815. https://doi.org/10.1039/c5ja00056d.

[19] van Elteren, J. T.; Šala, M.; Šelih, V. S. Perceptual Image Quality Metrics Concept in Continuous Scanning 2D Laser Ablation-Inductively Coupled Plasma Mass Spectrometry Bioimaging. Anal. Chem. 2018, 90 (9), 5916–5922. https://doi.org/10.1021/acs.analchem.8b00751.

[20] van Elteren, J. T.; Izmer, A.; Šelih, V. S.; Vanhaecke, F. Novel Image Metrics for Retrieval of the Lateral Resolution in Line Scan-Based 2D LA-ICPMS Imaging via an Experimental-Modeling Approach. Anal. Chem. 2016, 88 (14), 7413–7420. https://doi.org/10.1021/acs.analchem.6b02052.

[21] Gundlach-Graham, A.; Günther, D. Toward Faster and Higher Resolution LA–ICPMS Imaging: On the Co-Evolution of LA Cell Design and ICPMS Instrumentation. Anal Bioanal Chem 2016, 408 (11), 2687–2695. https://doi.org/10.1007/s00216-015-9251-8.

[22] Šala, M.; Šelih, V. S.; Stremtan, C. C.; Tămaş, T.; van Elteren, J. T. Implications of Laser Shot Dosage on Image Quality in LA-ICP-QMS Imaging. J. Anal. At. Spectrom. 2021, 36 (1), 75–79. https://doi.org/10.1039/d0ja00381f.

[23] van Elteren, J. T.; Šelih, V. S.; Šala, M. Insights into the Selection of 2D LA-ICP-MS (Multi)Elemental Mapping Conditions. J. Anal. At. Spectrom. 2019, 34 (9), 1919–1931. https://doi.org/10.1039/c9ja00166b.

[24] Jerše, A.; Mervič, K.; van Elteren, J. T.; Šelih, V. S.; Šala, M. Quantification Anomalies in Single Pulse LA-ICP-MS Analysis Associated with Laser Fluence and Beam Size. Analyst 2022, 147 (23), 5293–5299. https://doi.org/10.1039/d2an01172g.

[25] van Elteren, J. T.; Šelih, V. S.; Šala, M. Insights into the Selection of 2D LA-ICP-MS (Multi)Elemental Mapping Conditions. J. Anal. At. Spectrom. 2019, 34 (9), 1919–1931. https://doi.org/10.1039/c9ja00166b.

[26] van Elteren, J. T.; Metarapi, D.; Šala, M.; Šelih, V. S.; Stremtan, C. C. Fine-Tuning of LA-ICP-QMS Conditions for Elemental Mapping. J. Anal. At. Spectrom. 2020, 35 (11), 2494–2497. https://doi.org/10.1039/d0ja00322k.

CHAPTER 3

3.1. Nanoparticle-Assisted Signal Enhancement

Metallic nanoparticles (NPs) can enhance analytical signals in laser-based spectroscopic techniques through a complex interplay of physical and chemical mechanisms that synergistically improve plasma generation and analyte excitation[1,2,3,4]. One primary contribution arises from the localized increase in thermal conductivity and optical absorption induced by the NPs within the laser-induced plasma[5]. By concentrating and effectively channelling the laser energy, NPs facilitate more efficient heating and energy transfer to the target material, resulting in enhanced ablation and vaporization rates. Their intrinsically high surface-to-volume ratio provides an abundance of reactive sites that accelerate the atomization of the ablated species, leading to a more rapid and complete transition from condensed to gaseous phase, which is critical for subsequent excitation and ionization processes. Additionally, metallic NPs act as prolific electron donors during laser irradiation, significantly increasing the free electron density in the plasma. This increase lowers the plasma ignition threshold[6] and promotes more stable and intense plasma formation by enhancing seed-electron generation. A higher electron density improves collisional excitation and ionization probabilities, thereby increasing the emission intensities of analyte elements. Furthermore, the presence of NPs can modulate the plasma temperature and effective ionization potential, which selectively influences the excitation pathways of different elements. This modulation can result in preferential enhancement of specific emission lines or ionization stages, offering potential for improved analytical selectivity and sensitivity[7]. However, these enhancement effects are highly dependent on the physicochemical characteristics of the nanoparticles. NP size governs the extent of plasmonic resonance and surface area available for energy coupling; smaller NPs provide more surface sites but require higher packing densities to maintain effective plasmonic coupling, while larger NPs offer stronger individual plasmon resonances but may suffer from reduced surface coverage. The NP material itself determines optical properties such as plasmon resonance wavelength and extinction cross-section, which must be carefully matched to the laser excitation wavelength for maximal field enhancement. Concentration and spatial distribution of NPs on the sample surface critically influence the uniformity and reproducibility of the enhancement. Insufficient NP coverage results in weak plasmonic effects, whereas excessive loading can cause interparticle interactions such as tunnelling and shadowing, diminishing plasmon efficiency and leading to signal instability. Moreover, the interplay of these parameters must be balanced to avoid deleterious phenomena including spectral interferences arising from NP-related emission or scattering, self-absorption due to excessive local concentrations of ablated material, and potential morphological changes to the sample surface that could affect ablation uniformity. These challenges necessitate rigorous optimization of NP deposition protocols and laser parameters to ensure stable, reproducible, and maximized signal enhancement. When properly tuned, metallic NPs serve not only as catalysts for more efficient plasma formation

and analyte excitation but also as modulators of the plasma microenvironment, enabling substantial improvements in signal intensity and consequent reductions in limits of detection across a broad range of laser-based spectroscopic techniques.

3.2. Application of Nanoparticles in laser-based spectroscopies

The deliberate integration of metallic nanoparticles (NPs) to enhance laser–matter interactions has emerged as a transformative approach in analytical spectroscopy, most notably through Nanoparticle-Enhanced Laser-Induced Breakdown Spectroscopy (NELIBS), which has demonstrated improvements in limits of detection (LOD) of up to two orders of magnitude[6]. Central to this enhancement is the exploitation of Surface Plasmon Resonance (SPR) phenomena inherent to noble metal NPs such as gold (Au), silver (Ag), and platinum (Pt)[8,9]. Upon laser irradiation, these NPs exhibit collective oscillations of conduction electrons, resulting in intense, localized electromagnetic field enhancement at the NP–substrate interface[10]. This localized plasmonic field amplification is most significant in nanoscale gaps between closely spaced NPs, as well as at structural irregularities like sharp edges and tips, which act as electromagnetic "hot spots"[11]. Such intensified fields dramatically lower the laser-induced plasma breakdown threshold by facilitating seed-electron emission and promoting more efficient plasma ignition and growth[12]. Consequently, this enhanced photoablation efficiency affects not only the initial laser-matter interaction but also subsequent stages including particle generation, aerosol transport, vaporization, atomization, and ionization, all of which are crucial in determining analytical sensitivity. The application of similar plasmonic principles to Nanoparticle-Enhanced Laser Ablation Inductively Coupled Plasma Mass Spectrometry (NELA-ICP-MS) has resulted in substantial sensitivity improvements across a wide range of elements in both conductive and dielectric matrices. This effect is illustrated in Figure 3.1, where a linear scan of a copper standard shows a pronounced increase in the silver signal following the deposition of PtNPs. However, the underlying enhancement mechanisms in NELA-ICP-MS differ in certain aspects from those observed in NELIBS[13]. Experimental evidence confirms that NP-assisted plasmas exhibit higher

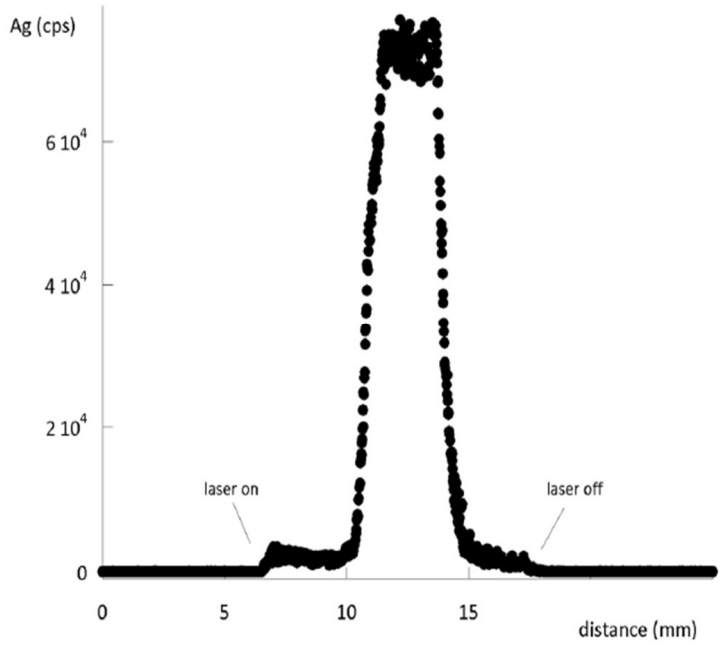


Fig 3.1. Silver signal profile for a 99.999% pure copper standard during a linear scan, showing the transition from an area without PtNPs to an area with PtNPs [13].

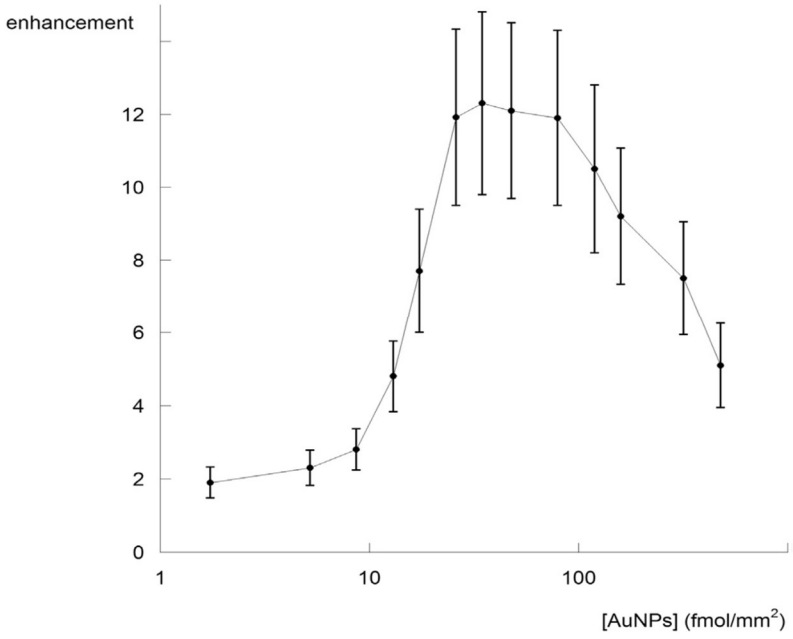


Fig 3.2. Enhancement of Ag vs [AuNPs] [13].

concentrations of atoms and molecules and persist longer than those generated by conventional ablation[14]. The extended plasma lifetime, coupled with slower cooling dynamics, promotes the formation of finer aerosols and thus a higher fraction of signal-contributing species delivered to the ICP torch. Enhancement in both NELA-ICP-MS and NELIBS is critically dependent on nanoparticle surface coverage as illustrated in Figure 3.2. At low NP densities, the improvement arises from a reduction in ablation threshold, as isolated NPs act as efficient electron donors and localized defects, leading to slightly increased ablation efficiency. Once the critical coverage is reached, collective oscillation of conduction electrons establishes strong plasmonic coupling with the laser field, amplifying local electromagnetic fields, elevating plasma temperature, and extending plasma persistence, thereby maximizing analytical sensitivity. At this stage, signal enhancement increases sharply, plateauing at approximately an order of magnitude gain. At excessively high NP loadings, however,

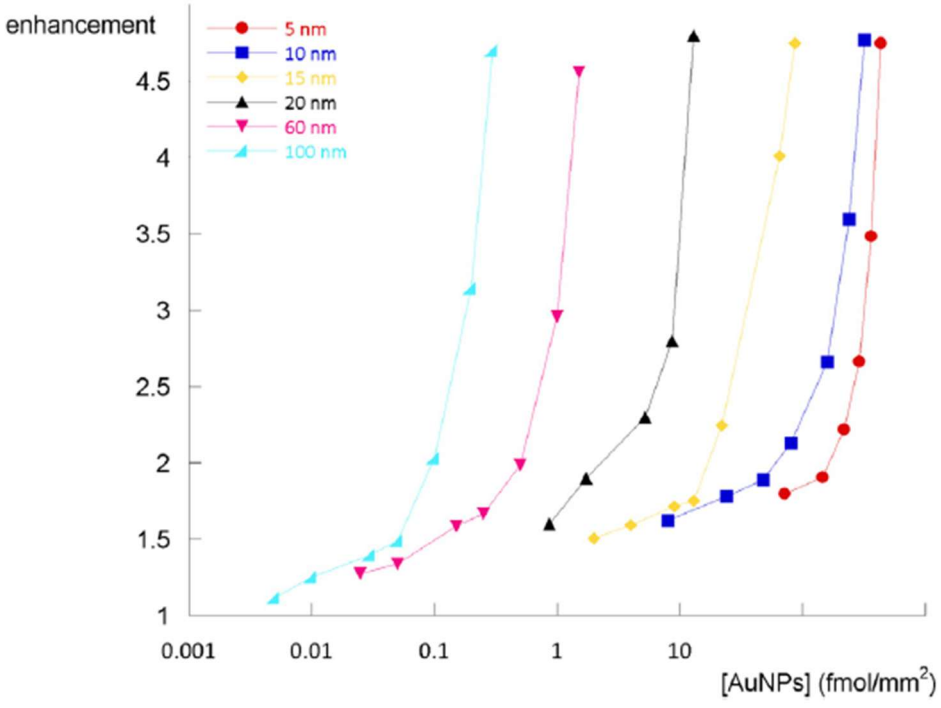


Fig 3.3. Enhancement of Ag vs AuNPs surface concentration (fmol/mm2) for different AuNPs sizes.[13].

aggregation and shadowing effects occur, while interparticle electron tunneling diminishes plasmon resonance, resulting in a decline in both enhancement and reproducibility. The magnitude of this enhancement is strongly influenced by NP size, composition, and optical characteristics. Smaller NPs require higher surface densities to maintain effective plasmonic coupling, while larger NPs can achieve maximum enhancement at lower surface coverage (Figure 3.3). Comparative studies further reveal that Au, Ag, and Pt nanoparticles differ in their enhancement efficiencies, primarily dictated by the degree of overlap between their surface plasmon resonance (SPR) and the laser excitation wavelength, as well as by their extinction cross-sections. Among these, PtNPs provide the most substantial enhancement due to their closer spectral alignment with common laser wavelengths (e.g., 213 nm) and smaller extinction cross-section[15]. The relationship between enhancement and laser power was also examined, with the results clearly illustrated in Figure 3.4. The signal intensity, both with and

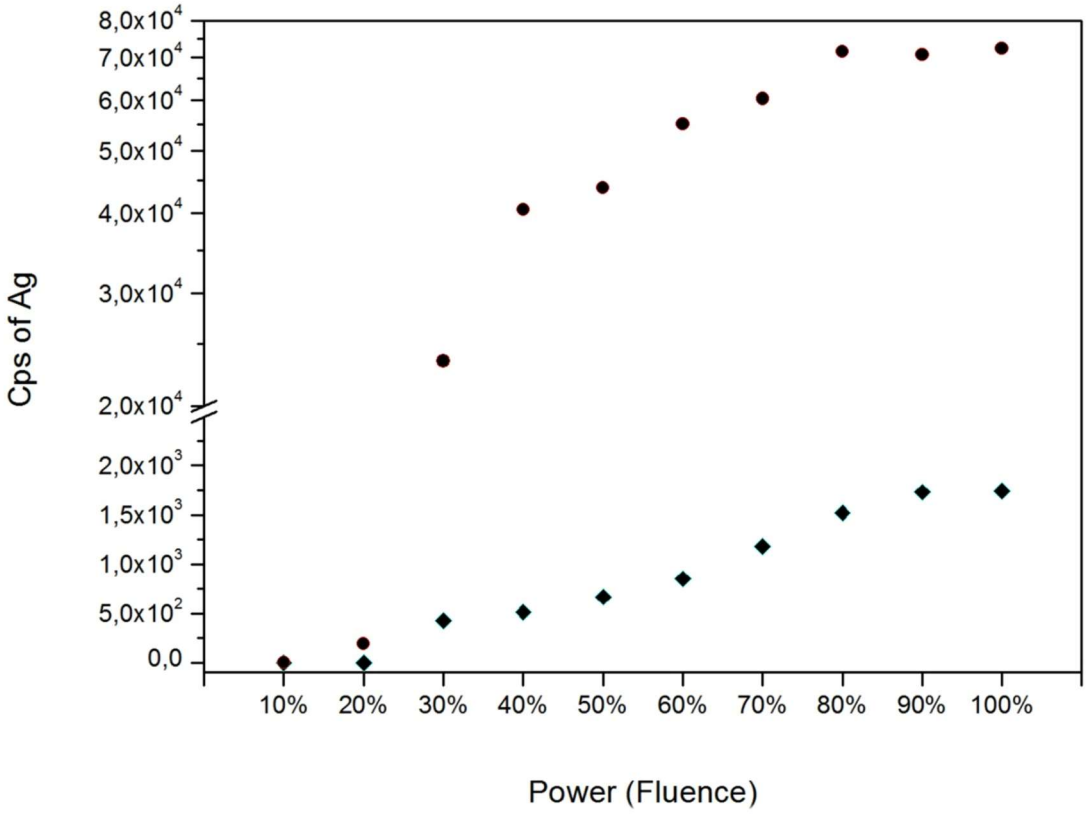


Fig 3.4. Ag signal as a function of laser fluence in LA-ICP-MS experiments on a Cu standard, ♦ with and ♦ without NPs.

without NPs, increases with rising laser power above the breakdown threshold (power <20%). Analysis of the data indicates that the presence of NPs enables the use of lower laser powers to achieve higher signal intensities, thereby reducing sample damage. Importantly, the breakdown threshold remains unchanged with the addition of NPs, suggesting that the enhancement effect arises not from a shift in the threshold but from improved energy coupling and more efficient ablation facilitated by the nanoparticles. Microscopic and spectroscopic analyses further reveal that NP-assisted ablation produces more uniform and cleaner craters,

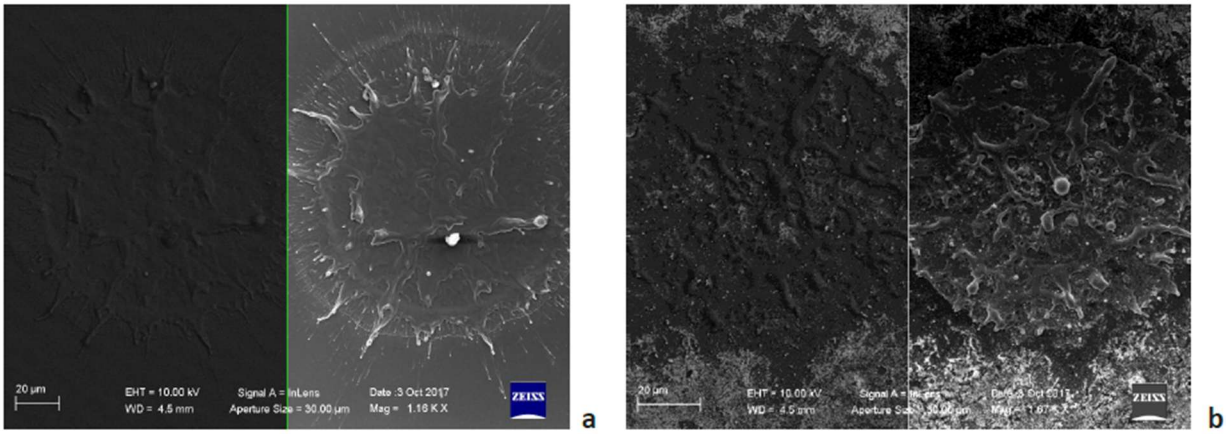


Fig 3.5. SEM images of craters on target of Silicon without AuNPs (a) and with AuNPs (b) produced after LA experiments.

with reduced evidence of melting or cracking (figure 3.5), and generates composite aerosols consisting of condensed analyte material on NP cores. These composite particles exhibit superior vaporization and ionization behavior, mitigating matrix effects and improving analytical reproducibility. Collectively, these observations indicate that NP-mediated enhancement in LA-ICP-MS arises from a synergy of electromagnetic field amplification, plasmon-assisted photoablation, and optimization of aerosol dynamics[16,17]. While both NELIBS and NELA-ICP-MS benefit from these mechanisms, their enhancement behavior differs with respect to analyte concentration. NELIBS enhancement is largely analyte-independent, whereas NELA-ICP-MS exhibits pronounced improvements at low analyte concentrations as shown in Figure 3.6, making it particularly effective for trace-level elemental determinations. From a practical perspective, both NELIBS and NELA-ICP-MS are experimentally straightforward and cost-effective to implement, requiring only the simple deposition of colloidal noble-metal NP solutions without any modification to existing instrumentation. Moreover, both techniques do not risk permanent contamination of the sample, as the deposited NPs are completely removed after just a few laser shots. While NELIBS provides a rapid and simple enhancement strategy, NELA-ICP-MS offers greater analytical depth, though it involves more complex aerosol–plasma interactions. Future directions in this field lie in tailoring NP properties -size, shape, composition, and arrangement- to finely control plasmonic coupling and maximize enhancement. The development of anisotropic NPs, core–shell architectures, and hybrid nanomaterials promises further improvements in field localization and thermal control during ablation. Moreover, integration with time-resolved spectroscopy and plasma diagnostics will provide deeper insights into NP-modulated plasma dynamics and chemical pathways. Such advances are expected to enable next-generation laser-based analytical platforms with unprecedented sensitivity, selectivity, and robustness

for applications ranging from environmental monitoring to materials science and biomedical diagnostics.

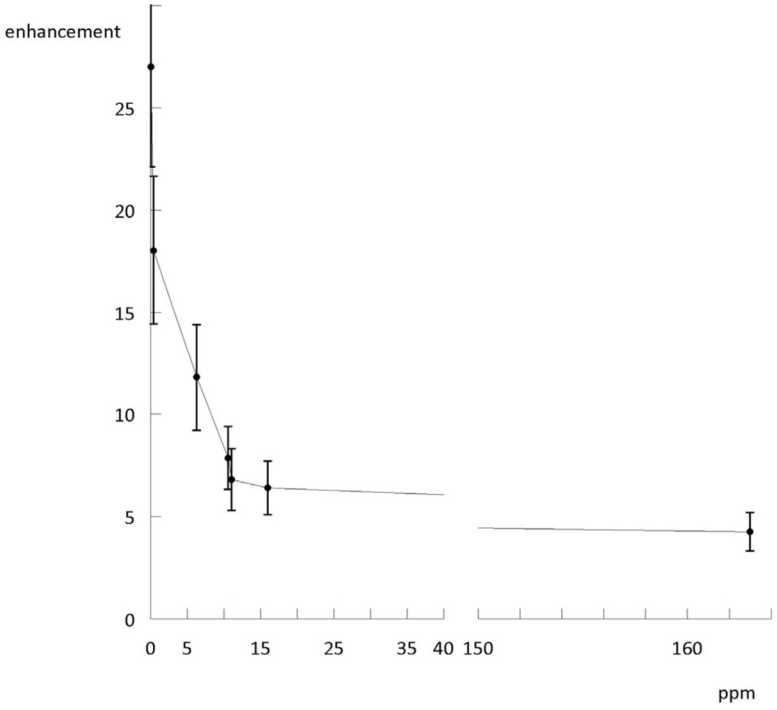


Fig 3.6. Enhancement of Ag vs [Ag][13].

References

[1] Nie, S.; Emory, S. R. Probing Single Molecules and Single Nanoparticles by Surface-Enhanced Raman Scattering. Science 1997, 275 (5303), 1102–1106. https://doi.org/10.1126/science.275.5303.1102.

[2] Adams, F. C.; Barbante, C. Nanoscience, Nanotechnology and Spectrometry. Spectrochimica Acta Part B: Atomic Spectroscopy 2013, 86, 3–13. https://doi.org/10.1016/j.sab.2013.04.008.

[3] Zhao, X.; Zhao, C.; Du, X.; Dong, D. Detecting and Mapping Harmful Chemicals in Fruit and Vegetables Using Nanoparticle-Enhanced Laser-Induced Breakdown Spectroscopy. Sci Rep 2019, 9 (1). https://doi.org/10.1038/s41598-018-37556-w.

[4] El-Saeid, R. H.; Abdel-Salam, Z.; Pagnotta, S.; Palleschi, V.; Harith, M. A. Classification of Sedimentary and Igneous Rocks by Laser Induced Breakdown Spectroscopy and Nanoparticle-Enhanced Laser Induced Breakdown Spectroscopy Combined with Principal Component Analysis and Graph Theory. Spectrochimica Acta Part B: Atomic Spectroscopy 2019, 158, 105622. https://doi.org/10.1016/j.sab.2019.05.011.

[5] De Giacomo, A.; Alrifai, R.; Gardette, V.; Salajková, Z.; Dell'Aglio, M. Nanoparticle Enhanced Laser Ablation and Consequent Effects on Laser Induced Plasma Optical Emission. Spectrochimica Acta Part B: Atomic Spectroscopy 2020, 166, 105794. https://doi.org/10.1016/j.sab.2020.105794.

[6] De Giacomo, A.; Gaudiuso, R.; Koral, C.; Dell'Aglio, M.; De Pascale, O. Nanoparticle-Enhanced Laser-Induced Breakdown Spectroscopy of Metallic Samples. Anal. Chem. 2013, 85 (21), 10180–10187. https://doi.org/10.1021/ac4016165.

[7] Galbács, G.; Kéri, A.; Kohut, A.; Veres, M.; Geretovszky, Zs. Nanoparticles in Analytical Laser and Plasma Spectroscopy – a Review of Recent Developments in Methodology and Applications. J. Anal. At. Spectrom. 2021, 36 (9), 1826–1872. https://doi.org/10.1039/d1ja00149c.

[8] Catanzaro, L.; Scardaci, V.; Scuderi, M.; Condorelli, M.; D'Urso, L.; Compagnini, G. Surface Plasmon Resonance of Gold Nanoparticle Aggregates Induced by Halide Ions. Materials Chemistry and Physics 2023, 308, 128245. https://doi.org/10.1016/j.matchemphys.2023.128245.

[9] Loiseau, A.; Asila, V.; Boitel-Aullen, G.; Lam, M.; Salmain, M.; Boujday, S. Silver-Based Plasmonic Nanoparticles for and Their Use in Biosensing. Biosensors 2019, 9 (2), 78. https://doi.org/10.3390/bios9020078.

[10] Teichmann, S. M.; Rácz, P.; Ciappina, M. F.; Pérez-Hernández, J. A.; Thai, A.; Fekete, J.; Elezzabi, A. Y.; Veisz, L.; Biegert, J.; Dombi, P. Strong-Field Plasmonic Photoemission in the Mid-IR at <1 GW/Cm2 Intensity. Sci Rep 2015, 5 (1). https://doi.org/10.1038/srep07584.

[11] Schertz, F.; Schmelzeisen, M.; Kreiter, M.; Elmers, H.-J.; Schönhense, G. Field Emission of Electrons Generated by the Near Field of Strongly Coupled Plasmons. Phys. Rev. Lett. 2012, 108 (23). https://doi.org/10.1103/physrevlett.108.237602.

[12] Radziemski, L. J. Lasers-Induced Plasmas and Applications, 2020. https://doi.org/10.1201/9781003066200.

[13] Mangone, A.; Mastrorocco, F.; Giannossa, L. C.; Comparelli, R.; Dell'Aglio, M.; De Giacomo, A. Nanoparticle Enhanced Laser Ablation Inductively Coupled Plasma Mass Spectrometry. Spectrochimica Acta Part B: Atomic Spectroscopy 2020, 163, 105731. https://doi.org/10.1016/j.sab.2019.105731.

[14] Koral, C.; De Giacomo, A.; Mao, X.; Zorba, V.; Russo, R. E. Nanoparticle Enhanced Laser Induced Breakdown Spectroscopy for Improving the Detection of Molecular Bands. Spectrochimica Acta Part B: Atomic Spectroscopy 2016, 125, 11–17. https://doi.org/10.1016/j.sab.2016.09.006.

[15] Creighton, J. A.; Eadon, D. G. Ultraviolet–Visible Absorption Spectra of the Colloidal Metallic Elements. J. Chem. Soc., Faraday Trans. 1991, 87 (24), 3881–3891. https://doi.org/10.1039/ft9918703881.

[16] De Giacomo, A.; Dell'Aglio, M.; Gaudiuso, R.; Koral, C.; Valenza, G. Perspective on the Use of Nanoparticles to Improve LIBS Analytical Performance: Nanoparticle Enhanced Laser Induced Breakdown Spectroscopy (NELIBS). J. Anal. At. Spectrom. 2016, 31 (8), 1566–1573. https://doi.org/10.1039/c6ja00189k.

[17] Holá, M.; Salajková, Z.; Hrdlička, A.; Pořízka, P.; Novotný, K.; Čelko, L.; Šperka, P.; Prochazka, D.; Novotný, J.; Modlitbová, P.; Kanický, V.; Kaiser, J. Feasibility of Nanoparticle-Enhanced Laser Ablation Inductively Coupled Plasma Mass Spectrometry. Anal. Chem. 2018, 90 (20), 11820–11826. https://doi.org/10.1021/acs.analchem.8b01197.

CHAPTER 4

In this chapter, two representative case studies are presented to illustrate the application of integrative approaches to Laser Ablation ICP-MS across markedly different sample matrices. The first concerns archaeological glass, an inorganic material with a rigid silicate network, while the second focuses on certified human serum, a complex organic biological sample. While the combination of complementary strategies can enhance signal fidelity and imaging accuracy, these examples also highlight that LA-ICP-MS, even as a stand-alone technique, can yield highly explanatory and illuminating results. Together, they underscore the method's adaptability and analytical power when addressing the distinct challenges posed by diverse material types.

4.1. Case study: glass artifacts founded at "Masseria Caione"

4.1.1. Glass: state of the art

Glass is one of humanity's oldest and most adaptable materials. Despite millennia of use, glassmaking remains a largely empirical and not fully understood craft. The earliest glass artifacts, dating to around 4,500 years ago, are attributed to ancient Egypt[1], where craftsmen melted sodium carbonate, silicates, and metallic oxides to form molten glass[2,3]. This was shaped in clay moulds or carved once cooled, and both finished objects and raw frit blocks were widely traded across the Middle East[4]. Large-scale glassmaking began in the 3rd millennium BCE and advanced significantly by 1500 BCE[5,6]. A major breakthrough came in the 1st century BCE with the invention of glassblowing in Syria and Palestine, revolutionizing production and making glass more accessible[7]. What was once a luxury for elites became, by the Roman era, an everyday material for vessels, windows, and household goods. Through the Middle Ages and Renaissance, innovations such as stained-glass windows, mirrors, and scientific glassware further expanded its uses[8]. Today, glass remains indispensable across architecture, science, and technology. Given its historical and economic significance, archaeological glass artifacts continue to warrant close study. Since the 1970s, SEM-EDX (Scanning Electron Microscopy with Energy Dispersive X-Ray Spectroscopy) has been central to archaeometric glass studies, valued for its reliable multi-elemental characterization[9]. Its drawbacks, however, include destructive sampling and limited trace sensitivity. To overcome these issues, it is often paired with techniques such as ICP-OES (Inductively Coupled Plasma Optical Emission Spectrometry) and ICP-MS (Inductively Coupled Plasma Mass Spectrometry), which provide greater precision for trace element detection, resulting in more comprehensive analyses[10]. Another widely used technique is INAA (Instrumental Neutron Activation Analysis), valued for its high sensitivity, precision, and capacity to analyse whole artifacts independent of homogeneity[11]. Its major limitation is the induced radioactivity, which restricts applications and

highlights the need for non-destructive alternatives. In this context, X-ray methods, particularly XRF[12] (X-ray fluorescence) and EPMA[13] (Electron Probe microanalysis) have been widely applied in glass studies due to their precision and adaptability. While effective, XRF is limited by its reliance on surface chemistry, which can be distorted by weathering, making complementary approaches essential. In parallel, ion beam techniques such as PIXE (Proton-Induced X-ray Emission) and PIGE (Particle-Induced Gamma-ray Emission) emerged as powerful non-destructive tools, combining high sensitivity with bulk compositional analysis; PIXE is particularly effective for subsurface characterization, while PIGE is well suited for profiling light elements. Their combination with PGAA (Prompt Gamma Activation Analysis) further enhanced analytical depth, though at the cost of demanding instrumentation[14]. These techniques have proven invaluable for characterizing both production and circulation of glass while preserving artifact integrity. Surface-focused techniques like XPS (X-ray Photoelectron Spectroscopy) and SIMS (Secondary Ion Mass Spectrometry) added the ability to probe alteration layers at nanometric to micrometric scales, providing detailed insights into corrosion and leaching processes[15,16]. Later, LA-ICP-MS became a benchmark method for glass archaeometry, delivering sub-ppm sensitivity, wide elemental coverage, and minimal sampling[17]. More recently, LIBS has gained attention as a versatile, rapid, and micro-invasive tool, particularly suited for detecting light elements[18]. Current research employs an integrated workflow of non-destructive, micro-destructive, and high-sensitivity methods. Within this framework, LA-ICP-MS stands out as a privileged tool, delivering unmatched sensitivity and elemental coverage with minimal impact on the artifact. Such combined strategies not only unlock detailed insights into composition, provenance, and technology but also safeguard the integrity of fragile glass heritage.

4.1.2. Archaeological framework

The Via Appia -often celebrated as one of the most important and enduring arteries of the Roman Empire- stretched from the heart of Rome to the bustling Adriatic port of Brindisi, opening a vital gateway between the capital and the eastern Mediterranean world[19]. Far more than a simple roadway, it was a conduit for commerce, military logistics, cultural

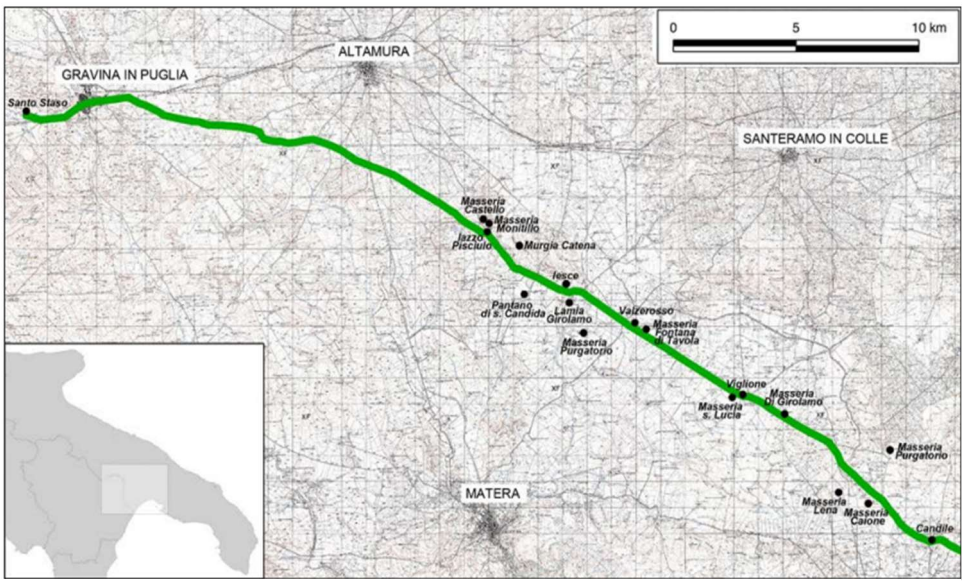


Fig 4.1. Stretch of Via Appia between Gravina and località Candile.

exchange, and imperial communication. Its strategic role earned it the epithet *regina viarum* (“queen of roads”) in antiquity, and its influence on the economic and political integration of Italy remained profound for centuries. Modern archaeological and historical research continues to explore this ancient route, shedding new light on its evolution and its relationship with the landscapes it traversed. In particular, recent systematic surface surveys along the Apulian stretch between Gravina and Taranto have begun to reveal how the Via Appia intersected with, absorbed, and sometimes reoriented pre-existing road systems, as well as how later networks were integrated into its structure. These studies aim to reconstruct the road’s life history -its construction phases, modifications, and the changing patterns of connectivity it supported- within the broader socio-economic and political dynamics of southern Italy. A key component of this research focuses on archaeological finds in the immediate vicinity of the road. One particularly significant site is Masseria Caione, located about 500 meters south of the Via Appia’s route as per Figure 4.1. Here, a collection of 36 exceptionally well-preserved glass fragments (Figure 4.2) has been recovered and subjected to detailed typological and archaeometric study (see appendix, Table S4.1 and S4.2). These



Fig 4.2. Representative selection of glass fragments.

artifacts -produced through a range of techniques including mold-blowing, free-blowing, matrix-blowing, and lampworking- reflect both local consumption patterns and broader trade networks. The majority are transparent, typically in varying shades of blue-green, although examples in colourless glass, opaque blue, and opaque green are also present. Most pieces show only minimal iridescent weathering, with occasional signs of opacification. Functionally, these glass objects encompass tableware, vessels for the storage and transport of liquids, lighting implements, and items of personal adornment. Typological analysis indicates that most date to the Roman Imperial period, particularly the 1st–2nd centuries AD, though later antique forms are also represented. With the exception of a single lamp type associated with later production, the assemblage does not extend beyond the 5th century AD. The archaeometric investigations, particularly the chemical analysis of the glass, are designed to address questions of technological continuity and change. By identifying whether the fluxes used in production were of mineral or vegetal origin, researchers can discern shifts in

manufacturing traditions over time[20]. Moreover, the detection of mineral fluxes traceable to Eastern sources could illuminate the movement of raw materials and the role of Apulia - especially its Adriatic ports- as nodes in long-distance trade routes linking Italy to the Eastern Mediterranean[21]. In this context, the analysis of trace elements plays a critical role[22,23]. Determining the recipes for ancient colorants and decolourants, and understanding how these interacted with base glass chemistry, allows scholars to reconstruct both technological choices and cultural preferences in glass production. In this contest LA-ICP-MS represents a proven technique in ancient glass studies. This method enables precise characterization of chemical composition, identification of raw materials (fluxes, stabilizers, colorants), and examination of surface alteration processes[24]. Such data not only contribute to understanding the technical aspects of ancient glassmaking but also provide a chemical fingerprinting method to trace supply networks and patterns of economic integration along the Via Appia's course through Apulia.

4.1.3. Materials and methods

The research project on archaeological glass was carried out at the laboratory of analytical chemistry at the Kemijski Institute in Ljubljana, where access to advanced analytical facilities allowed for both the execution of high-precision measurements and the refinement of methodological expertise. In this context, significant progress was made in understanding how to optimize analytical parameters, improve imaging protocols, and minimize artefacts, thereby enhancing the accuracy and interpretative reliability of the results. Analyses were performed using a 193 nm ArF* excimer laser ablation system (Analyte G2, Teledyne Photon Machines Inc., Bozeman, MT) coupled to an ICP-QMS instrument (Agilent 7900, Agilent Technologies, Santa Clara, CA). Ablation was conducted in a HelEx two-volume cell, with an aerosol washout time of approximately 0.5 s. Preliminary investigations were carried out to assess the applicability of the sum normalization method, as developed by van Elteren et al., to the archaeological glass samples under study[25]. The aim was to gain a deeper understanding of the raw materials employed in glass production, thereby providing more robust indications regarding the provenance of the raw materials and the historical period of manufacture. To this end, a tiny portion was carefully removed from each sample to reveal a fresh fracture surface for analysis, without compromising the overall integrity of the specimen. The only specimen analysed in its original surface state was the bead, which, as an ornamental artefact, differs in character from the other samples. For LA-ICP-MS calibration, the following reference materials were employed: NIST SRM glasses 610 and 612, with nominal concentrations of approximately 500 and 50 μg g^{-1}, respectively, for around 60 elements; synthetic glass standards B, C, and D from the Corning Museum of Glass, replicating ancient compositions; and Society of Glass Technology glass standards 2, 3, 4, and 5. Reference elemental oxide concentrations (in % [w/w]) for all these standards are reported in Table S4.3. The choice of the sum normalization approach -rather than relying solely on single-point calibration- was driven by the need for

greater analytical robustness in raster sampling mode. Raster sampling, as opposed to crater sampling, permits extended acquisition times and normalization based on the sum of 54 elemental oxides (major, minor, and trace elements)[26]. This not only improves accuracy by accounting for the complete compositional matrix but also minimizes elemental fractionation effects associated with deep craters, thereby yielding more reliable and representative bulk compositions. Instrument calibration was performed using NIST SRM 610, monitoring the isotopes ^{23}Na, ^{139}La, ^{89}Y, ^{232}Th, and ^{238}U, together with the U/Th ratio (≈1) and oxide ratios (^{248}/^{232}), as a function of instrumental parameters, with particular attention to the nebulizer gas flow[27]. The LA-ICP-MS parameters for raster analysis are reported in Table 4.1. Line scanning was conducted with a dosage (D) of 20, meaning that signals from 20 laser shots were integrated over an analysis time (AT) of 0.5 s, corresponding to a repetition rate (RR) of 40 Hz according to the relation:

$$RR = \frac{1}{AT} \times D$$

and to a scan speed of 40 µm/s according to the relation:

$$scan\ speed = \frac{beam\ sixe \times Rep\ rate}{dosage}$$

LA parameters	
Laser fluence	*4 J/cm^2*
Dosage	*20*
Spot size	*20 µm square*
RR	*40 Hz*
Scan speed	*40 µm/s*
Carrier gas flow rate	*He, 0.3 L/min*
ICP-MS parameters	
Rf power	*1500 W*
Plasma gas flow rate	*15 L/min*
Auxiliary gas flow rate	*0.9 L/min*
Ar makeup flow rate	*0.8 L/min*
Isotopes measured	*^{7}Li, ^{9}Be, ^{11}B, ^{23}Na, ^{24}Mg, ^{27}Al, ^{29}Si, ^{31}P, ^{39}K, ^{43}Ca, ^{45}Sc, ^{47}Ti, ^{51}V, ^{53}Cr, ^{55}Mn, ^{57}Fe, ^{59}Co, ^{60}Ni, ^{63}Cu, ^{66}Zn, ^{69}Ga, ^{75}As, ^{82}Se, ^{85}Rb, ^{88}Sr, ^{89}Y, ^{90}Zr, ^{93}Nb, ^{95}Mo, ^{107}Ag, ^{111}Cd, ^{115}In, ^{118}Sn, ^{121}Sb, ^{137}Ba, ^{139}La, ^{140}Ce, ^{141}Pr, ^{146}Nd, ^{147}Sm, ^{153}Eu, ^{157}Gd, ^{159}Tb, ^{163}Dy, ^{165}Ho, ^{166}Er, ^{169}Tm, ^{172}Yb, ^{175}Lu, ^{197}Au, ^{208}Pb, ^{209}Bi, ^{232}Th, ^{238}U*

Tab 4.1. LA and ICPMS parameters used for the analysis.

The analyses were performed by carrying out three linear scans, each 1 mm in length, for the 12 standards and five scans of the same length for the samples. The spectra obtained for the standards were processed individually in Excel: the signal data were averaged, blank-corrected, and the standard deviation and RSD% calculated[28]. The three blank-corrected averages were then further averaged to obtain the intensity values for all elements in each standard. The mean intensity values, together with the reference oxide concentrations of the standards, were imported into both the Excel file *Sum_Norm* and the dedicated software "SumNormApp" developed by the research group in Ljubljana, for ^{29}Si correction, calculation of oxide intensities, and generation of calibration curves with the corresponding response factors. From these calibration curves, the concentrations for each sample were subsequently calculated. Sum normalization was also applied in this study to map leaching and corrosion processes on selected samples, chosen based on their visible state of preservation. Mapping analyses were performed using two distinct approaches. In the first approach, analyses were conducted directly on the untreated sample surface. Once a region of interest was identified, a line of 3.465 mm was traced, and ablation was repeated 100 times along the same line, with a scan time of 0.50 s per pass. At each repetition, the laser focus was adjusted by 1 µm. All instrumental parameters were kept identical to the bulk analyses, except for the beam size, which was set to 35 µm × 35 µm, resulting in a scan speed of 70 µm/s. In this case, sum normalization was essential to correct for signal drift caused by variations in sampling depth during repeated ablation. The second approach involved embedding selected sample fragments in resin, followed by polishing. Samples were oriented so that the exposed face revealed the complete lateral profile, from the corroded surface to the unaltered bulk interior. Instrumental parameters were kept consistent with those used for the other mapping analyses, and 50 adjacent lines were ablated to construct the compositional image (Figure 4.3). This preparation enabled detailed mapping of compositional gradients across the corrosion layer while preserving the spatial relationship between the surface and the bulk glass.

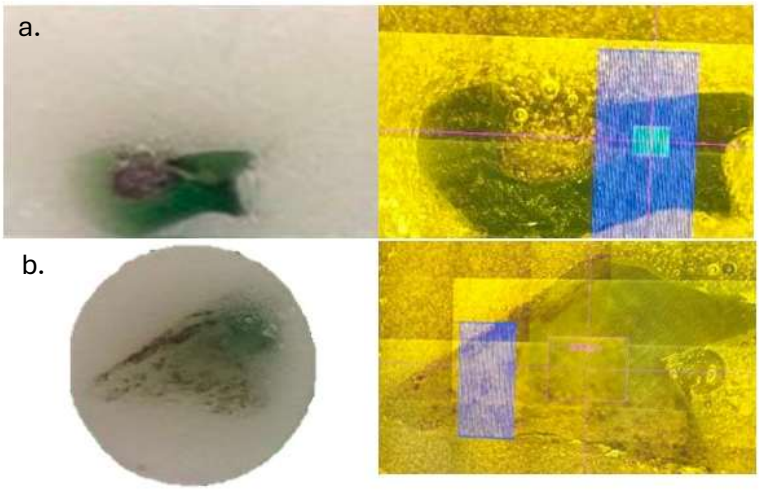


Fig 4.3. Glass samples a. G9 and b. G14 embedded in resin with the corresponding mapping trace obtained.

4.1.4.Results and discussion

Concentrations averaged over the five replicates on bulk are reported in Table S4.4. Data processing was performed using ImageJ and HDIP (Teledyne Photon Machines Inc., Bozeman, MT). CSV files exported from HDIP were imported into ImageJ, where the data corresponding to the five lines were converted into colour-scaled images. This approach enabled the visualization and rapid detection of outliers, while also allowing the calculation of oxide concentrations. Importantly, this procedure emphasizes a key advantage of LA-ICP-MS: the heterogeneity of the glass samples remains directly observable, in contrast to solution-based ICP-MS analyses, where sample digestion and mineralization processes can obscure or eliminate such spatial information. The data obtained through this procedure were employed to reconstruct the composition and infer the provenance of the raw materials used in the analysed artifacts, which in turn allowed for chronological interpretation of the assemblage. To further support these interpretations, a preliminary Principal Component Analysis (PCA)[29] was performed using the oxides of titanium, strontium, zirconium, barium, and chromium, which Brems and Degryse have identified as the most relevant indicators for determining the geological origin of silica as a raw material[30] . The biplot shown in Figure 4.4 illustrates that most of the analysed artifacts cluster closely together, suggesting either a shared origin of raw materials or the widespread practice of recycling glass cullet in secondary workshops[31]. This interpretation is further supported by the rare earth element (REE) patterns, normalized to crustal values (REE/crust)[32], which likewise display consistent profiles across the majority of

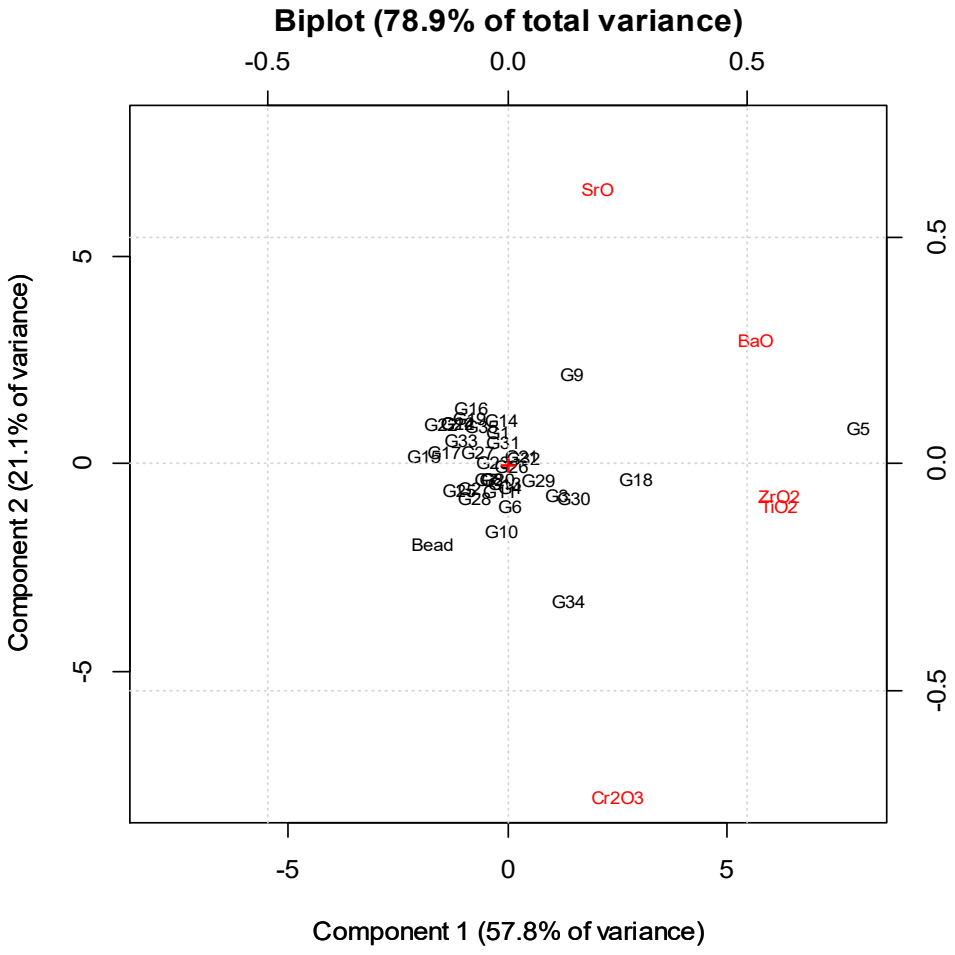


Fig 4.4. Biplot explaining the 78.9% of variance.

samples, reinforcing the evidence for a common provenance or extensive recycling practices (Figure 4.5). Nevertheless, several samples are clearly separated from the main cluster. Samples G5 and G18 plot at high positive values on PC1, characterized by elevated Zr and Ti concentrations, indicative of distinct silica sources or alternative production techniques[33]. G9, positioned at high positive values on PC2, is enriched in barium, suggesting a depositional

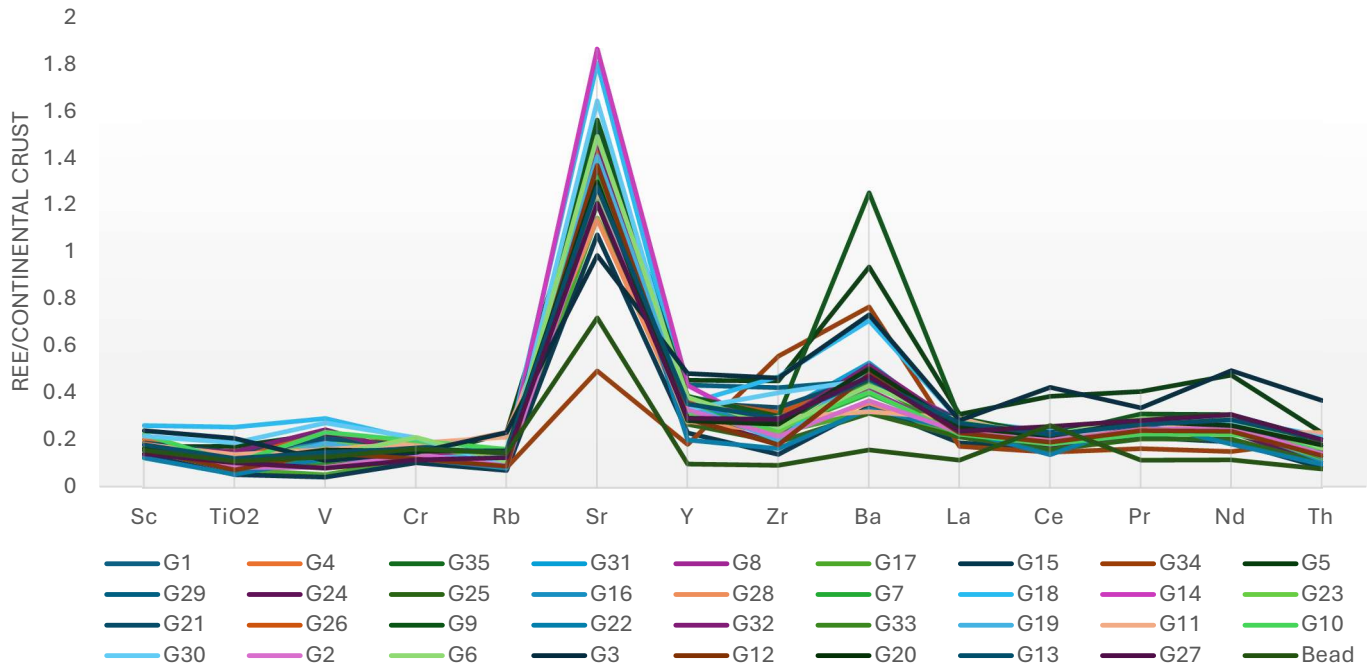


Fig 4.5. REE/continental crust patterns.

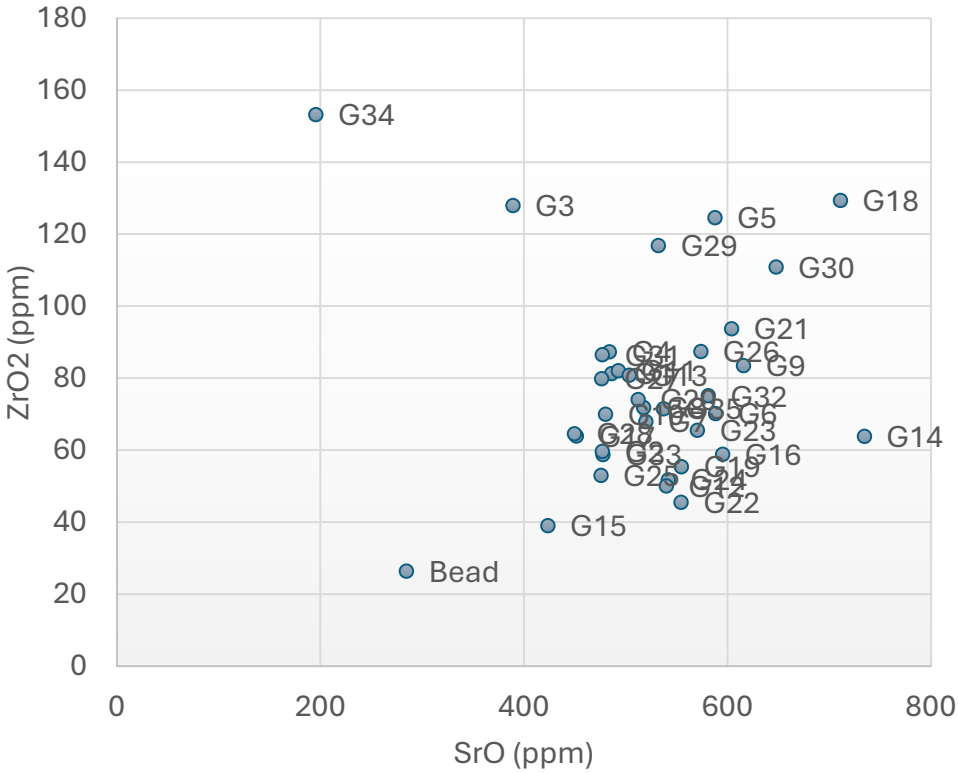


Fig 4.6. Graph SrO vs. ZrO2 for identifiying silica source.

environment strongly influenced by both marine and volcanic inputs. By contrast, G34 -the most recent and best-preserved artifact- stands apart from the main cluster, representing a unique case that likely derives from a continental silica source. This interpretation is supported by its low SrO content (<200 ppm) and elevated ZrO_2 levels (>150 ppm) (Figure 4.6). The chemical distinction between coastal and continental silica sources is well established[34]: glasses produced from coastal sands typically show low ZrO_2 (<100 ppm) and high SrO (>300 ppm), the latter linked to aragonite from seashells through bioaccumulation, as seen in Roman natron glasses. Thus, the SrO and ZrO_2 composition of G34 suggests an inland rather than a coastal origin. In addition, the REE profiles reveal Ce anomalies, observed as an inversion in the normalized patterns, for several samples that fall outside the main group, specifically G3, G5, G27, G34, and the bead. Cerium is a redox-sensitive element, and its behavior depends on the oxidation state of the melt: under oxidizing conditions, Ce tends to occur as Ce^{4+}, leading to positive anomalies, whereas under reducing conditions, Ce^{3+} dominates, producing negative anomalies[35]. From a geological perspective, positive Ce anomalies are relatively uncommon and are usually linked to the oxidative removal of tetravalent cerium by iron and/or manganese oxides[36]. However, they can be typical features of alkaline, carbonate-rich, and well-aerated lake waters, where oxidative conditions are prevalent. In the context of these artifacts, the observed Ce anomalies may therefore reflect variations in furnace atmosphere during glass production, differences in raw material sources, for instance, sands derived from such lake environments or subsequent post-depositional alterations. This suggests that these outlying samples were manufactured using distinct technological practices or sourced from geochemically different materials compared to the main cluster. The Mg vs. K plot in Figure 4.7 further confirms that most of the assemblage corresponds to Roman soda-lime-silica glass manufactured with natron as a flux[37]. A subset of samples, however, displays elevated

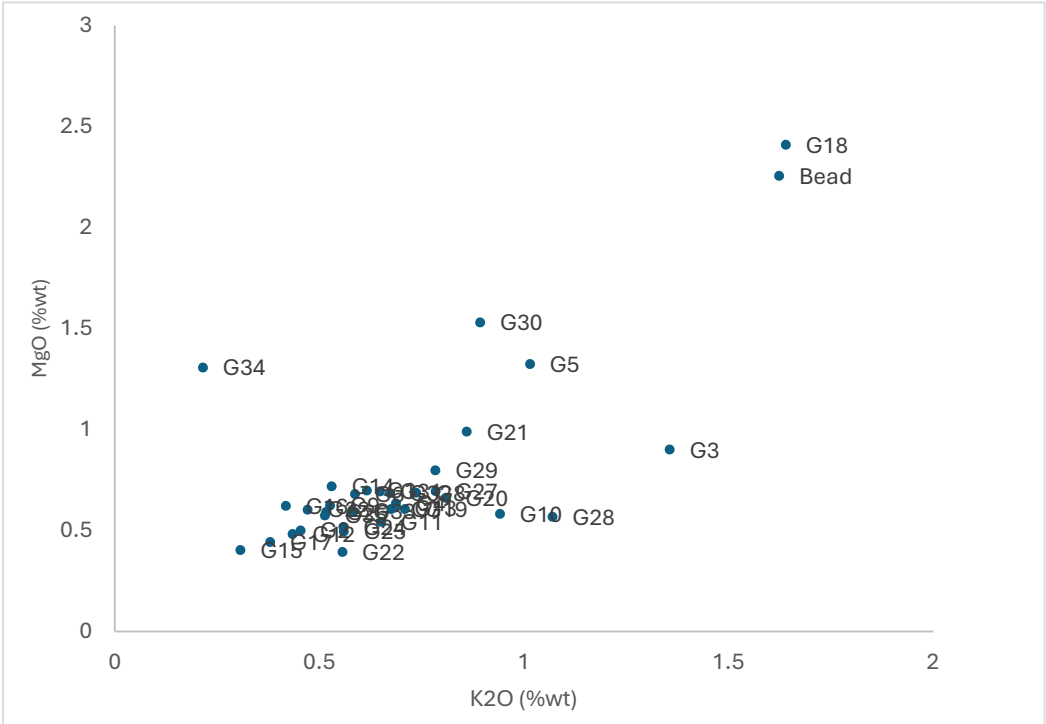


Fig 4.7. Graph MgO vs. K2O for identifying flushes.

potassium, likely introduced through contamination from wood-fired furnaces used for melting, a feature often recorded in Late Byzantine glass (6th–7th centuries CE) from the Levant and in earlier Roman contexts such as Carthage. In contrast, samples G18 and the Bead deviate significantly, reflecting the use of plant ash as a flux -a technological innovation associated with the Islamic period (7th–8th centuries CE), coinciding with the scarcity of natron. To refine the provenance of the natron-based glasses, TiO_2/Al_2O_3 vs. Al_2O_3/SiO_2 ratios were plotted following the approach by Freestone et al.[38,39] (Figure 4.8). This comparison

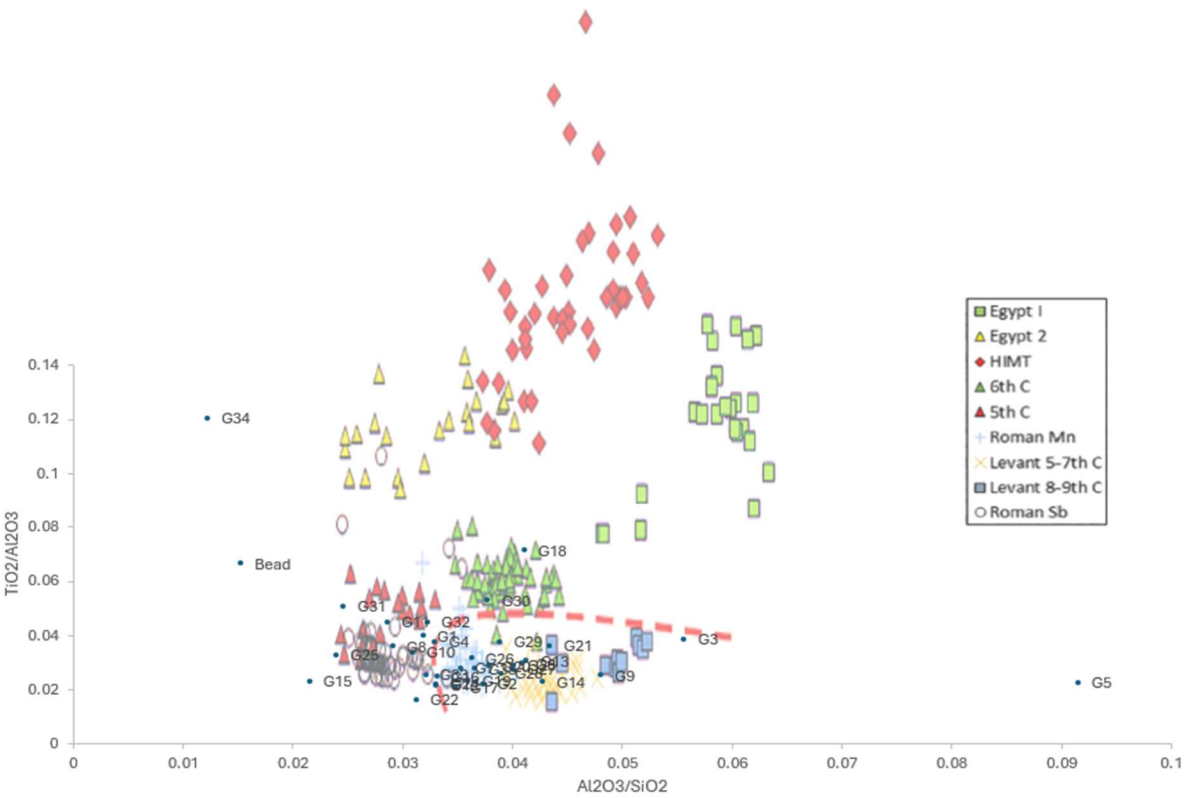


Fig 4.8. Graph TiO2/Al2O3 vs. Al2O3/SiO2 for silica source[38].

confirmed that most artifacts represent a compositional mixture of Egyptian (Roman Sb) and Levantine (Roman Mn) glass types, characteristic of the 1st–3rd centuries CE. In Egyptian glass production, antimony (Sb) was deliberately added in the form of Sb(V) to act as a decolourant[40]. Its role was to oxidize ferrous iron (Fe^{2+}), naturally present as an impurity in the sand and responsible for an undesirable blue-green coloration, to ferric iron (Fe^{3+}), which imparts a much weaker yellow hue. In contrast, Levantine glassmakers typically used manganese (Mn) instead of antimony for the same purpose. The addition of Mn^{4+} to a melt containing Fe^{2+} triggers the following redox reaction:

$$Mn^{4+}+Fe^{2+} \rightarrow Mn^{2+}+Fe^{3+}$$

This reaction produces Mn^{2+} and Fe^{3+}, both of which are only weakly colored, resulting in a glass that appears nearly colorless, though not perfectly transparent. The co-occurrence of Mn and Sb at concentrations well above natural impurity levels in the analysed samples strongly

suggests that these elements were deliberately introduced as decolourants. This dual signature supports the interpretation that many of the artifacts were produced through recycling practices, where Egyptian Sb-rich glass and Levantine Mn-rich glass were remelted and mixed together in secondary workshops. G34 meanwhile can be confidently identified as a later Egyptian glass production. Additional analyses focused on colorants and opacifiers to assess technological choices. The majority of samples exhibit a characteristic blue-green hue, consistent with the presence of Mn and Sb, deliberately introduced to decolorize the glass. An additional PCA was carried out using the oxides of Co, Cu, Pb, Sn, Sb, and Fe (wt%) to assess whether compositional clustering could be correlated with chromatic variation among the samples (Figure 4.9). Sample G19, the only artifact displaying a deep blue coloration, contains elevated cobalt levels -a technological signature well documented in the historical record- and shows no evidence of added opacifiers. Although the specimen initially appears opaque, this effect is due to a surface corrosion patina rather than intentional opacification. Conversely, G18 is distinguished by its opaque green glass, achieved through the intentional addition of copper and tin, a hallmark of Islamic-period glassmaking traditions[41]. Taken together, these results reveal a dynamic network of exchanges connecting the Mediterranean with the Middle East. The predominance of natron and silica sources traceable to Egyptian and Levantine contexts underscores the strategic importance of these regions, both as suppliers of raw materials and as centres of technological expertise. Evidence of Middle Eastern influence in the studied artifacts not only highlights the economic interconnectivity of the Roman and post-Roman world but also illustrates the cultural transmission of specialized production techniques. Crucially, such insights could not have been achieved through conventional bulk analyses: it is the high spatial resolution of LA-ICP-MS that allowed the detection of

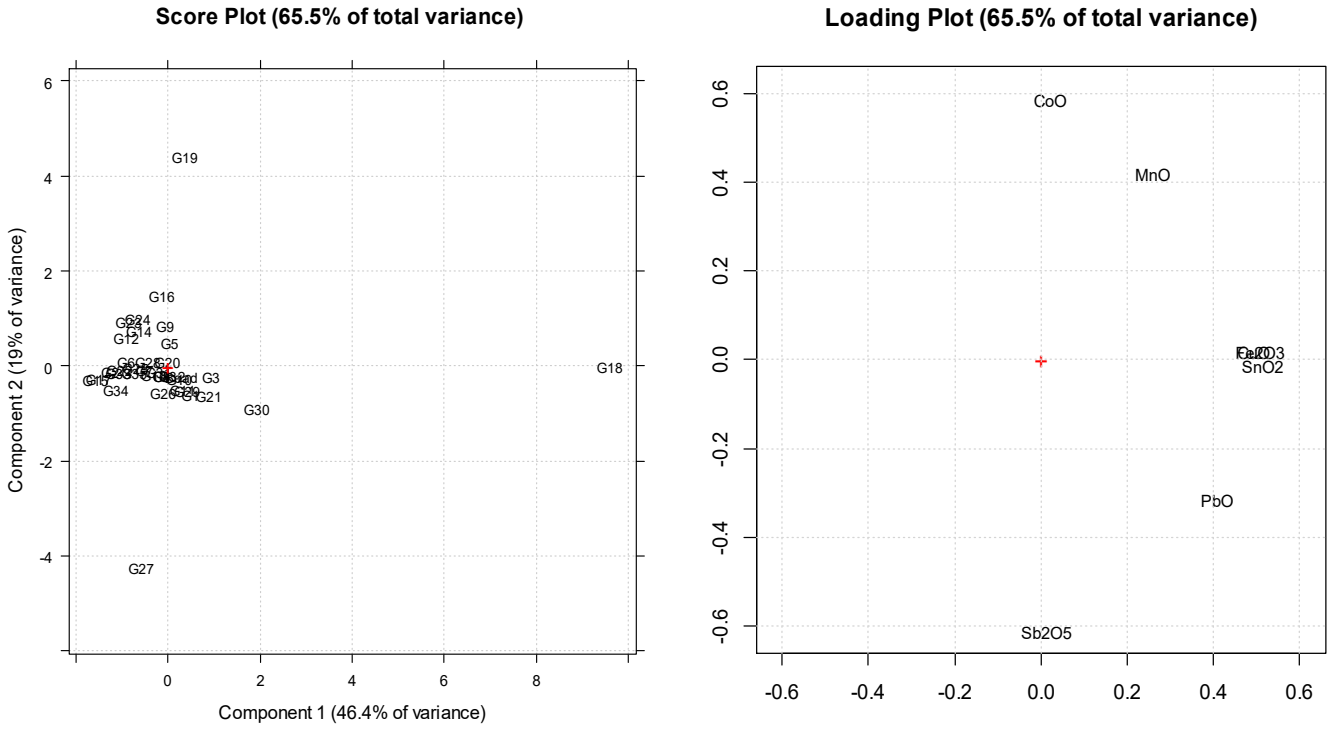


Fig 4.9. Score plot and loading of the first two PC, identifying colourants and opacifiers.

compositional heterogeneities and the reconstruction of raw material provenance. This demonstrates that the reliance of Roman workshops on Middle Eastern raw materials, together with the diffusion of distinctive technological practices, reflects the deeply interconnected nature of ancient trade routes and the far-reaching influence of Roman and later Islamic glassmaking traditions. A key factor in achieving these results is the ability of LA-ICP-MS to detect minor and trace elements with high sensitivity. This capability makes the technique uniquely suited for investigating surface alteration and corrosion processes in archaeological glass. By distinguishing compositional changes caused by alteration from the primary bulk chemistry, LA-ICP-MS not only refines the interpretation of technological choices but also strengthens provenance studies. This distinction is crucial, as it prevents signals related to raw material sourcing and trade networks from being obscured by post-depositional processes, thereby allowing a more accurate reconstruction of technological traditions and exchange dynamics. To explore these aspects, two contrasting artifacts were selected: one showing extensive surface alteration, with both patina and crust, and another that was comparatively well preserved. Depth-profile mapping was performed by ablating the same surface line repeatedly (100 successive passes, each one removing approximately 1 μm of material), enabling the reconstruction of compositional gradients across corrosion layers and into the unaltered bulk. This approach allowed the direct observation of elemental mobility and the enrichment or depletion of specific oxides within altered zones[42]. While glass is often regarded as a durable material, its long-term stability is strongly influenced by burial conditions. Corrosion is accelerated under both acidic and alkaline pH regimes, with water acting as the primary agent of degradation. Interaction with water leads to the leaching of alkali ions, which in turn increases the local pH and promotes further alteration. This process can be described as an ion-exchange mechanism, whereby protons from water replace alkali ions within the glass network[43]:

$$2H_2O \rightleftharpoons H_3O^+ + OH^-$$

$$\equiv Si–O–Na^+ + H_3O^+ \rightarrow \equiv Si–OH + Na^+ + H_2O$$

Such reactions progressively modify the glass surface, driving the formation of patinas and corrosion layers, as observed in the analyzed artifacts. To further demonstrate the potential of depth-resolved mapping, the same procedure was applied to the bead sample. In this case, the objective was to investigate its internal structure-specifically, whether it was composed entirely of glass or represented a glazed paste. Depth profiling proved particularly useful in this context, as it highlights the capability of LA-ICP-MS to probe beneath the surface and reconstruct compositional variations at depth. For this study, the CSV files of the mappings extracted from HDIP were uploaded to 'SumNormApp,' from which it was possible to generate the concentration maps of the 54 oxides. It can be seen that the bead is actually composed of clay core (higher in Al, Fe, Ca, K, Na, Mg) coated with a glassy paste (higher in Si, as per Figure 4.10), as revealed by the maps reported in Figure S4.1. Figures S4.2 and S4.3 show the maps for samples G9 and G14, corresponding to the best-preserved and most corroded specimens, respectively. Although patinas appeared particularly prominent, the corrosion layer seems to

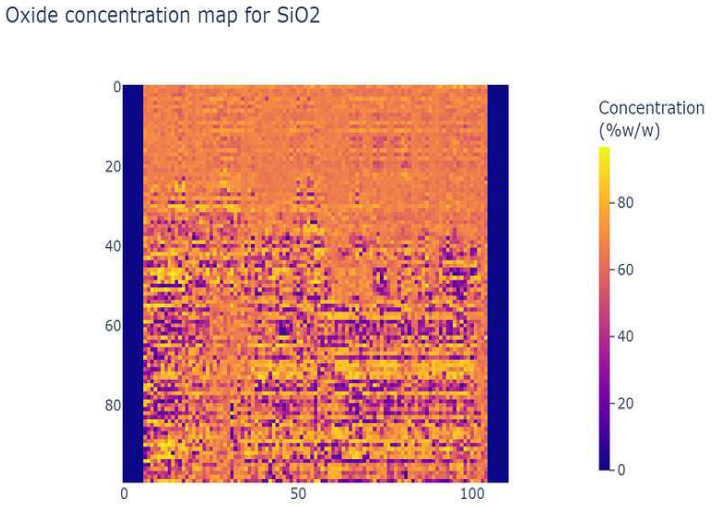


Fig 4.10. Silicon map for Bead.

affect only the first few micrometres. In G9, a distinct layer -corresponding to roughly the first 30 ablation lines- shows depletion of alkali and alkaline earth metals, as well as many heavy metal ions in trace (e.g. Co^{2+}), accompanied by an enrichment in Si[44]. In G14, the top few micrometres, corresponding to approximately the first five ablations and including part of the crust, exhibit increased concentrations of all elements typical of the burial environment. Below this initial layer, the compositional trends resemble those observed in G9. Interestingly, based on the visually observable deterioration, one might have expected a higher degree of corrosion. In some cases, these alkali-depleted surface layers appear to act as a protective barrier, limiting further glass deterioration[45]. To further highlights the importance of LA-ICP-MS in studying glass corrosion processes, the analysis was repeated on embedded samples presenting lateral sections. These same samples were subsequently examined using SEM-EDX[46]. As shown in the LA-ICP-MS maps in Figures S4.4 and S4.5, the depletion layer is less clearly discernible. This may be attributed to several factors. First, there is an instrumental effect related to how the maps were constructed: whereas in the previous analysis each ablation line removed only a few micrometres, in this case each pixel corresponds to the selected beam size (35 µm), reducing spatial resolution. Additionally, the embedding and polishing procedures may have altered the sample surface, and the presence of the resin signal could mask subtle compositional changes caused by leaching. SEM analyses were carried out using a Zeiss Sigma field emission scanning electron microscope (FE-SEM) operating at 0.5–20 kV. The instrument was equipped with an in-lens secondary electron (SE) detector, a backscattered electron (BSE) detector, and an INCA energy-dispersive X-ray spectroscopy (EDS) system. The results of the EDX analyses are presented in Figures 4.11 and 4.12, showing maps of the main oxides involved in the corrosion process, and in Figures S4.6 and S4.7, which display the sequential spectra acquired on the lateral sections. These observations corroborate the LA-ICP-MS findings in the side profiles, revealing no distinct depletion layer. Together, these results indicate that while LA-ICP-MS provides high-resolution

insight into compositional gradients in corroded glass, certain sample preparation and instrumental factors can limit the visibility of subtle surface alterations.

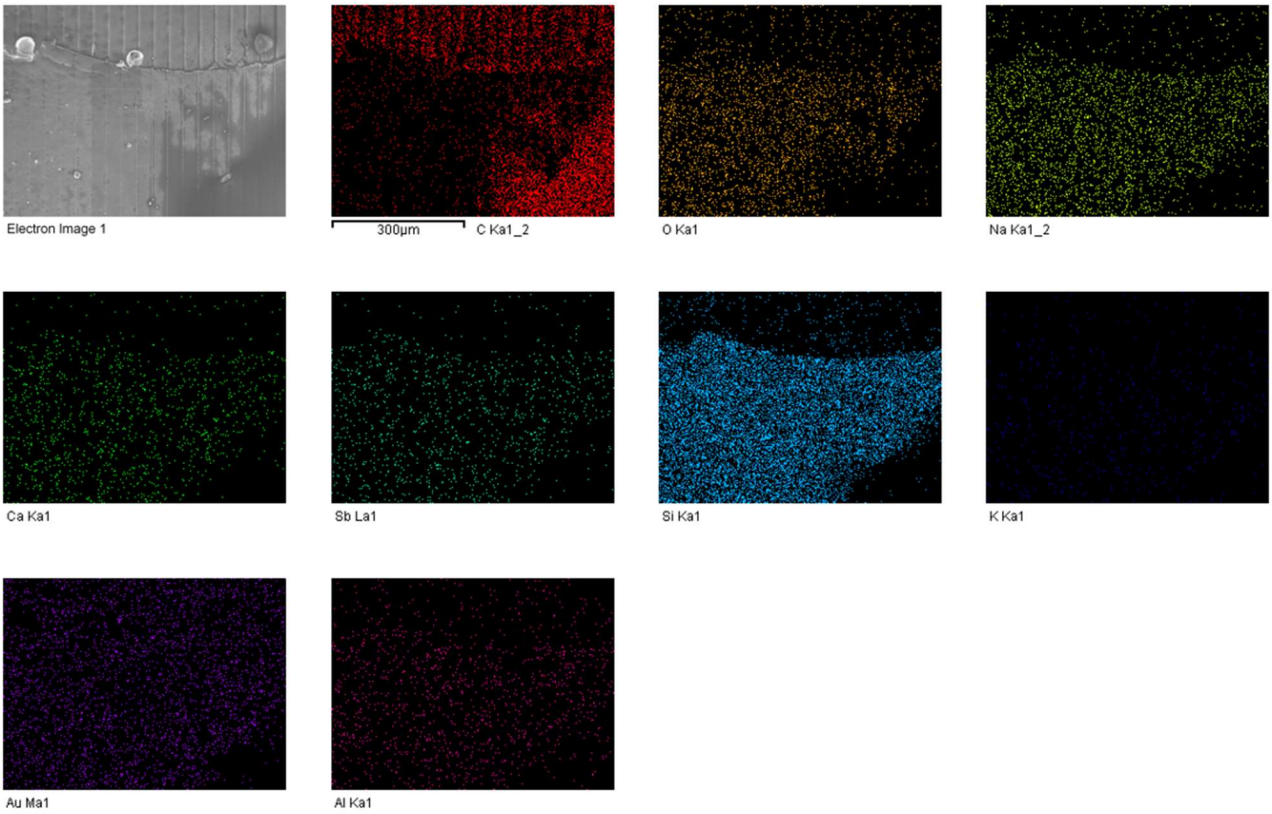


Fig 4.11. EDX maps of sample G9.

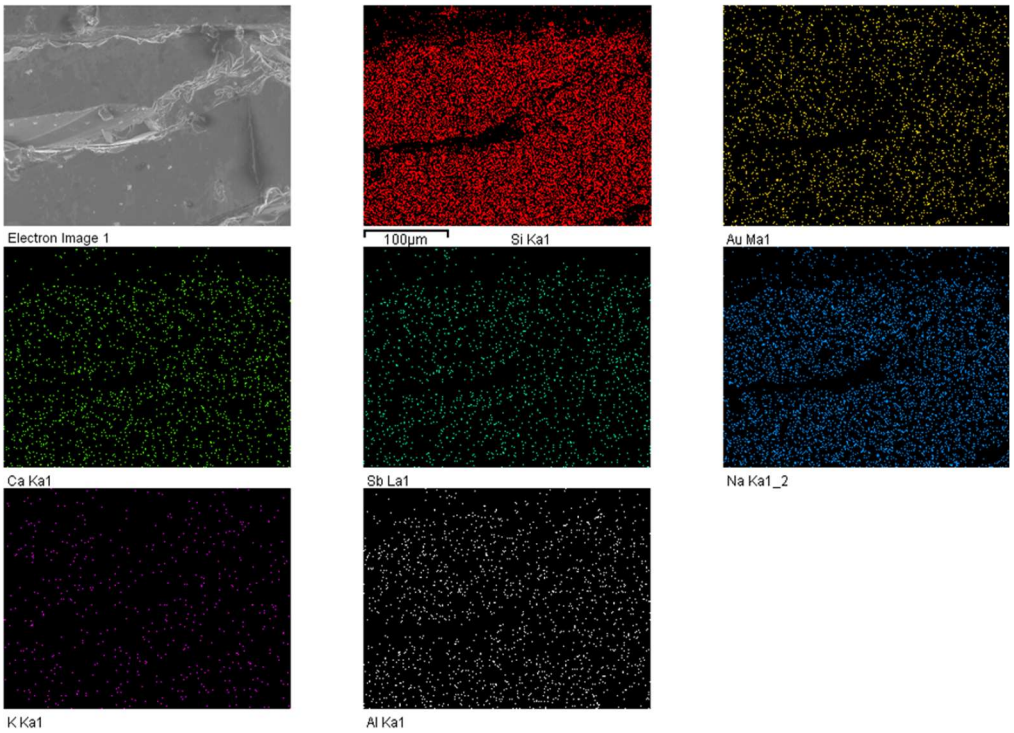


Fig 4.12. EDX maps of sample

4.1.5. Conclusions

This study demonstrates that LA-ICP-MS is a uniquely powerful tool for investigating both the compositional heterogeneity and corrosion processes of archaeological glass. Its high spatial resolution allows for the direct visualization of minor and trace element gradients, enabling the distinction between primary bulk chemistry and surface alteration. This capability is critical for accurate provenance analysis, technological interpretation, and reconstruction of ancient production practices. By applying depth-resolved mapping, we were able to observe the enrichment and depletion of specific oxides across corrosion layers, revealing mechanisms of elemental mobility and protective effects of alkali-depleted surface layers—insights that would be inaccessible through conventional bulk analyses. Furthermore, LA-ICP-MS successfully distinguished between fully glassy and composite bead structures, demonstrating its utility in elucidating internal artifact architecture. Complementary SEM-EDX analyses confirmed that sample preparation and instrumental limitations might obscure subtle features, highlighting the superior sensitivity of LA-ICP-MS in detecting fine-scale compositional changes. Overall, this work underscores the crucial role of LA-ICP-MS in archaeological glass studies, providing unparalleled resolution for provenance determination, technological reconstruction, and understanding of post-depositional alteration processes, thereby illuminating the complex networks of raw material exchange and technological innovation in antiquity.

4.2. Case study: certified human serum

4.2.1. Why LA-ICP-MS Matters

LA-ICP-MS has emerged as a transformative analytical technique for multi-elemental analysis of complex matrices. By combining high sensitivity, rapid analysis, and minimal sample preparation, LA-ICP-MS offers clear advantages over conventional digestion-based methods, which are often labour-intensive, contamination-prone, and destructive to valuable samples. Moreover, liquid-mode techniques require relatively large amounts of material to prepare solutions, making them less suitable when only limited or precious samples are available. Its capacity to deliver direct solid sampling, spatial resolution, and ultra-trace quantification positions LA-ICP-MS at the forefront of modern bioanalytical chemistry[47]. In clinical and toxicological contexts, where biological fluids and tissues must be interrogated at ever-lower concentrations of metals, this technique holds unprecedented potential to advance biomonitoring, diagnostics, and public health surveillance[48]. The refinement of LA-ICP-MS protocols is especially urgent for the study of metals in biological systems[49]. Essential trace elements such as iron, copper, zinc, and selenium play critical roles as cofactors in enzymatic reactions and in the regulation of cellular processes. Yet, even minor imbalances -levels only slightly above the thresholds set by public health authorities- can trigger metabolic dysfunction, oxidative stress, or more severe disease[50]. At the same time, non-essential metals such as lead, tin, cadmium, mercury, and arsenic pose an even greater challenge: lacking any

physiological role, they exhibit toxic properties at concentrations in the parts-per-billion (ppb) range[51]. In this landscape, the ultra-sensitivity and multi-element detection capability of LA-ICP-MS provide unique advantages over competing technologies. Among the biological matrices available, blood has become the preferred medium for trace metal analysis[52]. Circulating throughout the body, blood offers a dynamic snapshot of recent exposure and systemic distribution while remaining relatively easy to collect without invasive procedures. The adoption of dried matrix spot (DMS) sampling has further enhanced the utility of blood analysis[53]. Introduced in the 1960s for newborn screening[54], DMS sampling involves depositing small volumes (20–40 µL) of body fluids onto filter paper, thereby reducing invasiveness, simplifying storage and transport, and enabling retrospective analysis, which allows stored samples to be re-examined later as new analytical techniques or research questions emerge[55]. When coupled with LA-ICP-MS, DMS sampling enables direct, multi-element analysis while avoiding laborious pre-treatment and the use of hazardous reagents[56]. This DMS–LA-ICP-MS combination offers key benefits: reduced sample requirements, lower detection limits, broad linear dynamic ranges, and high efficiency in elemental quantification[57]. Nevertheless, the method remains underexplored, with only a handful of published studies demonstrating its reliability, often through sophisticated instrumentation such as TOF-MS[58,59] and femtosecond laser ablation[60] or novel devices as cryogenic ablation cells[61]. Despite its promise, LA-ICP-MS still faces several challenges in biological applications[62,63]. Chief among these is the lack of standardized reference materials for calibration, which hampers quantitative reliability, as well as the challenge of identifying a suitable internal standard. Various external calibration approaches have been proposed[64], ranging from solution-based calibration -where a nebulized aerosol is combined with the laser ablation plume- to the synthesis of metal-spiked polymer blocks or homogenized, spiked tissue samples (e.g., liver, kidney, heart)[65]. While effective, these methods are often labor-intensive, costly, and not easily generalizable across laboratories. As a result, alternative strategies have gained traction, particularly the preparation of laboratory-based standards such as gel polymers or dried droplets. Matrix-matched gelatine calibrants, for instance, have demonstrated strong potential for accurate quantification, providing reproducibility while maintaining compatibility with biological matrices[66]. Achieving ever-lower limits of detection (LOD) also requires overcoming polyatomic interferences, which can severely compromise analytical accuracy. Signal amplification using metallic nanoparticles (NPs) represents a particularly promising approach[67]. When applied to sample surfaces, NPs can boost analyte signals, enhance signal-to-noise ratios, and enable detection at the low-ppb level. Although this strategy has been successfully employed for inorganic analytes, its application to organic compounds remains largely unexplored, with matrix–NP interactions likely to differ markedly. Among the various candidates, platinum nanoparticles (Pt NPs) produced by pulsed laser ablation in liquid (PLAL) stand out for their exceptional stability in aqueous environments, even in the absence of stabilizers. This stability minimizes unwanted interactions with biological matrices while ensuring consistent signal enhancement. Pt was chosen not only for these properties but also for its strong surface plasmon resonance (SPR), which occurs around 270 nm—close to the 213 nm wavelength of the ablation laser. This near overlap allows partial coupling of the laser energy with the nanoparticles, enhancing localized

absorption and further improving analytical sensitivity. Building on these advances, the present study investigates the potential of nanoparticle-enhanced LA-ICP-MS (NELA-ICP-MS) using Pt NPs to refine trace metal detection in organic samples. Our goal is threefold: first, to investigate the development of standardized matrix-matched calibrants that can ensure quantitative reliability across laboratories; second, to elucidate the mechanisms by which Pt NPs interact with organic samples to enhance analyte signals; and third, to push the limits of detection and quantification down to the low-ppb range for both essential and toxic metals in biological matrices. By addressing these objectives, this research not only strengthens the analytical foundation of clinical toxicology but also broadens the applicability of LA-ICP-MS across fields such as environmental health, pharmacology, and forensic science. Ultimately, the refinement of LA-ICP-MS into a universally applicable, sensitive, and reliable methodology will represent a significant advance in bioanalytical chemistry. It will provide clinicians, toxicologists, and researchers with a powerful tool for monitoring human exposure to metals—bridging the gap between cutting-edge instrumentation and real-world challenges in public health.

4.2.2. Evaluation of Gelatine as a Matrix-Matched Standard for Human Serum

Quantitative accuracy remains a key challenge in applying LA-ICP-MS to biological samples, largely due to the lack of certified reference materials that mimic human matrices. To address this, we investigated gelatine as a reference standard, building on its proven utility in studies with complex matrices such as blood and tissues[68]. In these applications, gelatine-based calibrants have shown strong potential to mimic matrix effects, providing improved reproducibility and reliability in elemental quantification compared to conventional external calibration strategies. Gelatine, derived from the partial hydrolysis of collagen, is especially attractive in this context because of its proteinaceous composition, mechanical stability, and ability to incorporate metals in a homogeneously distributed form. These properties allow it to approximate the biochemical environment encountered in biological samples, thereby reducing matrix-related biases that often compromise quantification. While the use of gelatine for calibration has been validated in challenging solid matrices like tissues, its adaptation to fluid-based systems such as human serum remains underexplored. Serum presents unique analytical challenges due to its lower protein content, distinct viscosity, and dynamic elemental background, all of which can influence ablation behaviour and plasma ionization. By extending the application of gelatine calibrants to human serum, this study seeks to evaluate their potential as a reproducible, laboratory-prepared standard that could facilitate accurate trace metal quantification and improve the accessibility and standardization of LA-ICP-MS workflows across laboratories.

4.2.2.1. Reagents and calibration standards

Certified reference materials (CRM) Seronorm™ Trace Element Serum, Level I and Level II (Sero, Billingstad, Norway) were used. The lyophilized serum standards were reconstituted with ultrapure water following the manufacturer's instructions. Ultrapure water (resistivity 18 MΩ·cm) was produced using an Arium® Mini purification system (Sartorius AG, Germany). For the preparation of multi-element calibration standards, porcine skin-derived gelatine (bloom strength ~300 g; Sigma-Aldrich, USA) was selected. A multi-element Quality Control Standard containing 48 elements at 100 ppm (LabKings, USA) was employed as the stock solution for calibration. In addition, NIST SRM 610 and NIST SRM 612 glass reference materials were used both as external calibrants and for routine instrumental performance checks.

4.2.2.2. Dried serum and gelatines spot sample preparation

Gelatine droplets were prepared following the protocol described by Šala et al.[69], with modifications to adapt the method for trace metal calibration in serum-like matrices. In parallel, two calibration curves were established to cover the expected concentration ranges of both major and minor elements. The first curve targeted the major elements Ca, Fe, Li, Cu, and Zn**,** which are typically present in biological samples at relatively high levels; standards were prepared at concentrations of 10, 20, 50, and 100 ppm. The second curve was designed for the minor and toxic elements Co, As, Sn, Pb, Al, V, Cr, Ni, Mn, Hg, and Cd**,** which occur in serum at ultra-trace levels. According to the certified values of the available serum reference materials, these elements are usually found within the 0.1–10 ppb range. To reproduce this scale, gelatine-based standards were prepared at 10, 5, 1, 0.5, and 0.1 ppb, along with a blank, ensuring adequate coverage of the low-concentration domain relevant for biomonitoring. The calculation of the required stock solution volumes accounted for the significant water loss occurring during oven drying. This effect, measured by weighing samples before and after heating, showed an average reduction of about 90% of the initial water content**,** corresponding to an effective concentration factor of approximately ten (e.g., an initial working volume of 10 mL resulting in ~1 mL of final dried material). Incorporating this correction was essential to ensure accurate final concentrations in the dried gelatine calibrants. For preparation, 1 g of porcine skin-derived gelatine (bloom strength ~300 g) was dissolved in 5 mL of ultrapure water, after which the remaining water was added. The mixture was homogenized in an ultrasonic bath at 50 °C for 30 minutes, producing a uniform gel matrix. Following this step, the calculated volumes of multi-element standard solution were added, and the mixture was equilibrated for an additional 10–15 minutes to ensure homogeneous distribution of analytes within the gel. To avoid inhomogeneous gelation caused by sudden cooling, microscope slides were preheated on the lid of the ultrasonic bath prior to deposition, thereby minimizing the risk of thermal shock and premature solidification. Subsequently, a droplet (~40 µL) of each concentration was carefully deposited onto the preheated slides and dried in an oven at 95 °C for one hour, resulting in solidified gelatine spots suitable for LA-ICP-MS analysis. In parallel with the calibration standards, serum samples were deposited on both microscope slides and Parafilm substrates in order to directly compare the effects of different surface properties on sample

morphology during drying in air[70]. The two substrates represent materials with markedly different surface energies and degrees of hydrophobicity: glass slides provide a relatively hydrophilic surface that promotes droplet spreading, while Parafilm is strongly hydrophobic, favoring the retention of a more spherical droplet shape. This comparative approach was undertaken to systematically evaluate how these substrate-dependent behaviors influence the evaporation dynamics, distribution of solutes, and formation of microstructural features such as ring deposits or cracks. Such factors are not trivial, as the drying process can strongly affect the homogeneity of analyte distribution within the dried spot. Inhomogeneous deposits often lead to “coffee-ring” effects or complex crack patterns that alter the effective sampling area and may bias ablation efficiency during LA-ICP-MS analysis[71]. Cracks, in particular, introduce variability in ablation depth and plume formation, thereby compromising both precision and quantitative accuracy. By comparing substrates of contrasting wettability, this study aims to identify the conditions that minimize these unwanted effects and yield reproducible, uniformly distributed dried spots suitable for reliable analysis. Moreover, the evaluation of different support materials provides insight into the interplay between matrix composition and substrate surface chemistry, an aspect that is often overlooked in bioanalytical applications of dried matrix spot sampling. Selecting an optimal support not only improves analytical reproducibility but also enhances the potential for standardization across laboratories, thereby contributing to the development of more robust and universally applicable LA-ICP-MS methodologies.

4.2.2.3. LA-ICP-MS Methodology

The first evaluations focused on the behaviour of serum droplets deposited on different substrates. When dried on glass slides, the serum exhibited extensive cracking and surface inhomogeneity. A 3D optical interference microscope (Zegage PRO HR, Zygo Corporation, Middlefield, CT, USA) was employed to characterize these irregularities and subsequently to measure the droplet volumes in both samples and standards. Measurements were carried out using a 50× objective lens, providing a lateral resolution of 0.173 µm and a surface topography repeatability of ≤3.5 nm. The dried serum on glass revealed pronounced cavities and large surface variations, which can be attributed to its lower viscosity and higher fluidity, leading to greater spreading across the glass substrate. Based on these observations, subsequent LA-ICP-MS analyses were performed using gelatine standards deposited on glass and serum samples deposited on Parafilm, the latter offering a more suitable substrate due to its hydrophobic nature. Analyses were carried out using a 193 nm ArF excimer laser ablation system* (Analyte G2, Teledyne Photon Machines Inc., Bozeman, MT, USA) coupled to an inductively coupled plasma quadrupole mass spectrometer (ICP-QMS; Agilent 7900, Agilent Technologies, Santa Clara, CA, USA). Ablation was performed within a HelEx two-volume ablation cell, which provided efficient aerosol transport and a washout time of approximately 0.5 s, thereby minimizing signal tailing and maximizing temporal resolution. The optimized LA-

ICP-MS operating conditions are summarized in Table 4.2. Particular attention was given to the selection of laser fluence, which was carefully adjusted according to the physicochemical properties of the matrix and its interaction with the laser beam. Since matrices with different densities, viscosities, and thermal conductivities exhibit distinct ablation behaviours, the amount of material removed can vary significantly even under identical laser settings. The fluence was therefore optimized to ensure the production of well-defined, reproducible craters, while at the same time preventing excessive penetration into or ablation of the underlying

LA parameters	
Laser fluence	*3.5 J/cm^2 for NIST; 0.53 J/cm^2 for serum and gelatines*
Dosage	*20*
Spot size	*35 µm square*
RR	*40 Hz*
Scan speed	*70 µm/s*
Carrier gas flow rate	*He, 0.3 L/min*
ICP-MS parameters	
Rf power	*1500 W*
Plasma gas flow rate	*15 L/min*
Auxiliary gas flow rate	*0.9 L/min*
Ar makeup flow rate	*0.8 L/min*

Tab 4.2. LA and ICPMS parameters used for the analysis.

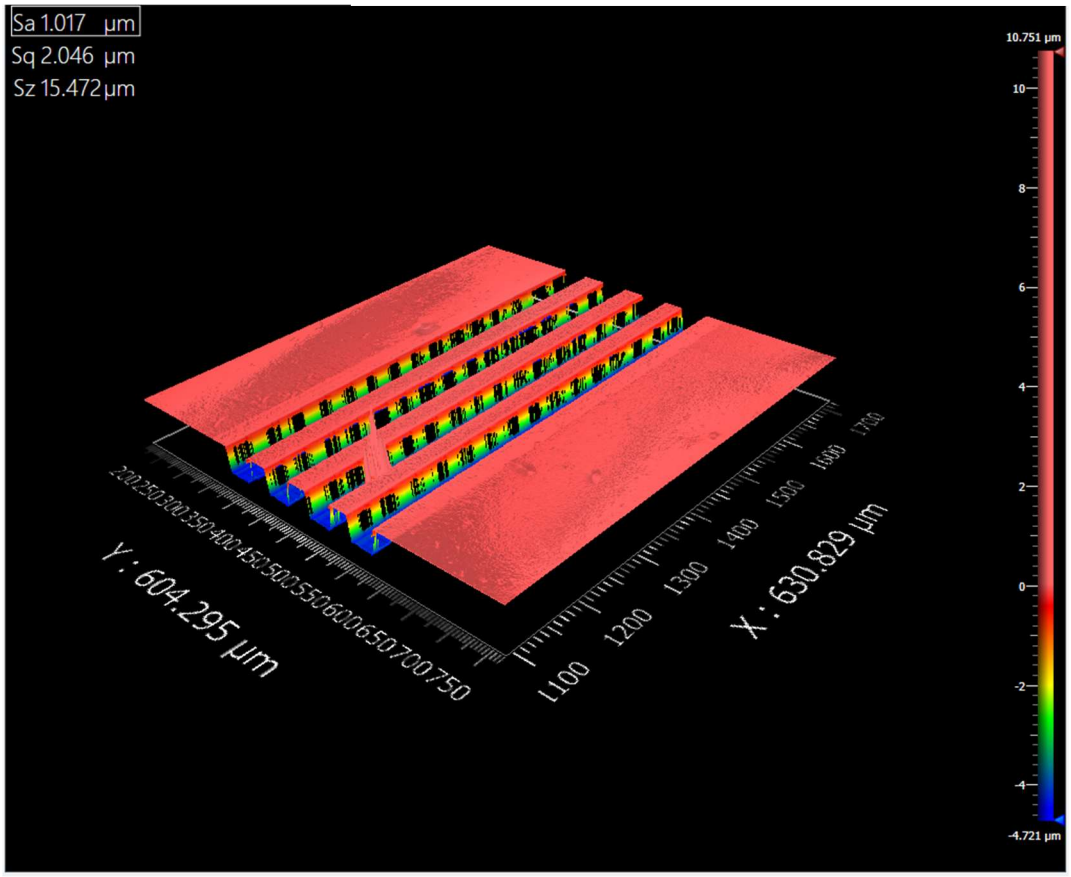
substrate. This precaution was essential, as ablation of the support material could not only damage the sample integrity but also contribute additional elemental signals or matrix effects, thereby introducing significant bias into the analytical results and undermining quantification accuracy. These considerations highlight a broader methodological challenge: when standards and samples are prepared on substrates or matrices with differing ablation characteristics, there is a risk of introducing systematic inaccuracies into quantitative measurements. Unless ablated volumes are rigorously characterized and accounted for, or unless matrix-matched standards are employed, differences in laser–matrix coupling may compromise the comparability of analytical signals. Consequently, careful control of laser fluence, crater geometry, and substrate compatibility was essential to establish reproducible conditions for both gelatine standards and serum samples. In the ICP-MS acquisition method, the dwell times were adjusted so that the total window of time per sweep remained constant at 0.5 s. For minor and trace element analysis, Al was assigned a dwell time of 35 ms, as it is the first element in the selected periodic sequence and shows minimal spectral interferences, while all other monitored isotopes were measured with a dwell time of 40 ms. For major elements, the dwell times were set to 66 ms for Mg and 70 ms for the remaining isotopes. The slightly shorter dwell time for Mg reflects its high natural abundance and strong signal intensity, which would otherwise risk detector saturation; this adjustment ensured accurate measurement of Mg while allowing longer dwell times to be allocated to less abundant elements. Two line scans were performed on the NIST glass standards, whereas four lines were acquired for both gelatine

and serum droplets. In the case of gelatines, the lines were evenly spaced, reflecting the assumption of homogeneous analyte distribution as demonstrated in previous studies. For serum droplets, however, line scans were deliberately designed to differ in length and were spaced at approximately 500 µm intervals, in order to capture potential heterogeneities and provide cross-sectional information on signal variability across the droplet surface. The raw LA-ICP-MS data were processed to correct for baseline, normalize signal intensities, and integrate peak areas base following the procedure of Longerich[28], thereby ensuring consistency across the different ablation conditions. To ensure quantitative comparability, the ablation volumes generated under these conditions were subsequently characterized by 3D optical interference microscopy, allowing the measured crater geometry to be directly linked with the analytical signal and providing a robust basis for cross-matrix evaluation between standards and serum samples. Figures 4.13 and 4.14 show the 3D interferometric images and the corresponding cross-sectional crater profiles for gelatine and serum droplets. The gelatine samples demonstrated good reproducibility in the ablation process, with an average crater depth of approximately 4.3 µm, confirming the reliability of the ablation geometry. In contrast, the serum droplets, although less uniform in surface morphology, exhibited shallow surface grooves of roughly 0.5 µm, while the laser-induced ablation crater reached approximately 4 µm in depth. These observations indicate that, despite the lack of fully reproducible crater geometry in serum, approximate elemental concentrations may still be derived by applying volume-correction methods as a complementary strategy. Determining the density of the serum was therefore important in order to estimate the sample volume for potential correction during LA-ICP-MS analysis. To this end, several serum droplets were carefully collected from the Parafilm and weighed on an analytical scale yielding a total mass of 31.126 mg. The corresponding volume was measured using a pycnometer, giving 0.0223 mL ± 0.0008 (SD). The density was then calculated as D = m/V = 1.396 g/mL. Building on this, volume correction was further explored by ablating entire serum droplets, previously acquiring interferometric images of droplets to directly evaluate the removed volume. To overcome the variability caused by uncontrolled spreading of larger droplets, a refined strategy was then introduced, where serum was deposited as microdroplets of 50 µL each. This ensured more reproducible droplet geometries, improved control over ablation conditions, and facilitated more consistent quantitative evaluation. The optimized mapping parameters used for these experiments are summarized in Table 4.3, and were specifically selected to guarantee complete ablation of the deposited droplet while minimizing, as far as possible, ablation of the underlying glass substrate.

LA parameters	
Laser fluence	*2.99 J/cm²*
Dosage	*20*
Spot size	*35 µm square*
RR	*40 Hz*
Scan speed	*70 µm/s*
Carrier gas flow rate	*He, 0.3 L/min*

ICP-MS parameters	
Rf power	*1500 W*
Plasma gas flow rate	*15 L/min*
Auxiliary gas flow rate	*0.9 L/min*
Ar makeup flow rate	*0.8 L/min*

Tab 4.3. LA and ICPMS parameters used for microdroplets mapping.



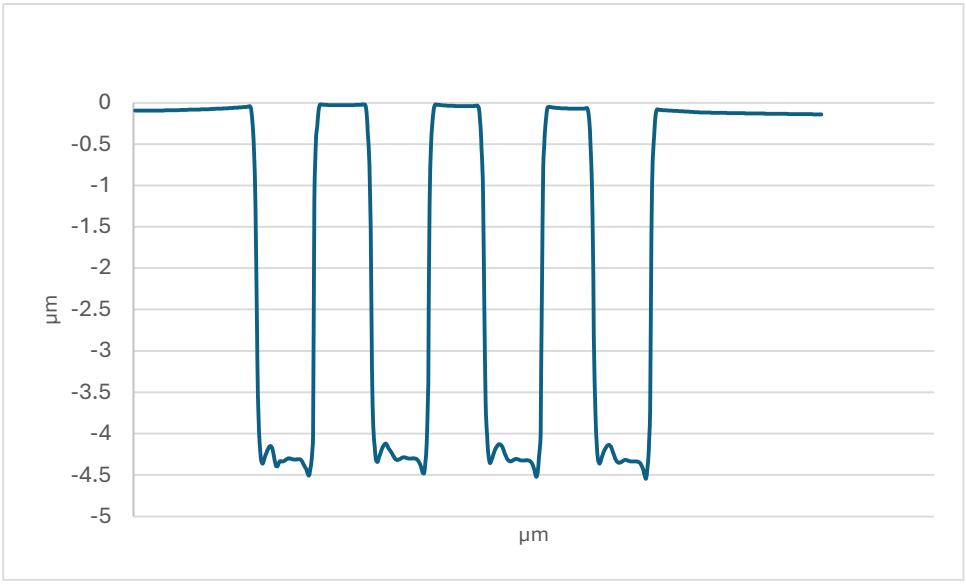
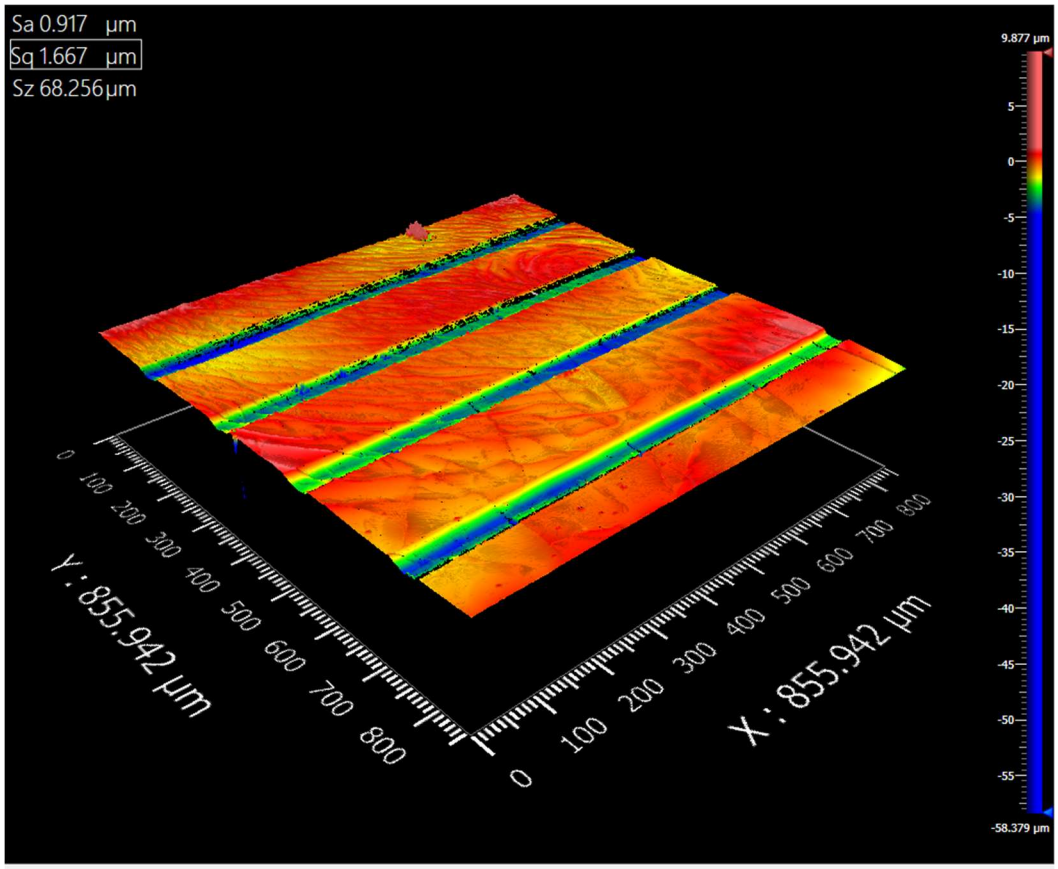


Fig 4.13. 3D interferometric image and corresponding cross-sectional profiles of ablation lines on gelatine.



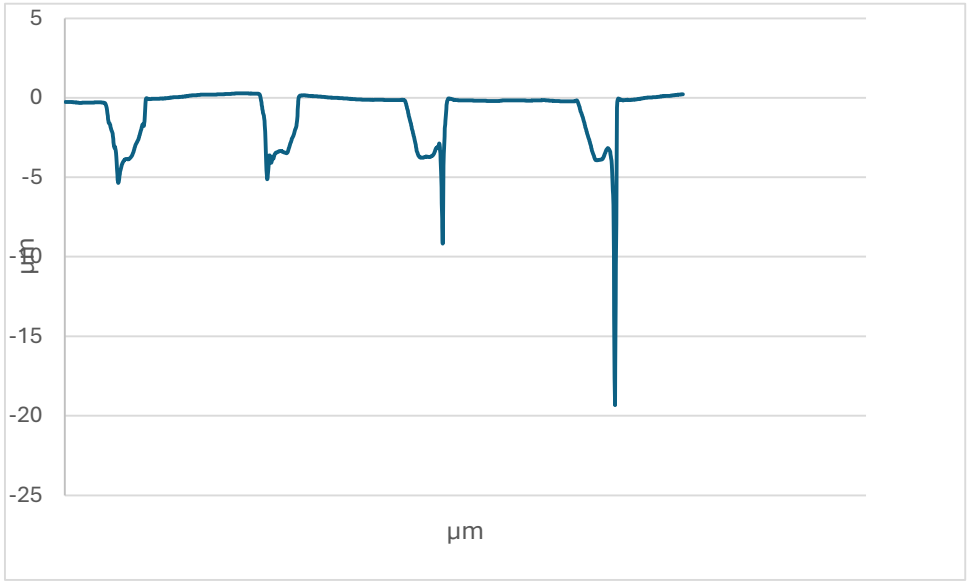


Fig 4.14. 3D interferometric image and corresponding cross-sectional profiles of ablation lines on serum.

4.2.2.4. Results and discussion

Table S4.5 reports all the average signals, expressed in counts per second (CPS), together with the estimated errors for the analyses performed on the elements of interest that are present in serum at minor and trace concentration levels. For the gelatine samples, the analyses did not yield satisfactory results. No distinguishable signal could be separated from the bulk background; and in those cases where a signal was observed, it remained constant across gelatine samples of different concentrations. This suggests that the measured response originates mainly from the matrix itself rather than from the added elements, preventing the generation of calibration curves for estimating the concentrations of these elements in the serum standards. The poor performance of gelatine as a surrogate matrix can be attributed to its significantly higher organic content compared to serum. Gelatine in fact is composed of approximately 98–99% protein when dry. In contrast, human serum typically contains about 70–75% water, with proteins constituting around 7–8% of its composition. This disparity in organic content leads to differences in viscosity and affects nebulization and ionization processes in the plasma, giving rise to strong matrix effects. As a result, the apparent signal is largely independent of the true analyte concentration. Furthermore, decomposition of organic matter contributes to background noise and polyatomic interferences, making it difficult to distinguish genuine trace-element signals from the matrix response. In addition, the chemical composition of gelatine does not mimic the ionic strength, salt composition, or protein distribution of serum, which further undermines its suitability as a matrix-matched standard. For the serum standards, although the signals were not particularly high, it was nevertheless possible to obtain an estimate of the concentrations. The measured signals, together with the certified concentrations provided in the production certificates of the two serum standards, were used in a comparative approach: one standard was treated as the reference and the other as the “unknown.” The resulting concentration estimates are reported in table 4.4. Although the uncertainties associated with these concentration estimates remain relatively high, there is still a good agreement between the certified and the experimentally determined values. This outcome provides preliminary confirmation that gelatine is not a suitable matrix-matched

	Al	*V*	*Cr*	*Mn*	*Co*	*Ni*	*As*	*Cd*	*Sn*	*Sb*	*Hg*	*Pb*
L1 cert	2.38	0.23	1.5	9.4	0.99	5.06	0.32	0.135	0.28	33.3	1.2	0.75
L1 (from L2)	2±4	0.4±0.3	4.8±0.4	7±3	0.8±1	8±11	0.1±0.2	0.03±0.04	0.2±0.5	24±4	2.0±0.6	0.5±0.4
L2 cert	89	0.65	4.96	14.8	3.03	9.7	0.21	0.09	0.3	9.9	1.99	0.69
L2 (from L1)	100±170	0.4±0.3	1.55±0.13	19±8	4±4	6±9	0.5±0.8	0.4±0.6	0.5±1.4	14±2	1.2±0.4	1.0±0.8

Tab 4.4. Comparison of certified and experimentally determined concentrations for the standard sera expressed in ppb.

standard for serum analysis, since its markedly higher organic fraction produces significant analytical interferences that compromise trace-element quantification. The same approach was employed for the analysis of elements present at higher concentrations in serum. Again, the concentrations determined through comparison of the two sera produced reliable results. The instrumental signal in cps and the data are presented in table 4.5 and 4.6. In this case, the

	Li7	*Mg24*	*Ca43*	*Ca44*	*Fe56*	*Cu63*	*Zn66*
L1	218000±40000	840000±80000	11900±500	190000±20000	83000±9000	37000±5000	4700±600
L2	427000±102000	2000000±130000	25300±1500	400000±20000	117000±7000	62000±2000	7300±400

Tab 4.5. Instrumental signals for sera.

	Li	***Mg***	***Ca43***	***Ca44***	***Fe***	***Cu***	***Zn***
L1 cert	5.06	19.3	97	97	1.4	1.128	1.46
L1 (from L2)	7±2	15.5±1.8	65±5	66±8	1.35±0.17	1.17±0.16	1.25±0.17
L2 cert	14.4	36.9	139	139	1.91	1.961	1.94
L2 (from L1)	10±3	16±5	206±15	204±24	2.0±0.2	1.9±0.3	2.3±0.3

Tab 4.6. Comparison of certified and experimentally determined concentrations for the standard sera expressed in ppm.

analysis of the gelatines yielded well-defined calibration curves (Figure S4.8), which were constructed and calculated using OriginPro 9.0 (OriginLab Corporation, Northampton, MA, USA). However, the values estimated for the serum using these curves were not directly comparable, further supporting the proposed hypothesis. Given the strong matrix effects and analytical interferences observed for gelatin, it became evident that this material does not represent a suitable matrix-matched standard for serum analysis. Nevertheless, its preparation was sufficiently optimized to yield calibration curves with good linearity (R^2 values), indicating that the instrumental response could still be reliably described within this matrix. On this basis, an alternative strategy was explored, relying on a non–matrix-matched calibration approach[72]. Specifically, this method involved the complete ablation of the deposited gelatine and serum droplets, with correction of the instrumental signal by normalizing to the droplet volumes measured prior to ablation using interferometric techniques. This volume correction minimized variability due to droplet size differences and improved the accuracy of quantification, particularly for elements present at higher concentrations in serum, where signal-to-noise ratios are more favourable. Serum standard Level 1 was treated as the ‘unknown’ to evaluate the robustness of the approach. The CPS data were then exported to ImageJ as image files, enabling the determination of mean signal intensities for individual droplets. The resulting mappings, shown in Figure 4.15, provide a visual representation of the spatial distribution of the signals and ensure consistent measurement across all droplets for subsequent comparative analysis.

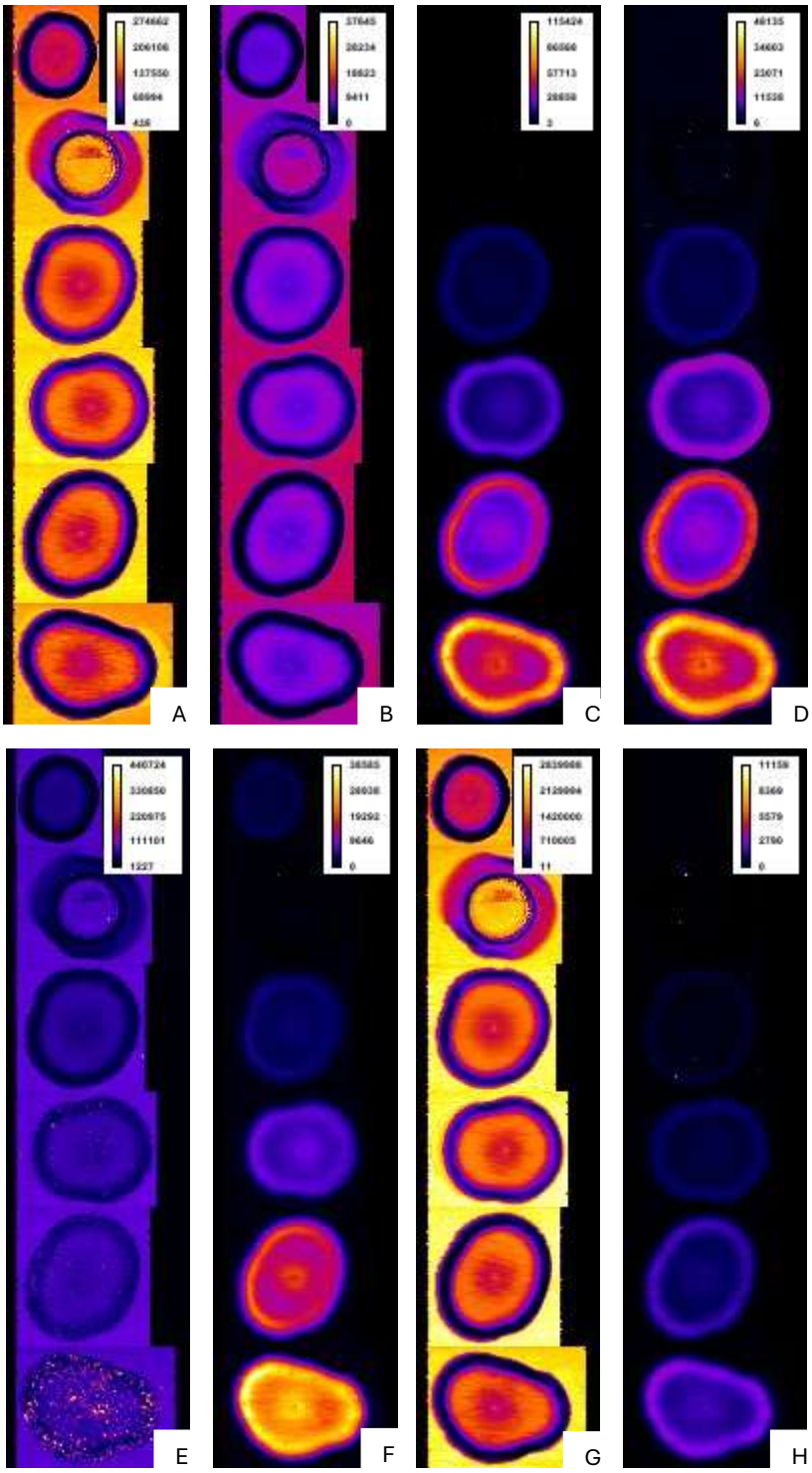


Fig 4.15. Elemental signal maps for A) ^{43}Ca, B) ^{44}Ca, C) Co, D) Cu, E) Fe, F) Li, G) Mg, H) Zn, displayed from top to bottom for serum and gelatine samples at 0 (blank), 10, 20, 50, and 100 ppm.

As is also evident from the maps, the signals for Ca, Fe, and Mg remain largely constant across the different gelatine samples, most likely due to a contribution from the glass slide, which was partially ablated along with the sample because higher fluence values were necessarily applied to achieve complete sample ablation. In contrast, Co exhibits a lower signal in the serum than

in the blank, making it impossible to determine its concentration from the calibration curve. For Li, Cu, and Zn, semi-quantitative calculations were performed. The measured signals (in CPS) were normalized to the ablated droplet volumes (expressed in mL), and the resulting calibration curves were constructed by relating these normalized signals to the corresponding volume

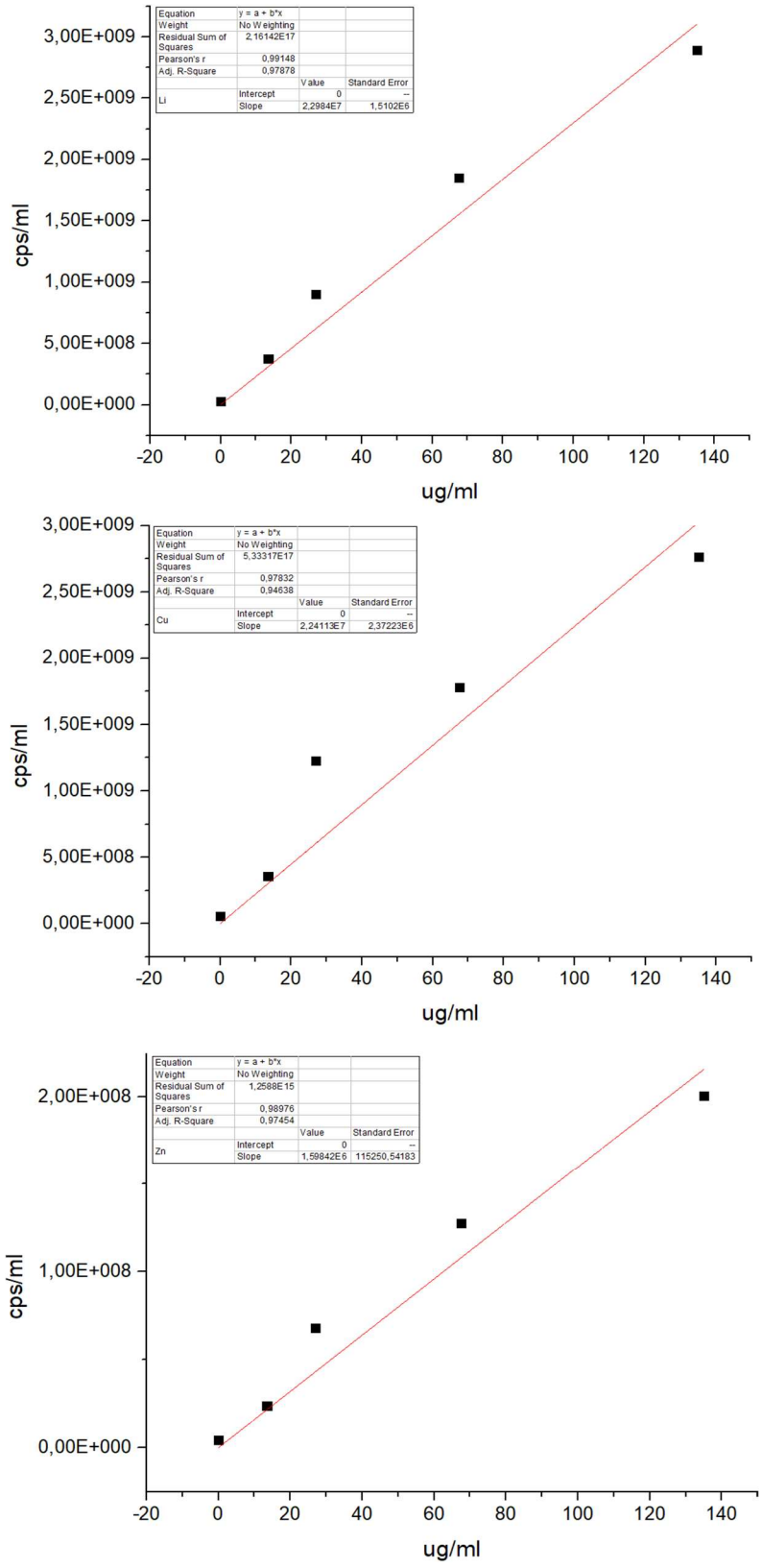


Fig 4.16. Elemental calibration curves for Li, Cu and Zn in gelatine for non-matrix matched calibration.

concentrations (µg/mL). These volume concentrations were obtained by dividing the concentrations of the standards by the known density of the gelatin, which is 1.35 g/mL. The resulting calibration curves are shown in Figure 4.16. For all elements, the regression intercept was constrained to zero, an approach that improves the robustness of the calibration by ensuring that the analytical response remains proportional to the concentration over the studied range. The signals recorded for the serum samples were then used to calculate their respective volume concentrations. These concentrations were subsequently divided by the measured density of the serum, which is 1.396 g/mL. The certified and expected values for the serum are reported in table 4.7. In this study, the uncertainty of the concentrations calculated

	Certified Concentration	**Expected Concentration**
Li	5.06	8±3
Cu	1.128	3.0±1.7
Zn	1.46	3±8

Tab 4.7. Certified and calculated serum concentrations.

from the calibration curves is reported as the standard error (SE) rather than a 95% confidence interval (CI). This approach was chosen because, in some cases, the propagated error was comparable to or larger than the measured value. Reporting the SE provides a direct measure of the precision of the analytical estimate without implying a confidence range that could extend to unrealistic or non-physical values. Furthermore, the SE accurately reflects the variability arising from the regression and standard measurements, ensuring a transparent representation of the measurement uncertainty. Although this procedure enhanced reproducibility and enabled preliminary quantification, it does not fully compensate for the lack of matrix matching. Therefore, it should be considered a proof-of-concept approach, offering valuable insights while still requiring further validation before application to trace-level analyses or more complex matrices.

4.2.3. PtNPs as signal enhancers for Serum Trace Elements

The primary aim of this study is to improve LOD and achieve more accurate quantification of elements present at low or trace concentrations. Accomplishing this requires both robust standardization and innovative strategies to enhance analyte signals while minimizing matrix-related interferences that can compromise analytical precision. In this context, we investigate the enhancement of LA-ICP-MS signals through the application of Pt NPs produced via PLAL. The Pt NPs were first characterized in their as-prepared form using TEM and SEM to determine morphology, size distribution, and uniformity. Following deposition onto serum samples, SEM analysis was performed to examine the interactions between the nanoparticles and the biological matrix, providing insight into how these interactions influence the laser ablation process, subsequent plasma ionization, and ultimately the enhancement of analytical signals. To further contextualize the benefits of nanoparticle-assisted analysis, a comparative study

with laser-induced breakdown spectroscopy (LIBS) was conducted, highlighting differences in signal amplification, analytical sensitivity, and precision between the two techniques. By combining cross-calibration, nanoparticle-enhanced detection, and inter-technique comparison, this work advances the analytical capabilities of LA-ICP-MS, offering a more sensitive, reliable, and versatile methodology for trace metal determination in biological samples.

4.2.3.1. Materials and methods

Seronorm™ Trace Element Serum levels I and II were obtained in lyophilized form and reconstituted with ultrapure water according to the manufacturer's recommendations. Ultrapure water, exhibiting a resistivity of 18 MΩ·cm, was produced using an Arium® Mini purification system (Sartorius AG, Germany). For sample support, Parafilm M (PM-996, Bemis Company, Inc., USA) was employed and deposited on ultrapure silicon wafers prior to introduction into the ablation chamber. The platinum target used for nanoparticle synthesis was purchased from Goodfellow Cambridge Ltd. (UK). PtNPs were synthesized by PLAL. This method offers a direct and clean route for nanoparticle production, yielding colloids free from stabilizers or synthetic residues and avoiding the use of hazardous reagents or extreme synthesis conditions. The principle of PLAL relies on irradiating a solid target with a pulsed laser beam of defined wavelength and irradiance while the target is immersed in a liquid. The laser-target interaction generates plasma and induces the formation of a cavitation bubble, from which nanoparticles nucleate and disperse in the liquid phase. Nanoparticles produced by this technique possess pristine ligand-free surfaces, which enhance their reactivity compared to chemically stabilized analogues. In this work, an ns Nd:YAG laser (Quanta System PILS-GIANT) was employed, operating at a wavelength of 1064 nm with an irradiance of 71 GW·cm^{-2}. The laser beam was focused by a 5 cm focal length lens onto a platinum target immersed in 3 mL of Milli-Q water contained in a quartz cuvette. The resulting colloids were characterized by transmission electron microscopy (TEM) and scanning electron microscopy (SEM). TEM was employed to determine nanoparticle size and concentration, whereas SEM was used to investigate particle morphology, both after deposition of a single colloidal drop on Parafilm and following multiple droplet depositions on the serum sample. For TEM analysis, a concentrated nanoparticle suspension was prepared by pipetting 2 mL of the colloid into two Eppendorf tubes, followed by centrifugation at 9000 rpm for 15 minutes. After discarding the supernatant, the pellet was redispersed in ethanol to facilitate drying. The two suspensions were then combined, and aliquots of the resulting solution were deposited on carbon-coated copper grids. TEM micrographs were acquired at different magnifications, and the particle size distribution was evaluated by statistical analysis. Representative images are shown in Figure 4.17. Image analysis was performed using IMAGEJ software, and statistical treatment of size data was carried out in OriginPro 9 (OriginLab Corporation). Frequency-count analysis was used to

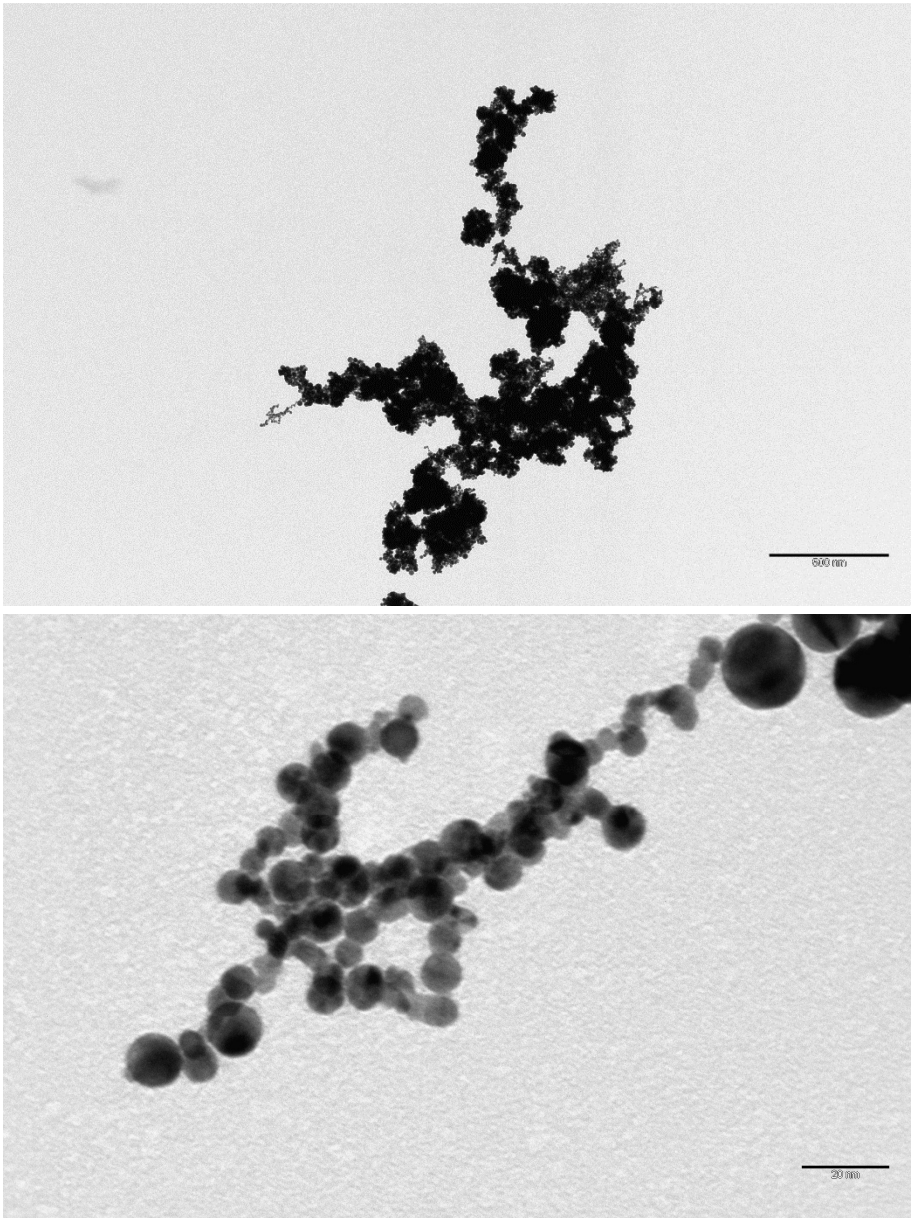


Fig 4.17. TEM images representing PtNPs.

construct a histogram of nanoparticle diameters, which was fitted with a log-normal function, as shown in Figure S4.9. The analysis yielded an average nanoparticle diameter of 13.4 nm with a standard deviation of 4.5 nm. The concentration of PtNPs in solution was determined by ultraviolet–visible (UV-Vis) absorption spectroscopy, analyzing the surface plasmon resonance (SPR) band and applying the Lambert–Beer law:

$$A(\lambda) = \varepsilon c\, l$$

where A(λ) is the absorbance of the colloidal solution at a specific wavelength λ, l is the optical path length (1 cm), ε is the molar extinction coefficient ($m^2 \cdot mol^{-1}$), and c is the nanoparticle concentration. The extinction coefficient was estimated using the empirical relation reported by Feng et al.[73] for platinum nanocrystals at 550 nm:

$$\ln \varepsilon = \mathrm{k} \ln D + b$$

where D is the nanoparticle diameter (nm), with constants k=−0.16 and b=1.77. For a mean particle diameter of 13.4 nm, the extinction coefficient was calculated as 3.849 $mL \cdot mg^{-1} \cdot cm^{-1}$. SPR spectra were then acquired for a 1:5 diluted suspension (Figure S4.10), and the absorbance at 550 nm was used to calculate the concentration according to the Lambert–Beer law. The concentration of PtNPs in solution was determined to be 0.096 $mg \cdot mL^{-1}$. Dried serum spot samples were prepared using two different approaches, depending on the requirements of LA-ICP-MS and LIBS analysis. In the first approach, 20 µL aliquots of serum were carefully pipetted onto a Parafilm support and left to dry overnight in a desiccator maintained at 20 ± 1 °C and 50 ± 5% relative humidity. For specimens intended for NELA-ICP-MS analysis, increasing volumes of nanoparticle suspension (20, 40, 100, 160, 300, and 500 µL) were applied onto the dried spots. These volumes were obtained by sequential additions of 20 µL, allowing each layer to dry completely before the next application. Once dried, the Parafilm discs containing the serum spots were carefully cut with a bistoury and mounted onto ultrapure silicon wafers. In the second approach, 1 µL of serum was pipetted onto the support, immediately followed by 1 µL of ultrapure water, and allowed to dry; this sequence was repeated once more with an additional 1 µL of serum and 1 µL of water. For samples designated for NELA-ICP-MS and NELIBS analysis, the same procedure was followed, with the nanoparticle suspension replacing ultrapure water. For LA-ICP-MS analysis, a NexION 300× inductively coupled plasma mass spectrometer (PerkinElmer, USA) was coupled with an ESI NWR213 laser ablation system (ESI New Wave Research, Cambridge, UK), equipped with a 100 × 100 mm ablation chamber and a typical washout time of ~1 s. The instrumental parameters were tuned following a standard procedure: NIST SRM 612 (Gaithersburg, MD, USA) was ablated using a 100 µm diameter spot and a laser repetition rate of 20 Hz in line-scanning mode at a scan speed of 10 µm/s to maximize $^{238}U^+$ sensitivity while maintaining high sensitivity for a broad mass range, a low oxide ratio ($^{232}Th16O^+/^{232}Th^+$ < 0.6%) and similar $^{238}U^+$ and $^{232}Th^+$ sensitivities.

4.2.3.2. Results and discussion

The homogeneity of 20 µL serum drops was initially evaluated to determine the optimal regions for analysis and assess signal enhancement. This prompted the generation of a full-surface mapping of the samples, both with and without nanoparticles. For the mapping, a rectangular grid was defined with spots spaced 250 µm apart (Figure 4.18). Each spot was ablated for 5 seconds to minimize contamination from the support, with a 15-second interval between consecutive spots and a 30-second delay between lines. LA-ICP-MS parameters are reported in table 4.8. The recorded data was first processed in Excel and subsequently used to generate

LA parameters	
Laser fluence	*3.2 J/cm²*
Spot size	*75 µm round*
RR	*10 Hz*
Carrier gas flow rate	*He, 1 L/min*
ICP-MS parameters	
Rf power	*1600 W*
Plasma gas flow rate	*18 L/min*
Auxiliary gas flow rate	*1.2 L/min*
Ar makeup flow rate	*1.06 L/min*

Tab 4.8. LA and ICPMS parameters used for serum maps.

color-coded maps using a custom RStudio script (Figure S4.11). As shown in the color-coded maps for representative elements-selected among those most challenging to detect and present at varying concentrations (Figure 4.19), the coffee-ring effect was absent. Instead, element concentrations tended to increase towards the centre of the drop, indicating the presence of a Marangoni flow. The lighter central region corresponds to a fracture in the dry drop. The hydrophobic nature of the Parafilm prevented serum penetration, leading to this morphology and the fractures observed during drying. To verify that the central region was the most representative for analysis, a serum-nanoparticle system was tested. As illustrated in Figure 4.20, the platinum distribution was relatively homogeneous, with a slight increase towards the centre, mirroring the behaviour of the native elements. At this stage, analyses were performed on

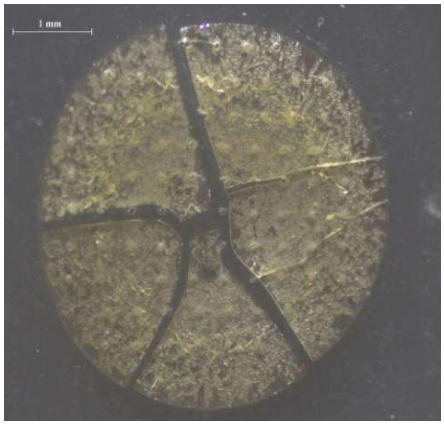


Fig 4.18. Optical microscopy image of serum sample after spatial mapping.

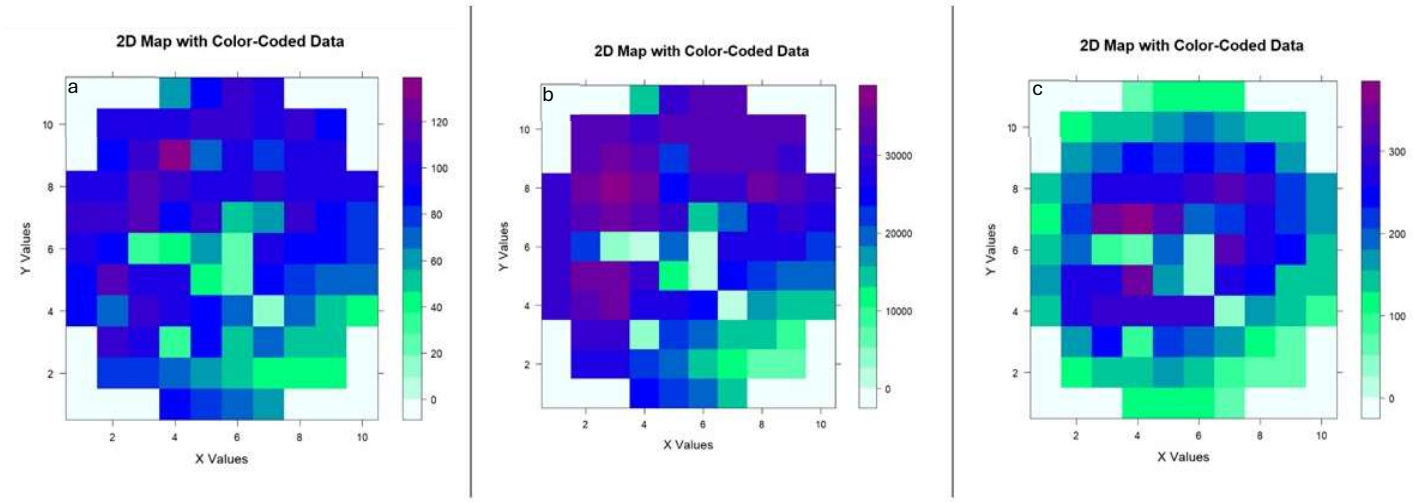


Fig 4.19. a) Co, b) Cu and c) As LA-ICP-MS maps acquired on serum drops.

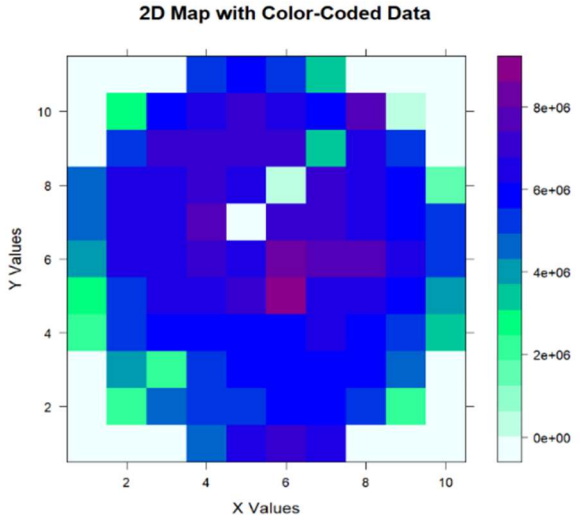


Fig 4.20. Pt LA-ICP-MS map acquired on serum+100 µL NPs deposition system.

serum Level 1 and 2 samples with varying NPs volumes to assess the enhancement effect. For each sample type, five replicates were acquired, with ablation carried out in linear scan mode, each line measuring 1 mm. The optimized parameters are listed in Table 4.9. Signal acquisition was processed following the method of Longerich, and the resulting data — reported in Tables S4.6 and S4.7 — were plotted as a function of the deposited NPs volumes for the different sample sets. Among the elements analysed, many produced a consistent signal.

LA parameters	
Laser fluence	*2.50 J/cm²*
Dosage	*20*
Spot size	*75 µm square*
RR	*20 Hz*
Scan speed	*75 µm/s*
Carrier gas flow rate	*He, 1 L/min*
ICP-MS parameters	
Rf power	*1600 W*
Plasma gas flow rate	*18 L/min*
Auxiliary gas flow rate	*1.2 L/min*
Ar makeup flow rate	*1.06 L/min*
Isotopes measured	*^{7}Li, ^{12}C, ^{23}Na, ^{24}Mg, ^{27}Al, ^{39}K, ^{43}Ca, ^{52}Cr, ^{57}Fe, ^{59}Co, ^{60}Ni, ^{63}Cu, ^{66}Zn, ^{82}Se, ^{118}Sn, ^{121}Sb, ^{197}Au, ^{208}Pb*

Tab 4.9. LA and ICPMS parameters used for serum raster analysis.

Spectra were recorded for Parafilm alone, as well as for water and NPs solution deposited on Parafilm. Some signal interference may arise from the Parafilm, which is inevitably partially ablated during measurement, and from impurities present in the water and platinum. A striking

enhancement was observed for Co, Ni, Sn, and Pb. For these elements, graphs were constructed showing the mean signal with error bars representing the 95% confidence interval as a function of the added NP volumes (Figure 4.21). Table 4.10 presents the linear regression equations for each data set for both L1 and L2, together with the corresponding standard errors of the slope and intercept.

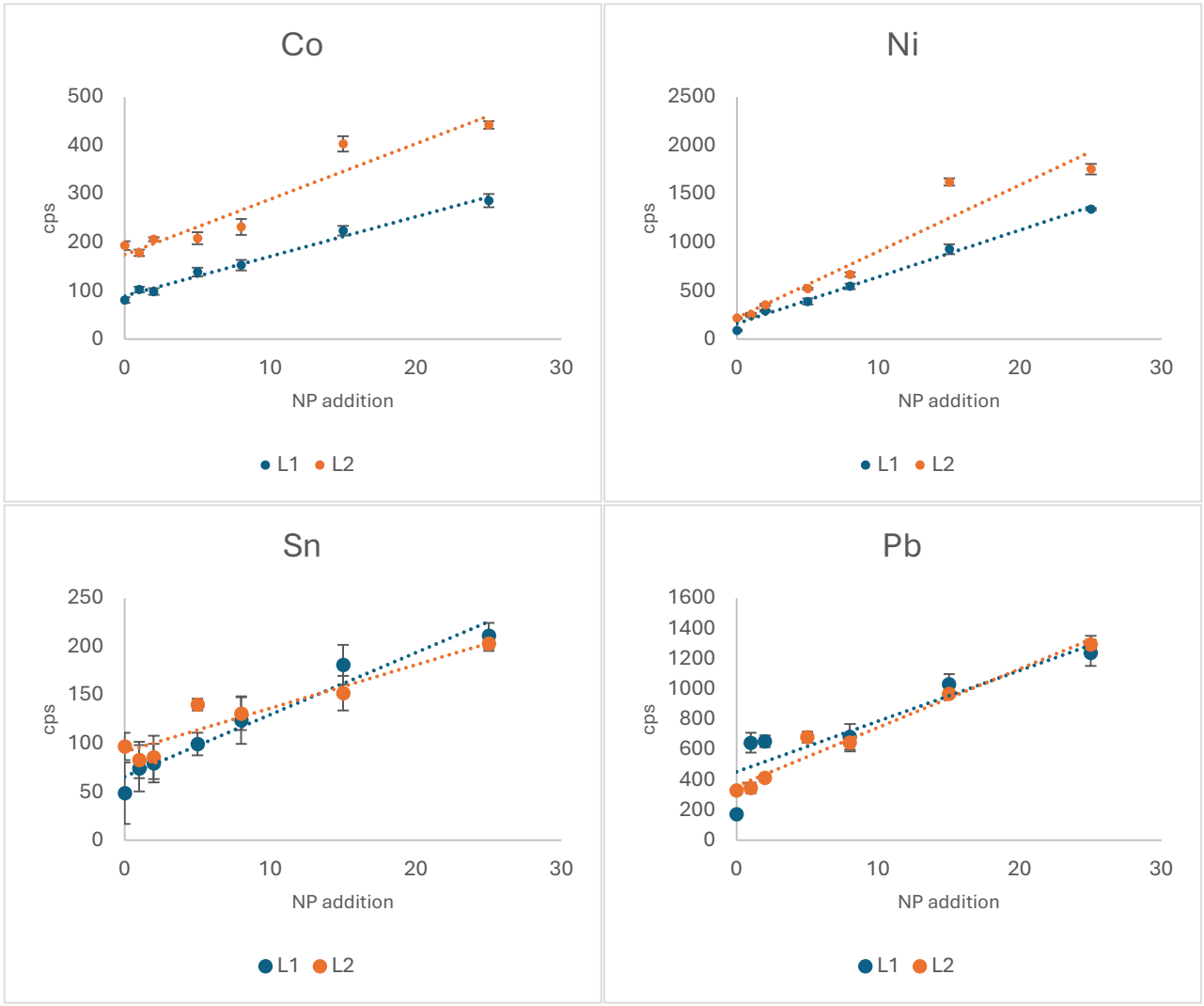


Fig 4.21. Plot of Signal (cps) versus the Number of Sequential NP Addition

		Lin. Reg.	Std. Err. X	Std. Err. Y
Co	*L1*	y = 8.2x + 89	0.4	5
	L2	y = 11.5x + 174	1.5	18
Ni	*L1*	y = 48x + 160	2	20
	L2	y = 69x + 220	9	100
Sn	*L1*	y = 6.4x + 66	0.6	7
	L2	y = 4.5x + 91	0.7	8
Pb	*L1*	y = 33x + 450	8	100
	L2	y = 39x + 360	3	40

Tab 4.10. Linear regression equations with standard errors for slope and intercept.

The standard deviation for the linear regression is notably higher for Pb and Sn compared to Co and Ni. This is likely due to the different chemical behaviour of these elements in ICP-MS: Pb and Sn are more volatile and tend to form stable oxides or other species during nebulization or in the plasma, which results in less consistent transport and partial suppression or instability of ionization, leading to greater fluctuations in the signal between injections. Additionally, in biological samples such as serum, Pb and Sn can strongly bind to proteins, lipids, or other organic molecules, creating more pronounced matrix effects that can alter nebulization efficiency and further increase signal variability. In contrast, Co and Ni, being transition metals, are mostly present as simple ionic species, with more stable transport and ionization and minimal interaction with the matrix, leading to a more consistent and reproducible signal. Enhancement was calculated according to the formula

$$E = \frac{cps\ X_{500\ \mu L\ NPs}}{cps\ X}$$

where the numerator represents the signal recorded for each element after the maximum addition of NPs (i.e., 25 drops of 20 µL each), and the denominator represents the signal measured for the untreated serum. The calculated values are reported in Table 4.11.

Element	Enhancement L1	Enhancement L2
Co	3.6	2.3
Ni	15.1	8.1
Sn	4.3	2.1
Pb	7.2	3.9

Tab 4.11. Calculated enhancement for serum L1 and L2.

Remarkably, signals for these elements were completely absent in Parafilm, in water, and in NPs solution deposited on Parafilm without added NPs, highlighting that the observed signals arise exclusively from the added nanoparticles. These elements are present in both sera at ppb

Element	Conc L1	Conc L2
Co	0.99	3.03
Ni	5.06	9.7
Sn	0.28	0.30
Pb	0.75	0.69

Tab 4.12. Certified elemental concentrations (ppb) for serum L1 and L2.

Levels (Tab 4.12) and are of critical toxicological relevance. Interestingly, after the addition of PtNPs, the relative signal enhancement is often greater at low analyte concentrations, whereas the slope of the calibration curve decreases as the concentration increases. At very low

concentrations, only a small number of atoms need to be ionized in the plasma, so the presence of metallic NPs can significantly improve aerosol formation, transport efficiency, and ionization by acting as an ionization buffer or an additional energy source, while matrix effects remain minimal. As a result, even a small absolute increase in signal produces a strong relative enhancement. However, as the analyte concentration rises, the plasma gradually approaches saturation, meaning it cannot efficiently ionize all the incoming atoms. This saturation effect, combined with stronger matrix interferences and possible interactions between NPs and analyte species, limits the beneficial impact of the NPs and causes the signal to level off rather than increase proportionally. Consequently, the calibration curve exhibits a lower slope at higher concentrations, reflecting the reduced sensitivity and partial saturation of the system. To gain a deeper understanding of the enhancement process, it was considered of interest to further investigate how the NPs interact with the organic matrix. For this purpose, SEM analyses were performed both on a serum sample with 400 µL of NPs deposited and, on a sample, consisting of NPs alone deposited on Parafilm. In the serum sample, backscattered electron (BSE) imaging revealed very bright spherical structures whose size is consistent with that of the NPs (Figure 4.22a); notably, they did not appear to be aggregated. In the split images (chemical contrast on the left, topographic contrast on the right), the bright spots observed in the chemical mode suggest the presence of heavy elements. However, the reduced contrast in the topographic mode, which is more sensitive to surface features, indicates that the NPs

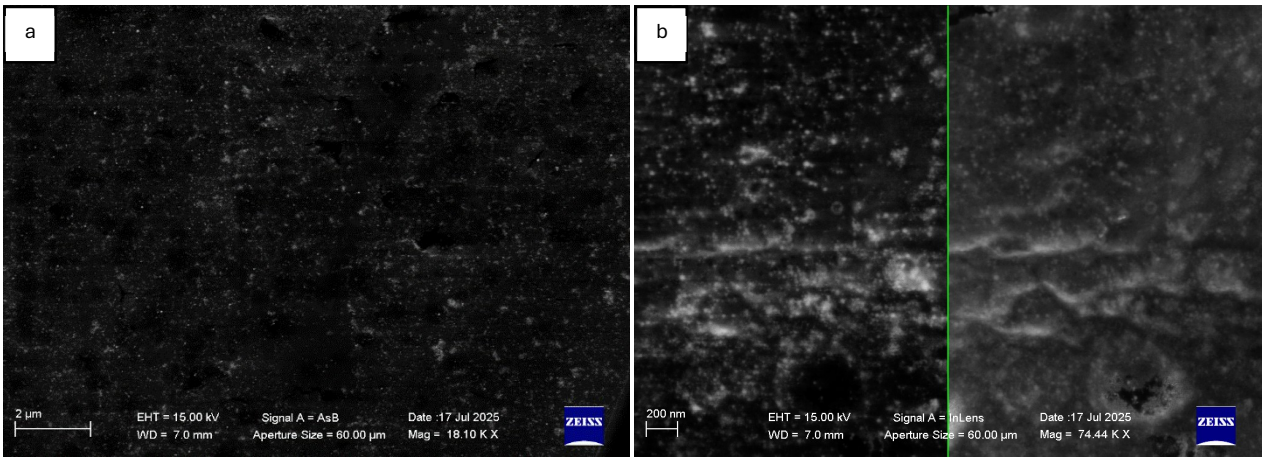


Fig 4.22. SEM images of serum with 400 µL NPs: (a) BSE mode; (b) split mode (chemical left, topography right).

are at least partially embedded within the serum matrix (Figure 4.22b). In contrast, for the sample with NPs alone, the BSE image appeared uniformly bright with numerous well-defined NPs (Figure 4.23a). In the split image, the enhanced contrast in the topographic mode confirmed that the particles were clearly located on the surface (Figure 4.23b). The sharper imaging compared to the serum sample suggests that, in the presence of serum, the NPs become incorporated into the matrix. Interestingly, some NPs appeared much larger in the “NPs-only” sample, while in the serum sample they seemed less distinct, likely because they were absorbed and embedded within the organic material, effectively masking part of their signal. Given the relatively large number and size of the NPs, these findings support the hypothesis that the serum matrix incorporates and partially conceals them. At this stage, the focus shifts toward developing a deeper understanding of the enhancement mechanisms

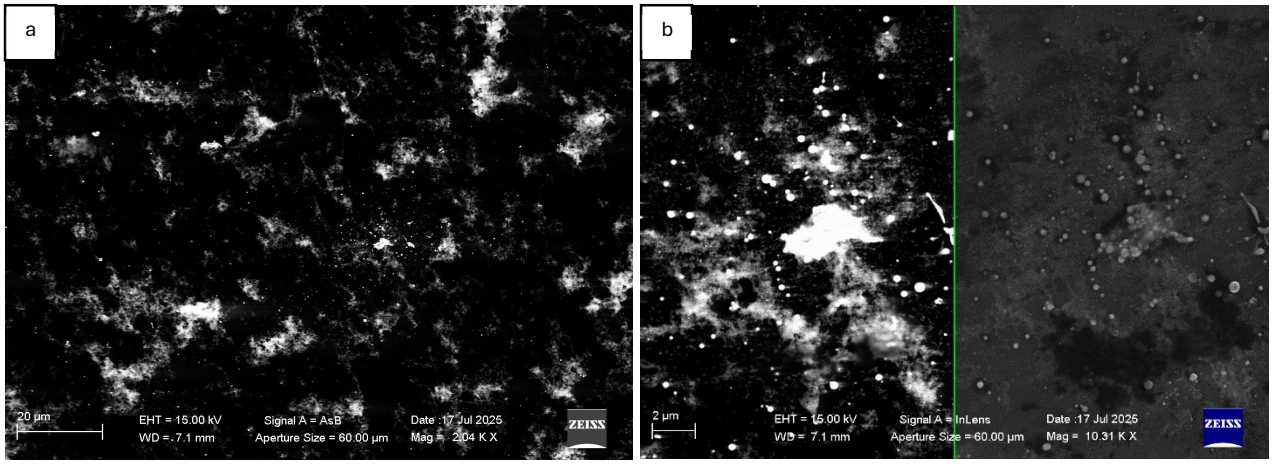


Fig 4.23. SEM images of NPs: (a) BSE mode; (b) split mode (chemical left, topography right).

induced by NPs. To pursue this objective, comparative analyses were conducted within the framework of LIBS. Notably, the earliest investigations into the use of NPs as signal enhancers in laser ablation–based techniques originated in this context, providing fundamental evidence of their remarkable ability to amplify spectral emissions[74]. Subsequent studies sought to elucidate the origin of this enhancement, identifying multiple contributing mechanisms, including localized electric field intensification near the NP surface, increased plasma density, and modified ablation dynamics at the laser–target interface. These findings demonstrate that the role of NPs in LIBS extends beyond simple signal amplification, involving complex interactions between laser energy absorption, plasma expansion, and nanoparticle-induced confinement effects. Building on these insights, the concept of nanoparticle-assisted enhancement was later translated to LA-ICP-MS. In this context, NPs play a dual role: they can modify the laser–matter interaction during ablation, improving material removal efficiency, while also influencing aerosol formation and transport toward the plasma. This dual action leads to improved sensitivity, lower detection limits, and, in some cases, enhanced spatial resolution. Accordingly, the samples analyzed by LA-ICP-MS were also subjected to LIBS investigations. Based on prior findings, the samples were prepared following also the second procedure described, optimized for LIBS analysis and involving complete sample ablation. In the first set of experiments, multiple LIBS shots were performed on single drops of serum and serum containing different NP volumes (Figure 4.24). The resulting spectra were superimposed to assess potential signal enhancements; however, no increase was observed (Figure 4.25). Subsequently, samples prepared specifically for LIBS were analysed using both techniques - complete ablation of the drop for LIBS (Figure 4.26) and four linear scan lines for LA-ICP-MS. In this case, the results were reversed: LA-ICP-MS measurements showed no enhancement (Table 4.13), whereas the LIBS spectra of major elements displayed higher peak intensities (Figure 4.27). Comparative

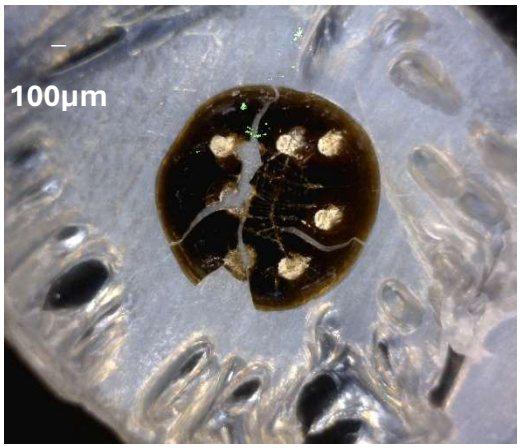


Fig 4.24. Multiple laser shots applied to a serum + nanoparticle droplet during LIBS analysis.

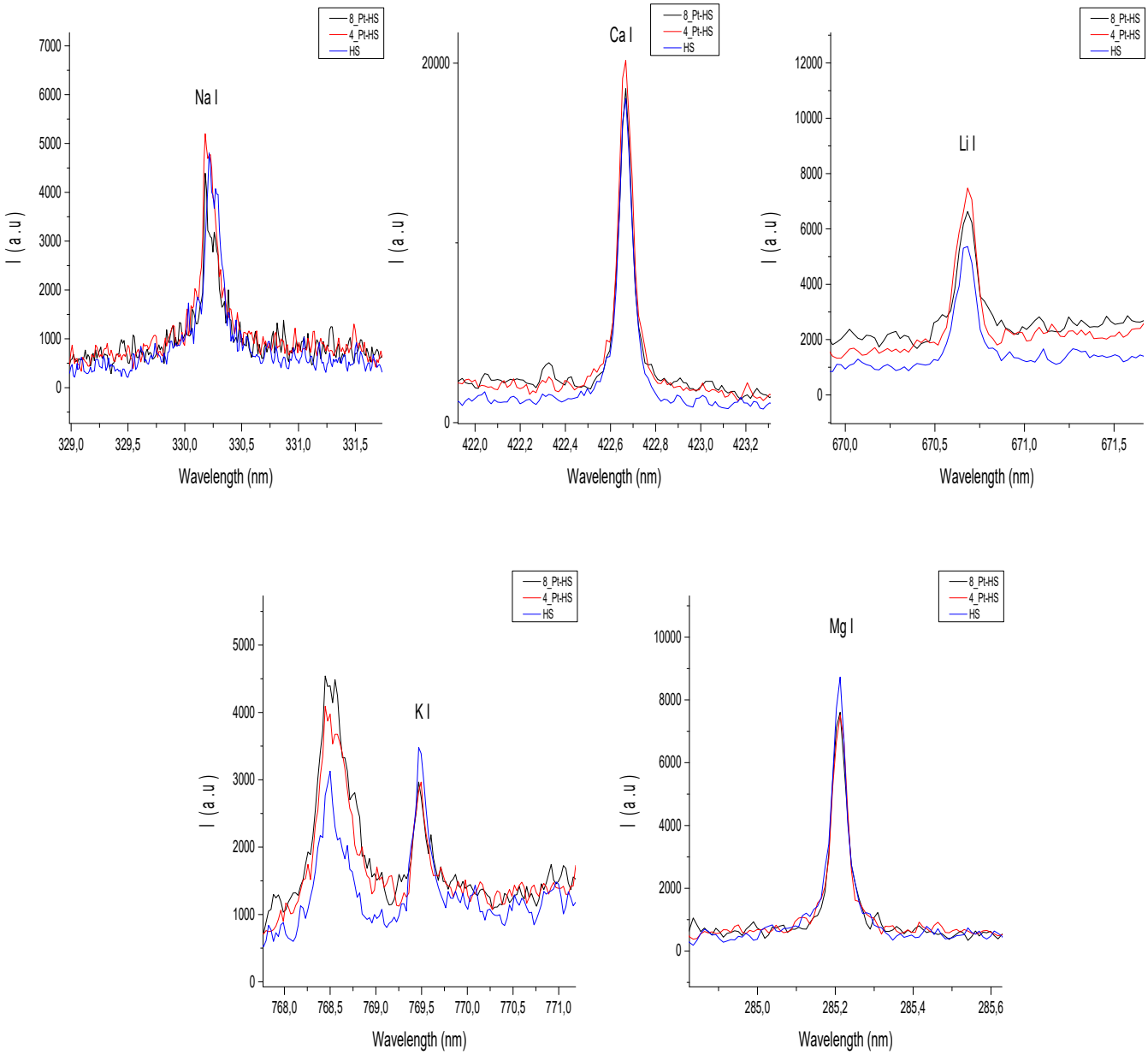


Fig 4.25. LIBS spectra recorded before and after the incremental addition of NPs.

analysis using LIBS and LA-ICP-MS suggests that NPs modulate plasma formation in distinct, technique-dependent ways. In LIBS, the plasmonic effect of NPs primarily promotes sample atomization, thereby intensifying spectral emission. In contrast, in LA-ICP-MS, the key objective is not only atomization but also the generation of a stable aerosol suitable for efficient

ionization in the ICP. Here, NPs act as thermal mediators, influencing ablation dynamics and particle

	Li7	*C12*	*Na23*	*Mg24*	*Al27*	*K39*	*Ca43*	*Cr52*	*Fe57*
L1+H2O	333548.7	3111472 1	3.81E+08	1349596	6257.44 1	1450050 4	14502.1 9	56328.8 6	1830.21 1
std err	4501.01 1	433261.2	2897353 6	22577.7 5	3441.12 5	224639	310.252 3	1166.60 3	66.1765 2
L1+NP	362775.5	2928910 7	5.22E+08	1195322	7351.28 3	1622110 0	12958.6 3	52905.7 3	1680.60 6
std err	14871.0 6	295927.5	5999428 2	24434.5 9	866.612 3	674865.9	323.627 8	1088.22 5	22.7804
L2+H2O	635409.3	3076044 1	8.38E+08	2952126	19458.3 5	2242054 5	22146.6 8	56117.4 9	4689.82 8
std err	22828.6 4	650031.3	1.05E+08	109082. 3	7963.50 1	813811.1	518.526 8	1593.38 9	1384.65 2
L2+NP	800160	3192035 0	7.83E+08	3005464	20536.9 1	3786574 5	23261.7 6	60031.4 9	2636.23 8
std err	52059.9 7	909238.3	1.14E+08	151754. 5	7950.46 8	5943970	1905.46 7	1747.36 5	185.747 8
	Co59	Ni60	Cu63	Zn66	Se82	Sn118	Sb121	Au197	Pb208
L1+H2O	71.6670 3	97.9172	32379.55	4795.68 7	66.4279 2	242.3339	1131.82 3	6862.45 9	202.295 2
std err	3.78122 8	8.240427	444.7793	110.794 1	29.2695 6	31.58075	17.9119 8	155.961 4	33.1786
L1+NP	59.2711 3	90.88594	28571.71	3892.60 5	21.1128 6	47.29266	1064.58 1	5733.80 9	254.294 6
std err	7.34573 3	8.766735	295.6455	118.955	14.8191 9	16.7243	120.127	65.9845 9	5.16700 7
L2+H2O	157.987 5	195.7832	53341.75	5955.55 1	48.7184 7	150.0737	405.426	24437.6 3	338.652 8
std err	11.6814 6	17.09834	2529.846	144.575	38.8706 4	26.59435	38.6683	821.378 3	27.6609 4
L2+NP	157.258 3	126.2509	56318	5854.25 5	84.9718 9	115.3499	340.578 8	23644.3 8	717.922 6
std err	14.1642 7	8.07283	3709.525	260.008	51.2462 6	18.34	22.3084 4	950.206 3	163.497 5

Tab 4.13. LA-ICP-MS signals (cps) recorded for serum samples without and with NPs, prepared according to the procedure optimized for LIBS analysis.

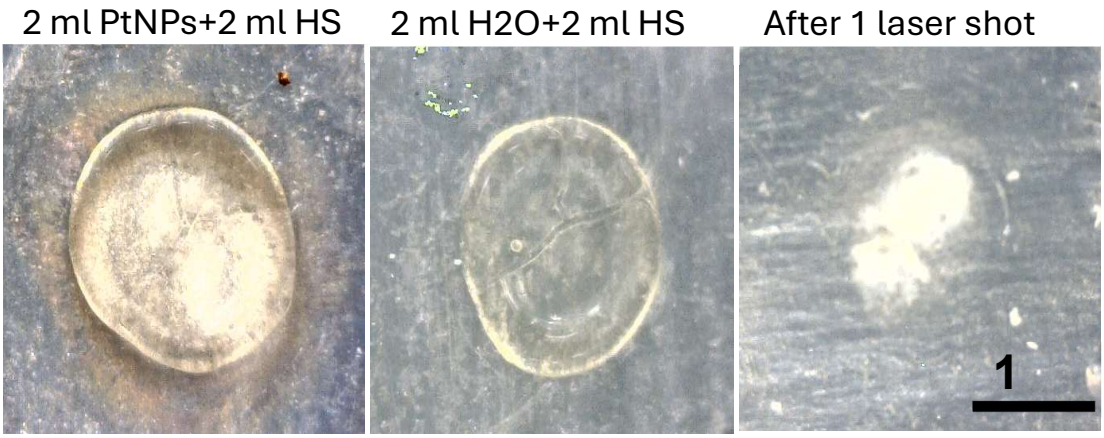
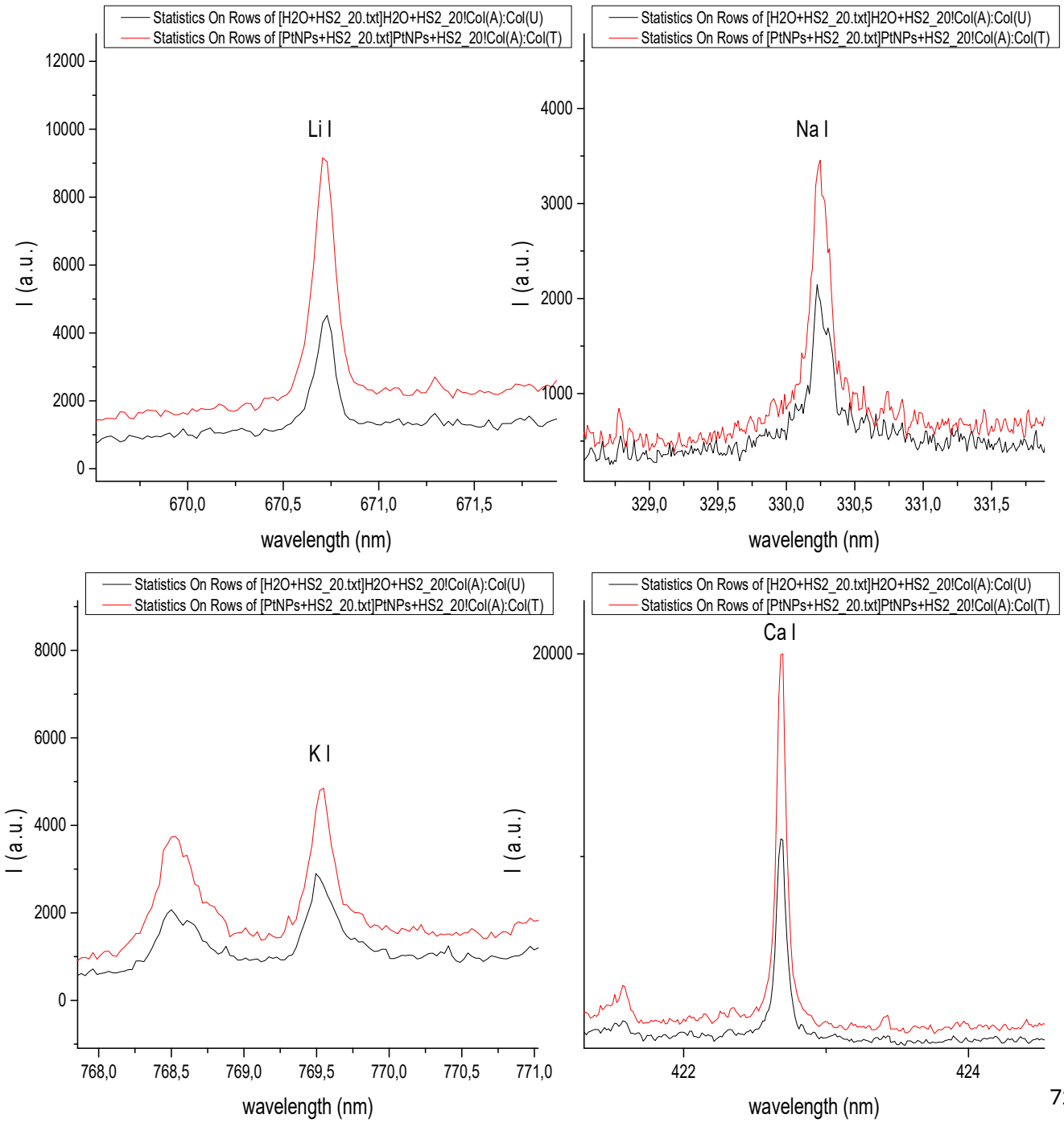


Fig 4.26. OM images of LIBS-prepared samples before and after laser ablation.

nucleation to favour the production of droplets and particulates of optimal size, while preventing the formation of excessively large clusters that could impair transport and ionization efficiency. Thus, the observed enhancement does not merely represent a quantitative signal increase but reflects the outcome of intricate interactions among laser energy absorption, NP-induced confinement, and plasma formation control. The parallel behavior observed across LIBS and LA-ICP-MS underscores a fundamental correspondence between the two techniques: in both cases, NPs modulate key stages of laser-induced plasma evolution—energy coupling, expansion, and relaxation—though with different analytical consequences. This parallelism highlights the value of cross-technique studies for disentangling the fundamental mechanisms of NP-induced enhancement and for guiding the rational design of nanoparticle-assisted analytical strategies. Overall, these results mark an



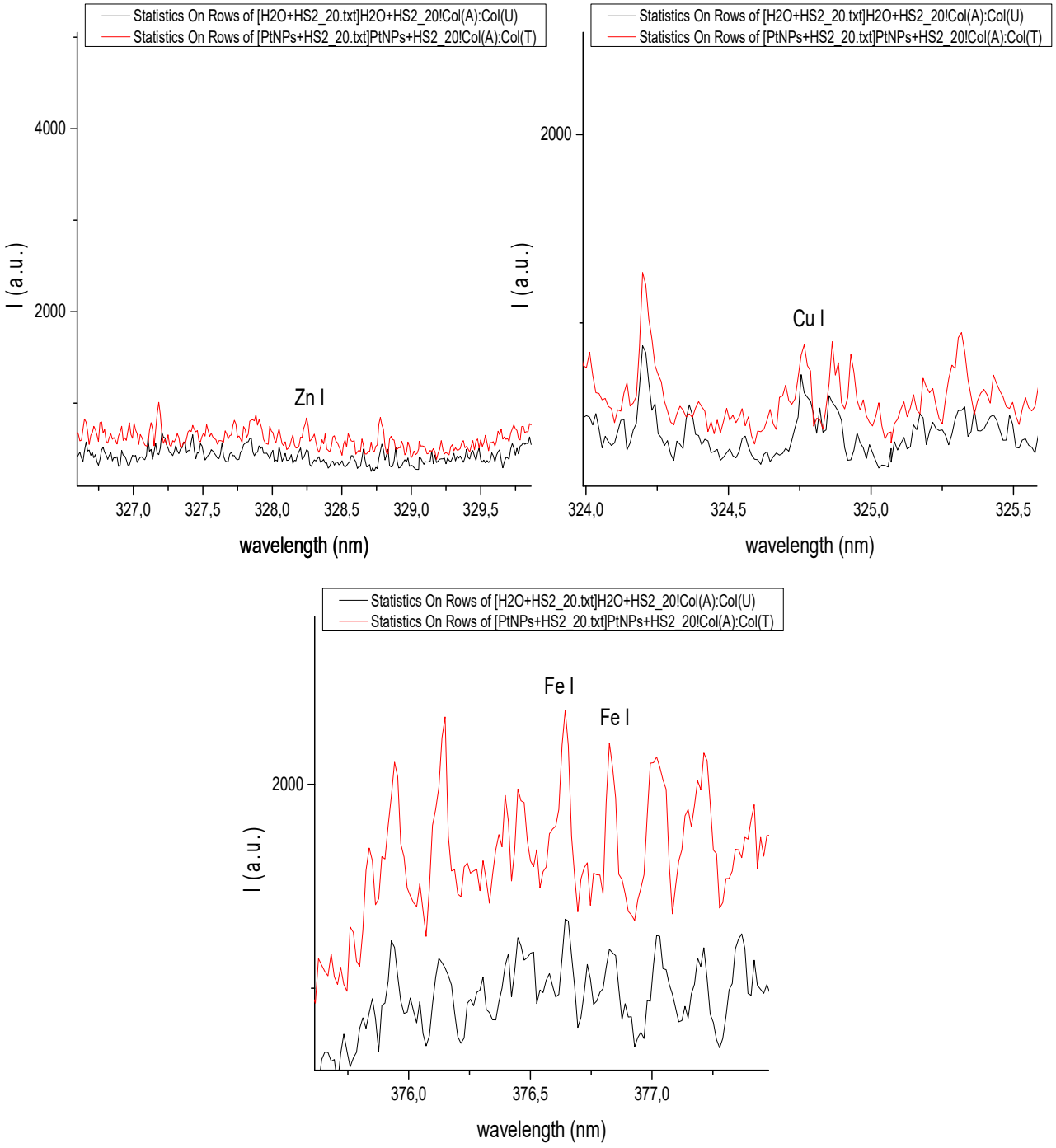


Fig 4.27. LIBS spectra recorded for samples prepared according to the procedure optimized for LIBS analysis.

important step toward the routine application of LA-ICP-MS in bioanalysis, paving the way for more accurate clinical and toxicological studies and enabling the monitoring of essential and toxic metal exposure in complex biological fluids, even at trace concentrations.

4.2.4. Conclusions

This study provides a comprehensive evaluation of methodological strategies to improve the quantitative accuracy and sensitivity of LA-ICP-MS for the analysis of trace and ultra-trace elements in biological matrices such as human serum. The results demonstrate that although gelatine has been widely applied as a calibration medium for solid biological materials, its high organic content and compositional mismatch with serum introduce significant matrix effects that preclude its use as a reliable matrix-matched standard for fluid samples. Nonetheless, the optimized preparation of gelatine spots enabled the construction of reproducible calibration curves, supporting its utility as a model system for methodological development. Building on this foundation, a complementary nanoparticle-assisted approach was investigated, revealing that the addition of platinum nanoparticles (PtNPs) synthesized by PLAL can markedly enhance analytical signals for selected trace elements, particularly Co, Ni, Sn, and Pb. The enhancement effect was found to depend on both analyte concentration and plasma dynamics, with greater relative amplification observed at lower concentration levels. Comparative analyses by LIBS and LA-ICP-MS further highlighted the distinct mechanisms of nanoparticle-induced enhancement in each technique, with plasmonic effects dominating in LIBS and ablation–aerosol formation dynamics playing a key role in LA-ICP-MS. Overall, this work advances the understanding of nanoparticle–matrix interactions in laser-based spectrochemical analysis and introduces a promising pathway toward improved detection limits, reproducibility, and standardization in bioanalytical applications of LA-ICP-MS.

References

[1] Henderson, J. Ancient Glass, 2013. https://doi.org/10.1017/cbo9781139021883.

[2] HENDERSON, J. THE RAW MATERIALS OF EARLY GLASS PRODUCTION. Oxford J Archaeology 1985, 4 (3), 267–291. https://doi.org/10.1111/j.1468-0092.1985.tb00248.x.

[3] Moretti, C.; Hreglich, S. Raw Materials, Recipes and Procedures Used for Glass Making. Modern Methods for Analysing Archaeological and Historical Glass, 2013, 23–47. https://doi.org/10.1002/9781118314234.ch2.

[4] SALEH, S. A.; GEORGE, A. W.; HELMI, F. M. STUDY OF GLASS AND GLASS-MAKING PROCESSES AT WADI EL-NATRUN, EGYPT IN THE ROMAN PERIOD 30 B.C. TO 359 A.D. Studies in Conservation 1972, 17 (4), 143–172. https://doi.org/10.1179/sic.1972.015.

[5] SHORTLAND, A. J.; TITE, M. S. RAW MATERIALS OF GLASS FROM AMARNA AND IMPLICATIONS FOR THE ORIGINS OF EGYPTIAN GLASS*. Archaeometry 2000, 42 (1), 141–151. https://doi.org/10.1111/j.1475-4754.2000.tb00872.x.

[6] SMIRNIOU, M.; REHREN, TH. DIRECT EVIDENCE OF PRIMARY GLASS PRODUCTION IN LATE BRONZE AGE AMARNA, EGYPT. Archaeometry 2010, 53 (1), 58–80. https://doi.org/10.1111/j.1475-4754.2010.00521.x.

[7] Stern, E. M. Roman Glassblowing in a Cultural Context. American Journal of Archaeology 1999, 103 (3), 441–484. https://doi.org/10.2307/506970.

[8] Rasmussen, Seth. (2012). How Glass changed the World. The History and Chemistry of Glass from Antiquity to the 13th Century

[9] Freestone I C, Greenwood R and Gorin-Rosen Y (2002) Byzantine and early Islamic glassmaking in the Eastern Mediterranean: production and distribution of primary glass. in G. Kordas (ed) Hyalos - Vitrum - Glass. Athens , 167-174.

[10] Freestone, I.C., Gorin-Rosen, Y., Hughes, M.J., 2000. Composition of primary glass from Israel. In: Nenna, M.-D. (Ed.), La Route du Verre: Ateliers primaires et secondaires de verriers du second millinaire av. J.-C. au Moyen-Age, pp. 65e84. Travaux de la Maison de l'Orient M_editerran_een no. 33. Lyon.

[11] Kuleff, I.; Djingova, R.; Penev, I. Analysis of Ancient and Medieval Glasses by INAA. Journal of Radioanalytical and Nuclear Chemistry, Articles 1984, 83 (2), 333–343. https://doi.org/10.1007/bf02037147.

[12] Aerts, A.; Velde, B.; Janssens, K.; Dijkman, W. Change in Silica Sources in Roman and Post-Roman Glass. Spectrochimica Acta Part B: Atomic Spectroscopy 2003, 58 (4), 659–667. https://doi.org/10.1016/s0584-8547(02)00287-2.

[13] Schibille, N.; Sterrett-Krause, A.; Freestone, I. C. Glass Groups, Glass Supply and Recycling in Late Roman Carthage. Archaeol Anthropol Sci 2016, 9 (6), 1223–1241. https://doi.org/10.1007/s12520-016-0316-1.

[14] Constantinescu, B.; Cristea-Stan, D.; Szőkefalvi-Nagy, Z.; Kovács, I.; Harsányi, I.; Kasztovszky, Z. PIXE and PGAA – Complementary Methods for Studies on Ancient Glass Artefacts (from Byzantine, Late Medieval to Modern Murano Glass). Nuclear Instruments and Methods in Physics Research Section B: Beam Interactions with Materials and Atoms 2018, 417, 105–109. https://doi.org/10.1016/j.nimb.2017.07.017.

[15] Barbana, F.; Bertoncello, R.; Milanese, L.; Sada, C. Alteration and Corrosion Phenomena in Roman Submerged Glass Fragments. Journal of Non-Crystalline Solids 2004, 337 (2), 136–141. https://doi.org/10.1016/j.jnoncrysol.2004.03.118.

[16] Dal Bianco, B.; Bertoncello, R.; Milanese, L.; Barison, S. Glasses on the Seabed: Surface Study of Chemical Corrosion in Sunken Roman Glasses. Journal of Non-Crystalline Solids 2004, 343 (1–3), 91–100. https://doi.org/10.1016/j.jnoncrysol.2004.07.002.

[17] Gratuze, B.; Blet-Lemarquand, M.; Barrandon, J.-N. Mass Spectrometry with Laser Sampling: A New Tool to Characterize Archaeological Materials. Journal of Radioanalytical and Nuclear Chemistry 2001, 247 (3), 645–656. https://doi.org/10.1023/a:1010623703423.

[18] Müller, K.; Stege, H. EVALUATION OF THE ANALYTICAL POTENTIAL OF LASER-INDUCED BREAKDOWN SPECTROMETRY (LIBS) FOR THE ANALYSIS OF HISTORICAL GLASSES*. Archaeometry 2003, 45 (3), 421–433. https://doi.org/10.1111/1475-4754.00119.

[19] Piepoli L., Il tratto della via Appia tra Gravina in Puglia e Taranto: primi dati sulle ricognizioni di superficie nei territori di Altamura, Santeramo in Colle e Laterza, in Thiasos 6, 2017, pp. 103-119.

[20] Zanini, R.; Moro, G.; Orsega, E. F.; Panighello, S.; Šelih, V. S.; Jaćimović, R.; van Elteren, J. T.; Mandruzzato, L.; Moretto, L. M.; Traviglia, A. Insights into the Secondary Glass Production in Roman Aquileia: A Preliminary Study. Journal of Archaeological Science: Reports 2023, 50, 104067. https://doi.org/10.1016/j.jasrep.2023.104067.

[21] Varberg, J.; Gratuze, B.; Kaul, F. Between Egypt, Mesopotamia and Scandinavia: Late Bronze Age Glass Beads Found in Denmark. Journal of Archaeological Science 2015, 54, 168–181. https://doi.org/10.1016/j.jas.2014.11.036.

[22] Robertshaw, P.; Wood, M.; Haour, A.; Karklins, K.; Neff, H. Chemical Analysis, Chronology, and Context of a European Glass Bead Assemblage from Garumele, Niger. Journal of Archaeological Science 2014, 41, 591–604. https://doi.org/10.1016/j.jas.2013.08.023.

[23] Šelih, V. S.; van Elteren, J. T. Quantitative Multi-Element Mapping of Ancient Glass Using a Simple and Robust LA-ICP-MS Rastering Procedure in Combination with Image Analysis. Anal Bioanal Chem 2011, 401 (2), 745–755. https://doi.org/10.1007/s00216-011-5119-8.

[24] Zanini, R.; Roman, M.; Cattaruzza, E.; Traviglia, A. High-Speed and High-Resolution 2D and 3D Elemental Imaging of Corroded Ancient Glass by Laser Ablation-ICP-MS. J. Anal. At. Spectrom. 2023, 38 (4), 917–926. https://doi.org/10.1039/d2ja00337f.

[25] van Elteren, J. T.; Tennent, N. H.; Šelih, V. S. Multi-Element Quantification of Ancient/Historic Glasses by Laser Ablation Inductively Coupled Plasma Mass Spectrometry Using Sum Normalization Calibration. Analytica Chimica Acta 2009, 644 (1–2), 1–9. https://doi.org/10.1016/j.aca.2009.04.025.

[26] Gratuze, B.; Blet-Lemarquand, M.; Barrandon, J.-N. Mass Spectrometry with Laser Sampling: A New Tool to Characterize Archaeological Materials. Journal of Radioanalytical and Nuclear Chemistry 2001, 247 (3), 645–656. https://doi.org/10.1023/a:1010623703423.

[27] Hattendorf, B.; Günther, D. Laser Ablation Inductively Coupled Plasma Mass Spectrometry (LA-ICPMS). Handbook of Spectroscopy, 2014, 647–698. https://doi.org/10.1002/9783527654703.ch17.

[28] Longerich, H. P.; Jackson, S. E.; Günther, D. Inter-Laboratory Note. Laser Ablation Inductively Coupled Plasma Mass Spectrometric Transient Signal Data Acquisition and Analyte Concentration Calculation. J. Anal. At. Spectrom. 1996, 11 (9), 899–904. https://doi.org/10.1039/ja9961100899.

[29] R. Leardi, C. Melzi, G. Polotti, CAT (Chemometric Agile Tool)

[30] Brems, D.; Degryse, P. Trace Element Analysis in Provenancing Roman Glass-Making. Archaeometry 2013, 56 (S1), 116–136. https://doi.org/10.1111/arcm.12063.

[31] Zanini, R.; Moro, G.; Orsega, E. F.; Panighello, S.; Šelih, V. S.; Jaćimović, R.; van Elteren, J. T.; Mandruzzato, L.; Moretto, L. M.; Traviglia, A. Insights into the Secondary Glass Production in Roman Aquileia: A Preliminary Study. Journal of Archaeological Science: Reports 2023, 50, 104067. https://doi.org/10.1016/j.jasrep.2023.104067.

[32] Hans Wedepohl, K. The Composition of the Continental Crust. Geochimica et Cosmochimica Acta 1995, 59 (7), 1217–1232. https://doi.org/10.1016/0016-7037(95)00038-2.

[33] Aerts, A.; Velde, B.; Janssens, K.; Dijkman, W. Change in Silica Sources in Roman and Post-Roman Glass. Spectrochimica Acta Part B: Atomic Spectroscopy 2003, 58 (4), 659–667. https://doi.org/10.1016/s0584-8547(02)00287-2.

[34] Freestone I. Primary glass from Israel and the Production of Glass in Late Antiquity and the early Islamic period(with Y Gorin-Rosen and M Hughes). La Route du Verre, M-D Nenna (ed), Lyon; Maison de l'Orient, TMOH 33, 65-84. 2000.

[35] Gvantsa Vachadze, Bernard Gratuze. Analysis of early Iron age glass beads (8th to 7th c. BC) from the Tsaishi necropolis (Georgia). Journal of Archaeological Science: Reports, 2025, 62, pp.105066. 10.1016/j.jasrep.2025.105066. hal-04974650.

[36] Pourret, O., Davranche, M., Gruau, G., Dia, A., 2008. New insights into cerium anomalies in organic-rich alkaline waters. Chem. Geol. 251 (1-4), 120–127. https://doi.org/ 10.1016/j.chemgeo.2008.03.002.

[37] Conte, S.; Matarese, I.; Vezzalini, G.; Pacciarelli, M.; Scarano, T.; Vanzetti, A.; Gratuze, B.; Arletti, R. How Much Is Known about Glassy Materials in Bronze and Iron Age Italy? New Data and General Overview. Archaeol Anthropol Sci 2018, 11 (5), 1813–1841. https://doi.org/10.1007/s12520-018-0634-6.

[38] Klimscha, F.; Karlsen, H.; Hansen, S.; Renn, J. Vom Künstlichen Stein Zum Durchsichtigen Massenprodukt . Innovationen in Der Glastechnik Und Ihre Sozialen Folgen Zwischen Bronzezeit Und Antike. Edition Topoi 2020. https://doi.org/10.17171/3-67.

[39] Freestone, I. C.; Barfod, G. H.; Chen, C.; Larson, K. A.; Gorin-Rosen, Y. Glass Production at Jalame, Israel: Process, Composition and Relationship to Roman Glass in Europe. Journal of Archaeological Science: Reports 2023, 51, 104179. https://doi.org/10.1016/j.jasrep.2023.104179.

[40] MIRTI, P.; LEPORA, A.; SAGUÌ, L. SCIENTIFIC ANALYSIS OF SEVENTH-CENTURY GLASS FRAGMENTS FROM THE CRYPTA BALBI IN ROME*. Archaeometry 2000, 42 (2), 359–374. https://doi.org/10.1111/j.1475-4754.2000.tb00887.x.

[41] Nadine Schibille, Islamic Glass in the Making: Chronological and Geographical Dimensions. 2022, Leuven: Leuven University Press (CC BY NC ND 4.0)

[42] Dal Bianco, B.; Bertoncello, R.; Milanese, L.; Barison, S. Glasses on the Seabed: Surface Study of Chemical Corrosion in Sunken Roman Glasses. Journal of Non-Crystalline Solids 2004, 343 (1–3), 91–100. https://doi.org/10.1016/j.jnoncrysol.2004.07.002.

[43] Doremus, R. H. Interdiffusion of Hydrogen and Alkali Ions in a Glass Surface. Journal of Non-Crystalline Solids 1975, 19, 137–144. https://doi.org/10.1016/0022-3093(75)90079-4.

[44] Zanini, R.; Roman, M.; Cattaruzza, E.; Traviglia, A. High-Speed and High-Resolution 2D and 3D Elemental Imaging of Corroded Ancient Glass by Laser Ablation-ICP-MS. J. Anal. At. Spectrom. 2023, 38 (4), 917–926. https://doi.org/10.1039/d2ja00337f.

[45] van Giffen, N. A. R.; Koob, S. P. Deterioration of Vitreous Materials. The Encyclopedia of Archaeological Sciences, 2018, 1–4. https://doi.org/10.1002/9781119188230.saseas0179.

[46] Genga, A.; Siciliano, M.; Famà, L.; Filippo, E.; Siciliano, T.; Mangone, A.; Traini, A.; Laganara, C. Characterization of Surface Layers Formed under Natural Environmental Conditions on Medieval Glass from Siponto (Southern Italy). Materials Chemistry and Physics 2008, 111 (2–3), 480–485. https://doi.org/10.1016/j.matchemphys.2008.04.057.

[47] Hachmöller, O.; Aichler, M.; Schwamborn, K.; Lutz, L.; Werner, M.; Sperling, M.; Walch, A.; Karst, U. Element Bioimaging of Liver Needle Biopsy Specimens from Patients with Wilson's Disease by Laser Ablation-Inductively Coupled Plasma-Mass Spectrometry. Journal of Trace Elements in Medicine and Biology 2016, 35, 97–102. https://doi.org/10.1016/j.jtemb.2016.02.001.

[48] Hanć, A.; Komorowicz, I.; Iskra, M.; Majewski, W.; Barałkiewicz, D. Application of Spectroscopic Techniques: ICP-OES, LA-ICP-MS and Chemometric Methods for Studying the Relationships between Trace Elements in Clinical Samples from Patients with Atherosclerosis Obliterans. Anal Bioanal Chem 2011, 399 (9), 3221–3231. https://doi.org/10.1007/s00216-011-4729-5.

[49] Parsons, P. J.; Barbosa, F., Jr. Atomic Spectrometry and Trends in Clinical Laboratory Medicine. Spectrochimica Acta Part B: Atomic Spectroscopy 2007, 62 (9), 992–1003. https://doi.org/10.1016/j.sab.2007.03.007.

[50] Alimonti A, Bocca B, Mannella E, Petrucci F, Zennaro F, Cotichini R, D'Ippolito C, Agresti A, Caimi S, Forte G. Assessment of reference values for selected elements in a healthy urban population. Ann Ist Super Sanita. 2005;41(2):181-7. PMID: 16244391.

[51] Lee, J.-Y.; Kim, J.-H.; Choi, D.-W.; Lee, D.-W.; Park, J.-H.; Yoon, H.-J.; Pyo, H.-S.; Kwon, H.-J.; Park, K.-S. The Association of Heavy Metal of Blood and Serum in the Alzheimer's Diseases. Toxicological Research 2012, 28 (2), 93–98. https://doi.org/10.5487/tr.2012.28.2.093.

[52] Heitland, P.; Köster, H. D. Biomonitoring of 37 Trace Elements in Blood Samples from Inhabitants of Northern Germany by ICP–MS. Journal of Trace Elements in Medicine and Biology 2006, 20 (4), 253–262. https://doi.org/10.1016/j.jtemb.2006.08.001.

[53] Demirev, P. A. Dried Blood Spots: Analysis and Applications. Anal. Chem. 2012, 85 (2), 779–789. https://doi.org/10.1021/ac303205m.

[54] Guthrie, R.; Susi, A. A SIMPLE PHENYLALANINE METHOD FOR DETECTING PHENYLKETONURIA IN LARGE POPULATIONS OF NEWBORN INFANTS. Pediatrics 1963, 32 (3), 338–343. https://doi.org/10.1542/peds.32.3.338.

[55] Moreda-Piñeiro, J.; Cocho, J. A.; Couce, M. L.; Moreda-Piñeiro, A.; Bermejo-Barrera, P. Trace Elements in Dried Blood Spots as Potential Discriminating Features for Metabolic Disorder Diagnosis in Newborns. Metallomics 2021, 13 (5). https://doi.org/10.1093/mtomcs/mfab018.

[56] Chantada-Vázquez, M. P.; Moreda–Piñeiro, J.; Cantarero–Roldán, A.; Bermejo-Barrera, P.; Moreda-Piñeiro, A. Development of Dried Serum Spot Sampling Techniques for the Assessment of Trace Elements in Serum Samples by LA-ICP-MS. Talanta 2018, 186, 169–175. https://doi.org/10.1016/j.talanta.2018.04.049.

[57] Hsieh, H.-F.; Chang, W.-S.; Hsieh, Y.-K.; Wang, C.-F. Using Dried-Droplet Laser Ablation Inductively Coupled Plasma Mass Spectrometry to Quantify Multiple Elements in Whole Blood. Analytica Chimica Acta 2011, 699 (1), 6–10. https://doi.org/10.1016/j.aca.2011.05.002.

[58] Cizdziel, J. V. Determination of Lead in Blood by Laser Ablation ICP-TOF-MS Analysis of Blood Spotted and Dried on Filter Paper: A Feasibility Study. Anal Bioanal Chem 2007, 388 (3), 603–611. https://doi.org/10.1007/s00216-007-1242-y.

[59] Metarapi, D.; Schweikert, A.; Jerše, A.; Schaier, M.; van Elteren, J. T.; Koellensperger, G.; Theiner, S.; Šala, M. Semiquantitative Analysis for High-Speed Mapping Applications of Biological Samples Using LA-ICP-TOFMS. Anal. Chem. 2023, 95 (19), 7804–7812. https://doi.org/10.1021/acs.analchem.3c01439.

[60] Aramendía, M.; Rello, L.; Bérail, S.; Donnard, A.; Pécheyran, C.; Resano, M. Direct Analysis of Dried Blood Spots by Femtosecond-Laser Ablation-Inductively Coupled Plasma-Mass Spectrometry. Feasibility of Split-Flow Laser Ablation for Simultaneous Trace Element and Isotopic Analysis. J. Anal. At. Spectrom. 2015, 30 (1), 296–309. https://doi.org/10.1039/c4ja00313f.

[61] Li, F.; Lei, X.; Li, H.; Cui, H.; Guo, W.; Jin, L.; Hu, S. Direct Multi-Elemental Analysis of Whole Blood Samples by LA-ICP-MS Employing a Cryogenic Ablation Cell. J. Anal. At. Spectrom. 2023, 38 (1), 90–96. https://doi.org/10.1039/d2ja00282e.

[62] Guo, W. Quantitation And Imaging Analysis Of Biological Samples By LA-ICP-MS. At.Spectrosc. 2021, 42 (4). https://doi.org/10.46770/as.2021.068.

[63] Theiner, S.; Foels, E.; Koellensperger, G. Advancing Elemental Analysis by Collision/Reaction Cell Technology and Micro-Droplet Calibration for Bioimaging Applications by LA-ICP-TOFMS. Analytica Chimica Acta 2024, 1332, 343345. https://doi.org/10.1016/j.aca.2024.343345.
[64] Mervič, K.; Šala, M.; Theiner, S. Calibration Approaches in Laser Ablation Inductively Coupled Plasma Mass Spectrometry for Bioimaging Applications. TrAC Trends in Analytical Chemistry 2024, 172, 117574. https://doi.org/10.1016/j.trac.2024.117574.
[65] Grijalba, N.; Legrand, A.; Holler, V.; Bouvier-Capely, C. A Novel Calibration Strategy Based on Internal Standard–Spiked Gelatine for Quantitative Bio-Imaging by LA-ICP-MS: Application to Renal Localization and Quantification of Uranium. Anal Bioanal Chem 2020, 412 (13), 3113–3122. https://doi.org/10.1007/s00216-020-02561-4.
[66] Schweikert, A.; Theiner, S.; Šala, M.; Vician, P.; Berger, W.; Keppler, B. K.; Koellensperger, G. Quantification in Bioimaging by LA-ICPMS - Evaluation of Isotope Dilution and Standard Addition Enabled by Micro-Droplets. Analytica Chimica Acta 2022, 1223, 340200. https://doi.org/10.1016/j.aca.2022.340200.
[67] Mangone, A.; Mastrorocco, F.; Giannossa, L. C.; Comparelli, R.; Dell'Aglio, M.; De Giacomo, A. Nanoparticle Enhanced Laser Ablation Inductively Coupled Plasma Mass Spectrometry. Spectrochimica Acta Part B: Atomic Spectroscopy 2020, 163, 105731. https://doi.org/10.1016/j.sab.2019.105731.
[68] Moreda-Piñeiro, J.; Cantarero-Roldán, A.; Moreda-Piñeiro, A.; Cocho, J. Á.; Bermejo-Barrera, P. Laser Ablation Inductively Coupled Plasma Mass Spectrometry for Multi-Elemental Determination in Dried Blood Spots. J. Anal. At. Spectrom. 2017, 32 (8), 1500–1507. https://doi.org/10.1039/c7ja00168a.
[69] Šala, M.; Šelih, V. S.; van Elteren, J. T. Gelatin Gels as Multi-Element Calibration Standards in LA-ICP-MS Bioimaging: Fabrication of Homogeneous Standards and Microhomogeneity Testing. Analyst 2017, 142 (18), 3356–3359. https://doi.org/10.1039/c7an01361b.
[70] Sobac, B.; Brutin, D. Desiccation of a Sessile Drop of Blood: Cracks, Folds Formation and Delamination. Colloids and Surfaces A: Physicochemical and Engineering Aspects 2014, 448, 34–44. https://doi.org/10.1016/j.colsurfa.2014.01.076.
[71] Deegan, R. D.; Bakajin, O.; Dupont, T. F.; Huber, G.; Nagel, S. R.; Witten, T. A. Capillary Flow as the Cause of Ring Stains from Dried Liquid Drops. Nature 1997, 389 (6653), 827–829. https://doi.org/10.1038/39827.
[72] Mervič, K.; Šelih, V. S.; Šala, M.; van Elteren, J. T. Non-Matrix-Matched Calibration in Bulk Multi-Element Laser Ablation – Inductively Coupled Plasma – Mass Spectrometry Analysis of Diverse Materials. Talanta 2024, 271, 125712. https://doi.org/10.1016/j.talanta.2024.125712.
[73] Feng, E. Y.; Zelaya, R.; Holm, A.; Yang, A.-C.; Cargnello, M. Investigation of the Optical Properties of Uniform Platinum, Palladium, and Nickel Nanocrystals Enables Direct Measurements of Their Concentrations in Solution. Colloids and Surfaces A: Physicochemical and Engineering Aspects 2020, 601, 125007. https://doi.org/10.1016/j.colsurfa.2020.125007.
[74] De Giacomo, A.; Gaudiuso, R.; Koral, C.; Dell'Aglio, M.; De Pascale, O. Nanoparticle-Enhanced Laser-Induced Breakdown Spectroscopy of Metallic Samples. Anal. Chem. 2013, 85 (21), 10180–10187. https://doi.org/10.1021/ac4016165.

APPENDIX

Table S4.1. List of archaeological glass samples and associated contextual information.

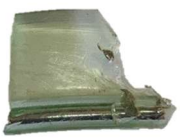
Sample number	Shape	Type	Color	N. fragments	Period dating
Bottles, Jugs					
1-2-3-4	Bottle	Isings 50/51	Transparent, Blue-green	4 handles	Roman early imperial
5	Bottle	Isings 104b	Transparent, Blue-green	1 bottom	Roman late imperial
6	Jug	1	Transparent, Green	1 edge	
Dishes, Bowls					
7	Dish	Isings 5 or 47	Transparent, Blue-green	1 bottom	Roman early imperial
8	Dish	Isings 97a	Opaque, Green	1 bottom	Roman late imperial
9	Bowl	Isings 69b	Transparent, Green	1 edge	Roman early imperial
10	Bowl	Isings 44	Transparent, Green	1 bottom	Roman early imperial
11	Bowl	Isings 20	Transparent, Green	1 bottom	Roman early imperial
12-13	Ribbed bowl	Isings 3b/52b	Transparent, Green	2 sides	Roman early-middle imperial
14	Bowl	Isings 108	Transparent, Green	1 bottom	Roman late imperial
15-16	Bowl	Isings 115	Transparent, Green-Colorless	2 edges	Late antique
17	Dish	1	Transparent, Blue-green	1 bottom	Roman early imperial
18	Dish	2	Opaque, Green	1 bottom	Roman early imperial
19	Dish	3	Opaque, Blue	1 edge	Roman middle imperial
20	Dish/Bowl	1	Transparent, Green	1 foot with two rebounds	Roman early imperial
21	Bowl	1	Transparent, Blue-green	1 bottom	Roman late imperial/ Late anqtique
22	Bowl	2	Transparent, Green	1 edge	Late anqtique
23	Bowl/Cup	1	Transparent, Yellow-green	1 edge	Late anqtique
Glasses					
24-25	Cup 1 and 2	Isings 37	Transparent, Green	2 bottoms	Roman early-middle imperial
26	Glass	Isings 33	Transparent, Colorless	1 bottom	Roman early imperial

27	Glass	Isings 21	Transparent, Colorless	1 side with diamond pattern	Roman early imperial
28	Glass	1	Transparent, Green	1 edge	
29	Glass	2	Transparent, Green	1 edge	
Glasses-Lamps					
30	Glass/Lamp	Isings 106b	Transparent, Green	1 bottom	Late antique
31-32-33	Lamp	Isings 134	Transparent, Green	3 edges	Late antique
34	Lamp	Uboldi III.1	Green	1 bottom	Late antique
35	Olla	Isings 67a	Transparent, Yellow-green	1 side	Roman early imperial
36	Bead	1	Opaque, Blue-Green	1 entire	

Table S4.2. Photographic inventory of archaeological glass samples, including a scale bar for reference.

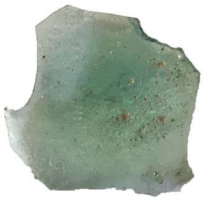
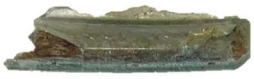


Sample number	Picture
1	
2	
3	

4	
5	
6	
7	
8	
9	
10	

11	
12	
13	
14	
15	
16	
17	
18	

19	
20	
21	
22	
23	
24	
25	
26	

27	
28	
29	
30	
31	
32	
33	
34	

35	
Bead	

Table S4.3. Oxide concentrations (in % [w/w]) for reference calibration standards.

	N612	*N610*	*DLH6*	*DLH7*	*DLH8*	*CMG-B*	*CMG-C*	*CMG-D*	*SGT2*	*SGT3*	*SGT4*	*SGT5*
Li2O	8.94E-03	1.04E-01	6.46E-05	0.014248	0.03123							
BeO	0.01040741	1.32E-01										
B2O3	1.10E-02	1.13E-01	0.000999	0.024158	0.037171				12.86	0.2	0.19	
Na2O	13.7	13.4	14.328	13.884	13.616	17	1.07	1.2	3.85	0.22	15.45	15.65
MgO	1.13E-02	7.16E-02	0.002354		0.022467	1.03	2.76	3.94		0.04		
Al2O3	2.03	1.95	1.634	1.673	1.755	4.36	8.70E-01	5.3	2.49	0.13	3.02	1.12
SiO2	7.21E+01	69.7	73.708	73.881	73.334	6.20E+01	3.43E+01	53.86	80.8	55.33	69.49	72.74
P2O5	1.07E-02	9.46E-02				8.20E-01	1.40E-01	3.93				
K2O	8.78E-03	6.54E-02		0.006795	0.027926	1	2.84	11.3	0.23	11.12	0.57	0.42
CaO	11.9	11.4	10.269	10.179	10.613	8.56	5.07	14.8	0.2	0.1	4.24	
Sc2O3	6.12E-03	6.98E-02	4.6E-05	0.0102	0.022395							
TiO2	7.34E-03	7.54E-02				8.90E-02	7.90E-01	3.80E-01	3.50E-02	2.00E-02	4.10E-02	3.40E-02
V2O5	6.93E-03	8.03E-02		0.012891	0.02707	3.60E-02						
Cr2O3	5.32E-03	5.96E-02	0.000512	0.008711	0.017523							
MnO	5.00E-03	5.73E-02	0.000116	0.008664	0.018646	2.50E-01		5.50E-01				
Fe2O3	7.29E-03	6.55E-02				3.40E-01	3.40E-01	5.20E-01	7.50E-02	1.60E-02	9.90E-02	4.30E-02
CoO	4.51E-03	5.21E-02	3.81E-05	0.008518	0.017952	4.60E-02	1.80E-01	2.30E-02				
NiO	4.94E-03	5.84E-02	0.00028	0.007839	0.017536	9.90E-02						
CuO	4.73E-03	5.52E-02	0.000839	0.008662	0.018863	2.66E+00	1.13E+00	3.80E-01				
ZnO	4.87E-03	5.73E-02	9.96E-05	0.007667	0.019216	1.90E-01	5.20E-02	1.00E-01			3.28E+00	
Ga2O3	4.96E-03	5.82E-02	2.69E-05	0.008952	0.019115							
As2O5	5.48E-03	4.99E-02								0.67		
SeO2	2.29E-03	1.94E-02										

Rb2O	3.43E-03	4.66E-02	4.37E-05	0.007328	0.015476				
SrO	9.27E-03	6.10E-02	0.000189	0.008514	0.017431	1.90E-02	2.90E-01	5.70E-02	
Y2O3	4.86E-03	5.87E-02	0.000317	0.029943	0.020571				
ZrO2	5.12E-03	6.05E-02	0.000216	0.009671	0.018505				
Nb2O5	5.56E-03	6.65E-02	4.29E-05	0.01103	0.022361				
MoO3	5.61E-03	6.26E-02	0.000599	0.009468	0.018367				
Ag2O	2.53E-03	2.88E-02	1.07E-05	0.008165	0.010786				
CdO	3.21E-03	3.08E-02		0.008121	0.017362				
In2O3	4.70E-03	5.25E-02	1.21E-05	0.008645	0.018052				
SnO2	4.90E-03	5.46E-02				4.00E-02	1.90E-01	1.00E-01	
Sb2O5	4.61E-03	5.26E-02				4.60E-01	3.00E-02	9.70E-01	
BaO	4.39E-03	5.05E-02	4.47E-05	0.007929	0.01617	1.20E-01	11.4	5.10E-01	
La2O3	4.22E-03	5.16E-02	2.93E-05	0.008291	0.016383				
CeO2	4.72E-03	5.56E-02	1.84E-05	0.008622	0.017171				
Pr2O3	4.44E-03	5.24E-02	1.17E-05	0.008824	0.017028				
Nd2O3	4.14E-03	5.02E-02	0.000117	0.008023	0.016513				
Sm2O3	4.37E-03	5.25E-02	1.16E-05	0.007514	0.015388				
Eu2O3	4.12E-03	5.18E-02	1.16E-05	0.008568	0.016905				
Gd2O3	4.35E-03	5.18E-02	1.15E-05	0.008726	0.017025				
Tb2O3	4.33E-03	5.03E-02	0.000104	0.00861	0.017692				
Dy2O3	4.07E-03	5.02E-02	1.15E-06	0.00855	0.017089				
Ho2O3	4.39E-03	5.14E-02	1.15E-05	0.008672	0.017561				
Er2O3	4.35E-03	5.20E-02	1.14E-05	0.00861	0.017174				
Tm2O3	4.20E-03	4.97E-02	1.14E-06	0.008566	0.017371				
Yb2O3	4.46E-03	5.12E-02	1.14E-05	0.008756	0.017365				
Lu2O3	4.38E-03	5.19E-02	0.000114	0.00904	0.017944				
Au2O3	5.35E-04	2.65E-03							
PbO	4.15E-03	4.59E-02	5.39E-05	0.006905	0.012495	6.10E-01	36.7	4.80E-01	3.17E+01
Bi2O3	3.37E-03	4.28E-02	7.8E-05	0.007436	0.01514				
ThO2	4.30E-03	5.20E-02							
UO2	4.24E-03	5.24E-02	1.13E-06	0.008541	0.016924				

Table S4.4. Oxide concentrations (in % [w/w]) for archaeological glass fragments with relative standard deviations.

	Ag2O	Al2O3	As2O5	Au2O3	B2O3	BaO	BeO	Bi2O3	CaO	CdO	CeO2	CoO	Cr2O3	CuO	Dy2O3	Er2O3	Eu2O3	Fe2O3	Ga2O3	Gd2O3	Ho2O3	In2O3	K2O	La2O3	Li2O	Lu2O3	MgO
G1	4.96E-05	2.261623	0.000896	3.74E-05	0.037163	0.033545	0.000584	0.000325	6.438465	0.000262	0.001775	0.00168	0.002328	0.009116	0.000148	9.12E-05	4.74E-05	0.458818	0.000332	0.000158	2.99E-05	1.15E-05	0.616151	0.000841	0.000075	1.51E-05	0.696306
Std	5.72E-05	0.461671	0.000442	3.89E-05	0.00707	0.008749	0.001146	0.002266	1.063	0.000 9	0.000448	0.004802	0.000391	0.002341	7.27E-05	4.96E-05	2.51E-05	0.105 78	0.000134	9.04E-05	1.64E-05	8.21E-06	0.151958	0.000162	0.000393	1.18E-05	0.169532
G2	5.08E-05	2.657354	0.000493	4.73E-05	0.025 18	0.024083	0.000785	6.19E-05	7.739315	0.000299	0.001488	0.000513	0.002643	0.001237	0.000172	0.000106	5.27E-05	0.296525	0.000379	0.000214	3.56E-05	8.65E-06	0.453657	0.000834	0.000837	2.48E-05	0.498355
Std	0.000355	0.000582	0.00041	4.88E-05	0.005 79	0.003659	0.001703	0.000243	1.065203	0.000909	0.000256	0.000366	0.000392	0.000287	9.47E-05	5.66E-05	3.06E-05	0.051856	0.000148	0.000127	1.96E-05	1.71E-05	0.076703	0.000139	0.000295	2.31E-05	0.078475
G3	7.18E-05	3.705211	0.000726	5.04E-05	0.024186	0.047956	0.000864	6.10E-05	10.91504	0.000319	0.003141	0.001454	0.002768	0.049913	0.000274	0.000163	4.89E-05	0.833676	0.000527	0.000 26	4.75E-05	2.37E-05	1.356082	0.001006	0.001442	2.53E-05	0.898649
Std	6.87E-05	0.905011	0.000518	5.43E-05	0.007635	0.015892	0.001324	0.000205	7.093146	0.000821	0.001069	0.001343	0.000521	0.037639	0.000131	9.23E-05	4.95E-05	0.298 04	0.000294	0.000186	3.07E-05	2.39E-05	0.577024	0.000413	0.000642	2.28E-05	0.360457
G4	7.65E-05	2.369859	0.000752	5.76E-05	0.037212	0.029397	0.000934	0.000121	6.985662	0.000373	0.001363	0.001 17	0.003024	0.040115	0.000158	9.93E-05	4.89E-05	0.451867	0.000344	0.000197	3.48E-05	2.52E-05	0.687232	0.000866	0.001269	2.06E-05	0.633383
Std	0.000243	7.91864	0.000501	7.91E-05	0.006 93	0.004385	0.002542	0.000308	0.885913	0.001104	0.000224	0.000 77	0.004551	0.004469	9.37E-05	6.65E-05	3.23E-05	0.063 54	0.000145	0.000126	2.21E-05	1.61E-05	0.085019	0.000158	0.000413	2.19E-05	0.084057
G5	8.33E-05	5.325798	0.000622	4.88E-05	0.060648	0.061158	0.001024	0.000206	10.89574	0.000317	0.002861	0.001 51	0.002357	0.002539	0.000 35	0.000222	7.57E-05	0.665585	0.000536	0.000395	4.26E-05	7.82E-06	1.014609	0.001098	0.001576	1.98E-05	1.321727
Std	0.000166	5.136732	0.000507	6.99E-05	0.036 94	0.062972	0.001995	0.001509	8.409653	0.000815	0.002973	0.001371	0.000977	0.003025	0.000351	0.000233	7.54E-05	0.827333	0.000428	0.000374	3.49E-05	1.21E-05	1.252457	0.000489	0.001841	1.64E-05	1.648231
G6	4.45E-05	2.727915	0.000468	4.18E-05	0.040197	0.028309	0.000726	0.000031	8.577412	0.000281	0.000661	0.000548	0.003955	0.001413	0.000218	0.000117	5.68E-05	0.374744	0.000039	0.000212	4.13E-05	9.51E-06	0.586655	0.000982	0.000966	2.24E-05	0.678703
Std	9.74E-05	0.554923	0.000366	4.46E-05	0.009024	0.006186	0.001628	0.000787	1.367263	0.000907	0.000348	0.000401	0.001254	0.000502	0.000104	6.55E-05	3.03E-05	0.094252	0.000148	0.000121	2.19E-05	1.97E-05	0.164614	0.000018	0.000369	1.78E-05	0.150027
G7	5.53E-05	2.477848	0.000684	4.54E-05	0.038897	0.026 03	0.000862	0.000137	7.640249	0.000316	0.001436	0.001345	0.002718	0.063847	0.000159	9.40E-05	4.80E-05	0.383405	0.000358	0.000185	3.36E-05	2.84E-05	0.675648	0.000851	0.001 01	2.19E-05	0.604954
Std	8.71E-05	0.252246	0.000439	5.18E-05	0.006 83	0.002959	0.001878	0.000549	0.891724	0.000934	0.000183	0.000496	0.000353	0.007 37	8.07E-05	5.13E-05	2.63E-05	0.050038	0.000139	0.000119	1.86E-05	1.60E-05	0.078845	0.000121	0.000 35	2.28E-05	0.067384
G8	4.61E-05	2.100377	0.000599	3.23E-05	0.036 55	0.027063	0.000601	2.94E-05	6.807292	0.000 27	0.000417	0.001514	0.002535	0.012572	0.000 14	8.62E-05	4.42E-05	0.417358	0.000315	0.000161	3.01E-05	1.48E-05	0.736535	0.000825	0.000924	1.77E-05	0.685216
Std	7.32E-05	0.527383	0.000353	3.75E-05	0.007 262	0.007826	0.001365	0.000195	1.364834	0.000371	0.000426	0.000 429	0.000429	0.002873	7.11E-05	5.05E-05	2.43E-05	0.126058	0.000124	0.000 -05	8.64E-05	1.06E-05	0.219937	0.000123	0.000369	1.51E-05	0.205957
G9	8.82E-05	3.317709	0.000443	3.43E-05	0.037 92	0.081713	0.000879	0.000022	8.845 85	0.000 21	0.001645	0.001 186	0.002451	0.006774	0.000 24	0.000144	5.34E-05	0.571713	0.000406	0.000 25	3.94E-05	1.35E-05	0.525737	0.001048	0.001269	1.98E-05	0.621907
Std	0.000284	1.151049	0.000392	4.06E-05	0.009488	0.036491	0.000875	0.001485	2.260019	0.000634	0.000674	0.001 99	0.002207	0.043131	0.000131	8.76E-05	3.07E-05	0.268141	0.000163	0.000146	1.81E-05	4.73E-05	0.240087	0.000204	0.000704	1.49E-05	0.316764
G10	0.000101	2.131265	0.000494	8.00E-05	0.048 15	0.026469	0.001504	4.94E-05	6.094147	0.000509	0.001366	0.000 2	0.003673	0.010854	0.000 18	0.000115	5.50E-05	0.419799	0.000382	0.000225	3.72E-05	1.93E-05	0.941803	0.000803	0.000527	2.90E-05	0.580532
Std	0.000 17	0.345639	0.000826	8.01E-05	0.011662	0.005092	0.005086	0.000112	0.967578	0.001782	0.000281	0.000 069	0.002718	0.002857	0.000119	8.14E-05	4.22E-05	0.088634	0.000205	0.000181	2.92E-05	1.94E-05	0.226163	0.000181	0.000628	3.47E-05	0.113006
G11	7.23E-05	2.139439	0.000213	3.23E-05	0.048444	0.021043	0.000532	3.51E-05	5.872438	0.000208	0.001478	0.002 094	0.003499	0.029656	0.000 13	7.35E-05	4.12E-05	0.494415	0.000403	0.000137	3.08E-05	3.13E-05	0.650809	0.001037	0.001049	1.86E-05	0.540857
Std	8.01E-05	0.323315	0.000496	2.71E-05	0.007694	0.003311	0.000085	6.28E-05	0.822908	0.000 67	0.000279	0.000 511	0.000497	0.004473	6.37E-05	4.17E-05	2.24E-05	0.100861	0.000143	0.000 -05	1.73E-05	1.30E-05	0.119691	0.000177	0.000 37	1.51E-05	0.086549
G12	4.60E-05	2.390912	0.000522	4.70E-05	0.027192	0.031456	0.000748	0.000186	6.999676	0.000306	0.001 43	0.002 151	0.002272	0.002376	0.000157	9.14E-05	5.47E-05	0.282841	0.000379	0.000177	3.14E-05	8.70E-06	0.434271	0.000822	0.000806	1.86E-05	0.480485
Std	0.000172	0.317493	0.000354	4.68E-05	0.005687	0.004569	0.002053	0.000716	1.020505	0.000843	0.000219	0.001 03	0.000352	0.000489	8.00E-05	5.27E-05	2.91E-05	0.046462	0.000148	0.000114	1.65E-05	1.12E-05	0.066491	0.000134	0.000 28	1.53E-05	0.063162
G13	6.45E-05	2.769022	0.000 67	4.57E-05	0.032555	0.030099	0.000696	5.09E-05	7.298716	0.000 34	0.000666	0.001 701	0.003051	0.019468	0.000196	0.000109	5.44E-05	0.425089	0.000423	0.000211	3.52E-05	1.94E-05	0.683362	0.000967	0.001191	2.32E-05	0.610409
Std	9.63E-05	0.552021	0.000439	5.14E-05	0.007625	0.008841	0.001595	0.000114	1.415931	0.000809	0.000501	0.000 693	0.000648	0.004102	0.000108	6.04E-05	2.86E-05	0.100729	0.000 18	0.000137	1.66E-05	1.36E-05	0.189275	0.000421	0.000	2.18E-05	0.135776
G14	5.10E-05	2.789826	0.000615	4.66E-05	0.029235	0.030861	0.000843	8.22E-05	10.06505	0.000321	0.001665	0.000 93	0.002823	0.001182	0.000199	0.000117	5.71E-05	0.353608	0.000419	0.000209	4.07E-05	8.42E-06	0.530219	0.001021	0.000033	2.33E-05	0.716868
Std	0.000174	0.455981	0.000412	5.49E-05	0.007 73	0.006212	0.002253	0.000186	1.947705	0.000939	0.000339	0.000 315	0.000577	0.000 31	0.000107	6.64E-05	3.34E-05	0.079 82	0.000168	0.000121	2.42E-05	2.07E-05	0.104415	0.000209	0.000418	1.81E-05	0.130359
G15	3.37E-05	1.659 39	0.000352	2.94E-05	0.019664	0.022422	0.000 51	1.43E-05	6.459032	0.000187	0.001258	0.000 164	0.001967	0.000516	0.000108	6.37E-05	3.93E-05	0.206204	0.000 29	0.000117	2.22E-05	5.28E-05	0.307039	0.000673	0.000564	1.37E-05	0.401447
Std	0.000119	0.428087	0.000273	3.34E-05	0.004983	0.007076	0.001305	2.52E-05	1.587148	0.000 53	0.000344	9.55E-05	0.000399	0.000263	5.84E-05	3.62E-05	2.49E-05	0.065747	0.000118	7.73E-05	1.37E-05	1.23E-05	0.107256	0.000135	0.000247	1.29E-05	0.125717

G16	3.96E-05	2.315697	0.000933	3.20E-05	0.026504	0.032128	0.000675	5.72E-05	7.419218	0.000209	0.001378	0.001285	0.002282	0.001448	0.000146	8.83E-05	5.22E-05	0.317376	0.000331	0.000168	3.35E-05	6.65E-06	0.417975	0.00085	0.001016	1.67E-05	0.620423
Std	0.000103	0.474629	0.000447	3.76E-05	0.005441	0.007546	0.001722	0.000154	1.457206	0.000662	0.000317	0.000767	0.000348	0.000408	7.54E-05	5.03E-05	2.73E-05	0.078797	0.000134	9.14E-05	1.61E-05	1.04E-05	0.097554	0.000157	0.000358	1.42E-05	0.138478
G17	6.48E-05	2.552869	0.000394	3.33E-05	0.02114	0.0212	0.000625	0.000174	7.136857	0.000241	0.001281	0.000381	0.002289	0.000847	0.000167	9.96E-05	4.41E-05	0.24151	0.000326	0.000173	3.48E-05	8.57E-06	0.379944	0.000801	0.000691	1.73E-05	0.44065
Std	0.000156	0.394599	0.000285	4.01E-05	0.004012	0.003564	0.001504	0.000743	0.848412	0.00065	0.000206	0.000335	0.000346	0.000465	7.91E-05	5.27E-05	2.30E-05	0.046298	0.000123	8.82E-05	1.73E-05	1.94E-05	0.065441	0.000111	0.00025	1.40E-05	0.108701
G18	0.000505	2.459624	0.001814	4.74E-05	0.044642	0.046326	0.000773	6.46E-05	7.614072	0.000261	0.001764	0.002282	0.003778	1.692607	0.000169	0.000104	4.70E-05	1.394487	0.00045	0.000178	3.64E-05	0.000636	1.639799	0.001007	0.001613	2.21E-05	2.407854
Std	0.00016	0.284094	0.000659	4.59E-05	0.008537	0.007029	0.001052	5.37E-05	1.088733	0.000401	0.000585	0.000944	0.000465	0.247408	8.59E-05	5.60E-05	2.47E-05	0.198545	0.000149	0.000103	1.78E-05	0.000122	0.25285	0.000199	0.000463	1.81E-05	0.305591
G19	5.44E-05	2.397693	0.001047	3.65E-05	0.029694	0.032712	0.00064	2.43E-05	7.521919	0.000268	0.001512	0.001895	0.00233	0.11187	0.000176	9.63E-05	4.96E-05	0.593521	0.00053	0.000179	3.28E-05	3.09E-05	0.709168	0.00082	0.000951	1.81E-05	0.60518
Std	0.000112	0.383135	0.000503	3.85E-05	0.006964	0.006863	0.001511	4.79E-05	1.289171	0.000892	0.000353	0.000146	0.000399	0.023752	9.31E-05	5.39E-05	2.77E-05	0.11403	0.000176	9.89E-05	1.71E-05	1.56E-05	0.119758	0.000157	0.000361	1.49E-05	0.12066
G20	5.09E-05	2.676228	0.000544	3.76E-05	0.039212	0.033023	0.000714	0.000209	7.515514	0.000235	0.001629	0.001847	0.002856	0.030681	0.000183	0.000108	4.76E-05	0.571971	0.000379	0.000209	3.09E-05	2.04E-05	0.80885	0.000904	0.00111	1.99E-05	0.66059
Std	9.00E-05	0.506937	0.000324	3.77E-05	0.010184	0.005769	0.00141	0.000729	1.24089	0.000722	0.000287	0.000635	0.000523	0.00534	8.72E-05	5.78E-05	2.68E-05	0.225444	0.000142	0.000111	1.56E-05	1.35E-05	0.173502	0.000137	0.000399	1.66E-05	0.128258
G21	5.45E-05	2.804995	0.000773	4.34E-05	0.038872	0.030863	0.000734	7.60E-05	8.475597	0.000275	0.001731	0.001551	0.003243	0.013127	0.000177	0.000108	5.13E-05	0.578349	0.000424	0.000197	3.69E-05	1.75E-05	0.859793	0.001002	0.001144	2.06E-05	0.98746
Std	9.94E-05	0.556681	0.000469	4.51E-05	0.009697	0.009299	0.001935	0.000315	2.174328	0.000786	0.000482	0.000504	0.000593	0.003602	9.46E-05	6.09E-05	3.08E-05	0.165748	0.000173	0.000121	1.89E-05	1.25E-05	0.22633	0.000211	0.00043	1.80E-05	0.26343
G22	2.54E-05	2.388913	0.000354	3.32E-05	0.034764	0.021899	0.000531	8.28E-05	8.096361	0.000157	0.001036	0.00142	0.002198	0.012769	0.00014	7.54E-05	3.30E-05	0.281487	0.000357	0.000169	2.22E-05	1.29E-05	0.556045	0.000865	0.000509	1.42E-05	0.392662
Std	4.34E-05	0.464612	0.000198	3.51E-05	0.009968	0.009378	0.000951	0.000366	1.384835	0.00038	0.000035	0.000267	0.000331	0.003117	6.80E-05	4.27E-05	1.63E-05	0.143019	0.000125	8.61E-05	1.17E-05	7.98E-06	0.272133	0.000124	0.000355	1.06E-05	0.187575
G23	5.33E-05	2.762549	0.000453	4.69E-05	0.067222	0.030304	0.000733	0.000198	8.753025	0.000292	0.001509	0.001412	0.003459	0.001294	0.000194	0.000111	4.43E-05	0.335754	0.000409	0.000206	3.19E-05	8.55E-06	0.471245	0.000936	0.000842	2.03E-05	0.60149
Std	0.000131	0.476352	0.000404	5.47E-05	0.014671	0.010026	0.002993	0.000764	1.857602	0.000845	0.000598	0.000712	0.003134	0.000733	0.00011	6.95E-05	2.80E-05	0.111128	0.000183	0.000015	2.00E-05	1.87E-05	0.118538	0.000261	0.000431	2.03E-05	0.190078
G24	5.42E-05	2.337718	0.000551	4.34E-05	0.060674	0.031755	0.000754	4.62E-05	6.595469	0.000322	0.001287	0.001417	0.002384	0.00132	0.000156	8.95E-05	4.82E-05	0.281023	0.000363	0.000172	3.11E-05	8.22E-06	0.559031	0.000789	0.000852	2.00E-05	0.51587
Std	0.000164	0.22358	0.000359	4.91E-05	0.00938	0.003529	0.001884	0.000125	0.764346	0.000913	0.000176	0.000667	0.000323	0.000259	7.98E-05	5.86E-05	2.96E-05	0.035238	0.000151	0.000011	1.89E-05	2.03E-05	0.066326	0.000115	0.000329	2.04E-05	0.063247
G25	4.63E-05	1.77626	0.000829	3.72E-05	0.036294	0.02061	0.000684	0.00034	6.165006	0.000242	0.001193	0.001903	0.002658	0.023128	0.000116	6.89E-05	3.90E-05	0.328979	0.000324	0.000136	2.85E-05	1.83E-05	0.559732	0.00076	0.000851	1.86E-05	0.49368
Std	6.83E-05	0.318466	0.000446	4.21E-05	0.007107	0.003585	0.001741	0.0025	1.087619	0.000759	0.000224	0.000615	0.000439	0.000111	7.15E-05	4.31E-05	2.09E-05	0.066159	0.000131	9.24E-05	1.72E-05	1.26E-05	0.117646	0.00012	0.000321	1.77E-05	0.093612
G26	4.86E-05	2.521001	0.002112	4.14E-05	0.039521	0.029519	0.000697	2.97E-05	6.8632	0.000306	0.001428	0.000844	0.002577	0.002118	0.000183	0.000112	5.03E-05	0.376796	0.000364	0.000191	3.71E-05	1.04E-05	0.516507	0.000936	0.000971	2.21E-05	0.59049
Std	7.25E-05	0.231572	0.000697	4.32E-05	0.006308	0.003374	0.001514	6.12E-05	0.662342	0.000853	0.000176	0.000163	0.000373	0.003139	8.22E-05	6.08E-05	2.76E-05	0.049791	0.000134	0.000111	1.84E-05	1.19E-05	0.061229	0.000111	0.000329	1.50E-05	0.077549
G27	5.05E-05	2.658623	0.001449	3.67E-05	0.046127	0.03088	0.000544	0.000153	7.294461	0.000223	0.001914	0.000184	0.002181	0.001107	0.000192	0.000116	5.37E-05	0.415904	0.000354	0.000207	3.06E-05	9.25E-06	0.783817	0.000846	0.001126	1.87E-05	0.69285
Std	7.95E-05	0.855925	0.000613	4.10E-05	0.012961	0.011043	0.001067	0.000647	2.368612	0.000531	0.000656	8.18E-05	0.000513	0.000464	9.60E-05	8.03E-05	3.03E-05	0.137452	0.000184	0.000117	1.86E-05	1.70E-05	0.278924	0.000152	0.000622	1.86E-05	0.266231
G28	5.69E-05	2.888371	0.000567	3.33E-05	0.034156	0.023435	0.00058	0.000261	6.272089	0.000214	0.001509	0.002233	0.002925	0.019905	0.000137	8.02E-05	4.40E-05	0.496842	0.000404	0.000144	2.81E-05	1.55E-05	1.069429	0.000838	0.001223	1.57E-05	0.56702
Std	0.000107	0.849998	0.00059	4.01E-05	0.006869	0.004839	0.000953	0.001112	1.202754	0.000497	0.000797	0.005561	0.001413	0.005802	7.29E-05	4.60E-05	2.52E-05	0.238732	0.00017	8.59E-05	1.54E-05	1.11E-05	0.265341	0.000389	0.000569	1.30E-05	0.130816
G29	3.69E-05	2.701012	0.000756	3.18E-05	0.0384	0.029716	0.000607	0.000794	7.045192	0.000222	0.001638	0.001295	0.002548	0.013876	0.000206	0.000125	5.33E-05	0.504851	0.000352	0.000224	4.07E-05	1.35E-05	0.783529	0.000988	0.001083	1.89E-05	0.79680
Std	5.47E-05	0.555851	0.000376	3.50E-05	0.00727	0.006685	0.00101	0.006325	1.220678	0.000571	0.00036	0.000293	0.000363	0.003238	8.26E-05	5.80E-05	2.76E-05	0.130878	0.000118	0.00001	1.78E-05	8.98E-06	0.202935	0.000156	0.000387	1.42E-05	0.207865
G30	6.38E-05	2.457185	0.001422	4.65E-05	0.055770	0.030008	0.000778	0.000102	7.136231	0.000283	0.001632	0.001559	0.003092	0.009563	0.000185	0.000113	4.72E-05	0.757114	0.000402	0.000202	3.77E-05	1.92E-05	0.892793	0.000971	0.001099	2.42E-05	1.52816
Std	0.000136	0.277862	0.000589	4.52E-05	0.009143	0.004908	0.001523	0.000459	0.984974	0.000861	0.000303	0.000559	0.000525	0.001492	9.08E-05	6.61E-05	2.69E-05	0.121615	0.000146	0.000119	2.05E-05	1.30E-05	0.131734	0.000177	0.000487	2.01E-05	0.206231
G31	4.16E-05	1.782584	0.000636	3.24E-05	0.03028	0.034637	0.000588	8.93E-05	5.566963	0.000194	0.001702	0.000099	0.002027	0.050239	0.000148	8.60E-05	5.88E-05	0.465706	0.00024	0.000162	3.35E-05	2.23E-05	0.648305	0.000841	0.00105	1.67E-05	0.69236

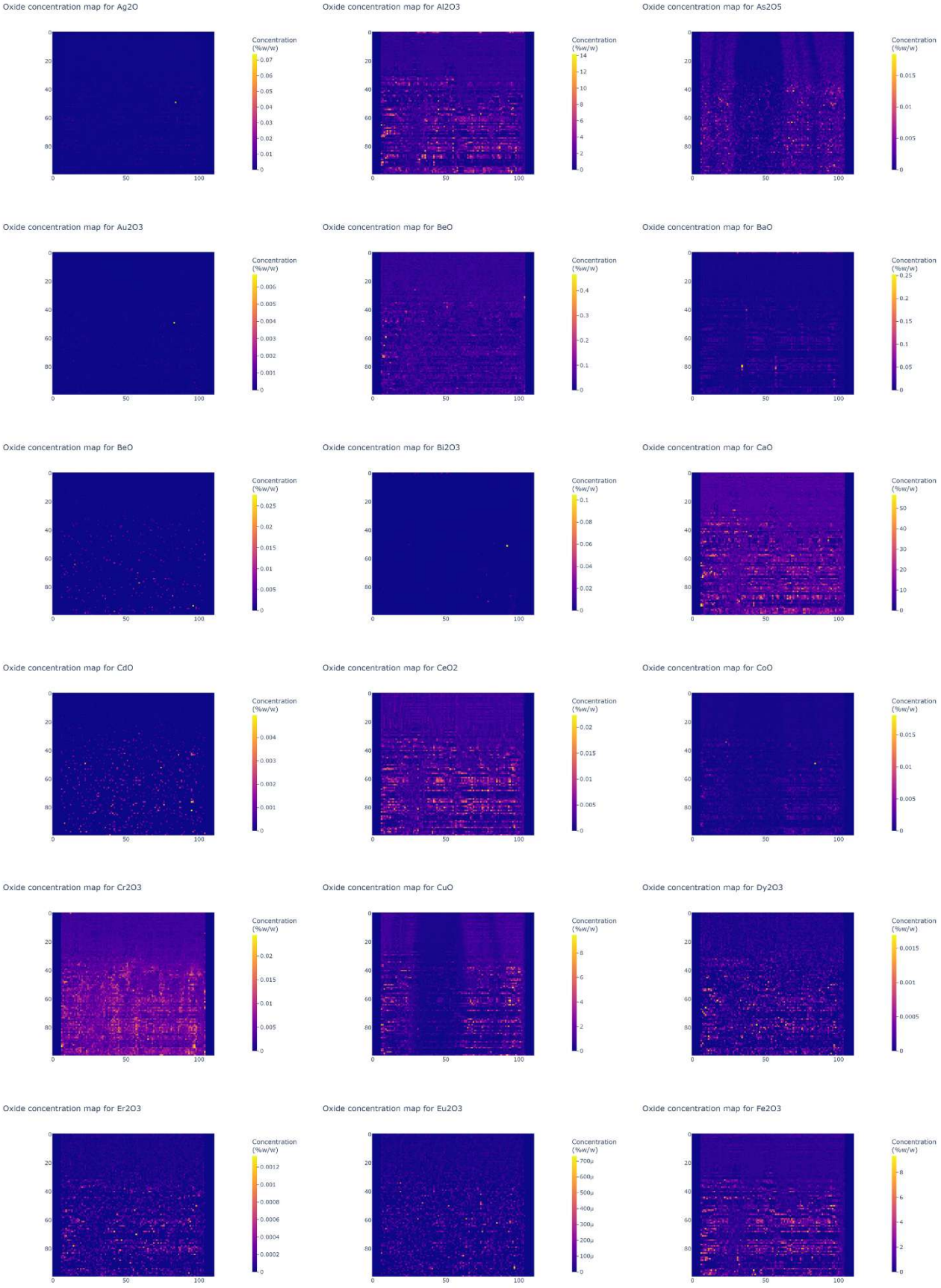
Std	4.96E-05	0.817095	0.000383	3.31E-05	0.008973	0.015299	0.001036	0.000391	2.343 78	0.000583	0.000667	0.000479	0.000508	0.023344	0.000 1	6.09E-05	3.34E-05	0.216282	0.000131	0.000124	1.71E-05	1.27E-05	0.317157	0.000145	0.000614	1.45E-05	0.300985
G32	5.12E-05	2.315921	0.001185	3.64E-05	0.041166	0.033956	0.000657	3.97E-05	7.252897	0.000232	0.001512	0.001352	0.002555	0.00699	0.000165	9.43E-05	5.20E-05	0.442713	0.000324	0.000188	3.26E-05	1.21E-05	0.671922	0.000928	0.000977	1.78E-05	0.684448
Std	9.11E-05	0.564307	0.000526	3.65E-05	0.008366	0.016 74	0.001253	0.000125	1.275167	0.000689	0.000437	0.000536	0.000428	0.001526	8.33E-05	5.31E-05	2.96E-05	0.137071	0.000 14	0.000115	1.85E-05	1.01E-05	0.228521	0.000278	0.000467	1.52E-05	0.216223
G33	4.89E-05	2.316707	0.000426	4.39E-05	0.031971	0.029379	0.000577	1.43E-05	7.482767	0.000246	0.001561	0.000 6	0.002333	0.004504	0.000159	0.000 1	5.05E-05	0.334939	0.000354	0.000178	3.23E-05	9.07E-06	0.582 72	0.000831	0.000869	1.84E-05	0.591843
Std	0.000172	0.402 88	0.000302	4.68E-05	0.008 09	0.006107	0.001435	2.85E-05	1.534172	0.000948	0.000373	0.000166	0.000 43	0.001011	8.87E-05	4.01E-05	2.32E-05	0.069773	0.000148	9.67E-05	1.77E-05	1.07E-05	0.127237	0.000135	0.000348	1.77E-05	0.133 12
G34	0.000215	0.887527	0.029539	3.26E-05	0.023579	0.050127	0.000547	5.17E-05	11.58 23	0.000246	0.001115	0.001938	0.003 58	0.006701	9.18E-05	5.93E-05	2.45E-05	0.214456	0.000202	0.000 1	2.01E-05	1.27E-05	0.215729	0.000619	0.001802	1.32E-05	1.305442
Std	0.000117	0.194763	0.006006	3.99E-05	0.005345	0.011823	0.001373	0.000154	2.042278	0.000453	0.000283	0.001562	0.000582	0.001759	5.91E-05	4.21E-05	1.83E-05	0.058 94	9.58E-05	7.86E-05	1.33E-05	9.60E-06	0.111479	0.000104	0.000634	1.29E-05	0.356175
G35	4.72E-05	2.585221	0.000489	3.04E-05	0.038828	0.032496	0.000593	0.000213	7.678385	0.000227	0.001573	0.001395	0.002121	0.010878	0.000167	9.84E-05	5.41E-05	0.368233	0.000321	0.000182	3.62E-05	9.34E-06	0.513478	0.000966	0.000918	1.83E-05	0.572553
Std	5.93E-05	0.756768	0.000284	3.24E-05	0.007404	0.010572	0.001081	0.001658	1.591411	0.000672	0.000486	0.000398	0.000347	0.003283	8.43E-05	5.18E-05	2.98E-05	0.124742	0.000126	0.000101	1.82E-05	8.87E-06	0.184075	0.000137	0.000411	1.50E-05	0.196412
Bead	0.000295	1.151323	0.001 63	6.40E-05	0.031602	0.010518	0.000543	0.001356	5.543367	0.000229	0.001944	0.000384	0.003031	0.589 3	6.40E-05	3.47E-05	2.24E-05	0.539447	0.000195	8.72E-05	1.32E-05	3.22E-05	1.623581	0.000412	0.000859	1.17E-05	2.253546
Std	0.000161	0.860818	0.001 21	0.00027	0.009437	0.014317	0.001258	0.004575	1.727859	0.000521	0.001653	0.000162	0.000872	0.488459	5.51E-05	3.30E-05	2.02E-05	0.236676	0.000121	9.59E-05	1.13E-05	1.73E-05	0.720233	0.000233	0.000443	1.79E-05	1.010 95

	MnO	MoO3	Na2O	Nb2O5	Nd2O3	NiO	P2O5	PbO	Pr2O3	Rb2O	Sb2O5	Sc2O3	SeO2	SiO2	Sm2O3	SnO2	SrO	Tb2O3	ThO2	TiO2	Tm2O3	UO2	V2O5	Y2O3	Yb2O3	ZnO	ZrO2
G1	0.738707	0.000323	16.91731	0.000317	0.000897	0.001526	0.29271	0.051265	0.000199	0.001096	0.171757	0.000438	0.240389	70.86577	0.000178	0.002537	0.048598	2.40E-05	0.000168	0.08989	1.53E-05	0.000103	0.003054	0.001012	8.58E-05	0.002577	0.008129
Std	0.163694	0.000189	3.83932	0.000111	0.000289	0.000419	0.059803	0.0116	5.48E-05	0.000296	0.02855	0.000142	0.029517	3.877069	9.40E-05	0.000651	0.008086	1.46E-05	6.46E-05	0.026493	1.30E-05	3.69E-05	0.000718	0.000283	6.31E-05	0.000888	0.002147
G2	0.201549	0.000187	16.26826	0.000215	0.000802	0.000824	0.251463	0.001501	0.000193	0.000793	0.002371	0.000423	0.339477	71.11108	0.000185	0.000301	0.04769	2.74E-05	0.00014	0.058855	2.17E-05	0.000142	0.001507	0.001008	0.000131	0.001445	0.005966
Std	0.021883	0.000199	2.033512	8.06E-05	0.000205	0.000341	0.034002	0.000335	4.81E-05	0.000206	0.000445	0.00014	0.040417	2.646096	0.000104	0.000106	0.005895	1.77E-05	5.96E-05	0.011468	1.92E-05	4.75E-05	0.000332	0.000214	9.40E-05	0.000613	0.001089
G3	0.466468	0.000224	14.0893	0.000459	0.001566	0.000859	0.415758	0.03044	0.000266	0.001998	0.032365	0.000596	0.327355	66.57788	0.000227	0.006803	0.038894	3.90E-05	0.000358	0.142473	2.12E-05	0.000181	0.002015	0.001481	0.000178	0.006112	0.012792
Std	0.230705	0.000201	7.248889	0.000201	0.000605	0.000707	0.152725	0.014551	0.000121	0.000842	0.007823	0.00035	0.067187	8.667115	0.000112	0.005371	0.012857	2.02E-05	0.000131	0.054883	1.79E-05	7.15E-05	0.000767	0.00072	0.000129	0.00838	0.003754
G4	0.456631	0.000283	15.38878	0.000309	0.000817	0.001095	0.404626	0.023827	0.000186	0.001043	0.045357	0.000505	0.402559	71.87201	0.000199	0.005768	0.048388	2.98E-05	0.000158	0.088817	2.03E-05	0.000102	0.002112	0.001062	0.000114	0.002401	0.008732
Std	0.043819	0.000246	1.584805	0.000112	0.000243	0.000502	0.083922	0.004007	4.88E-05	0.000229	0.005343	0.000161	0.144686	1.981387	0.000125	0.001083	0.006253	1.95E-05	6.90E-05	0.046673	1.87E-05	4.05E-05	0.000376	0.000217	0.000102	0.001724	0.001357
G5	0.718014	0.000362	20.89623	0.000481	0.00151	0.001049	0.252235	0.004362	0.000321	0.001998	0.001367	0.00043	0.354882	58.20635	0.000371	0.000661	0.058741	3.55E-05	0.000225	0.119365	2.11E-05	0.000152	0.004031	0.001393	0.000213	0.003301	0.012458
Std	0.820026	0.000256	24.46601	0.000471	0.001565	0.000476	0.236216	0.00446	0.000242	0.002167	0.000679	0.000236	0.219348	22.0501	0.000344	0.000682	0.029037	3.28E-05	0.000236	0.144671	1.91E-05	0.000114	0.004363	0.001355	0.000253	0.003834	0.014625
G6	0.400559	0.000281	19.17055	0.000248	0.000918	0.001443	0.221395	0.002938	0.00023	0.000962	0.005466	0.000424	0.312901	66.70399	0.000195	0.000286	0.058805	2.97E-05	0.000165	0.080562	2.04E-05	0.00014	0.002325	0.001174	0.000141	0.001714	0.007014
Std	0.105111	0.000213	3.103369	8.81E-05	0.000295	0.00051	0.038451	0.001036	5.77E-05	0.000268	0.002514	0.000143	0.050217	4.023446	0.000107	0.000113	0.009117	1.58E-05	6.10E-05	0.13605	1.66E-05	5.03E-05	0.000671	0.000239	9.32E-05	0.000943	0.001733
G7	0.379892	0.00028	16.7708	0.000261	0.000803	0.001029	0.299593	0.011595	0.000194	0.001094	0.032216	0.000437	0.341256	70.09993	0.000184	0.006979	0.051952	2.67E-05	0.000126	0.069206	1.91E-05	0.000116	0.001974	0.001017	0.000113	0.002176	0.006788
Std	0.044438	0.000222	1.644283	8.89E-05	0.000203	0.000353	0.03939	0.001455	4.38E-05	0.000201	0.003029	0.000132	0.03821	2.230154	0.000114	0.001108	0.005853	1.65E-05	5.01E-05	0.010583	1.69E-05	4.20E-05	0.000371	0.000179	8.62E-05	0.001025	0.000913
G8	0.632855	0.000326	15.49483	0.000261	0.000799	0.00151	0.341589	0.025596	0.000187	0.001005	0.111641	0.000395	0.25008	72.16277	0.000166	0.003474	0.051732	2.34E-05	0.000136	0.075374	1.57E-05	0.000106	0.002616	0.000928	9.56E-05	0.002627	0.007178
Std	0.107375	0.000191	2.910377	9.58E-05	0.000242	0.000404	0.077657	0.007215	4.72E-05	0.000311	0.012469	0.000123	0.044955	3.812868	8.32E-05	0.000005	0.007184	1.36E-05	5.71E-05	0.023383	1.31E-05	3.99E-05	0.000738	0.000221	7.19E-05	0.002556	0.002185
G9	1.008876	0.000302	15.36188	0.000312	0.000979	0.001299	0.179045	0.000793	0.000246	0.001059	0.00102	0.000407	0.235885	69.02845	0.000247	0.000167	0.061561	3.18E-05	0.000169	0.08334	1.97E-05	0.000123	0.002578	0.001183	0.000132	0.002417	0.008346
Std	0.265162	0.000197	4.274219	0.000132	0.000381	0.001472	0.057899	0.000543	7.49E-05	0.000421	0.000389	0.000124	0.059063	5.014832	0.000135	0.000167	0.011156	1.76E-05	8.46E-05	0.052198	1.48E-05	5.10E-05	0.001028	0.000362	9.71E-05	0.002917	0.00425
G10	0.828573	0.000543	18.62975	0.000271	0.000717	0.001739	0.439812	0.038731	0.000178	0.001395	0.174735	0.000555	0.591681	68.88878	0.000202	0.002602	0.048011	3.13E-05	0.000163	0.071813	2.68E-05	0.000143	0.00412	0.000943	0.000157	0.002156	0.006993
Std	0.165759	0.000472	4.169473	0.000125	0.000282	0.000665	0.087459	0.008808	6.03E-05	0.000405	0.024608	0.000212	0.110075	5.064498	0.000163	0.000716	0.006327	2.56E-05	8.60E-05	0.015434	2.95E-05	6.10E-05	0.001067	0.000241	0.000154	0.001464	0.001317
G11	0.639012	0.000342	14.01203	0.000329	0.000734	0.001885	0.227423	0.036054	0.000219	0.001833	0.184215	0.000451	0.214161	74.7054	0.000161	0.005986	0.04927	2.31E-05	0.000227	0.096096	1.59E-05	0.000175	0.002849	0.00085	8.61E-05	0.003398	0.008204
Std	0.08453	0.000175	1.96785	9.62E-05	0.000176	0.000591	0.032437	0.00727	4.69E-05	0.000404	0.025216	0.000114	0.027635	2.540488	8.13E-05	0.000942	0.007385	1.14E-05	7.29E-05	0.018273	1.11E-05	5.52E-05	0.000582	0.000183	6.03E-05	0.001087	0.001355
G12	0.765732	0.000237	15.65341	0.000211	0.000758	0.001469	0.245577	0.001019	0.00019	0.00078	0.000642	0.000393	0.307405	72.24761	0.000176	0.000146	0.053964	2.58E-05	0.000131	0.051537	1.85E-05	0.00012	0.002609	0.000895	0.000102	0.0016	0.005
Std	0.113271	0.000169	1.783017	6.69E-05	0.000204	0.000457	0.039145	0.000202	4.57E-05	0.00016	0.000217	0.000118	0.062878	2.612592	0.0001	6.58E-05	0.007377	1.53E-05	5.33E-05	0.008102	1.64E-05	3.91E-05	0.000514	0.000165	6.49E-05	0.00057	0.000751
G13	0.516771	0.000275	19.76172	0.000308	0.000911	0.001302	0.22518	0.018462	0.000211	0.001285	0.097826	0.00045	0.303524	67.03769	0.000198	0.004302	0.050319	2.73E-05	0.000197	0.084672	2.13E-05	0.000153	0.002616	0.001086	0.000143	0.002387	0.008077
Std	0.106549	0.000206	3.266884	0.000141	0.000339	0.000395	0.038474	0.006392	7.26E-05	0.000511	0.097352	0.000151	0.060507	4.041668	0.000133	0.001226	0.013229	1.86E-05	8.75E-05	0.035363	1.70E-05	6.21E-05	0.000696	0.000254	0.00011	0.002098	0.001841
G14	0.948349	0.000299	18.57867	0.00023	0.000963	0.001834	0.216964	0.00069	0.000229	0.000982	0.000216	0.000445	0.337868	65.23885	0.000218	0.000138	0.073441	3.29E-05	0.000124	0.063679	2.21E-05	0.000113	0.003204	0.001326	0.000134	0.002006	0.006385
Std	0.19266	0.000213	3.392661	8.67E-05	0.000268	0.000548	0.0387	0.000192	5.59E-05	0.000255	8.81E-05	0.000153	0.043515	4.466931	0.000122	7.26E-05	0.013951	2.01E-05	5.29E-05	0.016472	1.90E-05	5.32E-05	0.000846	0.000331	9.63E-05	0.000828	0.001278
G15	0.045656	0.000106	13.35842	0.00016	0.000614	0.000477	0.174295	0.00059	0.000168	0.000633	7.61E-05	0.000343	0.218621	77.03127	0.000132	9.11E-05	0.042351	1.89E-05	8.33E-05	0.03834	1.27E-05	9.95E-05	0.000789	0.000711	7.04E-05	0.000698	0.0039
Std	0.010688	0.000139	3.102104	6.67E-05	0.00022	0.000205	0.043458	0.000185	4.72E-05	0.000213	4.73E-05	0.000107	0.044743	4.291198	8.09E-05	5.15E-05	0.008152	1.23E-05	3.57E-05	0.012351	1.05E-05	3.54E-05	0.000266	0.000189	6.03E-05	0.000494	0.001

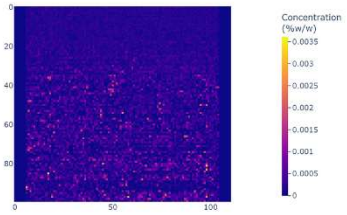
G16	1.722	0.001	16.60	0.000	0.000	0.001	0.228	0.004	0.000	0.000	0.028	0.000	0.249	69.87	0.000	0.000	0.059	2.63E	0.000	0.057	1.61E	0.000	0.003	0.001	8.94E	0.001	0.005
	55	574	144	206	821	455	093	189	179	717	878	403	373	053	165	272	506	-05	113	472	-05	117	675	157	-05	621	881
Std	0.294	0.000	2.900	8.20E	0.000	0.000	0.043	0.001	4.28E	0.000	0.003	0.000	0.057	4.124	9.39E	0.000	0.008	1.49E	4.74E	0.014	1.33E	3.98E	0.000	0.000	6.45E	0.000	0.001
	077	437	338	-05	227	373	237	086	-05	206	454	113	498	675	-05	104	381	-05	-05	036	-05	-05	911	274	-05	707	606
G17	0.047	0.000	15.39	0.000	0.000	0.000	0.194	0.000	0.000	0.000	0.000	0.000	0.249	73.20	0.000	0.000	0.045	2.71E	0.000	0.052	1.59E	0.000	0.000	0.001	0.000	0.001	0.006
	298	119	032	205	759	589	001	735	174	76	142	391	658	465	168	135	149	-05	123	99	-05	107	968	105	106	131	389
Std	0.005	0.000	1.835	7.10E	0.000	0.000	0.026	0.000	3.94E	0.000	7.76E	0.000	0.027	2.169	8.11E	6.39E	0.004	1.44E	4.95E	0.022	1.23E	3.56E	0.000	0.000	8.08E	0.000	0.001
	458	168	499	-05	185	276	333	154	-05	202	-05	107	593	884	-05	-05	228	-05	-05	013	-05	-05	275	2	-05	674	246
G18	1.305	0.000	19.64	0.000	0.000	0.002	0.994	0.084	0.000	0.001	0.050	0.000	0.289	59.85	0.000	0.171	0.071	2.81E	0.000	0.175	1.84E	0.000	0.005	0.001	0.000	0.011	0.012
	163	604	718	541	921	495	899	808	219	291	772	651	217	711	203	954	078	-05	213	303	-05	157	153	09	112	698	942
Std	0.186	0.000	2.389	0.000	0.000	0.000	0.146	0.016	5.06E	0.000	0.007	0.000	0.034	3.262	0.000	0.025	0.010	1.47E	7.15E	0.035	1.41E	5.07E	0.001	0.000	7.75E	0.002	0.002
	897	276	025	142	26	595	876	731	-05	254	436	157	306	928	111	62	948	-05	-05	808	-05	-05	054	226	-05	155	112
G19	1.071	0.000	19.53	0.000	0.000	0.003	0.291	0.002	0.000	0.001	0.005	0.000	0.266	66.59	0.000	0.000	0.055	2.85E	0.000	0.055	1.83E	0.000	0.003	0.001	0.000	0.002	0.005
	133	49	148	21	831	652	371	062	186	146	069	396	272	871	176	896	467	-05	13	64	-05	134	308	063	116	945	54
Std	0.208	0.000	3.684	8.55E	0.000	0.000	0.060	0.000	4.97E	0.000	0.000	0.000	0.042	3.811	9.63E	0.000	0.008	1.66E	5.03E	0.012	1.50E	4.96E	0.000	0.000	8.22E	0.001	0.001
	876	248	418	-05	254	829	135	494	-05	257	813	115	412	435	-05	234	443	-05	-05	906	-05	-05	696	256	-05	886	104
G20	0.552	0.000	15.52	0.000	0.000	0.001	0.293	0.012	0.000	0.001	0.044	0.000	0.274	70.79	0.000	0.005	0.051	2.29E	0.000	0.076	1.70E	0.000	0.002	0.000	0.000	0.002	0.007
	682	296	552	305	835	328	269	744	221	335	407	407	274	869	195	211	206	-05	176	653	-05	154	824	867	126	634	401
Std	0.079	0.000	2.227	0.000	0.000	0.000	0.050	0.002	5.04E	0.000	0.007	0.000	0.049	2.944	0.000	0.000	0.007	1.31E	6.15E	0.017	1.45E	4.97E	0.000	0.000	8.94E	0.001	0.001
	536	196	428	101	212	397	702	812	-05	323	475	13	687	77	109	945	519	-05	-05	005	-05	-05	678	183	-05	424	703
G21	0.756	0.000	19.83	0.000	0.000	0.001	0.318	0.053	0.000	0.001	0.184	0.000	0.296	64.56	0.000	0.004	0.060	2.92E	0.000	0.101	1.94E	0.000	0.003	0.001	0.000	0.003	0.009
	203	43	247	361	872	848	816	975	228	223	674	467	573	813	216	232	391	-05	168	406	-05	147	68	101	115	207	368
Std	0.165	0.000	4.333	0.000	0.000	0.000	0.089	0.013	6.64E	0.000	0.031	0.000	0.050	4.773	0.000	0.001	0.012	1.63E	6.43E	0.039	1.57E	5.13E	0.001	0.000	8.51E	0.002	0.002
	111	277	875	13	311	643	612	88	-05	381	216	154	798	717	117	058	132	-05	-05	114	-05	-05	033	279	-05	098	211
G22	0.328	0.000	10.93	0.000	0.000	0.001	0.184	0.006	0.000	0.001	0.034	0.000	0.184	76.42	0.000	0.002	0.055	1.79E	9.62E	0.039	1.32E	0.000	0.002	0.000	7.55E	0.001	0.004
	81	244	581	274	586	082	444	365	219	049	141	31	635	328	169	283	433	-05	-05	017	-05	118	178	62	-05	902	548
Std	0.073	0.000	2.451	7.59E	0.000	0.000	0.086	0.002	4.71E	0.000	0.003	8.70E	0.032	2.969	8.79E	0.000	0.009	9.88E	4.41E	0.015	1.01E	3.77E	0.000	0.000	5.60E	0.001	0.002
	616	133	197	-05	194	264	055	403	-05	289	423	-05	894	953	-05	894	11	-06	-05	86	-05	-05	692	134	-05	789	223
G23	0.647	0.000	16.74	0.000	0.000	0.001	0.214	0.000	0.000	0.000	0.000	0.000	0.327	68.86	0.000	0.000	0.057	2.63E	0.000	0.079	1.98E	0.000	0.003	0.000	0.000	0.002	0.006
	288	238	326	297	794	844	051	676	231	905	126	41	517	686	212	193	038	-05	123	346	-05	118	222	953	127	43	555
Std	0.180	0.000	4.294	0.000	0.000	0.001	0.056	0.000	8.03E	0.000	7.83E	0.000	0.098	5.033	0.000	0.000	0.013	2.00E	7.06E	0.210	1.90E	6.41E	0.000	0.000	0.000	0.001	0.002
	475	463	898	23	323	447	099	339	-05	254	-05	162	645	614	122	129	723	-05	-05	064	-05	-05	829	326	101	081	307
G24	1.153	0.000	17.12	0.000	0.000	0.002	0.262	0.000	0.000	0.000	0.000	0.000	0.337	70.60	0.000	0.000	0.054	2.52E	0.000	0.051	1.81E	7.50E	0.003	0.000	0.000	0.002	0.005
	116	608	442	185	745	156	195	682	179	924	327	41	281	754	167	169	174	-05	103	287	-05	-05	913	927	107	047	174
Std	0.118	0.000	1.648	6.86E	0.000	0.004	0.031	0.000	4.27E	0.000	0.000	0.000	0.031	2.219	0.000	7.39E	0.006	1.67E	4.83E	0.012	1.58E	3.36E	0.000	0.000	8.08E	0.000	0.000
	073	302	898	-05	221	75	177	143	-05	171	107	132	241	808	105	-05	062	-05	-05	111	-05	-05	622	181	-05	724	713
G25	0.468	0.000	15.35	0.000	0.000	0.001	0.282	0.011	0.000	0.000	0.059	0.000	0.280	74.00	0.000	0.003	0.047	2.40E	0.000	0.058	1.67E	0.000	0.001	0.000	8.89E	0.001	0.005
	756	279	359	2	652	292	49	481	163	861	761	411	303	719	139	728	558	-05	103	109	-05	103	932	821	-05	805	297
Std	0.069	0.000	2.557	7.47E	0.000	0.000	0.050	0.002	3.91E	0.000	0.006	0.000	0.058	3.490	8.44E	0.000	0.006	1.39E	4.31E	0.012	1.41E	3.54E	0.000	0.000	8.19E	0.000	0.001
	35	196	046	-05	179	374	968	345	-05	211	584	127	943	551	-05	806	853	-05	-05	225	-05	-05	468	173	-05	713	008
G26	0.891	0.000	17.63	0.000	0.000	0.001	0.210	0.026	0.000	0.000	0.360	0.000	0.293	69.47	0.000	0.001	0.057	3.09E	0.000	0.079	1.97E	0.000	0.004	0.001	0.000	0.002	0.008
	845	432	774	291	857	572	903	053	203	831	462	463	064	142	193	105	361	-05	156	411	-05	131	295	142	115	028	736
Std	0.086	0.000	1.742	8.36E	0.000	0.000	0.024	0.003	3.64E	0.000	0.035	0.000	0.030	1.995	9.84E	0.000	0.004	1.56E	5.43E	0.012	1.56E	4.05E	0.000	0.000	8.34E	0.000	0.001
	181	224	181	-05	213	751	845	19	-05	167	929	126	754	974	-05	259	479	-05	-05	541	-05	-05	632	198	-05	66	209
G27	0.022	0.000	19.69	0.000	0.000	0.000	0.121	0.024	0.000	0.001	1.481	0.000	0.270	66.31	0.000	0.000	0.047	2.68E	0.000	0.072	1.86E	0.000	0.001	0.000	0.000	0.002	0.007
	907	112	132	314	98	451	275	869	224	089	066	356	595	812	222	338	63	-05	198	463	-05	162	456	903	133	204	984
Std	0.008	0.000	7.728	0.000	0.000	0.000	0.032	0.008	7.66E	0.000	0.204	0.000	0.053	6.337	0.000	0.000	0.008	1.88E	9.70E	0.030	1.65E	6.48E	0.000	0.000	7.70E	0.001	0.003
	761	249	491	13	454	221	176	145	-05	394	797	135	037	757	123	124	641	-05	-05	972	-05	-05	554	35	-05	038	11
G28	0.442	0.000	13.28	0.000	0.000	0.001	0.305	0.006	0.000	0.002	0.032	0.000	0.233	74.16	0.000	0.003	0.044	2.23E	0.000	0.075	1.51E	0.000	0.003	0.000	8.05E	0.005	0.006
	957	24	791	311	754	737	188	899	185	009	52	444	25	367	157	178	935	-05	148	278	-05	105	043	858	-05	939	452
Std	0.098	0.000	2.588	0.000	0.000	0.000	0.086	0.001	7.12E	0.001	0.007	0.000	0.040	3.611	8.80E	0.000	0.007	1.35E	7.77E	0.049	1.20E	3.82E	0.003	0.000	6.10E	0.004	0.001
	469	148	078	163	241	721	62	569	-05	143	918	146	438	158	-05	932	343	-05	-05	645	-05	-05	881	263	-05	095	447
G29	0.657	0.000	16.99	0.000	0.000	0.001	0.345	0.042	0.000	0.001	0.155	0.000	0.235	69.46	0.000	0.003	0.053	3.13E	0.000	0.101	1.94E	0.000	0.003	0.001	0.000	0.002	0.011
	19	318	099	347	973	539	713	939	213	127	702	463	308	542	206	436	198	-05	2	271	-05	117	737	33	115	98	681
Std	0.123	0.000	3.332	0.000	0.000	0.000	0.086	0.009	4.66E	0.000	0.018	0.000	0.032	3.417	0.000	0.000	0.006	1.53E	7.19E	0.027	1.39E	3.63E	0.005	0.000	7.59E	0.001	0.002
	977	18	51	112	259	405	097	86	-05	307	537	119	431	394	103	886	612	-05	-05	762	-05	-05	948	301	-05	788	969
G30	1.020	0.000	19.62	0.000	0.000	0.002	0.544	0.078	0.000	0.000	0.267	0.000	0.318	65.04	0.000	0.004	0.064	2.90E	0.000	0.129	2.37E	0.000	0.004	0.001	0.000	0.003	0.011
	081	481	416	393	885	252	639	907	212	815	305	539	382	177	196	359	756	-05	208	976	-05	176	818	02	127	714	084
Std	0.123	0.000	2.264	0.000	0.000	0.000	0.065	0.015	4.87E	0.000	0.037	0.000	0.043	2.961	0.000	0.000	0.009	1.67E	7.28E	0.034	1.81E	5.59E	0.000	0.000	8.75E	0.001	0.002
	137	261	882	118	266	661	909	817	-05	196	647	158	359	932	1	777	164	-05	-05	606	-05	-05	813	2	-05	151	027
G31	0.466	0.000	17.09	0.000	0.000	0.000	0.311	0.015	0.000	0.000	0.049	0.000	0.235	72.28	0.000	0.006	0.047	2.78E	0.000	0.090	1.44E	9.41E	0.001	0.001	9.31E	0.002	0.008
	729	199	157	247	953	95	975	605	166	849	856	444	96	69	147		685	-05	169	289	-05	-05	795	129	-05	253	646

Std	0.173	0.000	6.481	0.000	0.000	0.000	0.130	0.006	6.66E	0.000	0.006	0.000	0.065	7.900	9.81E	0.002	0.009	1.50E	7.71E	0.046	1.15E	4.34E	0.000	0.000	8.62E	0.002	0.003
	596	135	917	126	411	324	748	546	-05	42	353	159	978	192	-05	396	863	-05	-05	741	-05	-05	845	447	-05	618	512
G32	0.791	0.000	15.08	0.000	0.000	0.001	0.280	0.030	0.000	0.000	0.160	0.000	0.273	71.73	0.000	0.002	0.058	2.49E	0.000	0.103	1.74E	0.000	0.004	0.000	0.000	0.002	0.007
	69	398	039	315	835	512	938	141	213	994	483	413	457	883	186	103	099	-05	143	731	-05	12	316	927	107	569	508
Std	0.123	0.000	2.302	0.000	0.000	0.000	0.053	0.008	5.85E	0.000	0.028	0.000	0.048	3.310	0.000	0.000	0.010	1.37E	6.31E	0.310	1.46E	4.58E	0.001	0.000	8.30E	0.002	0.002
	11	227	051	122	241	475	625	3	-05	376	178	131	625	827	106	623	365	-05	-05	433	-05	-05	283	217	-05	276	211
G33	0.202	0.000	15.59	0.000	0.000	0.000	0.302	0.004	0.000	0.000	0.005	0.000	0.286	72.10	0.000	0.000	0.047	2.30E	0.000	0.058	1.73E	0.000	0.001	0.001	9.77E	0.001	0.005
	107	235	223	223	82	766	08	18	188	976	018	402	1	437	171	766	761	-05	126	917	-05	132	595	001	-05	503	876
Std	0.044	0.000	3.179	8.75E	0.000	0.000	0.071	0.000	4.62E	0.000	0.000	0.000	0.042	4.193	9.35E	0.000	0.008	1.49E	4.86E	0.012	1.45E	4.25E	0.000	0.000	6.46E	0.000	0.001
	742	16	55	-05	211	285	671	824	-05	275	83	111	673	966	-05	179	274	-05	-05	247	-05	-05	399	244	-05	795	201
G34	0.049	0.000	12.64	0.000	0.000	0.001	0.086	0.020	0.000	0.000	0.004	0.000	0.236	72.46	9.76E	0.002	0.019	1.55E	0.000	0.106	1.39E	0.000	0.003	0.000	7.62E	0.014	0.015
	689	135	817	44	485	029	559	055	13	727	733	344	997	142	-05	802	542	-05	195	913	-05	131	454	562	-05	713	319
Std	0.011	0.000	2.765	0.000	0.000	0.001	0.024	0.005	3.18E	0.000	0.000	0.000	0.053	3.591	6.89E	0.000	0.002	1.06E	7.30E	0.031	1.16E	4.11E	0.004	0.000	6.25E	0.004	0.004
	668	142	895	119	176	018	244	371	-05	213	688	114	127	447	-05	722	985	-05	-05	399	-05	-05	231	168	-05	285	126
G35	0.388	0.000	16.37	0.000	0.000	0.000	0.233	0.010	0.000	0.001	0.061	0.000	0.230	70.74	0.000	0.001	0.053	2.84E	0.000	0.071	1.85E	0.000	0.001	0.001	9.79E	0.001	0.007
	341	232	676	285	977	856	078	606	209	013	797	415	207	753	195	556	7	-05	151	532	-05	114	688	183	-05	632	147
Std	0.095	0.000	3.889	0.000	0.000	0.000	0.060	0.003	5.22E	0.000	0.025	0.000	0.040	4.402	0.000	0.000	0.007	1.60E	6.24E	0.038	1.34E	3.87E	0.000	0.000	7.05E	0.000	0.002
	299	16	187	113	301	291	188	332	-05	35	006	121	452	193	101	525	325	-05	-05	809	-05	-05	574	363	-05	744	452
Bead	0.023	0.000	12.21	0.000	0.000	0.001	0.385	0.001	9.19E	0.001	0.002	0.000	0.228	75.26	8.74E	0.006	0.028	1.29E	7.72E	0.076	1.47E	5.54E	0.002	0.000	5.55E	0.007	0.002
	503	123	189	279	374	637	825	246	-05	261	07	391	691	585	-05	114	439	-05	-05	465	-05	-05	29	307	-05	217	634
Std	0.009	0.000	4.531	0.000	0.000	0.000	0.180	0.000	4.05E	0.001	0.001	0.000	0.082	6.170	7.51E	0.003	0.008	1.31E	6.92E	0.040	4.75E	3.06E	0.002	0.000	6.84E	0.010	0.001
	884	163	779	251	186	696	402	651	-05	53	61	157	095	419	-05	226	601	-05	-05	717	-05	-05	632	172	-05	385	196

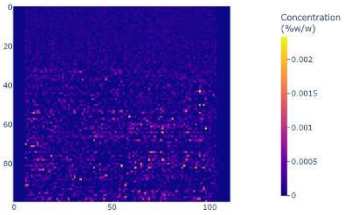
Figure S4.1. Oxide concentration maps for Bead.



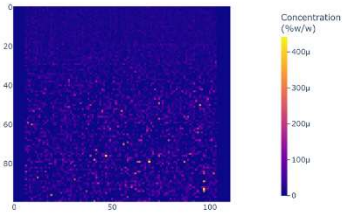
Oxide concentration map for Ga2O3



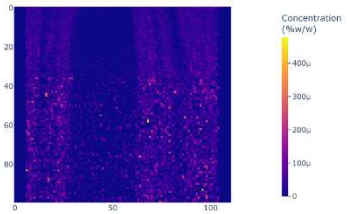
Oxide concentration map for Gd2O3



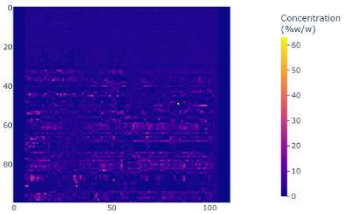
Oxide concentration map for Ho2O3



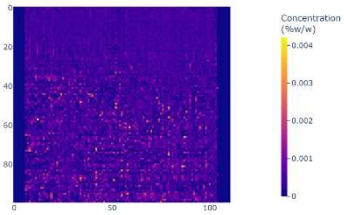
Oxide concentration map for In2O3



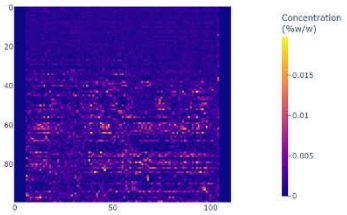
Oxide concentration map for K2O



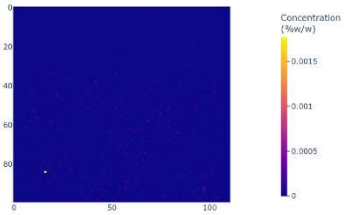
Oxide concentration map for La2O3



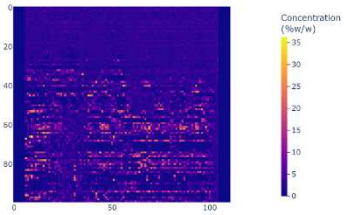
Oxide concentration map for Li2O



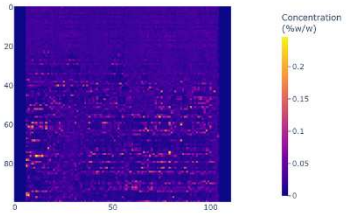
Oxide concentration map for Lu2O3



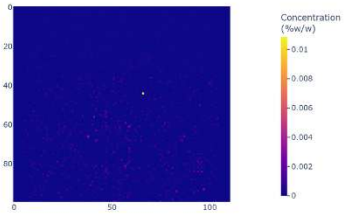
Oxide concentration map for MgO



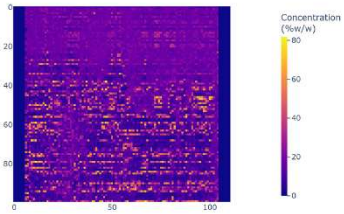
Oxide concentration map for MnO



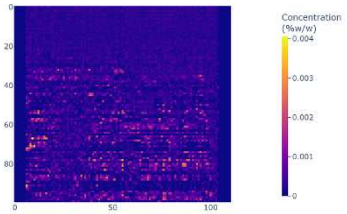
Oxide concentration map for MoO3



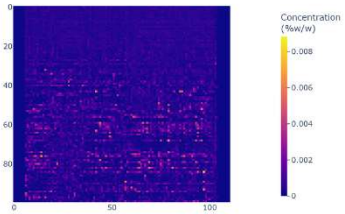
Oxide concentration map for Na2O



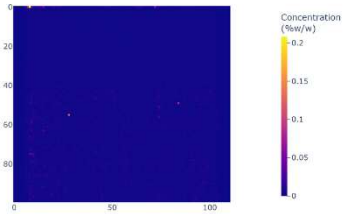
Oxide concentration map for Nb2O5



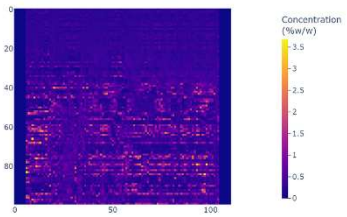
Oxide concentration map for Nd2O3



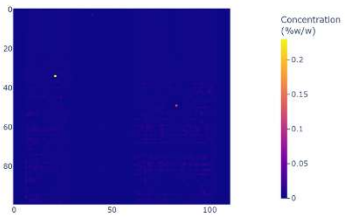
Oxide concentration map for NiO



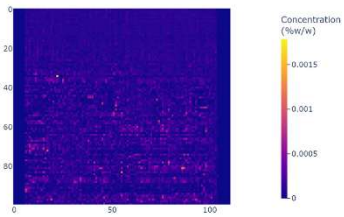
Oxide concentration map for P2O5



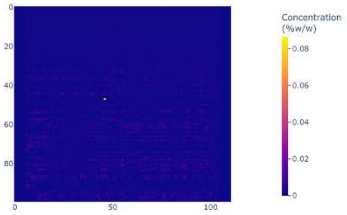
Oxide concentration map for PbO



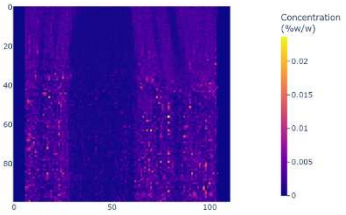
Oxide concentration map for Pr2O3



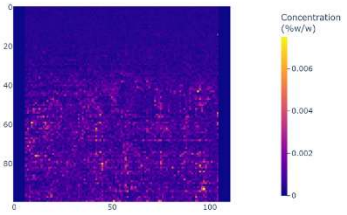
Oxide concentration map for Rb2O



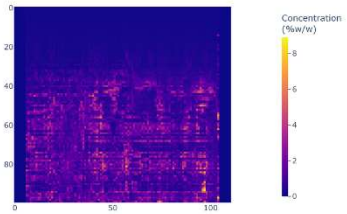
Oxide concentration map for Sb2O5



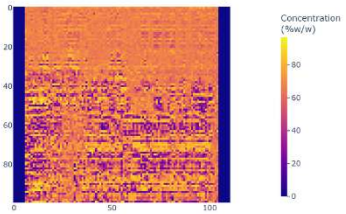
Oxide concentration map for Sc2O3



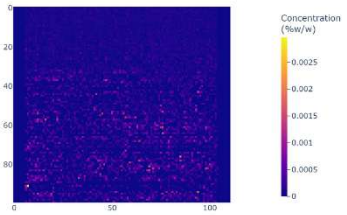
Oxide concentration map for SeO2



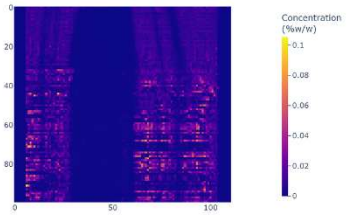
Oxide concentration map for SiO2



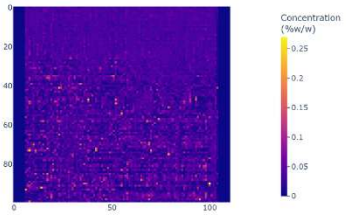
Oxide concentration map for Sm2O3



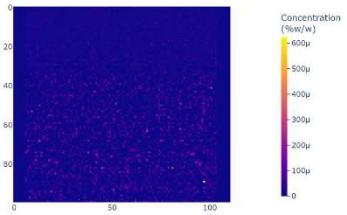
Oxide concentration map for SnO2



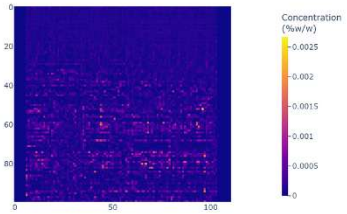
Oxide concentration map for SrO



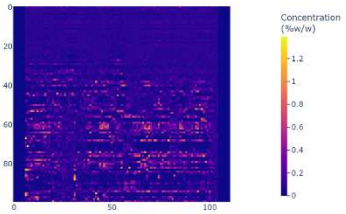
Oxide concentration map for Tb2O3



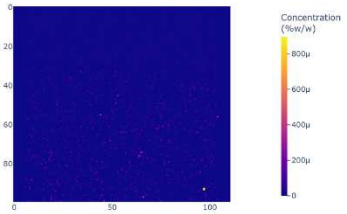
Oxide concentration map for ThO2



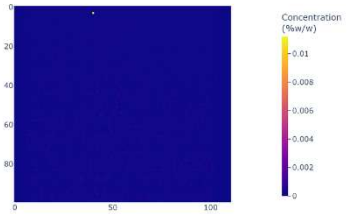
Oxide concentration map for TiO2



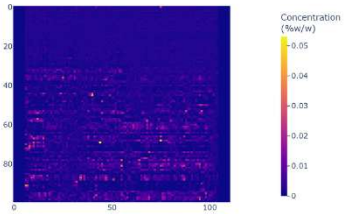
Oxide concentration map for Tm2O3



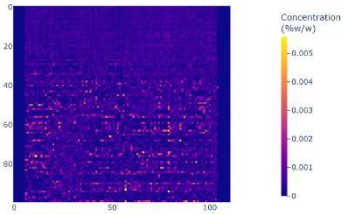
Oxide concentration map for UO2



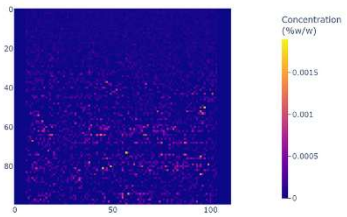
Oxide concentration map for V2O5



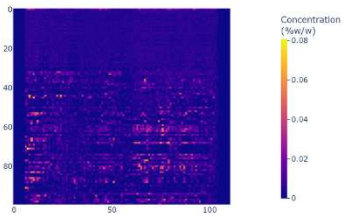
Oxide concentration map for Y2O3



Oxide concentration map for Yb2O3



Oxide concentration map for ZnO



Oxide concentration map for ZrO2

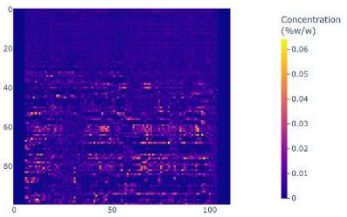
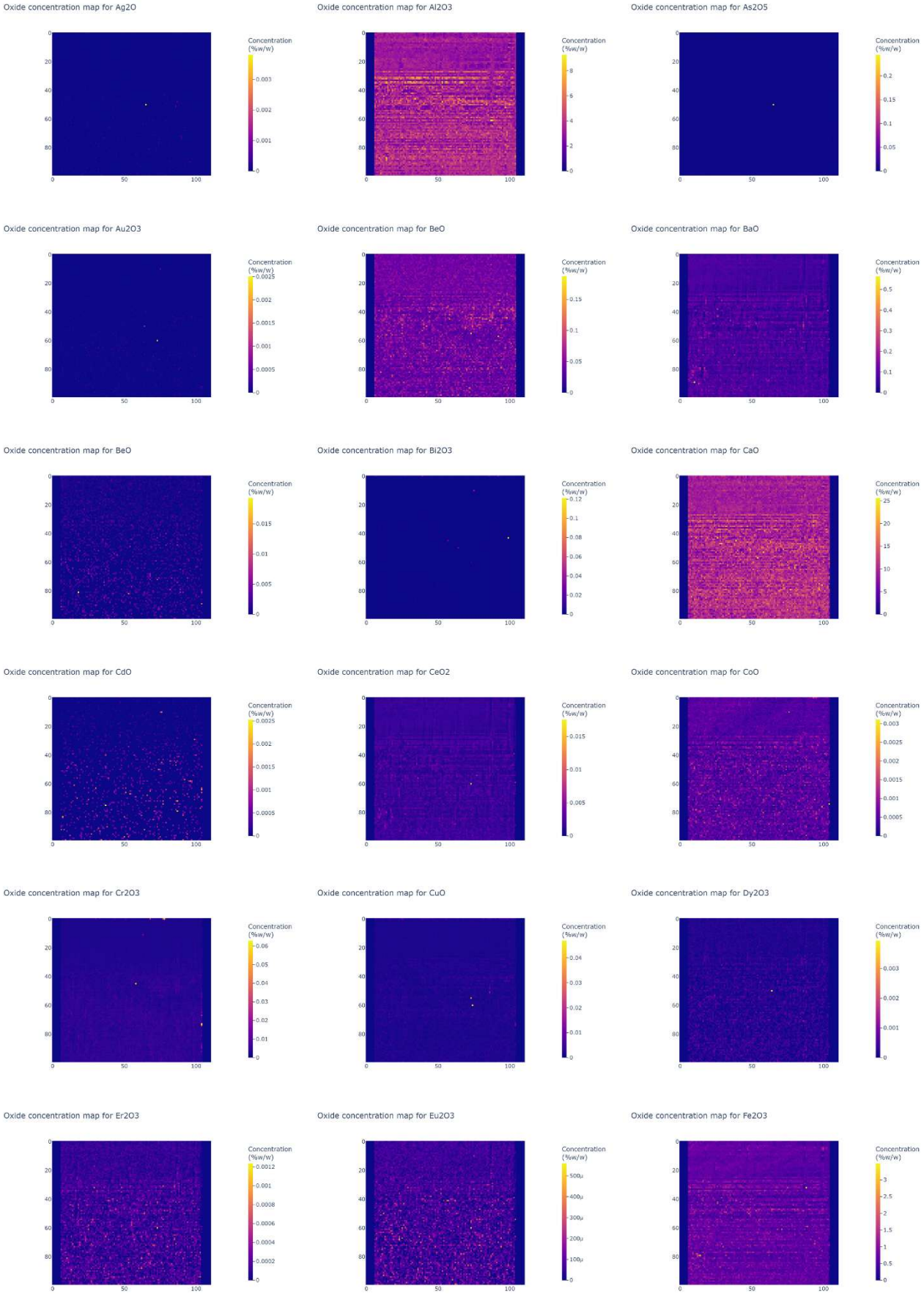
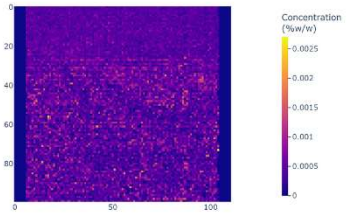


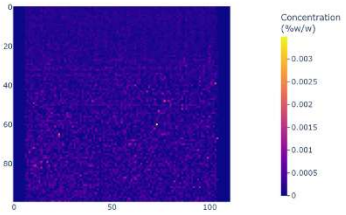
Figure S4.2. Oxide concentration maps for G9.



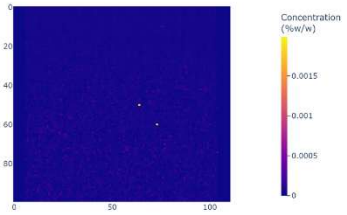
Oxide concentration map for Ga2O3



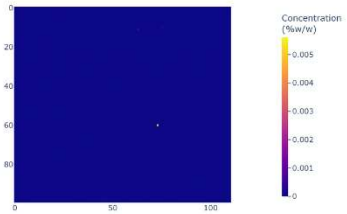
Oxide concentration map for Gd2O3



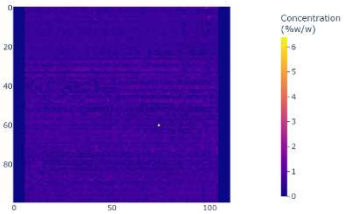
Oxide concentration map for Ho2O3



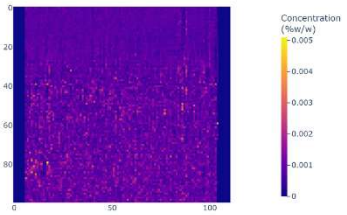
Oxide concentration map for In2O3



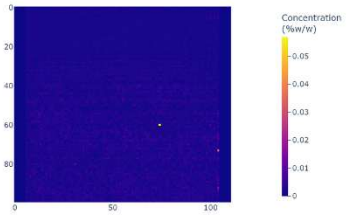
Oxide concentration map for K2O



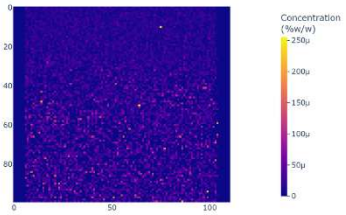
Oxide concentration map for La2O3



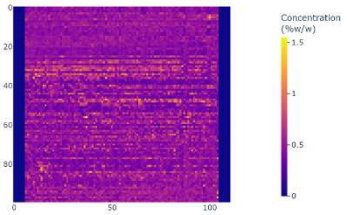
Oxide concentration map for Li2O



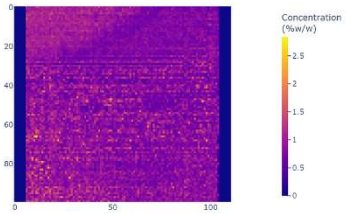
Oxide concentration map for Lu2O3



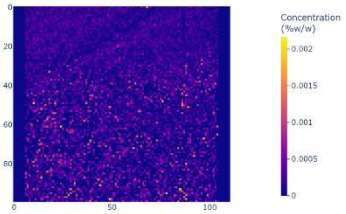
Oxide concentration map for MgO



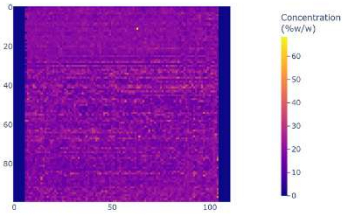
Oxide concentration map for MnO



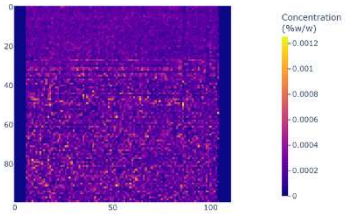
Oxide concentration map for MoO3



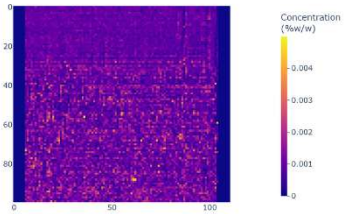
Oxide concentration map for Na2O



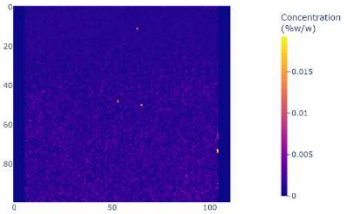
Oxide concentration map for Nb2O5



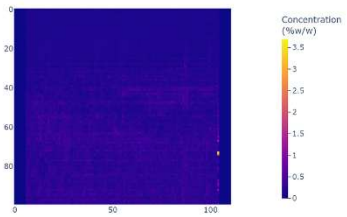
Oxide concentration map for Nd2O3



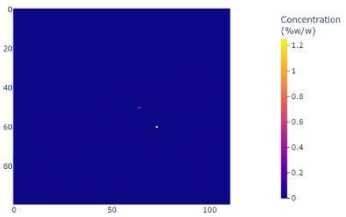
Oxide concentration map for NiO



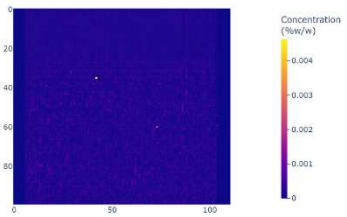
Oxide concentration map for P2O5



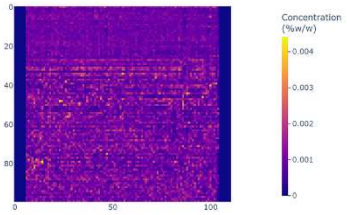
Oxide concentration map for PbO



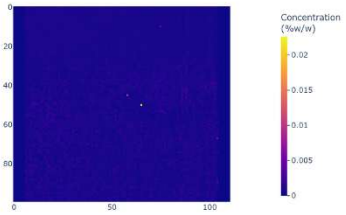
Oxide concentration map for Pr2O3



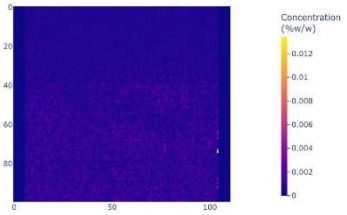
Oxide concentration map for Rb2O



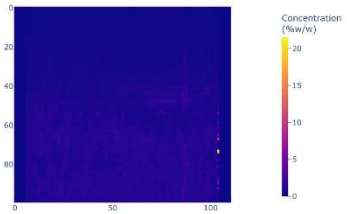
Oxide concentration map for Sb2O5



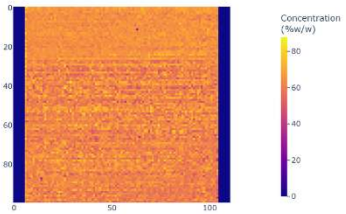
Oxide concentration map for Sc2O3



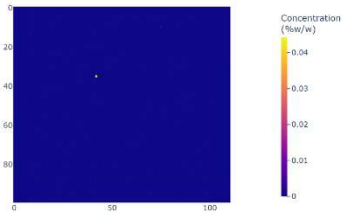
Oxide concentration map for SeO2



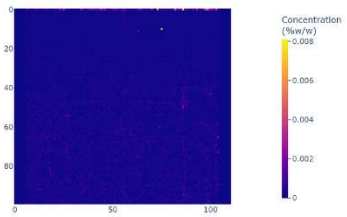
Oxide concentration map for SiO2



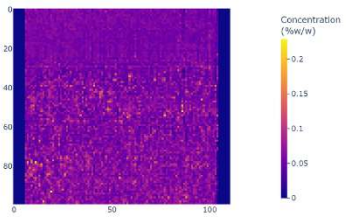
Oxide concentration map for Sm2O3



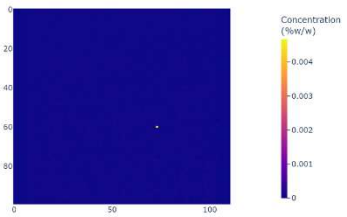
Oxide concentration map for SnO2



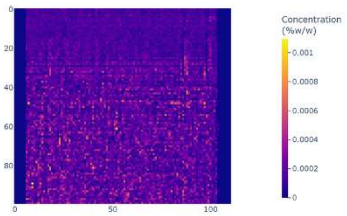
Oxide concentration map for SrO



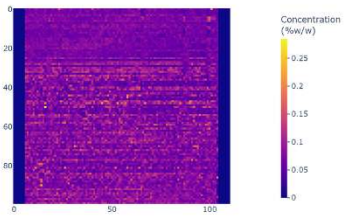
Oxide concentration map for Tb2O3



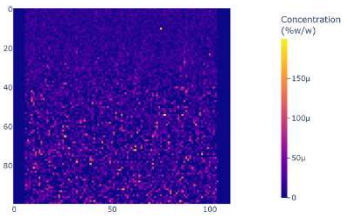
Oxide concentration map for ThO2



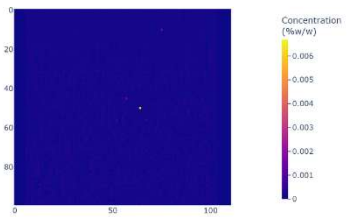
Oxide concentration map for TiO2



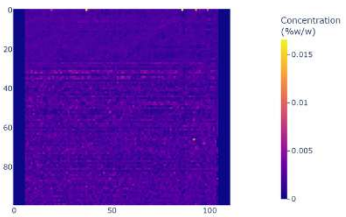
Oxide concentration map for Tm2O3



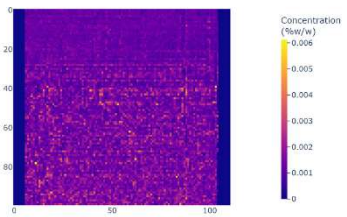
Oxide concentration map for UO2



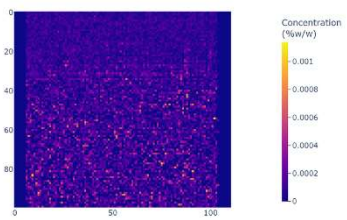
Oxide concentration map for V2O5



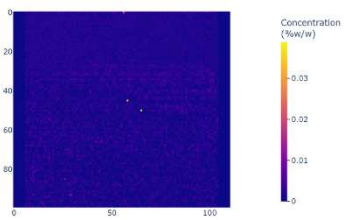
Oxide concentration map for Y2O3



Oxide concentration map for Yb2O3



Oxide concentration map for ZnO



Oxide concentration map for ZrO2

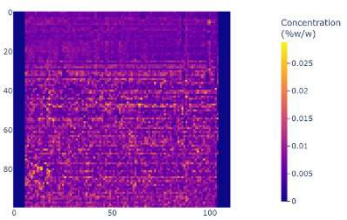
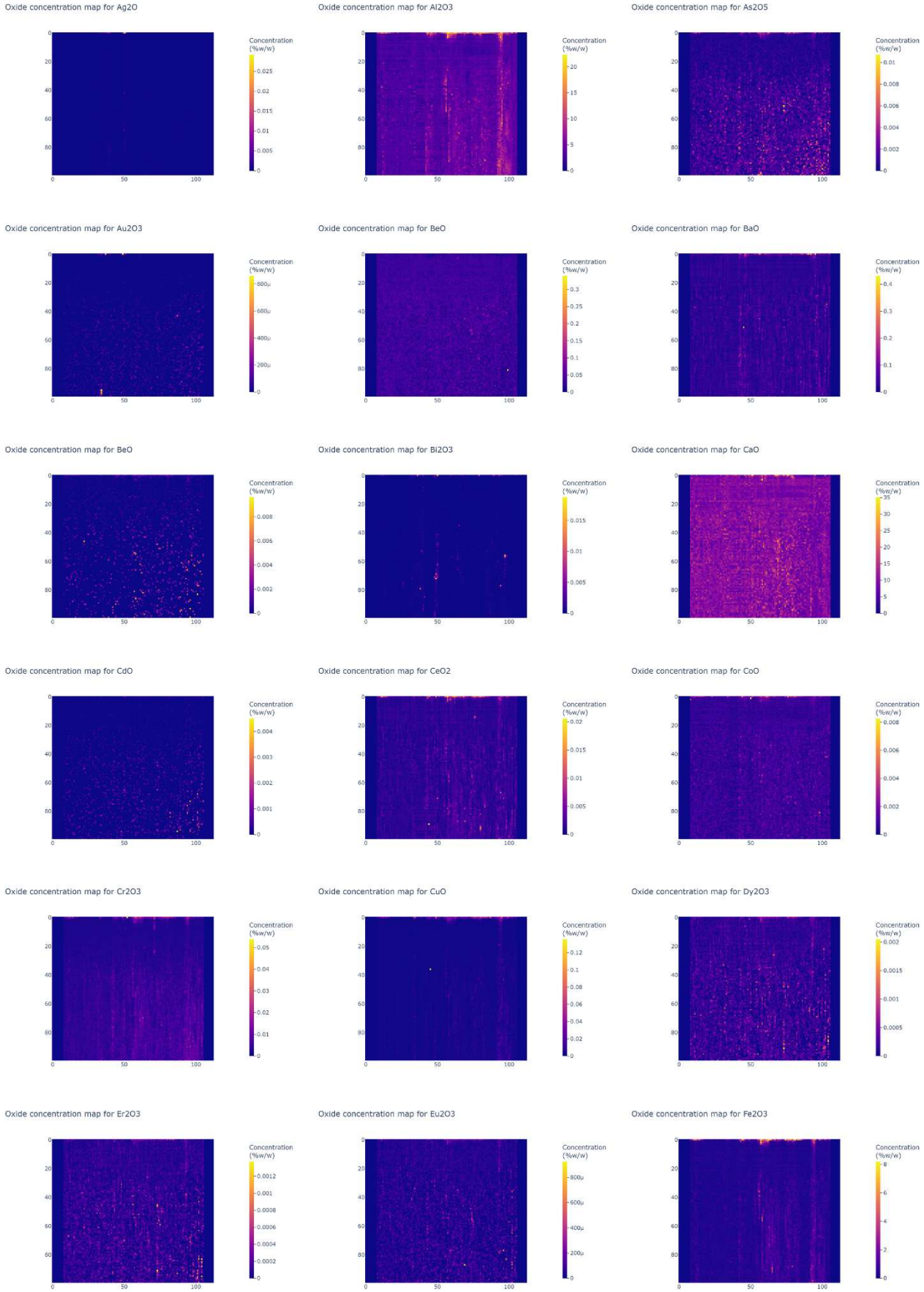
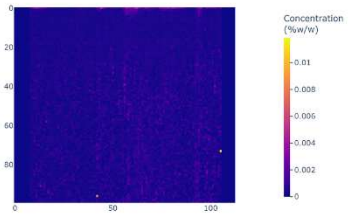


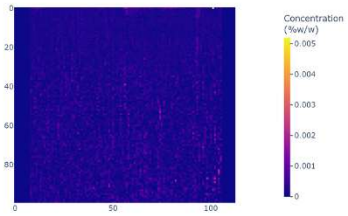
Figure S4.3. Oxide concentration maps for G14.



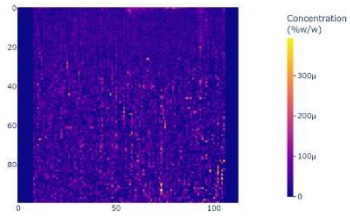
Oxide concentration map for Ga2O3



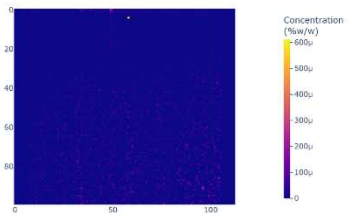
Oxide concentration map for Gd2O3



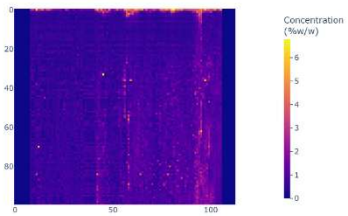
Oxide concentration map for Ho2O3



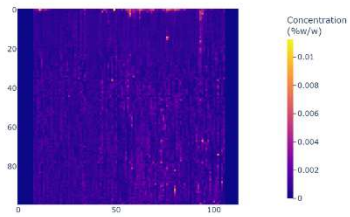
Oxide concentration map for In2O3



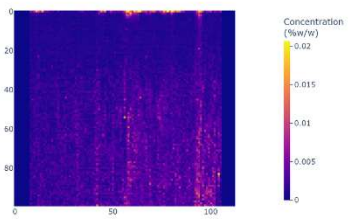
Oxide concentration map for K2O



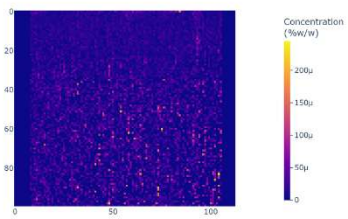
Oxide concentration map for La2O3



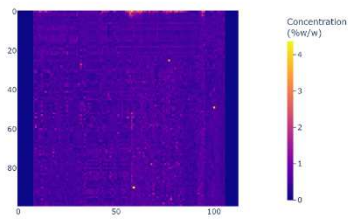
Oxide concentration map for Li2O



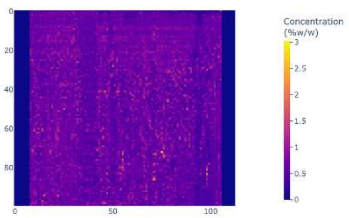
Oxide concentration map for Lu2O3



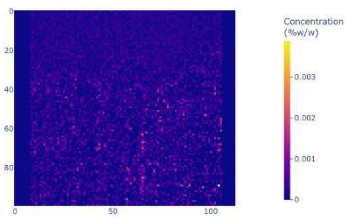
Oxide concentration map for MgO



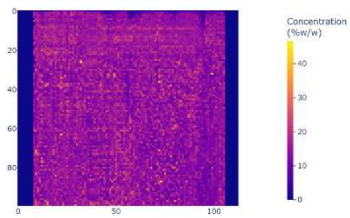
Oxide concentration map for MnO



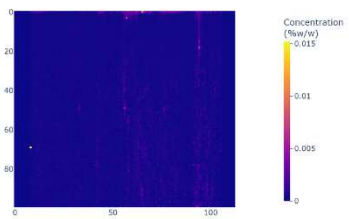
Oxide concentration map for MoO3



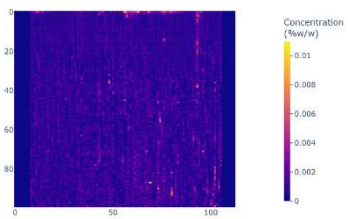
Oxide concentration map for Na2O



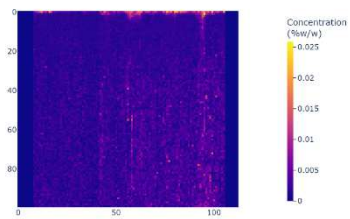
Oxide concentration map for Nb2O5



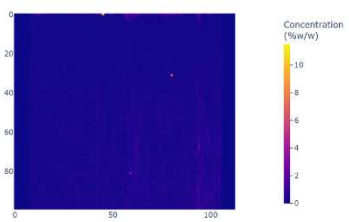
Oxide concentration map for Nd2O3



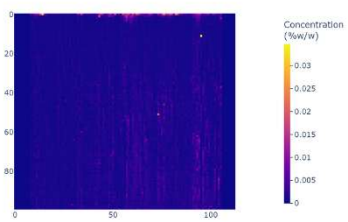
Oxide concentration map for NiO



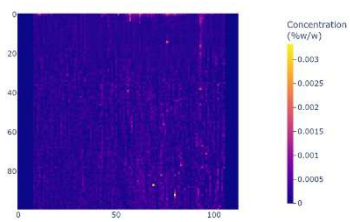
Oxide concentration map for P2O5



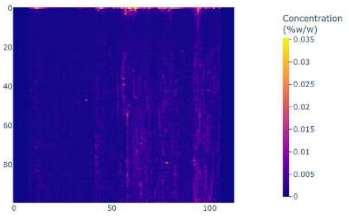
Oxide concentration map for PbO



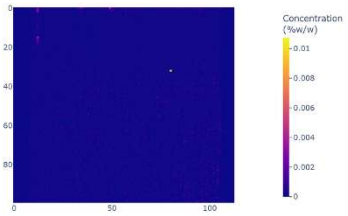
Oxide concentration map for Pr2O3



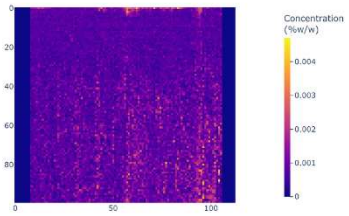
Oxide concentration map for Rb2O



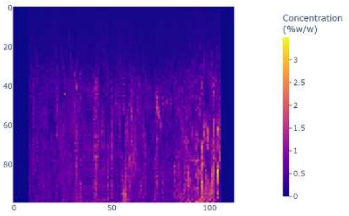
Oxide concentration map for Sb2O5



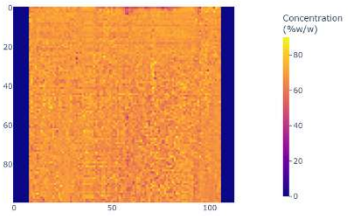
Oxide concentration map for Sc2O3



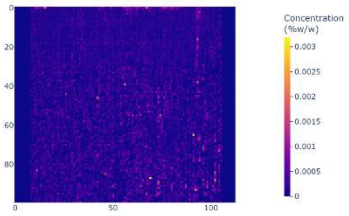
Oxide concentration map for SeO2



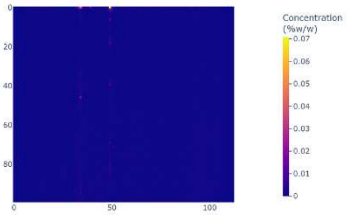
Oxide concentration map for SiO2



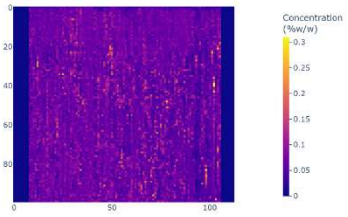
Oxide concentration map for Sm2O3



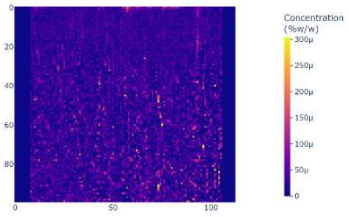
Oxide concentration map for SnO2



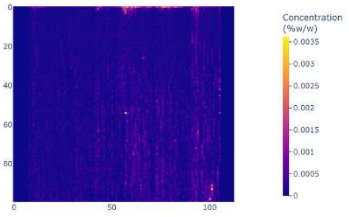
Oxide concentration map for SrO



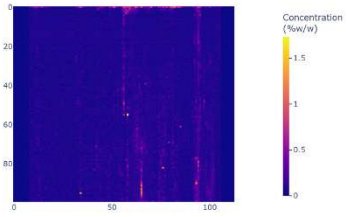
Oxide concentration map for Tb2O3



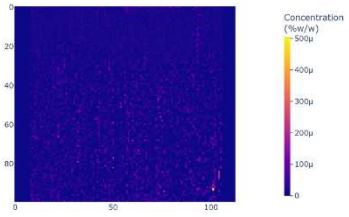
Oxide concentration map for ThO2



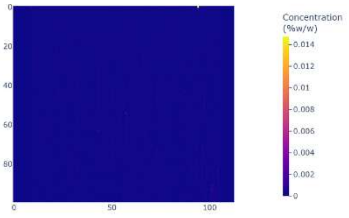
Oxide concentration map for TiO2



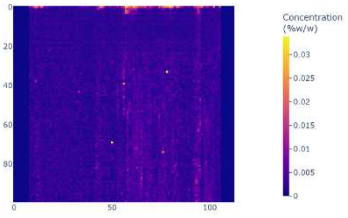
Oxide concentration map for Tm2O3



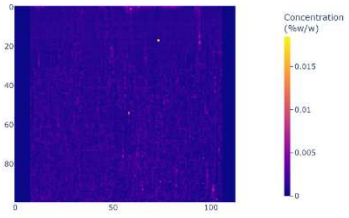
Oxide concentration map for UO2



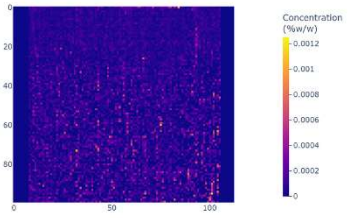
Oxide concentration map for V2O5



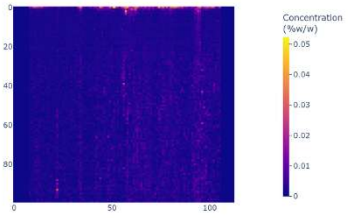
Oxide concentration map for Y2O3



Oxide concentration map for Yb2O3



Oxide concentration map for ZnO



Oxide concentration map for ZrO2

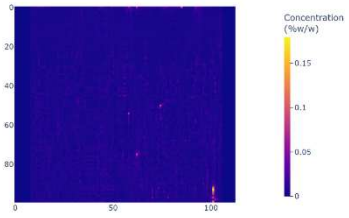
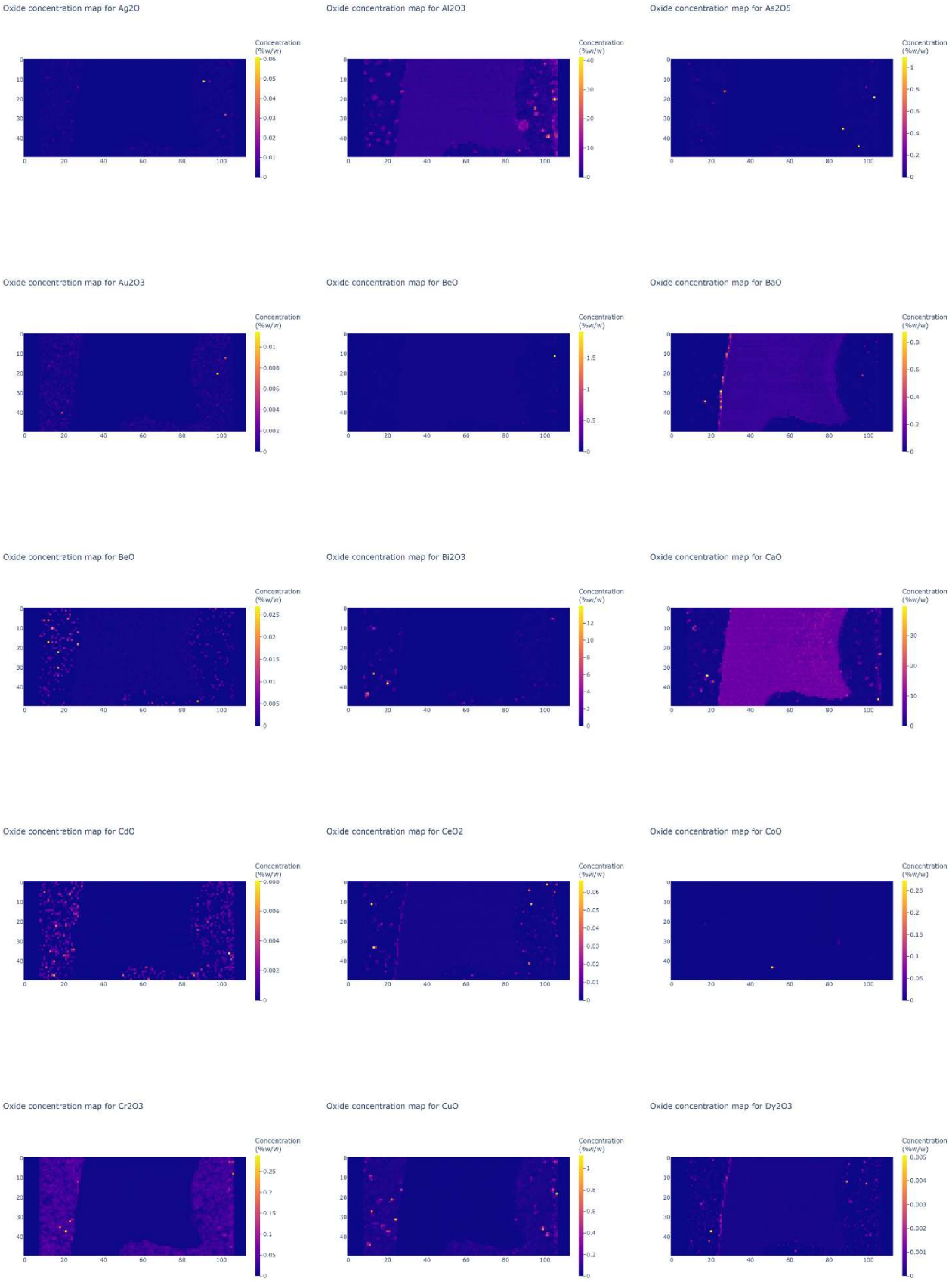
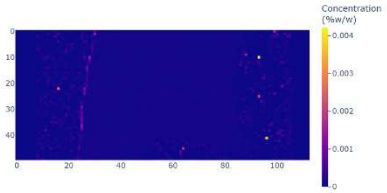


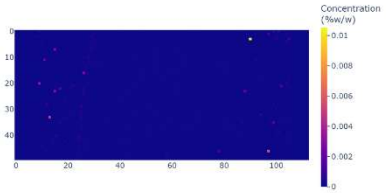
Figure S4.4. Oxide concentration maps for G9 embedded in resin.



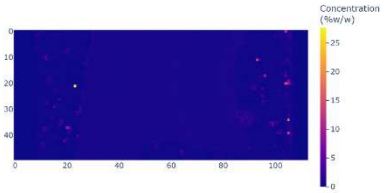
Oxide concentration map for Er2O3



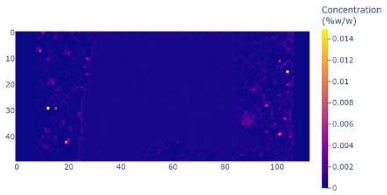
Oxide concentration map for Eu2O3



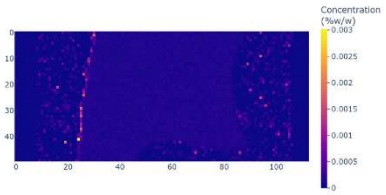
Oxide concentration map for Fe2O3



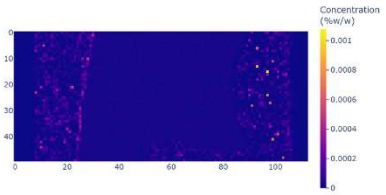
Oxide concentration map for Ga2O3



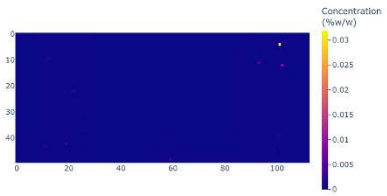
Oxide concentration map for Gd2O3



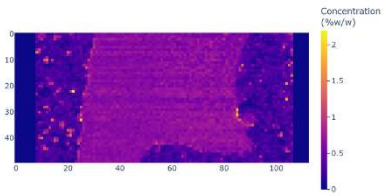
Oxide concentration map for Ho2O3



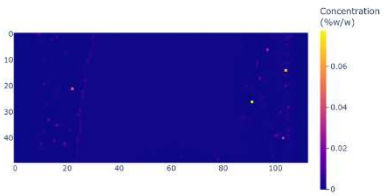
Oxide concentration map for In2O3



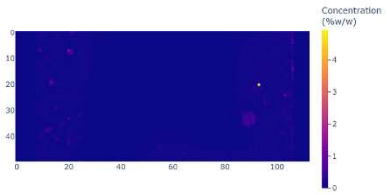
Oxide concentration map for K2O



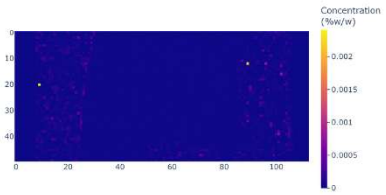
Oxide concentration map for La2O3



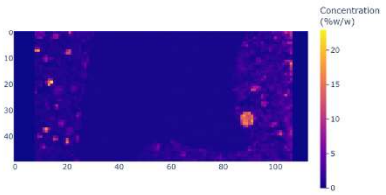
Oxide concentration map for Li2O



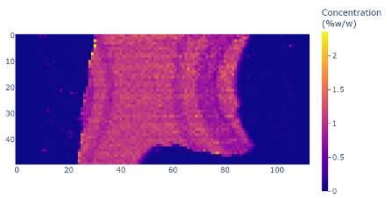
Oxide concentration map for Lu2O3



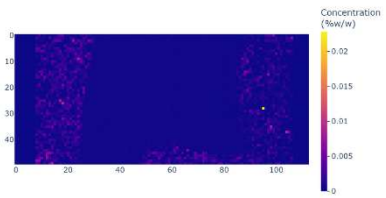
Oxide concentration map for MgO



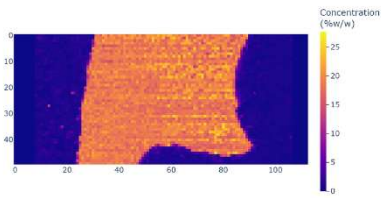
Oxide concentration map for MnO



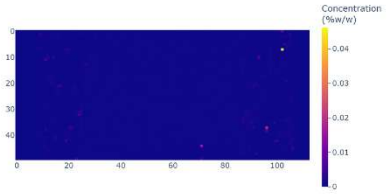
Oxide concentration map for MoO3



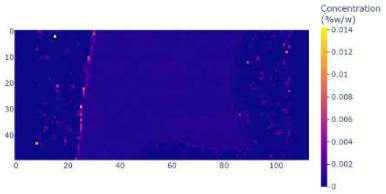
Oxide concentration map for Na2O



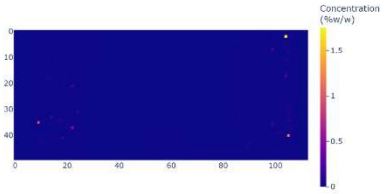
Oxide concentration map for Nb2O5



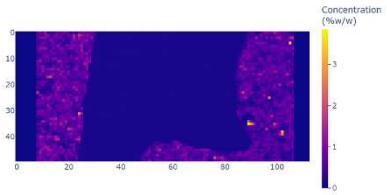
Oxide concentration map for Nd2O3



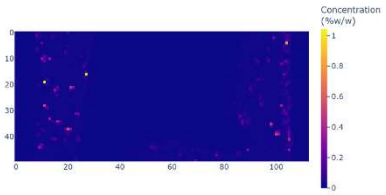
Oxide concentration map for NiO



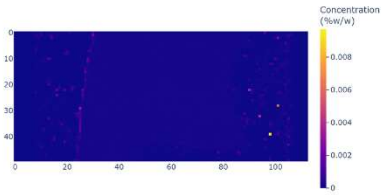
Oxide concentration map for P2O5



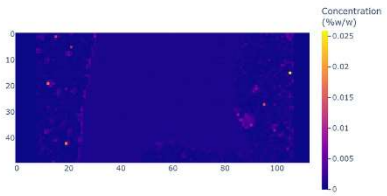
Oxide concentration map for PbO



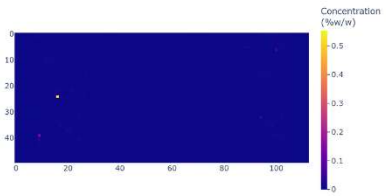
Oxide concentration map for Pr2O3



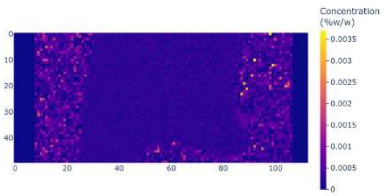
Oxide concentration map for Rb2O



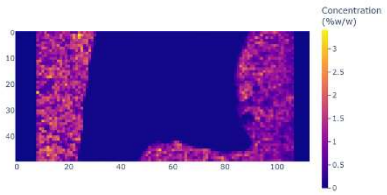
Oxide concentration map for Sb2O5



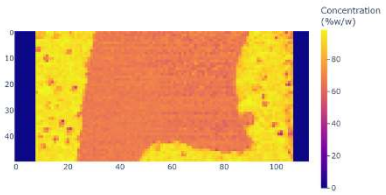
Oxide concentration map for Sc2O3



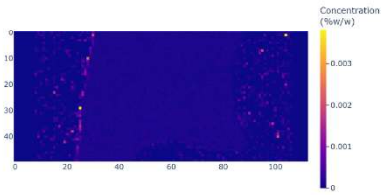
Oxide concentration map for SeO2



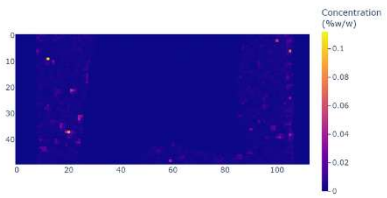
Oxide concentration map for SiO2



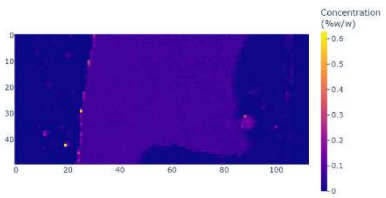
Oxide concentration map for Sm2O3



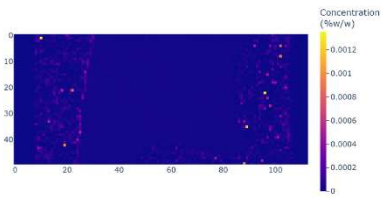
Oxide concentration map for SnO2



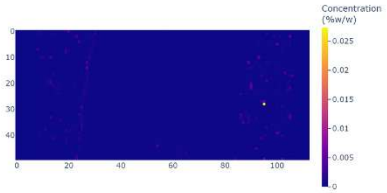
Oxide concentration map for SrO



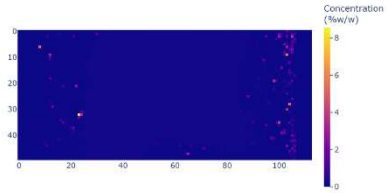
Oxide concentration map for Tb2O3



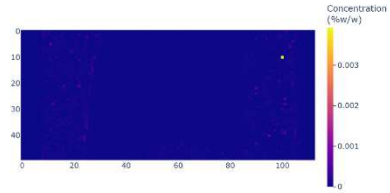
Oxide concentration map for ThO2



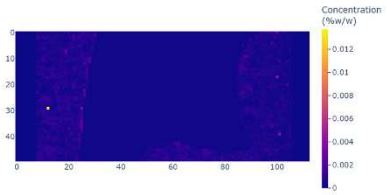
Oxide concentration map for TiO2



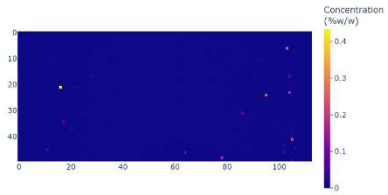
Oxide concentration map for Tm2O3



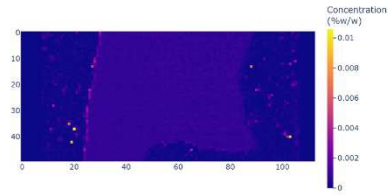
Oxide concentration map for UO2



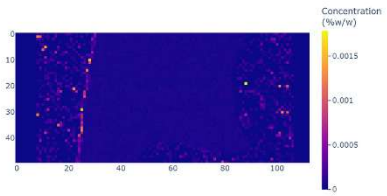
Oxide concentration map for V2O5



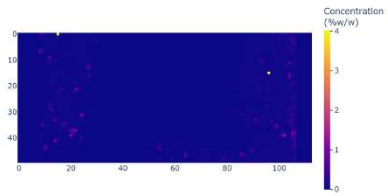
Oxide concentration map for Y2O3



Oxide concentration map for Yb2O3



Oxide concentration map for ZnO



Oxide concentration map for ZrO2

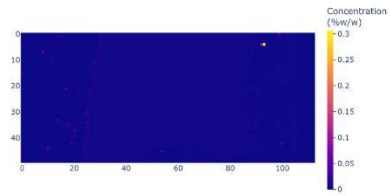
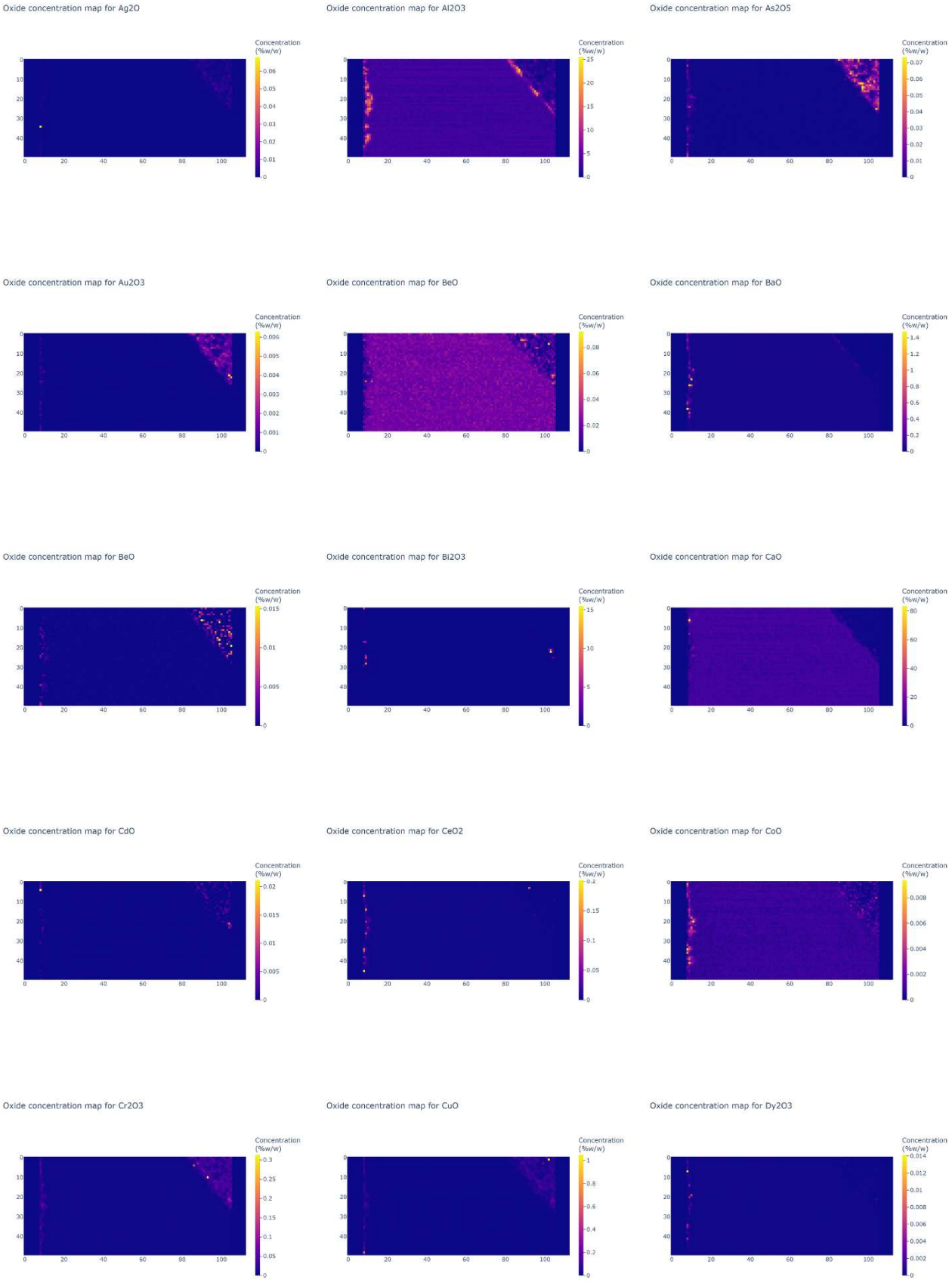
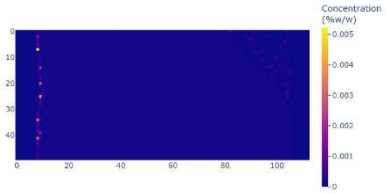


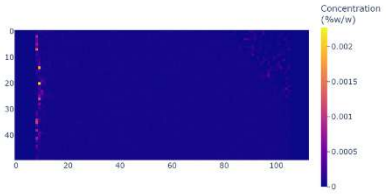
Figure S4.5. Oxide concentration maps for G14 embedded in resin.



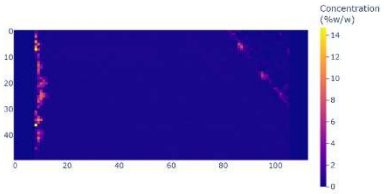
Oxide concentration map for Er2O3



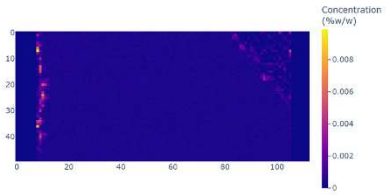
Oxide concentration map for Eu2O3



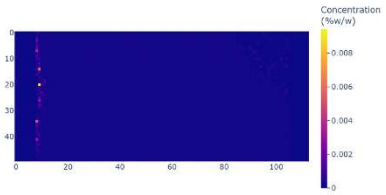
Oxide concentration map for Fe2O3



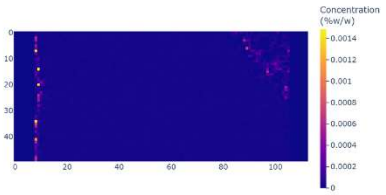
Oxide concentration map for Ga2O3



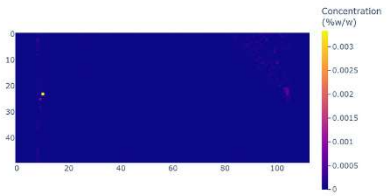
Oxide concentration map for Gd2O3



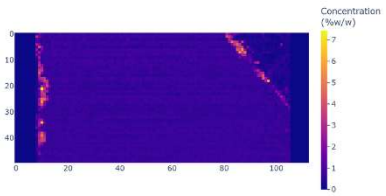
Oxide concentration map for Ho2O3



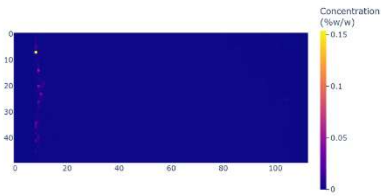
Oxide concentration map for In2O3



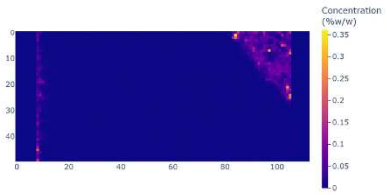
Oxide concentration map for K2O



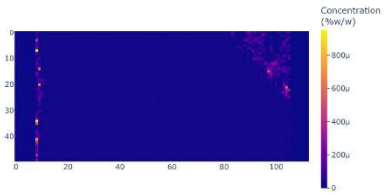
Oxide concentration map for La2O3



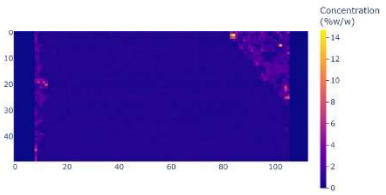
Oxide concentration map for Li2O



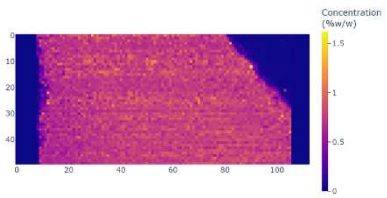
Oxide concentration map for Lu2O3



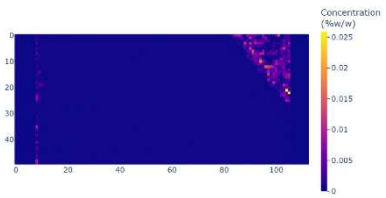
Oxide concentration map for MgO



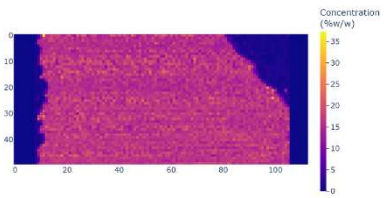
Oxide concentration map for MnO



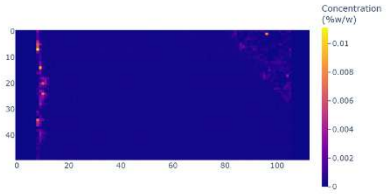
Oxide concentration map for MoO3



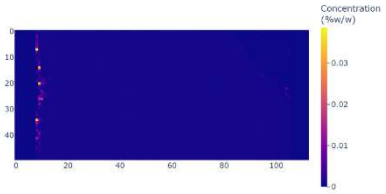
Oxide concentration map for Na2O



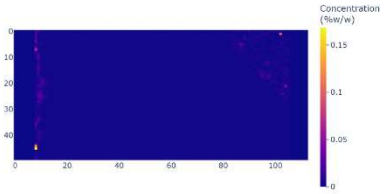
Oxide concentration map for Nb2O5



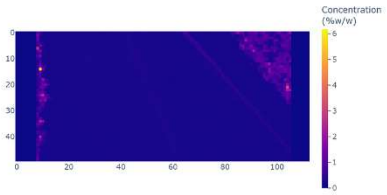
Oxide concentration map for Nd2O3



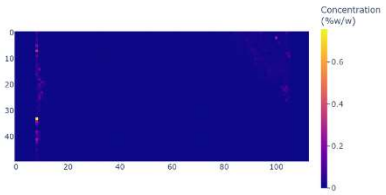
Oxide concentration map for NiO



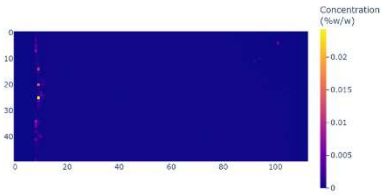
Oxide concentration map for P2O5



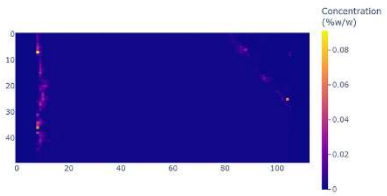
Oxide concentration map for PbO



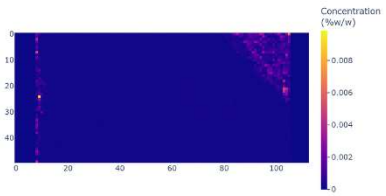
Oxide concentration map for Pr2O3



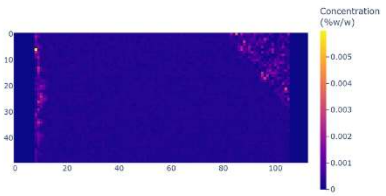
Oxide concentration map for Rb2O



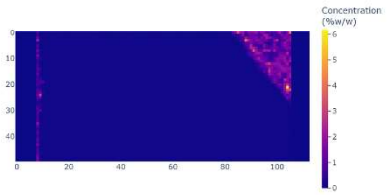
Oxide concentration map for Sb2O5



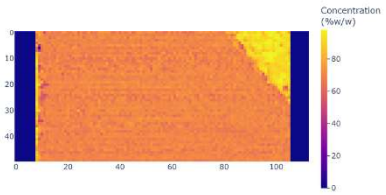
Oxide concentration map for Sc2O3



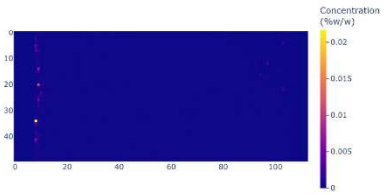
Oxide concentration map for SeO2



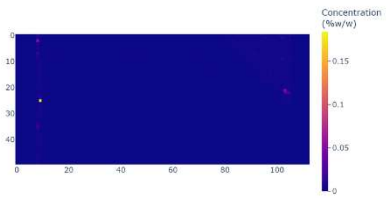
Oxide concentration map for SiO2



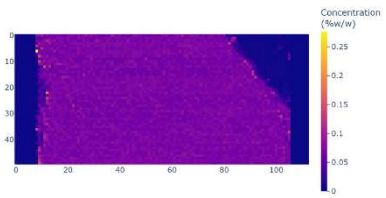
Oxide concentration map for Sm2O3



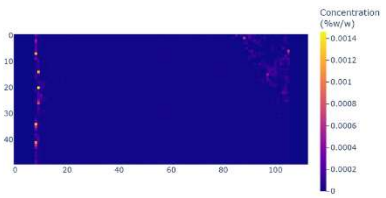
Oxide concentration map for SnO2



Oxide concentration map for SrO



Oxide concentration map for Tb2O3



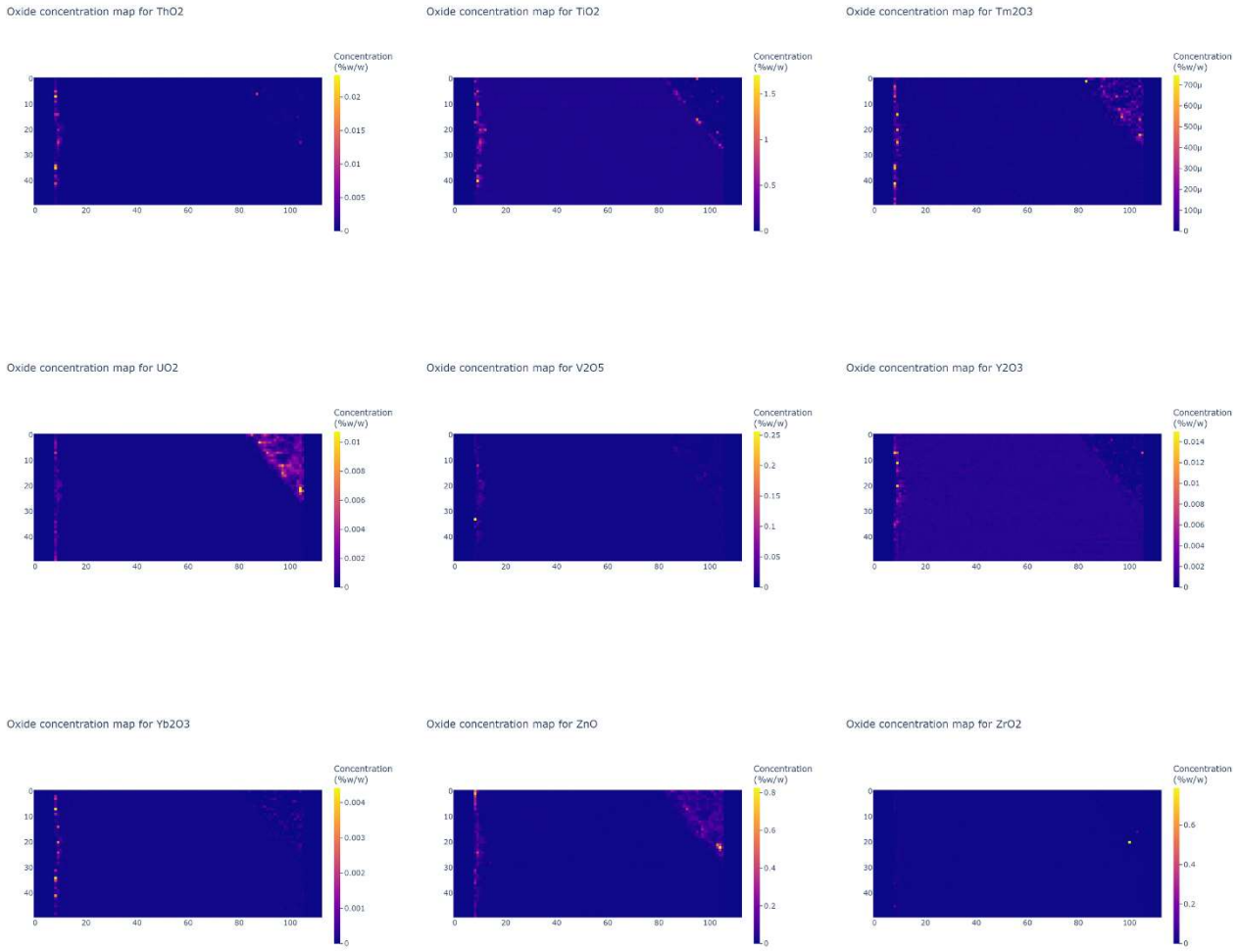
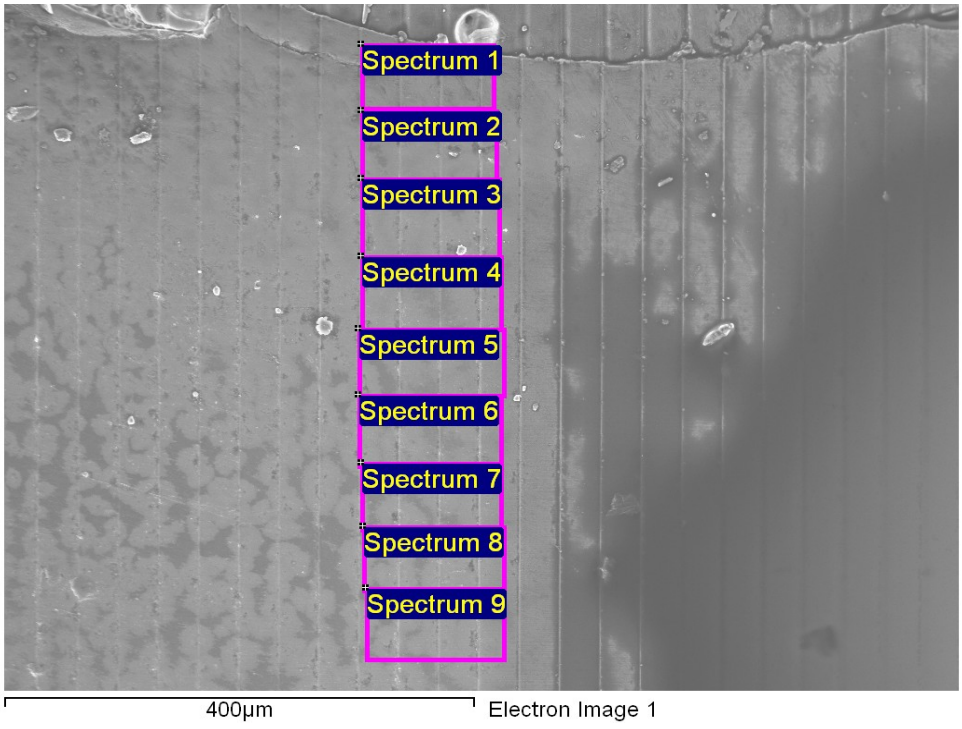


Figure S4.6. EDX spectra for G9.



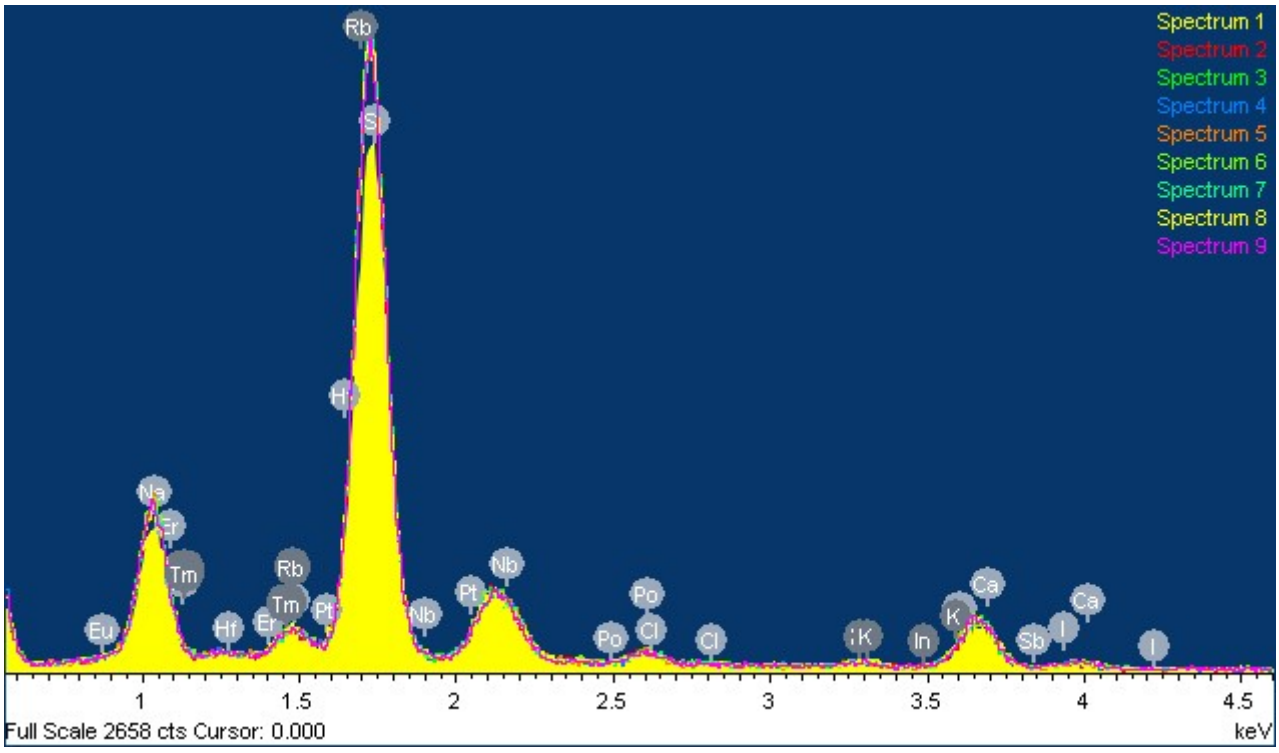
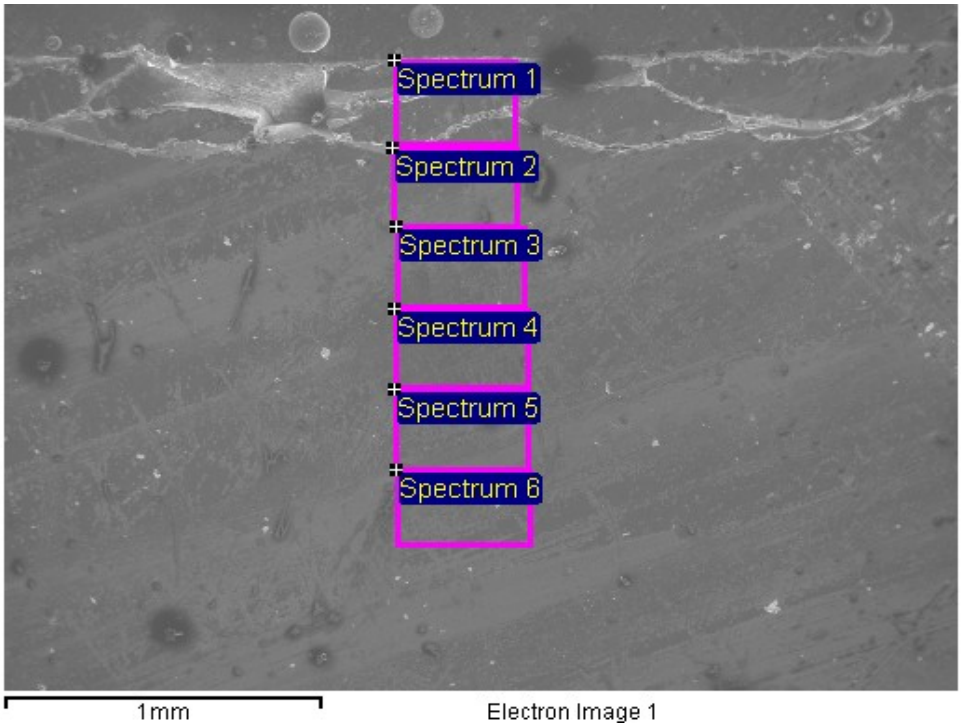


Figure S4.7. EDX spectra for G14.



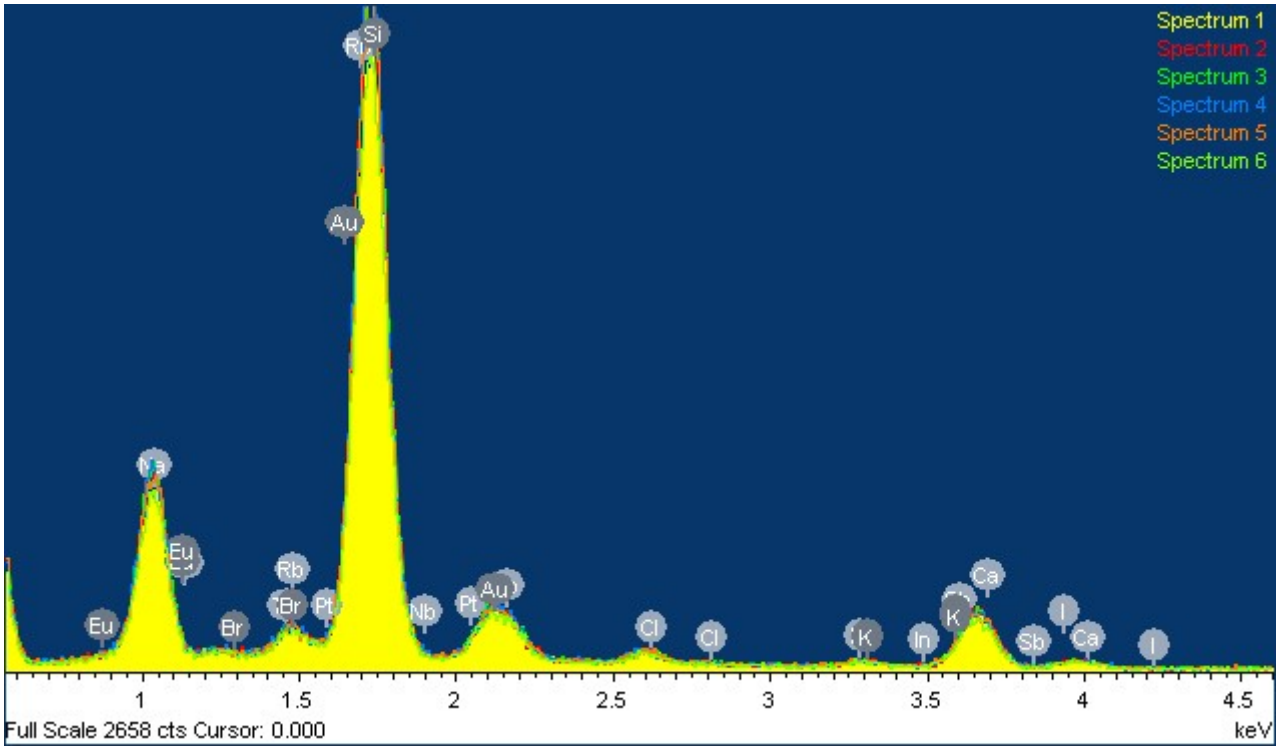
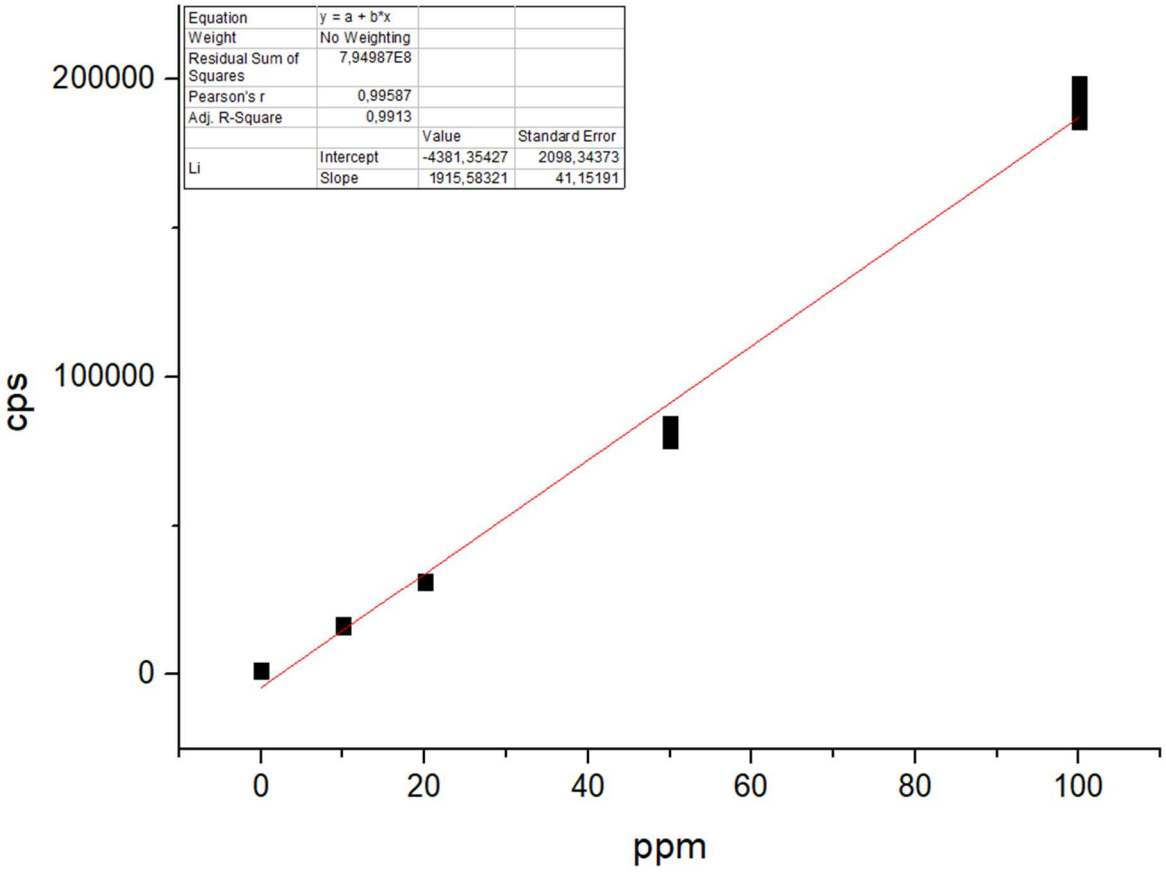
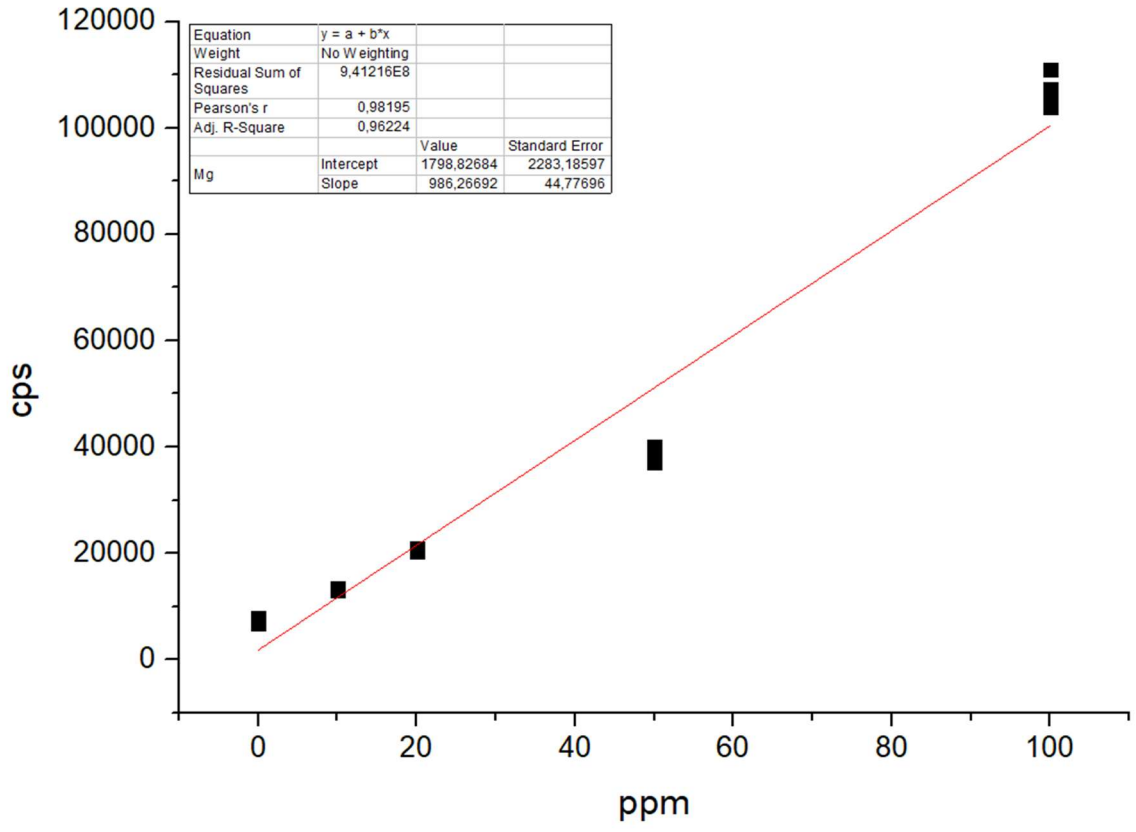


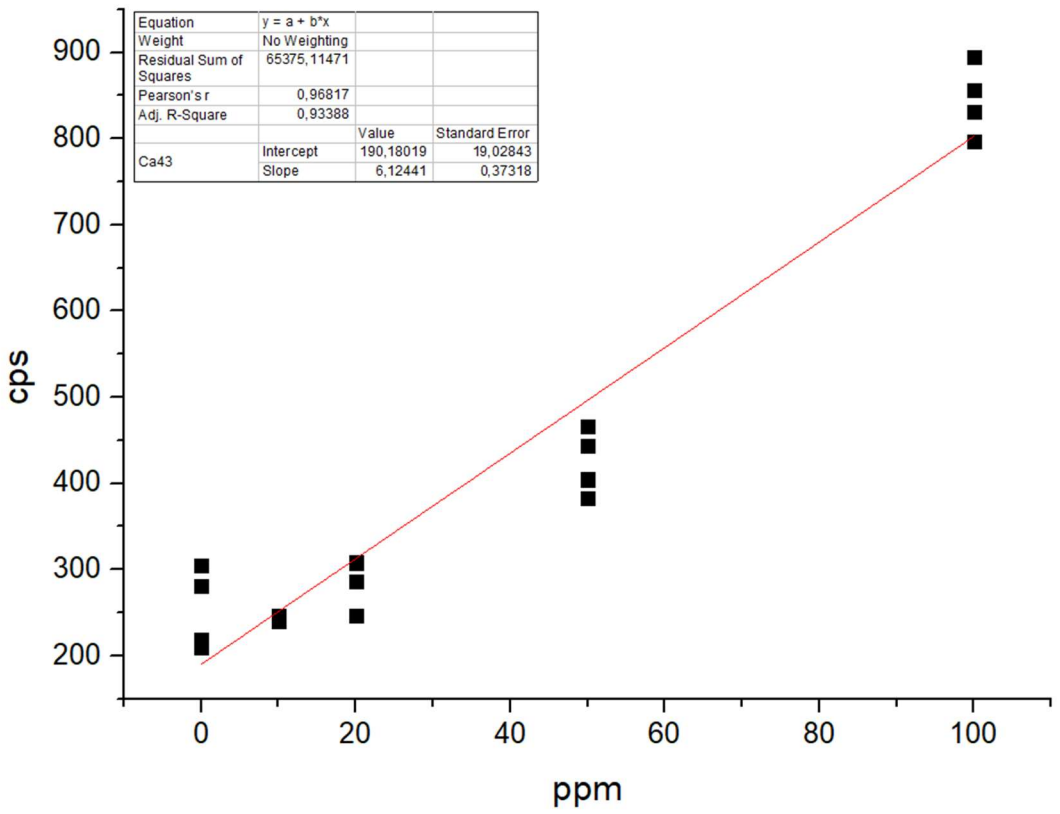
Table S4.5. CPS signals of elements detected at minor and trace concentration levels.

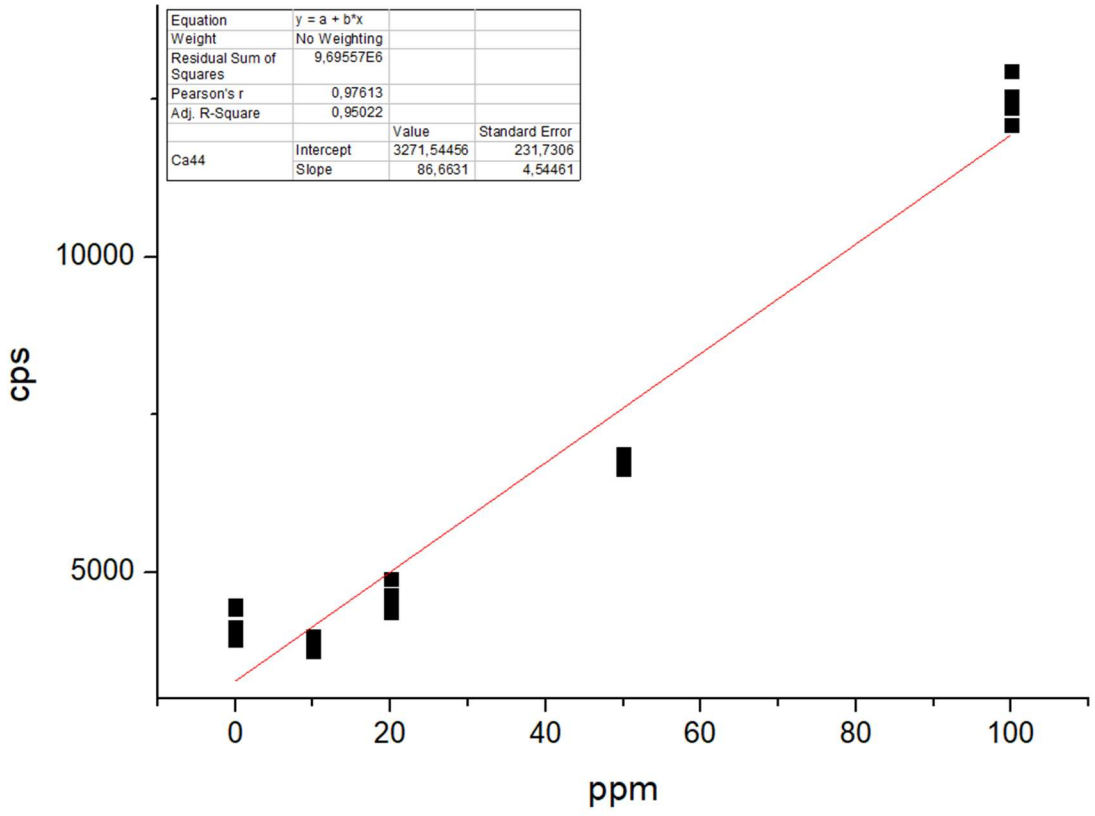
	Al27	*V51*	*Cr52*	*Mn55*	*Co59*	*Ni60*	*As75*	*Cd111*	*Sn118*	*Sb121*	*Hg201*	*Pb208*
						GELATINES						
Blank	2672±113	594±25	7650±260	189±50	9±19	19±15	32±26	10±7	42±54	49±11	271±60	11±16
0.1ppb	2281±80	401±19	7860±150	174±79	18±12	19±12	31±18	1±5	31±45	43±15	160±140	18±11
0.5ppb	2820±100	577±30	8120±170	185±62	31±22	8±25	35±33	6±8	24±29	45±21	200±110	43±24
1ppb	2334±93	580±26	8410±240	350±48	189±7	68±7	52±20	10±7	58±29	42±9	237±39	212±17
5ppb	2420±54	386±19	8230±150	115±98	8±22	28±44	41±14	3±4	26±20	50±5	229±25	19±8
10ppb	2306±68	578±28	7910±270	275±60	103±13	53±53	51±32	7±5	34±15	37±8	242±13	62±9
						SERUM						
L1	90±150	45±31	6160±470	599±205	45±52	78±94	27±26	5±7	20±45	705±65	897±95	68±33
L2	3600±500	70±15	6370±230	1190±340	164±30	95±73	39±55	15±8	33±63	289±44	900±270	91±58

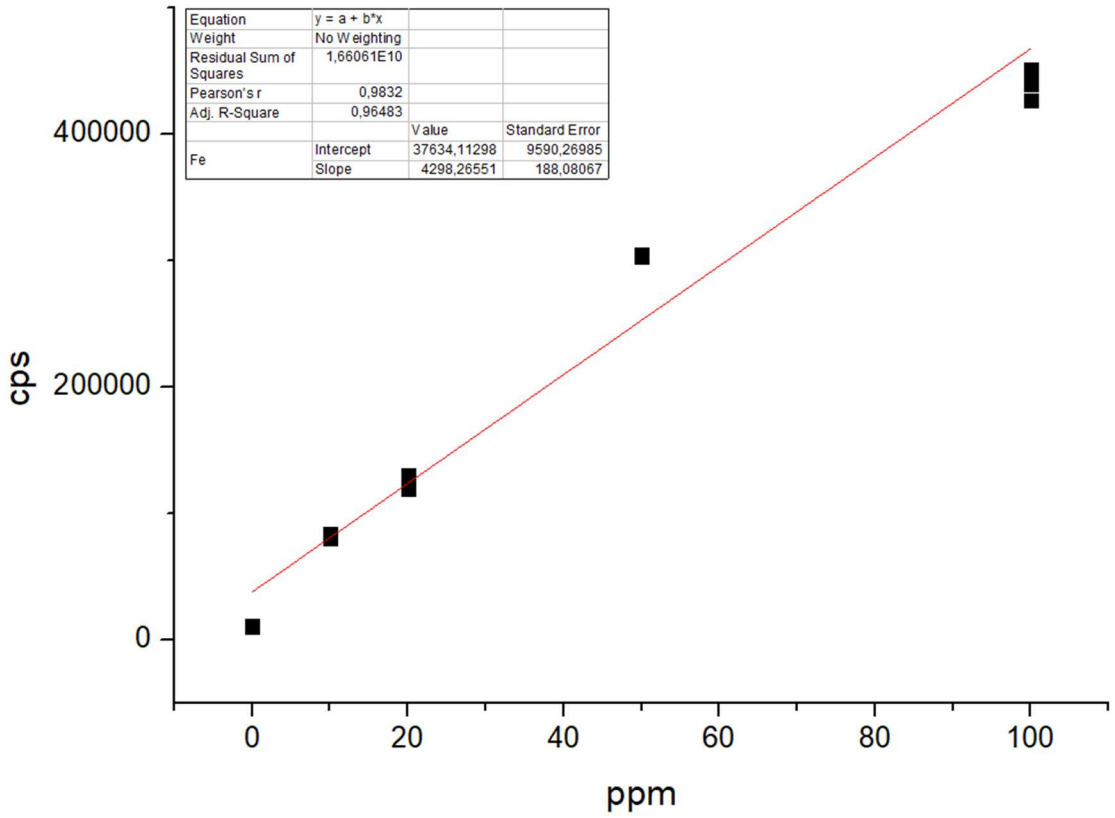
Figure S4.8. Elemental calibration curves for major constituents in gelatines.

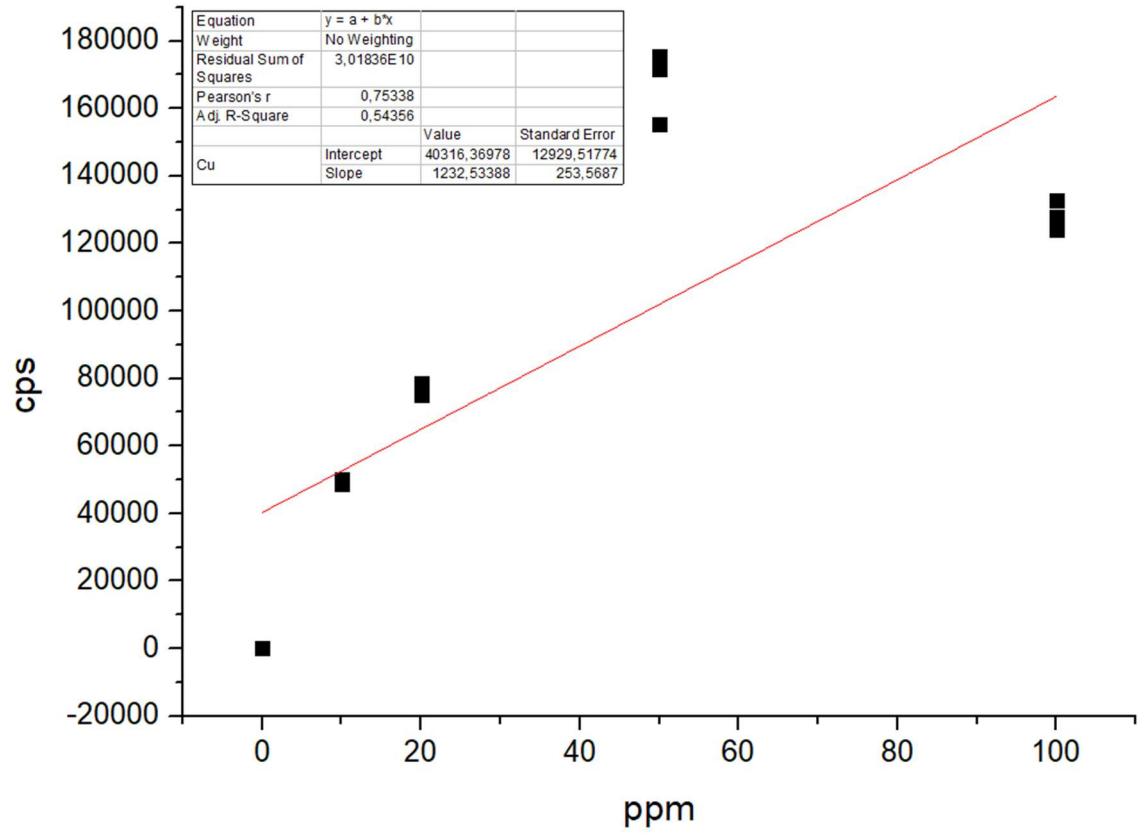





Equation y = a + b*x
Weight No Weighting
Residual Sum of Squares 65375,11471
Pearson's r 0,96817
Adj. R-Square 0,93388
Value Standard Error
Ca43 Intercept 190,18019 19,02843
Slope 6,12441 0,37318
cps
ppm
900
800
700
600
500
400
300
200
0
20
40
60
80
100


Equation y = a + b*x
Weight No Weighting
Residual Sum of Squares 9,69557E6
Pearson's r 0,97613
Adj. R-Square 0,95022
Value Standard Error
Ca44 Intercept 3271,54456 231,7306
Slope 86,6631 4,54461
cps
ppm
10000
5000
0
20
40
60
80
100


Equation y = a + b*x
Weight No Weighting
Residual Sum of Squares 1,66061E10
Pearson's r 0,9832
Adj. R-Square 0,96483
Value Standard Error
Fe Intercept 37634,11298 9590,26985
Slope 4298,26551 188,08067
cps
ppm
0
200000
400000
0
20
40
60
80
100


Equation y = a + b*x
Weight No Weighting
Residual Sum of Squares 3,01836E10
Pearson's r 0,75338
Adj. R-Square 0,54356
Value Standard Error
Cu Intercept 40316,36978 12929,51774
Slope 1232,53388 253,5687
cps
ppm
-20000
0
20000
40000
60000
80000
100000
120000
140000
160000
180000
0
20
40
60
80
100

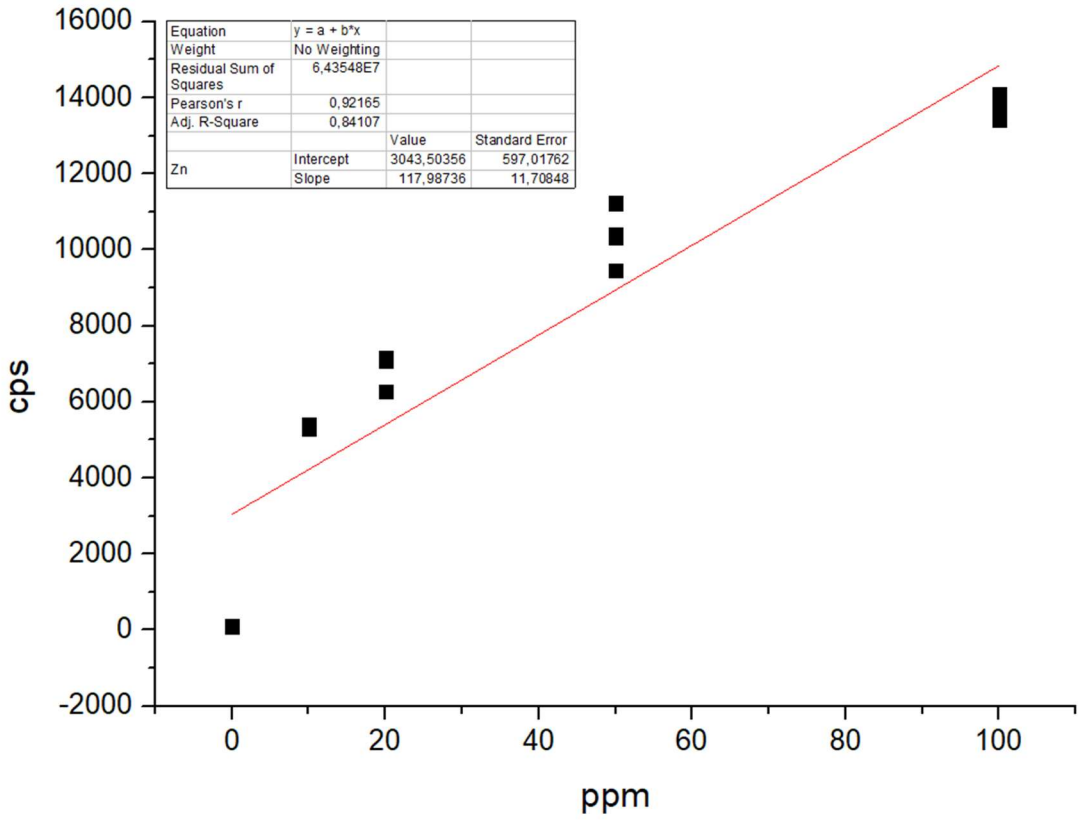


Figure S4.9. Size distribution histogram of PtNPs with log-normal fit.

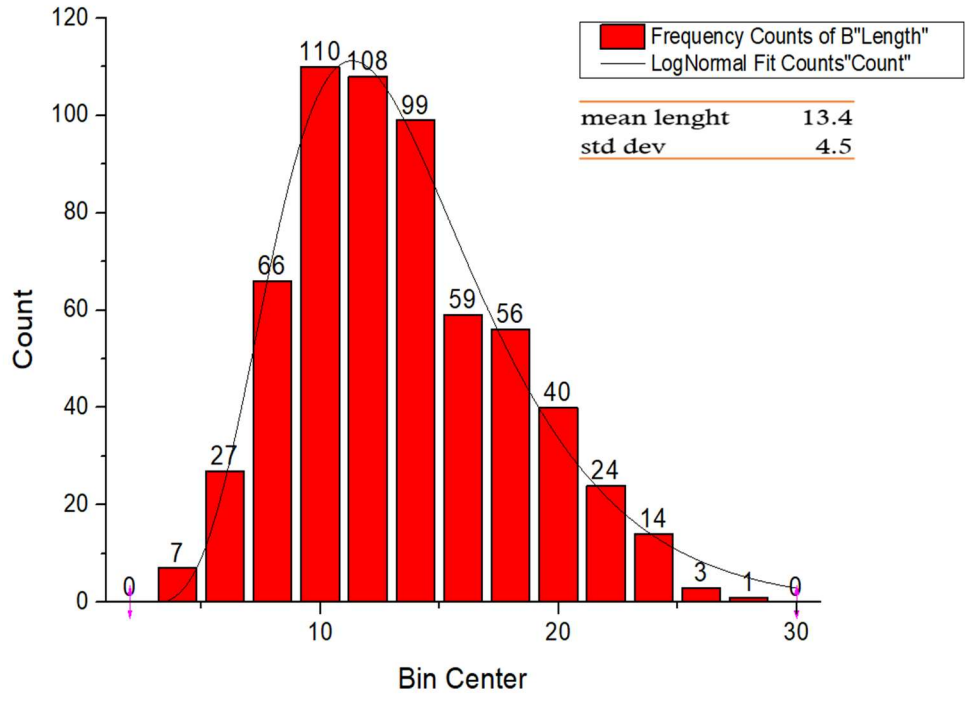


Figure S4.10. SPR spectrum for NPs diluted solution.

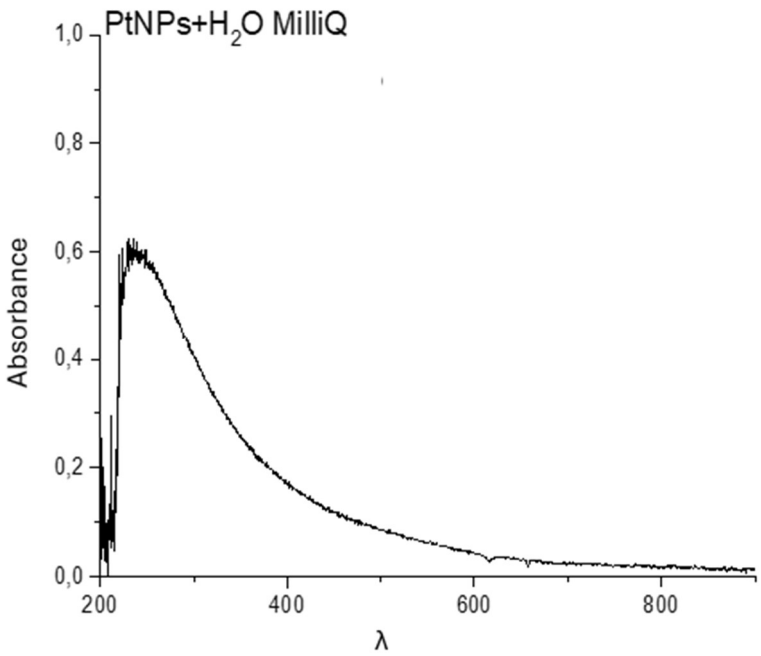


Figure S4.11. RStudio script for generating a colour-coded map.

```
# Sample 2D data

x <- 1:10
y <- 1:11
data <- matrix(c(“insert data”
), nrow = length(y), ncol = length(x), byrow = TRUE)


# Use a different color palette

colors <- colorRampPalette(c("azure", "springgreen", "blue", "darkmagenta"))(100)


# Transpose the data matrix to match the expectations of the levelplot function

data <- t(data)


# Create a levelplot with a color bar using the new color palette

levelplot(data, col.regions = colors,
      main = "2D Map with Color-Coded Data",
      xlab = "X Values", ylab = "Y Values",
      colorkey = list(labels = list(at = pretty(range(data), n = 5))))
```

Table S4.6. CPS signals of elements detected for serum L1 samples with varying NP volumes.

		Li7	C12	Na23	Mg24	Al27	K39	Ca43	Cr52	Fe57	Co59	Ni60	Cu63	Zn66	Se82	Sn118	Sb121	Au197	Pb208
L1		397689.1	28654145	6.18E+08	139845	1762.976	205997	16116.13	57975.83	2505.016	80.4015	88.86806	39258.06	4315.895	27.58221	48.67753	1422.59	7048.243	171.87
	std err	8328.425	244698.8	60231014	21726.92	142.0802	438672.9	438.1687	604.2785	215.5808	4.305674	5.296005	755.9971	40.33322	26.72375	22.82865	484.796	60.91824	11.55386
L1+1NP		431863.7	29938535	7.15E+08	142818	16507.68	234705	16054.58	60182.34	2595.582	102.3299	243.4989	38816.64	4521.969	-11.84	74.29102	926.9209	6794.033	644.4557
	std err	6637.535	196443.2	55460232	12664.4	7639.127	491261.9	343.2989	426.0096	224.3587	4.168393	5.910005	425.2522	32.15225	38.91501	17.20165	22.42211	33.08672	47.57993
L1+2NP		434134.9	28588421	5.07E+08	148429	16706.2	235403	16659.92	57378.71	2369.325	98.30757	291.829	38369.89	4889.807	-4.445	79.50856	947.3392	7001.884	653.3963
	std err	11479.77	399016.8	26612281	32900.73	3117.711	629673.1	206.0002	1139.272	168.4662	4.971792	6.889623	804.1731	109.7216	16.27656	14.31724	21.93358	108.3903	28.04044
L1+5NP		424237.4	27264172	1.02E+09	155842	28650.42	251073	16549.79	55100.02	2857.706	138.3679	389.1484	41979.4	4780.506	43.82188	99.31329	951.2671	6647.162	2069.149
	std err	9027.605	111314.4	1.03E+08	70361.8	18926.14	862350.7	297.9725	576.6367	296.8626	6.498644	21.73899	970.2377	59.86923	40.29204	8.322546	19.13379	43.24704	27.04018
L1+8NP		490271.8	29213547	3.75E+08	160388	6891.096	284813	18408.9	61277.34	2594.04	152.6963	545.6399	39898.26	5332.955	-10.09	124.0527	979.4945	7442.819	683.3997
	std err	24276.24	743661.3	64361488	46537.57	1580.711	196896.6	228.7365	1216.181	240.7506	7.724119	20.19258	870.9473	184.8486	22.28182	17.58295	35.07228	170.2109	61.18825
L1+15NP		434571.7	30192180	7.41E+08	151901	43773.07	207762	18644.19	62569.97	3861.474	223.7861	929.5604	43243.23	6254.026	1.9945	181.1745	1137.399	7268.693	1030.858
	std err	34203.58	127092.6	68263818	76711.47	29986.02	179895.3	891.1609	2401.883	981.4881	7.105636	36.93597	1516.123	151.7735	19.55053	14.69782	156.4271	272.0215	48.61377
L1+25NP		461041	29019399	7.9E+08	157771	13424.07	260814	19293.78	59327.01	2702.887	285.8662	1341.272	46385.87	6659.65	44.03189	211.2628	981.2181	8230.158	1238.282
	std err	13418.65	287610	61637751	26577.39	280.0402	122977.7	251.4428	826.8717	101.2059	9.875278	7.658826	816.252	185.3717	32.70488	9.581662	14.39872	63.19165	61.72472

Table S4.7. CPS signals of elements detected for serum L2 samples with varying NP volumes.

		Li7	C12	Na23	Mg24	Al27	K39	Ca43	Cr52	Fe57	Co59	Ni60	Cu63	Zn66	Se82	Sn118	Sb121	Au197	Pb208
L2		695263.7	30433773	5.07E+08	334563	23769.94	276666	28282.04	59771.47	3914.074	193.1668	215.6956	59409.99	6995.417	72.92981	96.85935	742.3545	26989.6	329.3765
	std err	13019.05	406497.5	32687846	51447.99	4476.726	663948.7	495.8623	893.1262	321.8268	6.55549	3.05993	1181.571	207.5555	16.15796	10.21645	377.9872	224.6711	11.08291
L2+1NP		656987.2	26242841	5.62E+08	289663	13073	320269	25528.99	51190.93	2640.822	178.2258	251.7573	52803.56	5460.366	35.43093	82.91866	300.0048	23299.22	345.8075
	std err	14446.41	276311.9	35057486	25229.05	610.8454	269531.6	275.5665	740.7276	104.1376	4.722518	12.91326	703.7708	103.1365	14.42204	13.47091	16.38666	344.9825	25.2207
L2+2NP		736655.1	28090573	6.45E+08	320321	23229.78	302824	27373.32	55516.59	3433.71	205.9279	354.4059	56978.47	6307.98	58.07475	85.54543	353.4443	24542.56	412.785
	std err	18855.92	455360.8	15264928	73115.59	7022.958	123802.8	926.8172	896.0772	228.7236	2.932213	7.870247	957.1558	102.6681	32.76721	16.09616	23.59473	459.8775	8.841823
L2+5NP		747767.4	27805100	5.7E+08	296894	12661.71	475531	24247.44	54055.43	2874.661	208.3354	521.8244	55704.89	6615.881	49.89619	139.998	326.9938	26097.16	680.9982
	std err	19621.98	347502	23724020	49943.18	1256.517	315378.6	416.1779	623.0915	164.0634	8.804625	7.449213	1008.609	71.21969	18.75106	4.381741	16.11288	407.6379	26.28932
L2+8NP		700792.2	27494036	5.49E+08	301183	33409.08	371403	25445.07	55564.26	3226.943	231.3475	667.2102	54923.45	6309.513	81.10753	130.8225	391.0178	23324.85	645.227
	std err	12655.08	240725.7	52312355	46397.17	19985.94	852607.4	313.2576	412.7623	295.8172	11.86206	16.64271	442.9456	79.30912	18.35646	12.22063	106.523	266.31	41.68598
L2+15NP		817969.3	31578491	6.4E+08	353295	24632.63	332578	22955.08	65617.99	5144.887	403.1152	1621.976	72976.14	9075.328	30.03951	151.8655	388.3563	29168.84	967.6801
	std err	39324.17	129700.1	20652182	16663.1	3001.551	166596.6	1430.496	3235.666	1316.506	11.51381	26.83313	4057.171	596.8948	30.77818	12.96856	14.49196	1051.667	17.87647
L2+25NP		744211.3	30246362	8.63E+08	284622	18624.29	399814	23164.93	62078.55	2722.69	442.0866	1755.152	57976.76	7308.789	8.95374	203.0736	303.0779	23629.86	1295.002
	std err	15202.39	177386.3	59898049	40027.47	977.5707	130148.6	537.7203	3937.747	62.98505	5.64282	39.06311	1225.662	49.93409	23.90721	5.445694	8.892101	248.9043	40.58963